A thesis on

Exploring Self-Sensing in Shape Memory Alloy Wire Actuators under Practical Loading Conditions

Submitted in partial fulfillment of the requirements for the degree

of

DOCTOR OF PHILOSOPHY

by

Sagar Mohan
166103018

Under the guidance of

Dr. Atanu Banerjee

Department of Mechanical Engineering
Indian Institute of Technology, Guwahati
August, 2023

CERTIFICATE

This is to certify that the work contained in the thesis entitled "**Exploring Self-Sensing in Shape Memory Alloy Wire Actuators under Practical Loading Conditions**" submitted by **Sagar Mohan**, Roll No. 166103018, has been carried out under my supervision for the partial fulfillment of degree of Doctor of Philosophy in the Department of Mechanical Engineering, Indian Institute of Technology Guwahati, and this work has not been submitted elsewhere for the award of any other degree.

Dr Atanu Banerjee
Associate Professor
Department of Mechanical Engineering
Indian Institute of Technology
Guwahati, Assam, India

Acknowledgment

First and foremost, I would like to express my sincere gratitude to my advisor, Dr Atanu Banerjee, for his continuous guidance and support to my PhD research from inception to completion. His patience, motivation, enthusiasm and immense knowledge brought my work to a higher level.

I would also like to thank the rest of my Doctoral committee members - Prof. Santosha K. Dwivedy, Prof. Karuna Kalita and Dr Prithwijit Guha for their encouraging comments and valuable suggestions and ideas to improve the quality of the work.

I would like to thank Mr Dhruba Jyoti Bordoloi, Scientific Officer and Mr Monuranjan Dowarah, Technical Staff of Vibration and Acoustics Laboratory, Department of Mechanical Engineering, IIT Guwahati for providing instruments to carry out the research work. I would also like to thank Prof. Sukhomay Pal, Faculty Incharge, Mr Nandan Kanan Das, Assistant Superintendent, Mr Gautam Gogoi, Jr Technician, Central Workshop; and Dr Manas Das, Faculty Incharge, Mr Pranjol Paul, Scientific Officer, Mr Jiten Basumatary, Technical Superintendent, Advanced Manufacturing Laboratory, IIT Guwahati for providing the necessary help while fabricating the experimental setups.

I would like to thank Prof. Debabrata Chakraborty, Dr Deepak Sharma, Dr Arnab Kumar De and Dr Sameer Kamal, IIT Guwahati, for their valuable guidance during my coursework.

I am thankful to my friends - Dr Anjaly, Manasa, Nayana, Joanne, Akhin, Sagar, Ashwathi, Rithima, Anupama, Akhila, Induchoodan, Vara Prasad, Kaushal and Madhuri, who provided much-needed distractions to rest my mind outside my research. I am also grateful to my colleagues - Animesh, Hema, Swarup, Tejdeep, Umesh and all of the previous MTech students for their stimulating discussions, cooperation and support during my research work.

Words cannot express my gratitude to my parents, K S Mohanan and Radha Mony, and my sister Soumya Mohan for their love and endless support. They have always stood behind me, through thick and thin, and I am greatly indebted. I lovingly dedicate this thesis to all of them. Finally, my warmest regards to everyone else, including all my well-wishers, for making me the person I am here today; thank you.

Sagar Mohan

Abstract

Shape Memory Alloy (SMA) wire actuators offer large force and displacement capabilities out of the stress and temperature-dependent martensitic phase transformation. Among the various modelling approaches in the literature, the one proposed by Boyd and Lagoudas (1996) is primarily used in analysing SMA-based components. In practice, partial actuation is often required and is enacted by aborting and subsequently resuming the phase transformation, exhibiting a minor hysteresis response. The existing models are found to be inaccurate in simulating such partial transformation cases. In this study, two novel yield parameters, which depend on the martensite volume fraction, have been proposed, yielding significant improvement in simulating the minor loop response of SMA. The corresponding model parameters are derived, satisfying certain practical aspects of the SMA behaviour. Using the modified model, pseudoelastic responses are simulated for different partial loading cases. These are compared against the same obtained from the existing models, illustrating the efficacy of the current approach. Following the proposed model, the discrete form of the system dynamics of an SMA wire actuator is formulated. Using this, an Extended Kalman Filter (EKF) has been developed, to estimate the system's output from the change in electrical resistance of the SMA wire during actuation. This approach eliminates the requirement of external sensors for feedback control. Using the developed EKF, the response of an SMA wire actuated system is estimated from the experimentally measured electrical resistance data of the SMA wire and are compared with the corresponding measured responses. The results reveal that a significant level of accuracy can be achieved with the proposed approach.

In practical situations, SMA wires are activated following resistive heating by passing an electrical current through them, whereas deactivation is enacted through environmental cooling or forced cooling. It is observed that for fine wires, the temperature is susceptible

to ambient conditions, *i.e.*, temperature, the velocity of wind, humidity etc., thus severely affecting the performance of these wire actuators. In this study, a particle filter-based state estimation technique has been developed to estimate the outcome of the Shape Memory Alloy wire actuated system, by using the change in electrical resistance data of the wire during actuation. Under stationary ambience, the developed particle filter-based estimator performs as well as the EKF-based estimators. However, both estimators fail when unwanted external cooling is introduced through a fan. To improve on it, both filters are modified, incorporating the convective heat transfer coefficient as an unknown to be estimated in addition to the system's state. The performance of both estimators are evaluated for various loading conditions in the presence of forced cooling of different extents and intensities. Under external cooling conditions, the proposed Particle Filter based estimator outperforms the same based on EKF in almost all loading situations.

In the literature, most of the existing studies harnessing SMA's self-sensing behaviour are limited to linear systems, actuated by SMA wires, undergoing proportional loading. In this study, an SMA wire actuated single degree-of-freedom manipulator, having non-linear force-displacement relation, is examined. The process and measurement models of the dynamic system are derived based on the modified Boyd and Lagoudas model, and a particle filter (PF) has been developed to estimate the system's response, from the measured electrical resistance of the wire. For natural convective cooling, the estimated response is satisfactory. Next, several forced cooling experiments are carried out, where a fan is switched on at different stages of actuation and for varying duration and speed. To address the inaccuracy of the estimated response in forced cooling cases, the PF is modified, appending the convective heat transfer coefficient as one of the parameters to be estimated, rendering significant improvement in estimation. Finally, the manipulator's initial condition is also adjusted to encounter a non-proportional loading situation, and the proposed filter is found to be effectively estimating the system response in this case as well.

Finally, an LSTM-based Deep Neural Network has been implemented to harness the self-sensing capability of SMA wire actuators subjected to forced cooling conditions. For each of the linear and non-linear SMA wire actuators, the neural network is trained for test

cases involving cooling duration of 1s and 5s, transpiring at different stages of actuation and of varying magnitudes. The trained network is then tested for cooling cases involving 3s duration. The resultant DNN provides an estimate of superior accuracy across all test cases, revealing the efficacy of the proposed neural network.

Contents

List of Figures

List of Tables

List of Symbols

M_s	Martensite start temperature
M_f	Martensite finish temperature
A_s	Austenite start temperature
A_f	Austenite finish temperature
C_M	Stress influence slope of SMA in the martensite phase
C_A	Stress influence slope of SMA in the austenite phase
σ_{M_s}	Initiation stress for forward transformation into martensite
σ_{M_f}	Completion stress for forward transformation into martensite
σ_{A_s}	Initiation stress for reverse transformation into austenite
σ_{A_f}	Completion stress for reverse transformation into austenite
ξ	Martensite volume fraction
$\boldsymbol{\varepsilon^t}$	Transformation strain
G	Gibbs free energy
$\boldsymbol{\sigma}$	Stress of SMA wire
$\boldsymbol{\varepsilon}$	Stress of SMA wire
T	Temperature of SMA wire
T_0	Reference temperature
$\boldsymbol{S}$	Effective compliance tensor
$\boldsymbol{\alpha}$	Effective thermal expansion tensor
C_v	Total specific heat
s_0	Total entropy at the reference state
u_0	Total internal energy at reference state
h_f	Transformation hardening function

$\dot{\xi}$	Rate of change of martensite volume fraction
$\boldsymbol{\Lambda}$	Transformation tensor
H	Maximum transformation strain upon complete detwinning
$\boldsymbol{\varepsilon^{t-r}}$	Value of transformation strain at the point of load reversal
$\boldsymbol{\sigma'}$	Deviatoric stress
$\bar{\sigma}'$	von Mises stress
$\bar{\varepsilon}^{t-r}$	Effective transformation strain at the point of reversal
$\|\| \, . \, \|\|^2$	Contraction of the enclosed tensor quantity
Θ	Thermodynamic force conjugate to ξ
Y_f	Threshold yield value
ϕ	Transformation function
ξ_r	Martensite volume fraction (ξ) at the point of reversal
α_M	Thermal expansion coefficient of pure martensite phase
α_A	Thermal expansion coefficient of pure austenite phase
E^M	Modulus of elasticity of pure martensite phase
E^A	Modulus of elasticity of pure austenite phase
$\boldsymbol{X}$	State variable vector
$\boldsymbol{u}$	Input vector
$\boldsymbol{w}$	Process noise
$\boldsymbol{f}$	Non-linear process vector function
$\boldsymbol{Y}$	Output of the system
$\boldsymbol{v}$	Measurement noise
$\boldsymbol{g}$	Non-linear measurement vector function
$\boldsymbol{Q}$	Process noise covariance matrix
$\boldsymbol{M}$	Measurement noise covariance matrix
t_{n+1}	Present time instant
t_n	Previous time instant
$()^-_{n+1}$	a-priori state estimate at present time instant t_{n+1}
$()^+_{n+1}$	posteriori state estimate at present time instant t_{n+1}
$\boldsymbol{P}$	State error covariance

$\boldsymbol{J}$	Jacobian of process vector function
$\bar{\boldsymbol{X}}$	Mean value of state variable vector
$\boldsymbol{K}_{n+1}$	Kalman gain
$\boldsymbol{H}$	Jacobian of measurement vector function
$V(t)$	Applied voltage at any time instant 't'
R_{sma}	Electrical resistance of the SMA wire
A_{surf}	Surface area of the SMA wire
T_a	Ambient temperature
λ	Latent heat of transformation
v_m	Volume of SMA wire
C_v^M	Heat capacity of SMA in complete martensite phase
C_v^A	Heat capacity of SMA in complete austenite phase
h	Heat transfer coefficient
A	Cross-section of the SMA wire,
K_s	Spring stiffness
δ	Compression of the spring
$2L_i$	Initial length of the SMA wire
$2L_c$	Current length of the SMA wire
ρ	Effective electrical resistivity of SMA
ρ_M	Electrical resistivity of SMA in complete martensite phase
ρ_A	Electrical resistivity of SMA in complete austenite phase
R_0	Fixed resistor in voltage divider circuit
V_t	Total voltage drop across the SMA wire and fixed resistor
V_r	Voltage drop across fixed resistor
V_{SMA}	Voltage drop across the SMA wire
e_{RMS}	RMS error in estimation
L_0	Unstretched length of the SMA wire
d	Diameter of SMA wire
e_0	Initial pre-strain of SMA wire
$q_i^{'}$	Conditional probability of the measured state with respect to each of the 'i' particle

q_i	Relative likelihood of each of the 'i' particle
$\boldsymbol{f}_p$	Modified non-linear process vector model
δ_{max}	Maximum spring displacement
σ_{max}	Maximum value of stress
R_p	Radius of the pulley
I_l	Second moment of inertia of the link about its axis of rotation
K_θ	Torsional stiffness of the spring
c	Damping coefficient
M_p	Payload mass
M_l	Mass of the link
g	Acceleration due to gravity
L_l	Effective length of the link
e	Offset distance of the SMA wire from the centre line of the link
θ	Angular position of the link about horizontal
$\dot{\theta}$	Velocity of the link
$\ddot{\theta}$	Acceleration of the link
$\hat{k}_T$	Tangent stiffness

Chapter 1

Introduction

1.1 Introduction

Objects in motion are inconceivable without an actuator. Various types of actuators, such as motors, hydraulic and pneumatic actuators, generate this motion. These actuators are best suited for large systems and are not applicable for miniaturised systems. With the reduction in the size of the components, smart materials-based actuators are a better choice. These materials include Piezoelectric, Magneto and Electrostrictive ceramics, Shape Memory alloys (SMA), etc. The SMA possess the maximum energy density of these materials but offers low actuation frequency [1]. SMAs are a unique group of materials, which can recall its high-temperature state, even after undergoing large strains while subjected to mechanical load. This attribute of SMA makes it one of the most viable solutions for miniature actuator applications.

Shape memory alloys generally exist in two different phases, namely the Martensite phase and the Austenite phase. The low-temperature phase of SMA is known as Martensite (M) Phase. They are reported to have a monoclinic crystal structure and possess low elastic modulus. The high-temperature phase of SMA is termed as Austenite (A) phase, commonly called as the parent phase. They have a body-centered cubic (BCC) crystal structure and possess a higher elastic modulus than martensite. A typical phase diagram of a thermally activated Shape Memory Alloy is shown in Fig 1.1, depicting all the different phases and transformation temperatures. Here, the four transformation temperatures,

martensite start, martensite finish, austenite start and austenite finish, are respectively denoted as M_s, M_f, A_s and A_f. These values are defined for SMA in zero-stress condition. However, the transformation temperatures increase with an increase in the stress, as depicted by the inclined straight lines originating from the respective temperature at zero stress, as illustrated in Fig.1.1. The slopes of these inclined lines corresponding to M_s and M_f, and A_s and A_f are denoted as C_M and C_A, respectively. They are also referred to as stress influence coefficients. σ_{M_s} represents the stress level at which SMA in A-phase starts directly transforming into M-Phase, while following a Pseudoelastic loading path. The forward transformation terminates at a stress of σ_{M_f}. The corresponding start and finish stress levels during the reverse transformation are denoted as σ_{A_s} and σ_{A_f}.

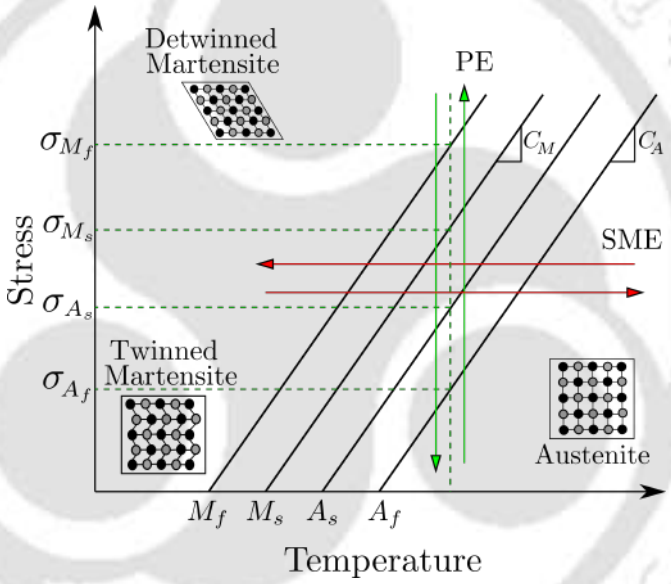

Figure 1.1: Schematic of stress (σ) - temperature (T) phase diagram of SMA.

1.2 Thermo-Mechanical Behaviour of SMA

Shape Memory Alloys (SMA) exhibit two distinct phenomena with changes in stress (σ) and temperature (T). They are known as Shape Memory Effect (SME) and Pseudoelasticity (PE). These are described briefly in the following section.

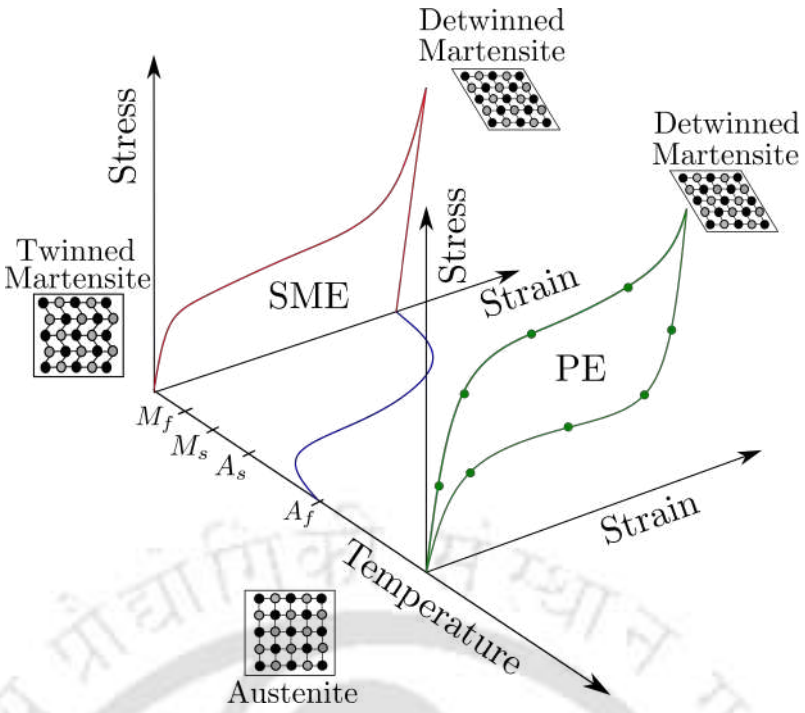

Figure 1.2: Stress (σ) - Strain (ε) - Temperature (T) plot showing SME and PE.

1.2.1 Shape Memory Effect

Figure 1.2 shows the Shape Memory Effect (SME) as exhibited by a typical SMA element. As SMA at the high temperature, is cooled below martensite start temperature (M_s), SMA in its initial austenite (A) phase, starts transforming into twinned martensite (TM) phase, until martensite finish temperature (M_f), at which point the full transformation concludes. This process is reversible and is known as forward transformation. In forward transformation, no macroscopic shape change is observed due to the formation of the self-accommodating variants of martensite [1]. While SMA in its TM phase is loaded above a critical stress (σ_s^{cr}), reorientation occurs depending on the direction of applied stress and crystallographic structure, which results in the formation of detwinned martensite (DM) phase. The reorientation or detwinning continues till the stress level of σ_f^{cr}, offering very low additional resistance to deformation. This yields a significant amount of strain for a minimal change in stress. Thereafter, SMA behaves elastically during unloading, offering a large residual strain. As the SMA in its DM phase is heated to a temperature above austenite start temperature (A_s), all variants of DM phase transforms to A phase, known as the reverse transformation, resulting in strain recovery, which continues till austenite finish temperature (A_f). This phenomenon of undergoing large deformation upon loading

and unloading, and subsequent recovery due to heating is termed as the Shape memory effect (SME).

1.2.2 Pseudoelasticity or Superelasticity

Figure 1.1 shows the constant temperature loading-unloading path resulting in SMA's Pseudoelastic (PE) response. As the SMA in its initial Austenite (A) phase is loaded at a constant temperature above A_f, it behaves elastically till σ_{M_s}. With further increase in load, DM starts forming directly from A. Above σ_{M_f}, A gets completely transformed into DM and behaves elastically upon further loading. A large amount of strain is observed at this point. Upon subsequent unloading, SMA acts elastically till σ_{A_s}, at which point reverse transformation from DM to A initiates, and concludes at a stress denoted as σ_{A_f}. A complete strain recovery is observed after this unloading process. The corresponding hysteretic behaviour of SMA can be witnessed in Fig 1.2.

1.3 SMA Wire Actuators

A transducer is a device which converts one form of energy into another. The actuator is an example of a transducer which transforms electrical energy into mechanical output. Miniaturization is the need of the hour, and SMAs are one of the best options for these types of actuators. SMAs have high energy density and can undergo and subsequently recover about 6-8% strain [1] upon thermal activation. Also, the availability of micron-size SMA wires, offers the perfect solution for the need of small-scale actuators. In addition to this, they offer clean, silent and maintenance-free operation. Moreover, they also show self-sensing capabilities, which obviate the need for an external feedback sensor. The major challenges of SMA wire actuators are their low actuation frequency and nonlinear hysteretic response. Additionally, SMA actuators are generally driven by thermal loading, wherein the change in the SMA wire's temperature initiates phase transformation, yielding actuation. In most cases, the temperature is controlled via resistive heating. This makes its actuation performance greatly dependent on the ambient conditions while operating.

1.4 Literature Review

Shape Memory Alloys have been one of the most prominent smart materials in the limelight of research for the past few decades. The literature survey herein initially discusses the history and development of SMAs, followed by their applications and control mechanisms. Then the different modelling approaches of SMA are discussed. Next, the various works related to the self-sensing applications of SMA are reviewed.

1.4.1 History and Applications of SMA

In 1938, Greninger and Mooradian [2] observed large strains in Cu-Zn alloys upon lattice transformations between FCC and BCC lattices during the heating and cooling cycles. Later, in the year 1963, Buehler [3], and his team discovered the Shape memory effect in Nickel-Titanium (Ni-Ti) alloy at the Naval Ordnance Laboratory (NOL). It was observed that when a Ni-Ti coil was immersed in hot water above 65°C, it went back to its initial straight shape rapidly. The name NITINOL (Nickel-Titanium Naval Ordnance Laboratory) was given in accordance with this discovery.

In the next few decades, SMA actuators were being developed for various commercial purposes. Ni-Ti springs were used to control the flow rate of fluids through tight spaces where conventional valves were ineffective. Their quick response, coupled with their simplicity, made them very popular [4]. Couplings and sleeves made from SMAs were on the rise, and their foolproof design made them the best alternative for titanium-based couplings. SMA-based fasteners and connectors were developed for navy and missile technology due to their incumbent corrosion and fire-resistant properties [5]. Some of the most popular applications include SMA-based eyeglass frames and cell phone antennas. The popular 'Eggo' headphones of Walkman from Sony were made using SMA [6]. SMA based micro-actuators for thermostats and mixing valves were also developed. Several monolithic devices were developed using SMA, which were flexible and provided frictionless motion [7]. High-pressure fuel injectors were one of the most successful applications of SMAs. Safety valves to control the flow of toxic gases and circuit breakers made of SMA wires to prevent the flow of high currents in electrical circuits were also developed

[8]. SMAs were used in the flaps of air-conditioning systems, to open and close them based on the ambient temperatures, avoiding the need for a feedback loop. SMA thermal actuators were also used as engine oil-level correcting devices in bullet trains in Japan [9].

Biocompatibility of SMA makes them one of the most viable options for medical applications over previously used stainless steel guide wires and catheters. Stents made from SMAs are now being used in angioplasty surgery to help people with narrow blood vessel condition in their hearts. Cardiovascular devices made using SMA wires are used as filters to clear coagulated blood streams [10]. Various endoscopic devices made from SMAs play an imperative role in shaping the non-invasive surgery techniques in the biomedical field [11]. SMA-based spacers are used to provide constant load, which helps in the correction of the spinal cord of scoliosis patients. SMA staples are used in the field of orthopaedics to quicken the healing process of a fractured bone [12]. Various microgrippers using spiral and net type SMA are developed to reduce the actuation time and increase the controllability of minimally invasive surgery devices [13]. SMA-based active forceps, which can change their shape upon electrical heating, are also developed to be used in laparoscopic surgery [14]. SMAs are also being used to actuate muscle wherein the urethra of old aged people are opened and closed using NiTi plates [15]. NiTi braces are used in orthodontic applications for remodelling the position of misaligned teeth [16].

Robotic grippers using SMA springs, which can generate two-jaw movement, are being developed [17]. An anatomically compliant human hand was built using rapid prototyping and actuated using muscles fabricated from SMA. Its low weight and high mobility make it suitable as a prosthetic hand for the handicapped [18]. Bio-inspired robotic grippers, actuated using a combination of SMA wires, have been devised to generate the varying grasping force required to hold objects of different weights, shapes, and configurations [19, 20, 21]. One of the major hindrances in using SMA actuators for prosthetic hands is their low actuation frequency. To overcome this issue, the SMA actuators are forced cooled, and their performance was found to be at par with the existing commercial solutions [22]. 3-D printed prosthetic arms, which mimic the human hand and finger structure, operated using SMA wires, have been developed. The printed hand skeleton was wrapped with silicon-based flesh, thus providing a human-hand like appearance and improving its

gripping capability [23].

SMAs are a compelling option for aerospace applications due to their large force-to-weight ratio. SMAs were explored for noise reduction and variable engine inlet technologies, to improve aircraft efficiency [24]. Scientists attempted to control the position of an aircraft flap using an SMA wire actuator. The swinging motion of the flap was controlled using an SMA wire actuator made of two antagonistically connected SMA wires [25]. The various grippers and positioners aboard the Mars Pathfinder mission of NASA were reported to be made of SMA [26]. Wing morphing is another field in which SMAs are rather effective. SMA actuators are used to alter the shape of an aircraft wing to reduce the drag acting on it, hence improving the aerodynamic efficiency [27]. Aircraft wings for small unmanned air vehicles with adaptive capability were explored, by using a combination of SMA wires and tubes. The shape of the wing was adjusted based on the varying flight conditions and was comparable to existing flight control mechanisms [28]. SMAs are also being used for altering the structure of the camber of the UAV wing's tail portion [29]. Parametric studies were conducted to determine the optimum height and width of the corrugated structure, actuated using SMA wires, to obtain a high lift-to-drag ratio. The modified FishBAC design was found to be very effective and generated a tail edge deformation of up to 10.7° [30].

SMAs are used in a wide variety of applications in the automotive industry [31]. Mechanisms to control the car mirror using SMA wires have been developed [32]. Electrically driven SMA wires in the configuration of a pantograph are designed to switch the rearview mirror position, to avoid nighttime glare [33]. An ergonomic and functional prototype of an adaptive door handle has been proposed. The vertical distance of the handle can be controlled by heating and cooling the SMA wires, which consequently can also improve the vehicle's aerodynamic efficiency [34]. Better sound-proofing techniques are being developed to counter the effect of weakening door sealing in cars. A radially expanding structure, actuated using an SMA wire, has been placed in the sealing cavity, pushing the sealing rubber against the frame, thus improving the acoustic insulation [35, 36].

The contribution of SMAs in the field of civil engineering has been prominent. Song *et al.* [37] demonstrated the active control of the motion of large structures using the

damping property of SMAs. These were also used to prevent crack growth in concrete and as structural reinforcements in the form of anchorages or restrainers. Iron-based pre-stressed SMA strips were used for strengthening concrete beams, with the advantages being higher cracking load capacity, reduced displacement, increased fatigue performance, and lower stress on the internal steel cables [38]. SMA-based damping mechanisms were found to be effective in reducing the dynamic response of buildings under varied seismic conditions, due to their high energy dissipation capability [39]. NiTi strands were also used to strengthen RC beams and were found to be superior to conventional ones, in reference to the crack recovery performance [40].

1.4.2 Constitutive Modelling of SMA

SMAs are becoming increasingly popular in defence, aerospace and biomedical applications. With increasing usage came the need for a well-defined mathematical model capable of describing the characteristic behaviour of the SMA. Various models have been proposed since the late 1980s. For the ease of understanding, these models can be classified into two categories, namely the *phenomenological* models and *thermodynamics*-based models. In *phenomenological* models, the constitutive equation, relating the stress (σ), strain (ε) and temperature (T) of SMA are derived from basic thermodynamics principles; however, the phase kinetics detailing the evolution of martensite volume fraction (ξ), are empirically defined based on experimental results. The advantage of this modelling approach is its simplicity and, thus, is very popular in typical engineering applications. In *thermodynamics*-based models, both the constitutive equations and phase kinetics are obtained from fundamental laws of thermodynamics, utilizing the thermodynamic potentials such as Gibbs free energy or Helmholtz free energy.

Tanaka [41] proposed the first phenomenological model for 1-D SMA element, considering material properties like modulus of elasticity, transformation strain and thermal expansion coefficient as constants, and the martensite volume fraction (ξ) was taken as an internal state variable. An exponential function was proposed as the phase kinetics relating the stress and temperature with ξ. Liang and Rogers [42] later proposed a model based on Tanaka's work, replacing the exponential model with a cosine model offering a

better fit with experimental data.

Brinson's model [43], proposed in 1993, provided a better representation of SMA's behaviour. In this model, the martensite volume fraction (ξ) was taken as the sum of temperature-induced martensite (ξ_T) and stress-induced martensite (ξ_s), taking into consideration the detwinning behaviour. The material constants were considered to be a linear combination of the properties of martensite and austenite volume fractions. Bekker and Brinson [44, 45] proposed a modified approach, stating the value of ξ to be dependent not only on its present state but also on the thermo-mechanical path. The phase transformation from $A \rightarrow M$ or $M \rightarrow A$ was denoted to occur in specified transformation zones, with no transformation transpiring in dead zones. Khandelwal and Buravalla [46] suggested a correction to the Brinson model [43] incorporating the coupling between the twinned and detwinned martensite phases in the dual transformation zone. Additionally, the irreversibility of the detwinning process was also proposed. Buravalla and Khandelwal [47] further revised Brinson's model [43] to take into consideration the various inconsistencies in the differential and integral form of constitutive equations. Additionally, a new approach was proposed [48] for arbitrary loading conditions in which a memory parameter was introduced. This was done to avoid inaccurate results in modelling where in certain loading cases, the value of ξ became greater than 1. Elahinia and Ahmadian [49, 50] showed that the above-mentioned phenomenological models could predict the SMAs' behaviour only in simple loading cases, where both stress and the temperature doesn't vary simultaneously. A few modifications to [42] and [43] were proposed, and it was reported to give better results compared to earlier models. In 2012, Banerjee [51] presented an algorithm to simulate an SMA wire subjected to arbitrary loading. To apply Brinson's model [44], one needs a prior knowledge of the loading path, to determine SMAs' state and zone of transformation. This was not possible with the existing approaches, for arbitrary loading cases. The proposed algorithm eases the process of determination of the transformation zone and the direction of transformation by using the rate of change of σ and T.

Boyd and Lagoudas [52, 53] formulated an SMA model based on thermodynamic principles. The martensite volume fraction (ξ) and the transformation strain (ε^t) were

taken as the internal state variables. The total strain was taken as a sum of the elastic and transformation strains. The Gibbs free energy was taken as the thermodynamic potential, and the constitutive equation relating the σ, T and ε was derived using the first and second law of thermodynamics. Transformation surfaces were defined, using which the state of SMA being in the elastic state or in the phase transformation state was determined. The model parameters were derived to replicate the full transformation response of SMA. The response obtained from the model for partial transformation cases was not examined. A polynomial hardening function which accounted for the interaction between M and A phases was defined.

It has been found experimentally that upon cyclic loading of SMA, strain accumulation takes place due to the development of plastic strain during phase transformation. Bo and Lagoudas [54, 55] found that the plastic strain ceased to develop after a large number of cycles. A 3-D constitutive model was developed to take into consideration the plastic strain accumulation during transformation. In addition to ξ, the plastic strain (ε_p), the back stress (β) and the drag stress (η) were considered as the internal variables. The evolution of transformation strain during the phase transformations and the evolution of β and η as a function of ξ were also discussed. The Gibbs free energy function was redefined, and instead of using a hardening function, both β and η are used, to model the interaction between M and A phases.

Following the previous studies, Qidwai and Lagoudas [56] proposed the numerical implementation of the SMA constitutive model using a return mapping algorithm, without considering the martensite reorientation. Two algorithms, namely, the closest point projection and the convex cutting plane, were proposed. The algorithms involve two steps, the elastic predictor step and the plastic corrector step. Closest point projection is an implicit method and is unconditionally stable, but it has a higher computational cost due to the evaluation of gradients and inversion of tensors. Convex cutting plane is an explicit method and is simpler to implement, but it is only locally convergent in reverse transformation. In addition to polynomial hardening, the cosine and exponential hardening functions were also implemented.

Later in 2007, Popov and Lagoudas [57] presented a 3-D constitutive model for poly-

crystalline SMA. It takes into account the development of stress-induced martensite from austenite and twinned martensite. It can be used for complex thermomechanical loading cases, which was previously not possible. Three new variables during martensite transformation were introduced, denoted as ξ_1, ξ_2, ξ_3. These represent the amount of martensite volume fractions obtained during $A \rightarrow TM$, $A \rightarrow DM$ and $TM \rightarrow DM$ transformations, respectively. The Gibbs free energies and the three hardening functions f_1, f_2, f_3 were also formulated. The constitutive model was numerically implemented using the return mapping algorithm. Branco *et al.* [58] adapted the Boyd and Lagoudas model [52] to properly simulate the minor loop hysteretic response of SMA, when load reversal takes place during phase transformation. The parameter Y in the constitutive model was modified, and the super-elastic response of NiTi wires was simulated and compared against the experimental response. The hysteretic response obtained from the model was found to mimic the same obtained experimentally closely. Lagoudas *et al.* [59] proposed an enhanced constitutive model for polycrystalline SMAs, following the approach discussed by Boyd and Lagoudas [52]. The model aims to capture SMA's smooth transition behaviour at the start and end of phase transformation. This was achieved by considering a smooth hardening function which appropriately delineates the inelastic response during phase change. Secondly, the transformation strain evolution kinetics was assumed as a function of stress (σ), to incorporate the re-orientation of different martensite variants. Additionally, a modified parameter Y was also used in the study to account for the stress-dependent nature of the hysteresis. Karakalas *et al.* [60] proposed a modified approach to accurately describe the partial transformation response of SMA. For this, a new hardening function and a reversal point memory parameter were employed. Here, a two scaled martensite volume fractions, one for forward ($\tilde{\xi}_{fwd}$) and another for reverse ($\tilde{\xi}_{rev}$) transformation were introduced to account for the minor loop response of SMA. Here, the scaled ξ was used only in the hardening functions, but is kept unaltered in the constitutive equation.

Kumar *et al.* [61] described a '*dissipationless band*' to model the minor loop response of SMA, based on the '*dissipationless curve*' theory introduced by Rajagopal and Srinivasa [62]. The *dissipationless band* is confined within the forward and reverse transformation

stress limits of the pseudo-elastic SMA response regime. The Helmholtz free energy is used to derive the evolution and transformation force equations. Several partial loading cases were simulated, and the model was found to estimate the minor hysteresis loops effectively.

Several other material models are available in the literature, yielding reasonable accuracy in representing structural responses under complete transformation cases. Here, only the ones that are based on Lagoudas and Boyd [52] are presented. Very few of these address the partial transformation cases, *e.g.*, [54],[58] and [60], and are primarily based on an empirical approach. Moreover, they do not satisfy some of the basic requirements as far as the phase diagram is concerned, and hence will be addressed in Chapter 2.

1.4.3 Control of SMA

SMA actuators are utilized in a wide variety of applications. As seen in Section 1.2, SMAs elongate and contract upon thermo-mechanical loading-unloading induced phase transformation, effectuating a non-linear and hysteretic system response. This adversely affects its precision control, necessitating complex control methods. Song *et al.* [63] presented one such mechanism to control the tip of an SMA wire actuated beam by varying the electric current passed through it. A control system consisting of a PD control, a feedforward mechanism and a compensator for hysteresis regulation was designed. Song *et al.* [64] designed another neural network-based feedforward controller to control SMA wire actuators. Elahinia and Ashrafiuon [65] proposed a non-linear control approach based on variable structure control, for position control of SMAs in rotary applications. The model was developed based on the non-linear dynamic model of the arm, and the constitutive relations and phase transformation model proposed by Liang and Rogers [42]. Teh and Featherstone [66] developed a control system for SMA force actuators. The output tension of the wire is related to the applied input power by a transfer function based on the frequency response analysis technique. Visioli [67] was one of the first to introduce fuzzy logic in SMA control applications. He proposed a method for tuning a PID controller using fuzzy logic to reduce both the overshoot and rise time, making it appropriate for industrial applications. Khodayari *et al.* [68] developed a fuzzy logic-

based PID control of SMA wire actuators. These actuators were used in prosthetic fingers with three degrees of freedom and were found to be effective with minimum overshoot and quicker stability.

1.4.4 Self-Sensing of SMA Wire Actuators

As discussed in Section 1.4.3, a proper feedback mechanism is required to control the nonlinear hysteretic behaviour of SMA. The feedback system consisting of sensors makes the system bulky and costly. To avoid this issue, the self-sensing capability of SMA has been explored in recent years, wherein the change in the electrical resistance of the SMA is used as a measure of the control variable. It has been found experimentally, that as the SMA wire's length changes during phase transformation, its resistance alters significantly. This is because, the resistivities of martensite and austenite phases are found to be different. The following literature discusses the self-sensing applications of SMA.

Ikuta *et al.* [69] first explored the self-sensing property of SMA in medical applications. A feedback mechanism was modelled, based on the change in electrical resistance of two antagonistically connected wires. In the early 2000s, Dunlop and Garcia [70] developed a Stewart platform whose motion was regulated by using SMA wire actuators. The extent of actuation by the SMA wires was controlled by switching the power supply, on or off.

To facilitate the precision control in the case of SMA, He *et al.* [71] conducted experiments under various stress and temperature conditions to study their effects on the electrical resistance of SMA wires. The strain and electrical resistance were reported to vary linearly during transformation, whereas the stress was found to have no effect. This linear behaviour makes it easy to control the SMA wire actuators. The impact of the R-phase on electrical resistance was also studied, and a modified phase diagram was proposed. Liu *et al.* [72] examined the self-sensing property of SMA for its application in civil structures. Both NiTi and NiTiCu alloys were studied for their sensing capability, and were found to be extremely sensitive to strain changes in the martensite phase. This self-sensing behaviour can be used for crack detection, by measuring the change in electrical resistance of the SMA wire.

In 2005, Dutta and Ghorbel [73] developed a mathematical model of the spring-biased

SMA wire system. An empirical relation for the heat transfer coefficient was assumed. The ξ-T relation was derived based on the Duhem hysteresis model, and a polynomial relating the strain and the martensite volume fraction was obtained, using the curve fitting technique. Simulations were carried out to show the model's capability to represent the strain-resistance behaviour of the SMA actuator. This technique was also able to simulate the minor loops. Cui *et al.* [74] proposed another mathematical model describing the relation between normalized electrical resistance change ($\Delta R/R$) and strain of an SMA wire. The total resistivity (ρ) is considered as a linear combination of electrical resistivity (ρ) of A, M and R phases based on their volume fractions. The electrical resistivity of each individual phase was taken as a linear function of temperature. Brinson's 1-D constitutive model [43] was considered, and numerical simulations were carried out. It was found that SMA in the martensite phase shows linear resistance-strain relation, while it was piece-wise linear in other phases. Lu *et al.* [75] also proposed a theoretical framework for self-sensing SMA actuators, by relating the change in the electrical resistance of the SMA wire as a function of its strain. The resistance model was developed based on a variable speed phase transformation constitutive model of SMA [76]. The influences of temperature on electrical resistivity, area of cross-section, and length of SMA wire, were fully incorporated, and a coupled temperature-stress-strain-resistance model was formulated.

One peculiar behaviour of the R-phase in SMA is that it has higher electrical resistance than A and M phases. This increases the modelling difficulty and hence is not desirable for self-sensing applications. To overcome this, Novak *et al.* [77] developed a model to simulate SMA's resistance change during B2-R-B19$'$ transformation. Experiments were carried out, and it was concluded that the electrical resistance of A, R and M increases with increasing temperature. Moreover, during the detwinning process, the electrical resistance of martensite also increases. Brammajyosula *et al.* [78] developed a model to simulate the effect of the presence of R-phase in SMA. The model was developed using Brinson's model [43], with required modifications to include the R-phase transformation. The resistivity (ρ) was modelled considering the variable sub-layer rule, and a linear variation of individual resistivities with temperature was assumed. The transient response of SMA was studied, and a non-linear relation between resistance and strain during cooling

was observed, due to the presence of the R-phase.

Malukhin and Ehmann [79] also investigated the self-sensing capability of SMA actuators. Experiments were conducted, and it was shown that at higher temperatures and lower pre-strain, the resistance-displacement plot could be approximated as a straight line. It was reported that the non-insulated wires developed faster responses, but exhibited higher fluctuations in comparison to insulated wires. Also, the effect of voltage steps on the response time was studied, and it was inferred that higher voltage steps yield lower response time. The disadvantage of using a Voltage or Current based control of SMA is that the control parameter changes with the degree of transformation undergone by SMA. To overcome this, Furst and Seelecke [80] developed a model based on power control instead of voltage or current. A numerical model for martensitic phase transformations in SMA was proposed based on transition probabilities. The proposed model satisfactorily simulated the variation in resistance with changes in temperature and phase transformation. The linearity in $R - \epsilon$ curve within the actuation range makes it very effective for position control applications.

In most real-world applications, the cooling of SMA to its original state is through natural convection, making the process slow. The study conducted by Lewis *et al.* [81] gave an insight into the effect of changing ambient conditions, on the SMA behaviour. Constant power was applied across the SMA using a controller, and the change in length of the wire was measured to determine its strain, at various constant air speeds. In addition, to demonstrating the self-sensing capability of SMA as a position sensor, its use as an anemometer is also illustrated. As cooling of the SMA wire is done, more power is supplied to maintain the resistance in the wire, same, and the excess power supplied is related to the airspeed in the form of a second-order polynomial.

In 2014, Josephine *et al.* [82] conducted experiments to determine the effect of antagonism on the hysteretic behaviour of SMA. It was found that antagonistically placed wires exhibited negligible hysteresis in comparison to that of a single wire. In concurrence with this, a system with two antagonistically placed wires was used to rotate a shaft, converting the linear motion of SMA to rotatory motion. A feedback mechanism was developed based on the difference in the resistances of the wires, which was used as

a feedback signal in a fuzzy logic PID controller. Josephine *et al.* [83] further developed a force sensor utilizing the Shape memory effect of SMA. An SMA wire with a cantilever beam as a bias element was used. As force is applied, the wire gets actuated, inducing a strain in the SMA which changes the resistance of the wire. This change in resistance was used to sense the force. The sensor was tested to study its force-resistance characteristics at different currents. At an excitation current of 26 mA, the response was found to be linear, without exhibiting the hysteresis loop. The sensor was calibrated at the operating current, and several experiments were conducted to demonstrate its reliability.

Gurung and Banerjee [84] developed an Extended Kalman Filter (EKF) to harness the self-sensing capability of the SMA wire actuator system. The modified constitutive model proposed by Vidyashankar *et al.* [47] was considered, and the phase diagram based kinetics by Bekker & Brinson [44] was followed. Implicit and explicit numerical integration schemes were used. It was found that the implicit scheme took about 33% lesser time than the explicit method. The estimated stress and displacement were compared to the same obtained from the model. An experimental set-up was also developed to measure the true displacement and the change in electrical resistance of the SMA wire, while subjected to particular voltage signals. Further, the measured resistance was used to estimate the change in length of the wire and compared with the experimentally measured change in length of the wire. The previous work was followed by replacing the EKF with an Unscented Kalman Filter (UKF). The estimated values of the displacement obtained using UKF were compared with those obtained using EKF to show that both methods yield the same accuracy. However, the UKF was reported to consume 50 % less computational time [85].

Gurley *et al.* [86] came up with an innovative technique to determine the length of a wire by measuring the voltage drop across two different points on the wire. Probes were placed at three positions on the wire. The first was fixed at the high-voltage end; the second was in the middle and at a fixed length from 1^{st} end, and the third was soldered to the low-voltage end, which moved with it. The advantage of this technique is that no prior knowledge of the electro-mechanical properties or the hysteresis behaviour of the SMA is required. But the issue of electrical noise during sliding and the corrosion of the

probe needs to be considered. Lambert *et al.* [87] used the above technique to control a ball on a beam system using the sliding-mode control mechanism. The constitutive law developed by Tanaka [41] was simulated in a multi-body dynamics software ADAMS, and the resistance was measured using Gurley's [86] method. The heat transfer coefficient was taken as a function of the Nusselt number, corresponding to a cylinder with a constant cross-section. Zamani *et al.* [88] proposed a novel technique to harness the self-sensing property of SMA. A laser-processed NiTi SMA wire actuator is presented, containing two different material compositions in the same monolithic wire. The two compositions behave differently for the same working conditions. One part shows Shape Memory Effect (SME) for actuation, and the other shows Pseudoelasticity (PE), enabling it to be used as a sensor. The applied stress must be lower than the pseudoelastic transformation stress, thus rendering a linear stress-strain behaviour in the pseudoelastic portion of the actuator. The electrical configuration is such that the current passes only through the shape memory region of the monolithic actuator. The dual resistance method [86] was used to determine the resistance of the two regions. A position estimator model was proposed based on Liang's model [42] to estimate the position of the actuator.

Lee and Kim [89] developed a self-sensing-based position control model for the SMA actuator, by exploiting its resistance-strain curves. The self-sensing model (SSM) comprises of two separate polynomials, fitted using the $R-\epsilon$ plots during heating and cooling paths. The SSM, coupled with a PID controller and fuzzy logic, was utilized for position control and was found to be better than the other strategies based on conventional curve-fitting techniques [90]. Abdullah *et al.* [91] developed a PID controller exploiting the self-sensing feature of SMA. The accuracy and response time of the proposed technique was improved by increasing the pre-tension acting on the SMA wire, thus revealing the feasibility of replacing the existing position sensors-based control systems, with cost-effective SMA-based ones. In recent years, the electrical resistance of the SMA wire has also been used to determine the start and finish points of phase transition during heating, and cooling [92]. A piece-wise linear regression model relating the electrical resistance of SMA wire and displacement was derived, which was used to estimate the actuation generated by the system. As an application, a thermal protection system is proposed, wherein

the input power to the actuator is cut off, upon completion of reverse transformation.

Neural networks have also been employed in the self-sensing application of SMA wire actuators. Bhargaw *et al.* [93] proposed an LSTM-based technique to estimate the actuation generated by an antagonistic SMA wire actuator, by utilizing the differential electrical resistance data. Experiments aimed at simulating a set of major and minor loops were carried out, and the network was trained to assimilate the hysteretic $R - \epsilon$ relation of SMA. The trained network was subsequently tested, and was reported to perform well under proportional loading conditions.

1.5 Scope of Present Work

Shape Memory Alloy (SMA) based actuators are an obvious choice for miniaturized systems, since they provide large displacements with high load-carrying capacity. Proper feedback controllers are required to tame the non-linear behaviour of SMA-based actuators. These controllers make the system bulkier, which can be avoided by utilizing the self-sensing capability of SMA, wherein the change in the electrical resistance of the SMA wire is used to determine the system output. In the literature, various empirical relations are derived based on the experimental results or system model, and are used to estimate the system response from the change in the electrical property of the SMA wire, during actuation. However, these approaches are system-specific, requiring sufficient experimental data to develop the corresponding relations. To overcome this problem, estimation techniques may be developed to predict the system output from the dynamic model of the system and a few experimental observations.

As seen in the literature, the self-sensing applications of SMA wire actuator systems are commonly modelled using phenomenological models. These models [43, 44, 48] have the advantage of being simple, but offer limited functionality in arbitrary loading cases. Additionally, in order to apply these models, the loading path must be known a priori, so as to apply the appropriate phase kinetics, requiring to follow non-trivial algorithms [51]. Here, the use of thermodynamic models may be more feasible in such situations. In the models of Boyd and his co-workers [52, 53], transformation surfaces dictate the state

and extent of transformation, making it more convenient for any practical loading cases. However, this class of models are developed considering the full transformation behaviour of SMA, and often yields imprecise results during partial transformation, wherein a load reversal occurs before the ongoing transformation is complete. Several approaches have been proposed in the literature to address the issue. However, these modified approaches are either computationally expensive [54], or are based on assumptions not conforming with existing literature [60]. Additionally, their effectiveness in complex loading situations has not been studied [58, 61]. Hence a modified approach is required to ameliorate the problem in simulating the minor loop response.

The heating of an SMA wire is generally carried out by resistive heating and is cooled naturally. The effect of the heat transfer coefficient on the temperature variation of the SMA wire is very prominent, particularly for thin wires. For a slight change in the heat transfer coefficient, the SMA wire's estimated temperature varies significantly [94]. This can lead to an improper prediction of SMA's transformation state. It has also been found that the heat transfer coefficient is not a constant value, but depends on ambient conditions [73]. It has mostly been considered a constant value, a linear [73], a quadratic [65], or a quartic function [95] of temperature. The heat transfer coefficient of a wire has also been reported to be evaluated from the Nusselt number relation [87]. Additionally, existing literature regarding the self-sensing application of SMA wire actuators examine its actuation, endured under natural convection or under protected immutable environments. However, when SMA wire actuators are subjected to forced cooling conditions, abrupt variations in the system response have been observed [96, 97]. Hence, better estimation methodologies to approximate the heat transfer coefficient in the case of thin SMA wires, may provide a better estimate of the system output in such cases.

Most of the existing studies examining the self-sensing behaviour of SMA wire actuators consider only linear systems, in which the stress and temperature of the wire vary monotonically, referred to as proportional loading. However, most practical systems have non-linear force-displacement characteristics. These SMA wire actuated systems endure actuation under not just proportional, but also arbitrary and non-proportional loading situations. This further accentuates the non-linearity of the SMA wire actuated system,

which in itself demonstrates a significant hysteretic behaviour during its loading-unloading cycles. Hence, an enhanced state estimator needs to be developed to effectively predict the system response of such systems under practical loading conditions, taking into account a combination of the SMA constitutive model, noisy electrical resistance data and system dynamics.

1.6 Objectives

To address the above issues, the following objectives are proposed:

1. Investigating the minor loop response of thermodynamically consistent phase kinetics based models [52], and modifying it to accurately delineate the partial transformation response of SMA wire actuators.

2. Developing an Extended Kalman Filter (EKF) based on the modified SMA constitutive model, to estimate the system response from the measured electrical resistance of SMA wire, while the system undergoes varying extent of phase transformation during both heating and cooling.

3. Developing a Particle Filter (PF) based state estimation technique for the SMA wire actuator, and investigating its performance in natural cooling conditions.

4. Modifying the developed EKF and PF based estimators to evaluate the response of the SMA wire actuated system, under forced cooling conditions.

5. Developing a PF based estimation methodology for an SMA wire actuated 1-DOF rotary manipulator exhibiting non-linear force-displacement relation, to evaluate the orientation of the link by harnessing the self-sensing capability of the SMA wire actuator and evaluating the filter's performance under varied loading conditions.

6. Examining the performance of data-driven techniques like Neural Networks in the self-sensing application of SMA wire actuators, in the presence of forced cooling conditions.

1.7 Organization of the Thesis

The above mentioned objectives are addressed in the following chapters.

- ***Chapter 2***: The thermo-mechanical model of Shape Memory Alloys (SMA), as proposed by Boyd and Lagoudas [52], is summarised. The limitation of the present model in simulating the partial transformation (PT) response of SMA has been presented. The existing approaches to accommodate the PT response, and their respective limitations are examined. Then the proposed modifications to account for the minor loop response of SMA are introduced. Finally, the simulated response obtained using the modified model is compared against the same obtained from the existing model, to demonstrate the efficacy of the proposed model in mimicking partial transformation response.

- ***Chapter 3***: The self-sensing capability of an SMA wire actuator and the viability of state estimation-based techniques have been discussed. An Extended Kalman Filter (EKF) has been developed using the process model involving the heat balance equation, coupled with force equilibrium and kinematic constraints, to estimate the state of the SMA wire actuator from the noisy electrical resistance data. An experimental setup is developed to measure the change in electrical resistance of an SMA wire, while being activated using resistive heating. Using the measured electrical resistance of SMA, the system response is estimated by the developed EKF and compared against the experimentally obtained one, and is discussed.

- ***Chapter 4***: This chapter explores a Particle Filter (PF) based state estimation technique to evaluate the actuation generated by an SMA actuator, under forced cooling conditions. Here, the SMA wire is intermittently cooled using a fan, for varying durations, intensities and at different stages of actuation. To improve the estimation accuracy, a modified PF is introduced, in which the heat transfer coefficient (h) is estimated along with the system's state. The output of the SMA actuated system is estimated using the modified filter following the measured electrical resistance information, and is presented.

- ***Chapter 5***: The self-sensing behaviour of an SMA wire actuated non-linear manipulator has been explored by employing a PF-based state estimation technique. The process model is derived, taking into account the heat balance equation, 1-D SMA constitutive model, kinematic model and the equation of motion, following a coupled thermo-mechanical approach. An experimental setup is fabricated, where the manipulator gets actuated under varied ambient conditions. The proposed filter estimates the position of the link, by utilizing the change in the electrical resistance of the SMA wire, under proportional and non-proportional loading conditions.

- ***Chapter 6***: Here, a neural network-based approach is developed to harness the self-sensing behaviour of the SMA wire actuators. Two LSTM-based networks are developed for the SMA wire actuated linear and non-linear systems. The trained network is used to evaluate the state of the systems from the change in the electrical parameters and inputs, and are compared against the measured observations.

- ***Chapter 7***: In this chapter the research contributions of the present work are summarized, and possible future works are presented.

Chapter 2

Constitutive Modelling of SMA

2.1 Introduction

In this chapter, the constitutive model for poly-crystalline shape memory alloys (SMA) proposed by Boyd and Lagoudas [52] is presented, and its shortcomings concerning the partial transformation (PT) response of SMA, are discussed. The existing refinements proposed to ameliorate the PT response, and their respective limitations are also briefly presented. From the observations based on the response of one-dimensional SMA elements, dictated by the phase diagram typically presented in the literature, modifications are proposed, to simulate the minor loop response of SMA. Finally, using the convex cutting return mapping algorithm, the responses of an SMA wire actuated linear system are simulated utilising the modified and existing models, and are compared to investigate the improvements achieved with the proposed model.

2.2 Constitutive Modelling of SMA

Boyd and Lagoudas [52] proposed a constitutive model for SMAs, in which the martensite volume fraction (ξ) and transformation strain ($\boldsymbol{\varepsilon^t}$) are considered as internal state variables. The Gibbs free energy (G), a function of the independent state variables, stress ($\boldsymbol{\sigma}$) and temperature (T), and internal variables ($\xi, \boldsymbol{\varepsilon^t}$) is considered as the thermodynamic

potential. It assumes the form,

$$G(\boldsymbol{\sigma}, T, \xi, \boldsymbol{\varepsilon^t}) = -\frac{1}{2\rho}\boldsymbol{\sigma} : \boldsymbol{S} : \boldsymbol{\sigma} - \frac{1}{\rho}\boldsymbol{\sigma} : \left[\boldsymbol{\alpha}(T - T_0) + \boldsymbol{\varepsilon^t}\right] + C_v\left[(T - T_0) - T\ln\left(\frac{T}{T_0}\right)\right] - s_0 T + u_0 + \frac{1}{\rho}h_f(\xi), \tag{2.1}$$

where, T_0 is reference temperature, $\boldsymbol{S}$ reflects effective compliance tensor, $\boldsymbol{\alpha}$ represents the effective thermal expansion tensor, C_v reflects the total specific heat, s_0 is the total entropy at the reference state, u_0 refers the total internal energy at reference state, ρ denotes the density, $h_f(\xi)$ states the transformation hardening function and (:) denotes the contraction of two tensors. The reorientation of martensite is neglected in this model. It is assumed that any change in the current state of the material is due to the change in martensite volume fraction (ξ). This change is also reflected in the material properties of SMA as,

$$\begin{aligned}
\boldsymbol{S}(\xi) &= \boldsymbol{S}^A + \xi(\Delta\boldsymbol{S}), \quad \text{where,} \quad \Delta\boldsymbol{S} = \boldsymbol{S}^M - \boldsymbol{S}^A,\\
\boldsymbol{\alpha}(\xi) &= \boldsymbol{\alpha}^A + \xi(\Delta\boldsymbol{\alpha}), \quad \text{where,} \quad \Delta\boldsymbol{\alpha} = \boldsymbol{\alpha}^M - \boldsymbol{\alpha}^A,\\
C_v(\xi) &= C_v^A + \xi(\Delta C_v), \quad \text{where,} \quad \Delta C_v = C_v^M - C_v^A,\\
s_0(\xi) &= s_0^A + \xi(\Delta s_0), \quad \text{where,} \quad \Delta s_0 = s_0^M - s_0^A,\\
u_0(\xi) &= u_0^A + \xi(\Delta u_0), \quad \text{where,} \quad \Delta u_0 = u_0^M - u_0^A.
\end{aligned} \tag{2.2}$$

Following the first and second law of thermodynamics [1], the strain tensor ($\boldsymbol{\varepsilon}$) and entropy (s) are obtained as,

$$\boldsymbol{\varepsilon} = -\rho\frac{\partial G}{\partial \boldsymbol{\sigma}} = \boldsymbol{S} : \boldsymbol{\sigma} + \boldsymbol{\alpha}(T - T_0) + \boldsymbol{\varepsilon^t}, \tag{2.3}$$

$$s = -\frac{\partial G}{\partial T} = \frac{1}{\rho}\boldsymbol{\sigma} : \boldsymbol{\alpha} + C_v\ln\left(\frac{T}{T_0}\right) + s_0, \tag{2.4}$$

respectively. Here, Eqn.(2.3) represents the constitutive equation of SMA relating the stress ($\boldsymbol{\sigma}$), the strain ($\boldsymbol{\varepsilon}$) and the temperature (T) of SMA. Substituting the Gibbs free

energy expression (Eqn.(2.1)) in Clausius-Planck inequality, yields

$$\boldsymbol{\sigma} : \dot{\boldsymbol{\varepsilon}}^t + \left(-\rho \frac{\partial G}{\partial \xi}\right) \dot{\xi} \geq 0. \tag{2.5}$$

The rate of evolution of transformation strain ($\boldsymbol{\varepsilon^t}$) is assumed as,

$$\dot{\boldsymbol{\varepsilon}}^{\boldsymbol{t}} = \boldsymbol{\Lambda} \dot{\xi}, \tag{2.6}$$

where, $\dot{\xi}$ represents the rate of change of martensite volume fraction. Here, $\boldsymbol{\Lambda}$ is referred as the transformation tensor, assuming the form,

$$\boldsymbol{\Lambda} = \begin{cases} \frac{3}{2} H \frac{\boldsymbol{\sigma}'}{\bar{\sigma}'} & , \quad \dot{\xi} > 0; \\ H \frac{\boldsymbol{\varepsilon}^{\boldsymbol{t-r}}}{\bar{\varepsilon}^{t-r}} & , \quad \dot{\xi} < 0; \end{cases} \tag{2.7}$$

where, H is the maximum transformation strain upon complete detwinning and $\boldsymbol{\varepsilon}^{\boldsymbol{t-r}}$ denotes the value of transformation strain ($\boldsymbol{\varepsilon^t}$) at the point of load reversal. The deviatoric stress ($\boldsymbol{\sigma}'$), the von Mises stress ($\bar{\sigma}'$) and effective transformation strain at the point of reversal ($\bar{\varepsilon}^{t-r}$) in Eqn.(2.7) can be expressed as,

$$\boldsymbol{\sigma}' = \boldsymbol{\sigma} - \frac{1}{3}\mathrm{tr}(\boldsymbol{\sigma})\mathrm{I}, \tag{2.8}$$

$$\bar{\sigma}' = \sqrt{\frac{3}{2}||\boldsymbol{\sigma}'||^2}, \tag{2.9}$$

$$\bar{\varepsilon}^{t-r} = \sqrt{\frac{2}{3}||\boldsymbol{\varepsilon}^{\boldsymbol{t-r}}||^2}. \tag{2.10}$$

Here, $||\ .\ ||^2$ denotes the contraction of the enclosed tensor quantity. Eqn.(2.6) is substituted in Eqn.(2.5), yielding,

$$\left(\boldsymbol{\sigma} : \boldsymbol{\Lambda} - \rho \frac{\partial G}{\partial \xi}\right) \dot{\xi} = \Theta \dot{\xi} \geq 0, \tag{2.11}$$

where, Θ is referred as the thermodynamic force conjugate to ξ. Substituting the expression for Gibbs free energy (Eqn.(2.1)) into Eqn.(2.11), one obtains,

$$\Theta(\boldsymbol{\sigma}, T, \xi) = \boldsymbol{\sigma} : \boldsymbol{\Lambda} + \frac{1}{2}\boldsymbol{\sigma} : \Delta\boldsymbol{S} : \boldsymbol{\sigma} + \boldsymbol{\sigma} : \Delta\boldsymbol{\alpha}(T - T_0) - \rho\Delta C_v \left[(T - T_0) - T \ln\left(\frac{T}{T_0}\right)\right] + \rho\Delta s_0 T - \rho\Delta u_0 - \frac{\partial h_f}{\partial \xi}. \tag{2.12}$$

As Θ attains a threshold value, the phase transinformation initiates, and is expressed with the transformation function (ϕ) as,

$$\phi = \begin{cases} \Theta - Y_f, & \text{when} \quad \dot{\xi} > 0, \quad (A \rightarrow M) \\ -\Theta - Y_f, & \text{when} \quad \dot{\xi} < 0, \quad (M \rightarrow A) \end{cases} \tag{2.13}$$

where, Y_f is the threshold yield value. During the phase transformation, the state of SMA has to lie on the transformation surface, which can be expressed in the form of Kuhn-Tucker conditions as,

$$\phi(\boldsymbol{\sigma}, T, \xi) = \Theta - Y_f \leq 0 \quad \text{and} \quad \phi\dot{\xi} = 0, \quad \text{for} \quad \dot{\xi} \geq 0; \tag{2.14}$$

$$\phi(\boldsymbol{\sigma}, T, \xi) = -\Theta - Y_f \leq 0 \quad \text{and} \quad \phi\dot{\xi} = 0, \quad \text{for} \quad \dot{\xi} \leq 0. \tag{2.15}$$

Equations (2.14) and (2.15) state that, during both the forward ($\dot{\xi} > 0$) and reverse ($\dot{\xi} < 0$) transformations, the transformation function, ϕ, should remain zero, *i.e.*,

$$\phi = 0, \qquad \forall \qquad \dot{\xi} \neq 0. \tag{2.16}$$

Further, amid an elastic response, *i.e.*, $\dot{\xi} = 0$, the transformation function (ϕ) stays negative. The hardening function $h_f(\xi)$, representing the non-linear interaction among phases, has been modelled using polynomial function [52], and exponential and cosine functions [1], to replicate the response obtained from other existing constitutive models

[41, 42]. The cosine hardening function is defined as [1],

$$h_f(\xi) = \begin{cases} \int_0^{\xi} -\frac{\rho\Delta s_0}{a_1}[\pi - \cos^{-1}(2\xi - 1)]d\xi + (a_3 + a_4)\xi, & \text{for} \quad \dot{\xi} > 0; \\ \int_0^{\xi} -\frac{\rho\Delta s_0}{a_2}[\pi - \cos^{-1}(2\xi - 1)]d\xi + (a_3 - a_4)\xi, & \text{for} \quad \dot{\xi} < 0. \end{cases} \tag{2.17}$$

In the case of Boyd and Lagoudas model [52], the model parameters associated with the constitutive model are derived by applying the transformation criteria, *i.e.*, Eqn.(2.16), at the four distinct thermo-mechanical states, corresponding to the beginning and end of both forward and reverse phase transformations; where the SMA is in the zero-stress state. The Boyd and Lagoudas model yields a response with reasonable accuracy in the case of full transformation, wherein the SMA undergoes a complete transition from martensite to austenite or vice-versa. However, the accuracy of the response predicted by the model during the partial transformation, wherein a load reversal occurs before the completion of the ongoing transformation, needs to be improved. Few approaches are proposed in the literature to mitigate the same; however, each of these has its own limitations. Hence, to obviate this issue, a modified technique has been presented in this study, in which a phase diagram based approach has been proposed to evaluate the minor loop response of SMA. Using this approach, the model parameters, a_1, a_2, a_3 and a_4, are derived and employed in the rest of this study.

2.3 Existing Approaches to Simulate Minor Loop Response

In the literature, several approaches are presented to improve the minor loop response of Boyd and Lagoudas model [52]. Bo and Lagoudas [54] proposed a thermo-mechanical model to simulate the minor loop response by introducing a memory parameter, which stores the transformation states corresponding to the points of load reversal. However, the accumulation of this memory parameter over many load reversals, and the methodology for wiping them out, makes the model complicated and computationally expensive. Karakalas *et al.* [60] proposed a modified hardening function by introducing a scaled martensite

volume fraction, to be used along with the already existing martensite volume fraction. Branco *et al.* [58], modified the hardening function and the yield parameter of Boyd and Lagoudas model [52, 53] to simulate the one-dimensional cyclic behaviour of SMA and was found to be adequate for simple loading cases like superelasticity. But its efficacy in complex loading cases has not been studied. Moreover, all these models [54, 58, 60], elucidating the minor loops, are based on the assumption that the transformation starts immediately upon load reversal, without showing any elastic response. This assumption does not conform with the well-established $\sigma - T$ phase transformation curve considered in the literature. Hence, to address the same, a modified approach is proposed to mimic the minor hysteresis loop response of SMA, appropriately.

2.4 Proposed Modifications to Account for Minor Loop

The minor hysteresis loop of SMA emanates, as the loading direction is reversed, before the completion of the ongoing transformation. The complete transformation of SMA from austenite to martensite or vice-versa may not always transpire, since actuators need to undergo varying degrees of actuation. Therefore, for practical applications, the SMA models are expected to simulate the partial transformation cases accurately. The Boyd and Lagoudas model [52], predict the SMA behaviour satisfactorily under full transformation cases. In the case of partial transformations, upon load reversal, the loading or unloading path traces an elastic response back to the complete transformation curve, not conforming with the well-established SMA phase diagram based response (Fig.2.1a). To obviate this, Branco *et al.* [58], modified the aforementioned model [52], to accommodate the minor hysteresis loop while simulating pseudoelasticity. However, the model, like many others [54, 60], is based on the assumption that the phase transformation starts immediately upon load reversal, which in general, is not valid. Following the typical phase diagram (refer Fig.2.1a) of SMA, one can infer that upon load reversal, the SMA initially exhibits an elastic response, followed by respective phase transformation, as dictated by the corresponding transformation surface. In this work, a novel approach is undertaken by modifying the yield parameter (Y_f), which is the threshold value of Θ (Eqn.(2.13)).

The associated model parameters are recalculated, to simulate the SMA behaviour under partial transformation cases, more realistically. The modifications are based on the following observations.

- The phase transformation does not initiate immediately upon the reversal of loading direction. Following the reversal, the response pursues an initial elastic loading or unloading path, until it reaches the required condition for the respective forward or reverse transformation to start.

- The size of the minor hysteresis loop proportionally increases with the extent of phase transformation in the loading direction. During the forward transformation ($\xi = 0 \rightarrow \xi = 1$), say, the load reversal occurs at two different points, *i.e.*, at ξ=0.5 and at ξ=0.8. It can be observed that the size of the hysteresis loop associated with a reversal at ξ=0.8 would be greater than the same corresponding to a reversal at ξ=0.5. Thus, the amount of energy dissipated during partial transformation must be proportional to the martensite volume fraction (ξ) at the point of reversal, denoted as ξ_r.

- Upon loading or unloading, as the value of the martensite volume fraction of SMA reaches $\xi = 1$ for forward transformation or $\xi = 0$ for reverse transformation, the minor hysteresis loop generated by the partial transformation should coincide with the major hysteresis loop.

To account for the above observations, the yield parameter Y_f, which is a constant in [52], has been redefined as a function of both ξ and ξ_r as,

$$Y_f = \begin{cases} Y_1 + Y_2\xi_r(1-\xi), & \forall \quad \dot{\xi} > 0 \\ Y_1 + Y_3\xi(1-\xi_r), & \forall \quad \dot{\xi} < 0 \end{cases} \tag{2.18}$$

Now, the seven model parameters, namely, $a_1, a_2, a_3, a_4, Y_1, Y_2$ and Y_3, involved in Eqn.(2.17) and Eqn.(2.18) are to be calculated, to simulate the SMA response under different loading conditions. These parameters are ascertained by solving seven independent

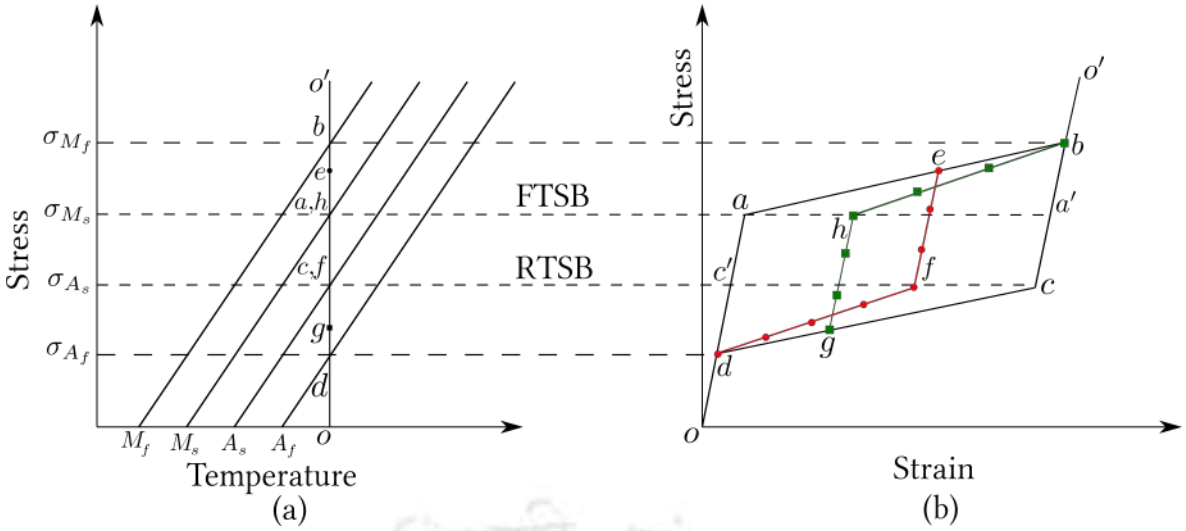

Figure 2.1: (a) Phase Diagram, and (b) Stress-Strain behaviour with minor loops for pseudoelasticity in SMA.

equations, out of which, four equations are framed to satisfy the transformation conditions corresponding to the start and completion of the major loop during both the forward and the reverse transformation, respectively. Other two equations are obtained, by applying the same, at the points of initiation of forward and reverse phase transformations, in the respective minor hysteresis loops. The final condition accounts for the continuity of Gibbs free energy at the point of reversal of loading direction.

Consider, a typical pseudoelastic response of SMA as shown in Fig.2.1b, when subjected to an isothermal loading-unloading path illustrated by the line $o-o'-o$ in Fig.2.1a. The observations are as follows.

- At the initial state 'o', the SMA comprises of complete Austenite phase ($\xi = 0$). Upon loading, following an elastic response, the forward transformation starts at 'a' (at σ_{M_s}), and the same gets completed at 'b' (at σ_{M_f}). Further, it again behaves elastically till o', as the loading continues.

- Similarly, during unloading, starting from the complete Martensite phase ($\xi = 1$) at point o', the reverse transformation begins at point c (at σ_{A_s}) and concludes at a point d (at σ_{A_f}). The rest of the response is elastic.

- The horizontal lines passing through σ_{M_s} and σ_{A_s} are referred to as Forward Transformation Start Boundary (FTSB) and Reverse Transformation Start Boundary

(RTSB), respectively. During loading or unloading, the SMA response is elastic until it crosses either of these boundaries in the respective loading direction.

- During reverse transformation $c \rightarrow d$, if the loading direction is suddenly reversed at 'g', initially, an elastic response is expected till point h, where it intersects with the FTSB and the forward transformation starts at point h and finishes at b.

- Similarly during the forward transformation $a \rightarrow b$, if the load is withdrawn suddenly at 'e', elastic response $e \rightarrow f$ is observed, until it touches the RTSB at 'f', resulting in the reverse transformation $f \rightarrow d$.

- One can observe from Fig.2.1 that during reverse transformation $c \rightarrow d$, even if the load is reversed from any point other than 'g', following an initial elastic response, the forward transformation always tends to start at the same stress level, σ_{M_s}. This asserts the fact that the FTSB must be a constant stress line, and the transformation initiates at the same stress level, irrespective of the strain or material composition at the point of reversal. A similar logic ensues in the definition of the RTSB being another constant stress line, at σ_{A_s}, no matter the value of ε and ξ.

- Within the FTSB and RTSB, the response is always elastic. When loading (or unloading) takes place, the energy supplied (or removed), helps it to overcome the barrier in the respective loading direction. If the loading direction is reversed before reaching the boundary, it behaves elastically again until it reaches the corresponding boundary in the opposite loading direction.

The above mentioned observations render the following conditions to be used to determine the model parameters.

- Beginning of forward transformation (point 'a' in Fig.2.1)
  $\sigma = \sigma_{M_s} = C_M(T_0 - M_s),\ \xi = 0,\ \xi_r = 0,\ T = T_0,\ \Theta = Y_f$

- Completion of forward transformation (point 'b' in Fig.2.1)
  $\sigma = \sigma_{M_f} = C_M(T_0 - M_f),\ \xi = 1,\ \xi_r = 0,\ T = T_0,\ \Theta = Y_f$

- Beginning of reverse transformation (point 'c' in Fig.2.1)

  $\sigma = \sigma_{A_s} = C_A(T_0 - A_s),\ \xi = 1,\ \xi_r = 1,\ T = T_0,\ \Theta = -Y_f$

- Completion of reverse transformation (point 'd' in Fig.2.1)

  $\sigma = \sigma_{A_f} = C_A(T_0 - A_f),\ \xi = 0,\ \xi_r = 1,\ T = T_0,\ \Theta = -Y_f$

- Beginning of partial reverse transformation (point 'f' in Fig.2.1)

  $\sigma = \sigma_{A_s} = C_A(T_0 - A_s),\ \xi = \xi_{r_f},\ \xi_r = \xi_{r_f},\ T = T_0,\ \Theta = -Y_f$

- Beginning of partial forward transformation (point 'h' in Fig.2.1)

  $\sigma = \sigma_{M_s} = C_M(T_0 - M_s),\ \xi = \xi_{r_h},\ \xi_r = \xi_{r_h},\ T = T_0,\ \Theta = Y_f$

  Here, ξ_{r_f} and ξ_{r_h} denote the numerical values of ξ at the corresponding points of reversal, f and h, in Fig.2.1, respectively. Also, $\xi_{r_f} = \xi_e$ and $\xi_{r_h} = \xi_g$, since $e \to f$ and $g \to h$ are elastic paths.

- Continuity of G at the point of reversal (points 'e' or 'g' in Fig.2.1) renders $h_f(\xi = \xi_r)|_{\dot{\xi}>0} = h_f(\xi = \xi_r)|_{\dot{\xi}<0}$, where the numerical values of ξ_r are ξ_e and ξ_g, respectively.

From the above conditions, the model parameters are determined as,

$$
\begin{aligned}
\rho\Delta s_0 &= -C\ H,\\
\rho\Delta u_0 &= \frac{1}{2}\rho\Delta s_0(M_s + A_f),\\
a_1 &= \frac{\pi}{(M_s - M_f)},\\
a_2 &= \frac{\pi}{(A_f - A_s)},\\
a_3 &= \frac{1}{4}\left[C_M^2(T_0 - M_s)^2 + C_A^2(T_0 - A_f)^2\right]\Delta S,\\
a_4 &= \left[\frac{\pi}{2} - \frac{(2\xi_r - 1)\cos^{-1}(2\xi_r - 1)}{4\xi_r} - \frac{\sqrt{1 - (2\xi_r - 1)^2}}{4\xi_r} - \frac{\pi}{4\xi_r}\right]\rho\Delta s_0\left(\frac{1}{a_1} - \frac{1}{a_2}\right),\\
Y_1 &= \frac{1}{2}\rho\Delta s_0\,(M_s - A_f) - a_4,\\
Y_2 &= \frac{\rho\Delta s_0\,[\pi - \cos^{-1}(2\xi_r - 1)]}{a_1\xi_r(1 - \xi_r)},\\
Y_3 &= \frac{\rho\Delta s_0\cos^{-1}(2\xi_r - 1)}{a_2\xi_r(1 - \xi_r)}.
\end{aligned}
\tag{2.19}
$$

where, M_s, M_f, A_s and A_f are martensite start, martensite finish, austenite start and austenite finish temperatures, respectively. The detailed derivations are illustrated in appendix A. Here, $C = C_A$ for reverse transformation and $C = C_M$ for forward transformation, where, C_A and C_M are the slopes of reverse and forward transformation boundaries, respectively. To imitate the non-linear nature of the inelastic response, represented by $f \rightarrow d$ and $h \rightarrow b$ in Fig.2.1, a new Y_f is defined as,

$$Y_f = \begin{cases} Y_1 + Y_2\xi_r \left(e^{\gamma(1-\xi)} - 1\right), & \forall \quad \dot{\xi} > 0 \\ Y_1 + Y_3(1-\xi_r) \left(e^{\gamma\xi} - 1\right), & \forall \quad \dot{\xi} < 0 \end{cases} \tag{2.20}$$

Following the above mentioned transformation and continuity conditions, the new model parameters are derived as,

$$\begin{aligned}
&\rho\Delta s_0 = -C\ H, \\
&\rho\Delta u_0 = \frac{1}{2}\rho\Delta s_0(M_s + A_f), \\
&a_1 = \frac{\pi}{(M_s - M_f)}, \\
&a_2 = \frac{\pi}{(A_f - A_s)}, \\
&a_3 = \frac{1}{4}\left[C_M^2(T_0 - M_s)^2 + C_A^2(T_0 - A_f)^2\right]\Delta S, \\
&a_4 = \left[\frac{\pi}{2} - \frac{(2\xi_r - 1)\cos^{-1}(2\xi_r - 1)}{4\xi_r} - \frac{\sqrt{1-(2\xi_r-1)^2}}{4\xi_r} - \frac{\pi}{4\xi_r}\right]\rho\Delta s_0 \left(\frac{1}{a_1} - \frac{1}{a_2}\right), \\
&Y_1 = \frac{1}{2}\rho\Delta s_0\left(M_s - A_f\right) - a_4, \\
&Y_2 = \frac{\rho\Delta s_0\left[\pi - \cos^{-1}(2\xi_r - 1)\right]}{a_1\xi_r\left(e^{\gamma(1-\xi_r)} - 1\right)}, \\
&Y_3 = \frac{\rho\Delta s_0\cos^{-1}(2\xi_r - 1)}{a_2(1-\xi_r)\left(e^{\gamma\xi_r} - 1\right)}.
\end{aligned} \tag{2.21}$$

The detailed derivations are illustrated in appendix B. The next section discusses the numerical implementation of the constitutive model, following the convex cutting return mapping algorithm. This is followed by a comparison of the simulated responses obtained from the proposed approach against the existing models.

2.5 Return Mapping Algorithm

At each time step, the model updates the stress ($\boldsymbol{\sigma}$), the martensite volume fraction (ξ) and the transformation strain ($\boldsymbol{\varepsilon}^t$), by solving a set of non-linear constitutive relation (Eqn.(2.3)), the flow rule (Eqn.(2.6)) and satisfying the Kuhn-Tucker conditions (Eqns.(2.14) and (2.15)). To take care of these, an iterative procedure is followed [56], which involves a predictor-corrector approach. First, the stress is predicted for the given increment in strain and temperature, based on the material properties obtained in the previous loading step. Then the current state is checked with respect to the transformation surface. If the predicted state is below the transformation surface, the response is elastic, and the same is assumed to be final. Else, the $\boldsymbol{\sigma}, \xi$ and $\boldsymbol{\varepsilon}^t$ are modified, iteratively, until it falls on the transformation surface. There are two approaches for modifying these parameters, namely, (i) the convex cutting algorithm, and (ii) the closest point projection algorithm. The former is explicit and has been used in this study. The convex cutting algorithm is discussed in the next section.

2.5.1 Convex Cutting Return Mapping Algorithm

Thermoelastic Prediction

Here, a thermo-elastic problem is solved, assuming the increment of the martensite volume fraction (ξ) and the transformation strain ($\boldsymbol{\varepsilon}^t$) as zero, *i.e.*,

$$\dot{\boldsymbol{\varepsilon}} = \dot{\boldsymbol{\varepsilon}}(t), \quad \dot{T} = \dot{T}(t), \quad \dot{\xi} = 0, \quad \dot{\boldsymbol{\varepsilon}}^t = 0. \tag{2.22}$$

At time t_{n+1}, using the given input values, strain ($\boldsymbol{\varepsilon}_{n+1}$) and temperature ($T_{n+1}$), the trail stress ($\boldsymbol{\sigma}^{(0)}_{n+1}$) and the value of the transformation function ($\phi^{(0)}_{n+1}$) are calculated, following Eqns.(2.3) and (2.13), respectively. The transformation function is then checked for a tolerance of $\phi \leq 10^{-8}$. If the conditions are satisfied, the current values ($\boldsymbol{\sigma}_{n+1}, \xi_{n+1}, \boldsymbol{\varepsilon}^t_{n+1}$) are taken as the final value, and one goes for the next time step ($t_{n+1} \rightarrow t_{n+2}$). If the conditions are violated, the predicted thermo-elastic state is outside the transformation

surface, and the transformation corrector is invoked to restore consistency, following,

$$\dot{\boldsymbol{\varepsilon}} = 0, \quad \dot{T} = 0, \quad \dot{\boldsymbol{\varepsilon}}^t = \boldsymbol{\Lambda}\dot{\xi}. \tag{2.23}$$

Transformation Correction

As the predicted elastic state violates the transformation conditions, *i.e.*, $\phi_{n+1}^{(0)} > 0$, the SMA is presumed to be undergoing phase transformation. Here, it is assumed that both strain ($\boldsymbol{\varepsilon}$) and temperature (T) are constant, *i.e.*, $d\boldsymbol{\varepsilon} = 0$ and $dT = 0$. One obtains $\frac{d\boldsymbol{\sigma}}{d\xi}$ from the differential form of the constitutive relation (Eqn.(2.3)) and the flow rule (Eqn.(2.6)) as,

$$\frac{d\boldsymbol{\sigma}}{d\xi} = \begin{cases} -\boldsymbol{S}^{-1} : \partial_{\boldsymbol{\sigma}}\phi, & \dot{\xi} > 0, \\ \boldsymbol{S}^{-1} : \partial_{\boldsymbol{\sigma}}\phi, & \dot{\xi} < 0. \end{cases} \tag{2.24}$$

Subsequently, the increment in stress for k^{th} iteration, at time t_{n+1}, is calculated as,

$$\Delta\boldsymbol{\sigma}_{n+1}^{(k)} = -\Delta\xi_{n+1}^{(k)} {\boldsymbol{S}_{n+1}^{(k)}}^{-1} : \begin{cases} \partial_{\boldsymbol{\sigma}}\phi_{n+1}^{(k)}, & \dot{\xi} > 0, \\ -\partial_{\boldsymbol{\sigma}}\phi_{n+1}^{(k)}, & \dot{\xi} < 0. \end{cases} \tag{2.25}$$

Linearizing the transformation function (ϕ) for the k^{th} iteration and equating it to zero, one obtains,

$$\phi_{n+1}^{(k)} + \partial_{\boldsymbol{\sigma}}\phi_{n+1}^{(k)} : \Delta\boldsymbol{\sigma}_{n+1}^{(k)} + \partial_{\xi}\phi_{n+1}^{(k)}\Delta\xi_{n+1}^{(k)} = 0. \tag{2.26}$$

Substituting Eqn.(2.25) into Eqn.(2.26), the increment of martensite volume fraction, ξ is obtained as,

$$\Delta\xi_{n+1}^{(k)} = \frac{\phi_{n+1}^{(k)}}{\pm\partial_{\boldsymbol{\sigma}}\phi_{n+1}^{(k)} : {\boldsymbol{S}_{n+1}^{(k)}}^{-1} : \partial_{\boldsymbol{\sigma}}\phi_{n+1}^{(k)} - \partial_{\xi}\phi_{n+1}^{(k)}}. \tag{2.27}$$

Here, the +ve sign and -ve signs are applicable for forward and reverse transformations, respectively. Consequently, the change in transformation strain (ε^t) is calculated following,

$$\Delta\boldsymbol{\varepsilon}_{n+1}^{t(k)} = \Delta\xi_{n+1}^{(k)}\boldsymbol{\Lambda}_{n+1}^{(k)}. \tag{2.28}$$

The transformation strain ($\boldsymbol{\varepsilon}^t$) and the martensite volume fraction (ξ) are subsequently

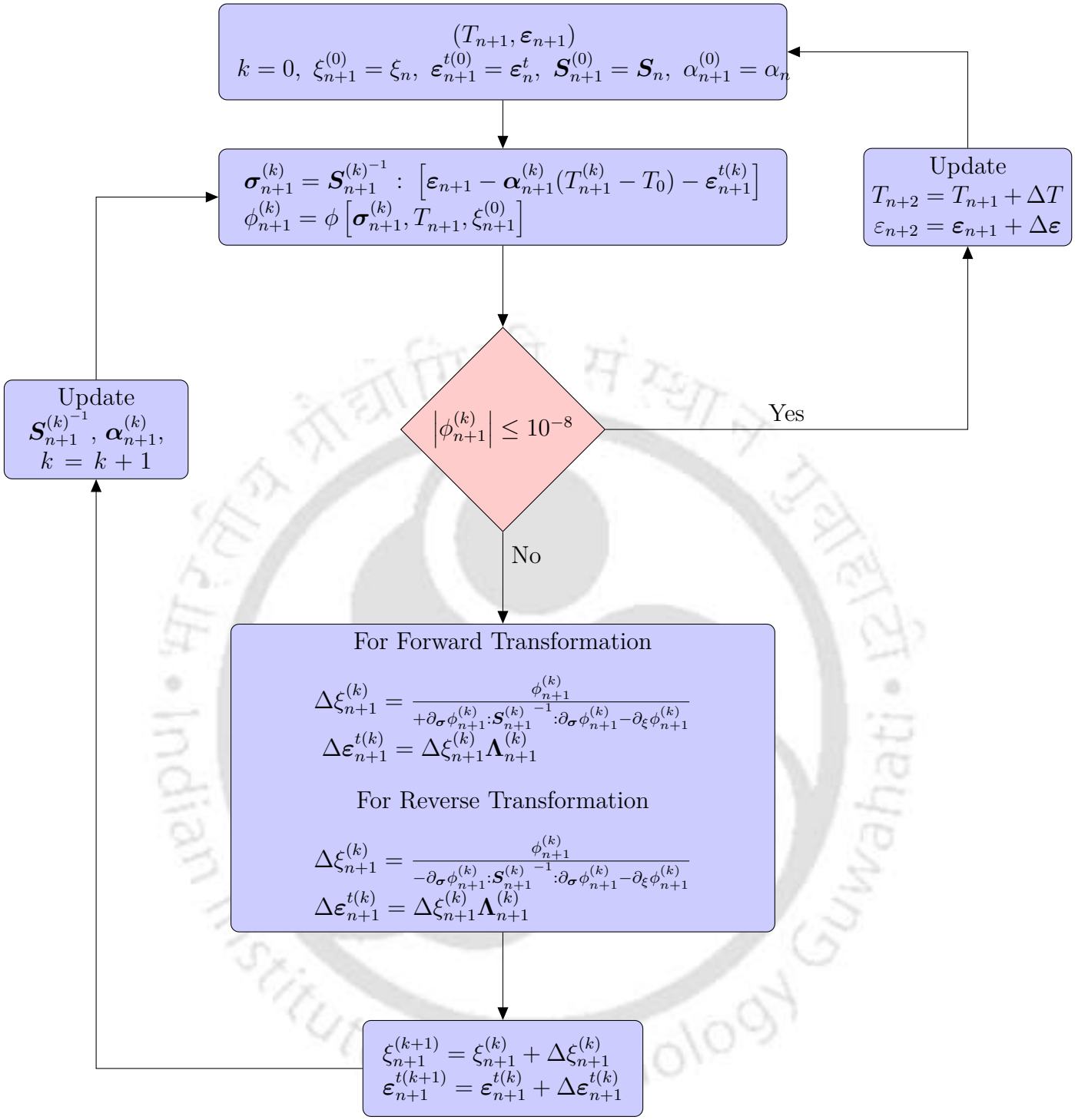

Figure 2.2: Flowchart of convex cutting plane algorithm [1].

updated as,

$$\boldsymbol{\varepsilon}_{n+1}^{t(k+1)} = \boldsymbol{\varepsilon}_{n+1}^{t(k)} + \Delta\boldsymbol{\varepsilon}_{n+1}^{t(k)}, \tag{2.29}$$

$$\xi_{n+1}^{(k+1)} = \xi_{n+1}^{(k)} + \Delta\xi_{n+1}^{(k)}. \tag{2.30}$$

Finally, with updated ξ and $\boldsymbol{\varepsilon}^t$, the values of $\boldsymbol{\sigma}$ and ϕ are recalculated and checked for tolerance. If $\phi \leq 10^{-8}$, then the updated values are taken as the final value. Else, the iterative procedure is continued ($(k+1) \rightarrow (k+2)$), until the final state lies on the transformation surface. Once the iteration converges, the updated values of $\boldsymbol{\sigma}$, ξ and $\boldsymbol{\varepsilon}^t$ are noted and then one proceeds for the next time step ($t_{n+1} \rightarrow t_{n+2}$). The algorithm is schematically depicted in Fig.2.2.

2.6 Results and Discussions

In this section, both the Boyd and Lagoudas model [52] and the same with modifications discussed in Section 2.4, are implemented in MATLAB R2019a, and the responses are compared. To evaluate the performance of the proposed approach, two pseudoelastic loading cases are considered, simulating partial transformation instances during both forward and reverse transformation cases. They are also compared with the corresponding responses obtained using the model of Branco *et al.* [58]. In the 1^{st} case, as illustrated in Fig.2.3a, an SMA wire initially at zero stress condition (point o), is stretched till 9% strain (point c), followed by complete unloading (point o'), at a constant temperature of $T_0 = 295\text{K} > A_f$. Again, it is partially stretched till 5% strain (point g), followed by a complete withdrawal of strain (point o''). In the 2^{nd} case, an SMA wire with an initial strain of 9% (point o), is unloaded at a constant temperature of $T_0 = 295\text{K}$, to recover the undeformed length completely (point c) as depicted in Fig.2.3b. It is again stretched back to induce 9% strain (point o'), followed by unloading till 4% strain (point g) and finally elongated back to 9% strain (point o''). The material parameters are illustrated in Table 2.1. In the case of the Boyd and Lagoudas model, the response is simulated, using the hardening function proposed by the authors as Eqn.(3.4.92) in [1]. The hardening model represented by Eqn.(17) in [58] has been used to simulate the response corresponding to Branco *et al.* . The simulated stress-strain responses for both the loading cases are illustrated in Fig.2.4. The responses obtained from the modified model, using both the linear Y_f defined by Eqn.(2.18) and exponential Y_f referred in Eqn.(2.20), are shown in the same figure, in red and blue, respectively. Since different hardening functions are used,

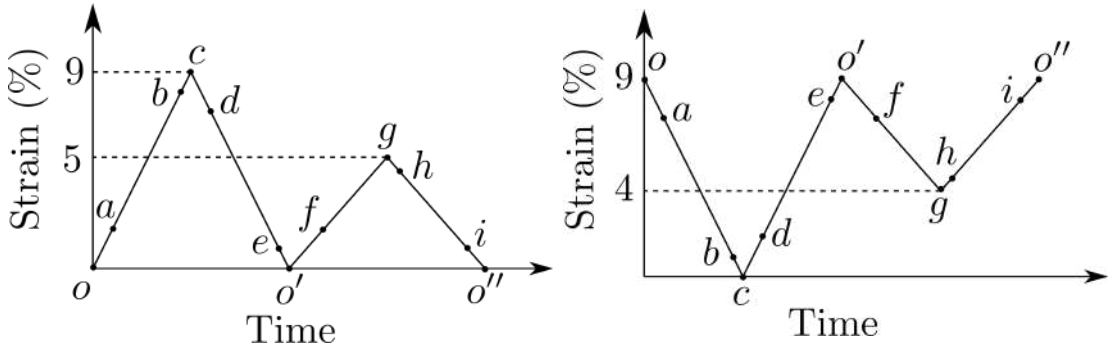

Figure 2.3: Loading pattern with load reversal during, (a) forward transformation, and (b) reverse transformation.

Table 2.1: Material parameters of SMA [58]

Material parameter	Value	Material parameter	Value
E^A	24 GPa	E^M	20 GPa
α_A	22×10^{-6} °C^{-1}	α_M	22×10^{-6} °C^{-1}
C_A	7×10^6 MPa/K	C_M	7×10^6 MPa/K
A_s	231.3 K	A_f	258.6 K
M_s	237.5 K	M_f	193.9 K

each of the models exhibits a different response curve for the same loading cycle. Hence, for better comparison, the cosine hardening function defined by Eqn.(2.17), is used for all three models and the corresponding results are depicted in Fig.2.5. Moreover, as the nature of the response obtained using the exponential Y_f (Eqn.(2.20)) is more realistic compared to the linear one (Eqn.(2.18)), the former one is presented here.

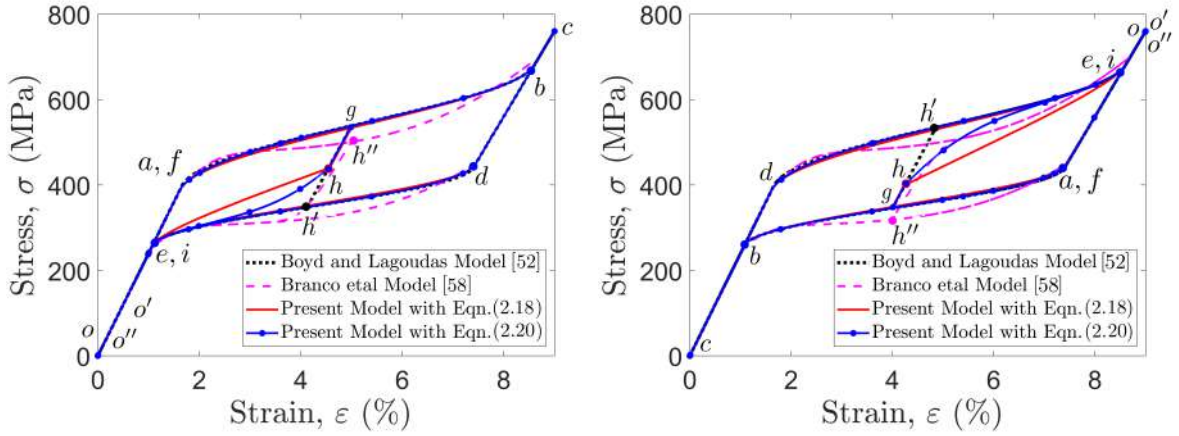

Figure 2.4: Stress-Strain response predicted by Boyd and Lagoudas [52], Branco *et al.* [58] and Modified Lagoudas model with load reversal during, (a) forward transformation, and (b) reverse transformation.

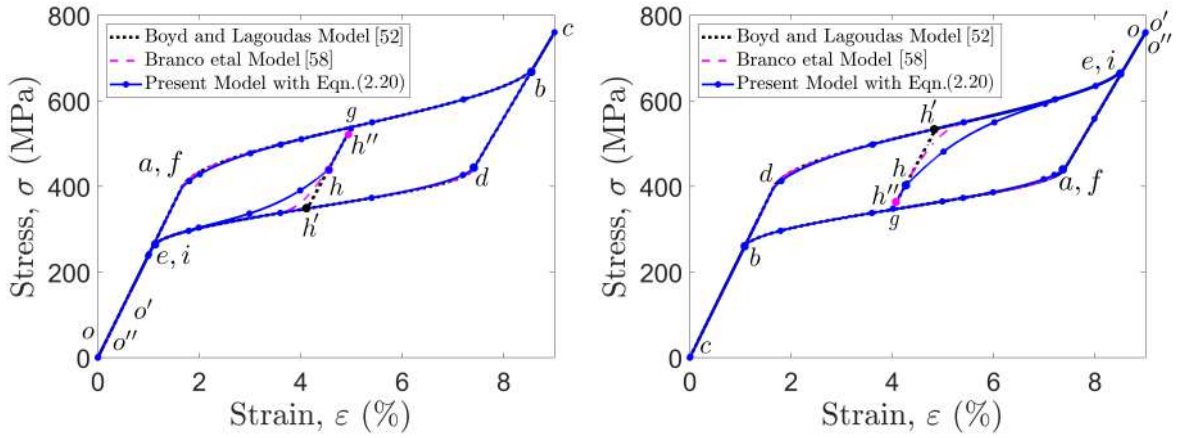

Figure 2.5: Stress-Strain response predicted by Boyd and Lagoudas [52], Branco *et al.* [58] and Modified Lagoudas model with load reversal during, (a) forward transformation, and (b) reverse transformation, using cosine hardening function.

In the 1^{st} case, upon stretching from 0 to 9% and subsequent unloading, the full transformation path $o \rightarrow a \rightarrow b \rightarrow c \rightarrow d \rightarrow e \rightarrow o'$ is identical for all the three models, as shown in Fig.2.5a. In the next loading cycle, where strain is increased to 5% and subsequently reduced to zero, the three responses deviate from the point of load reversal, defined as g. Here, h, h' and h'' are the points of initiation of reverse transformation (in the minor loop), as obtained from the modified approach, the Boyd and Lagoudas model and the model presented by Branco *et al.* , respectively. The $\sigma - \varepsilon$ response as obtained from [52], $g \rightarrow h' \rightarrow i \rightarrow o''$ (in dotted black), behaves elastically until it meets its major loop response curve for reverse transformation at h'. It implies that even if $\sigma < \sigma_{A_s}$, during $g \rightarrow h'$, the SMA behaves elastically, which is not correct. The model of Branco *et al.* [58], predicts the partial transformation, $g \rightarrow h'' \rightarrow i \rightarrow o''$ (in dashed magenta), starts as soon as the load reversal takes place, depicted by point h'', contravening the concept of $\sigma - T$ phase diagram (Fig.2.1a), according to which the transformation should start following an elastic unloading step. Whereas in the present approach, the minor loop response represented by $g \rightarrow h \rightarrow i \rightarrow o''$ (in blue), the reverse transformation starts at h, after an initial elastic unloading phase $g \rightarrow h$. Also, it can be verified from Fig.2.5a, that the reverse transformation for the partial loading case has started at the same stress as that of the major loop, *i.e.*, $\sigma_h = \sigma_d$.

The same can be observed in the 2^{nd} loading case (see Fig.2.3b) as well, the responses of

which are shown in Fig.2.5b. The full transformation curves for the three models are alike, as seen in the figure. After reducing the strain level to 4% and again stretching it back to 9%, a similar deviation is seen at the beginning of unloading (point 'g'). Here, h, h' and h'' are defined as the points at which the forward transformation starts upon reloading, as obtained from the current approach, and the model proposed by Boyd and Lagoudas [52] and the one presented by Branco *et al.* [58]. The model of Boyd and Lagoudas predicts elastic response upon reloading till h'. Whereas, the response obtained using the model of Branco *et al.* shows no elastic response, and the transformation starts immediately upon reloading. On the contrary, in the proposed approach, the forward transformation in the modified model, initiates only after σ_d, following an elastic response $g \rightarrow h$ (in blue).

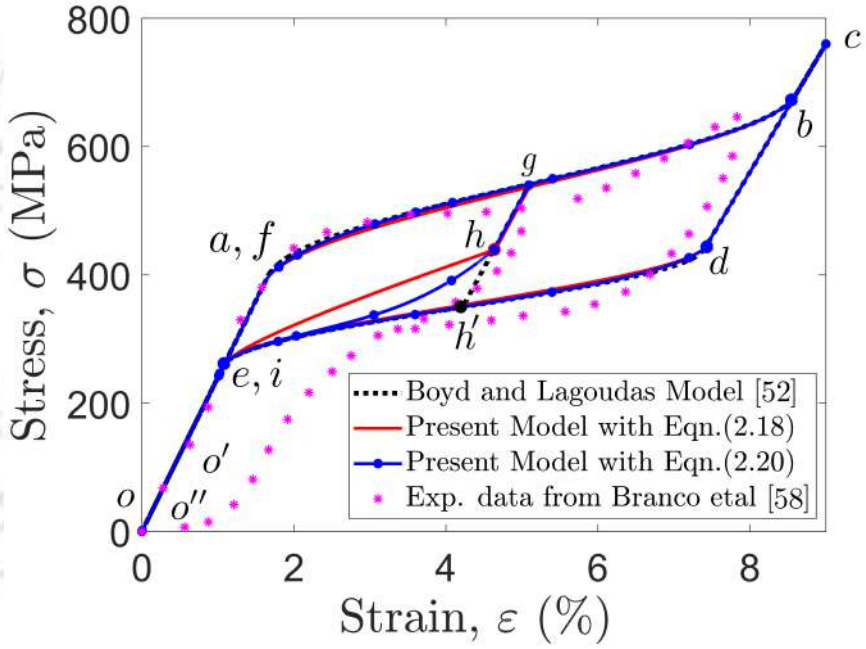

Figure 2.6: Stress-Strain response predicted by Boyd and Lagoudas [52] and modified model, compared against experimental data from Branco *et al.* [58], with load reversal during forward transformation

The real-world performance of the proposed model has been validated by comparing the simulation results with the experimental one presented by Branco *et al.* [58], and are shown in Fig.2.6. The simulation responses obtained from all the models are found to be qualitatively identical for the complete transformation case (major loop). Whereas, the minor loop response obtained following the model of Boyd and Lagoudas [52], exhibits an elastic response till h', where it coincides with the major loop response corresponding

to the reverse phase transformation. However, with the proposed approach, where $Y_f(\xi)$ is modelled as a linear function (Eqn.(2.18)), the initial response during unloading is found to be elastic (path $g \rightarrow h$), following which the response becomes non-linear due to the initiation of reverse phase transformation. It can be observed that the initial elastic unloading part does follow the experimental response qualitatively. However, the following inelastic response (path $h \rightarrow i$ depicted in red) does not meet the corresponding major loop response as found experimentally. To address this issue, the minor loop response using the modified $Y_f(\xi)$, expressed as an exponential function (Eqn.(2.20)) is simulated and presented in the same figure (in blue). This approach enables one to model both the initial elastic (path $g \rightarrow h$) as well as the following inelastic response (path $h \rightarrow i$ depicted in blue) during unloading, which is qualitatively in agreement with the experimental response. These responses demonstrate the efficacy of the proposed approach in capturing the minor loop response of an SMA wire.

2.7 Conclusions

In this chapter, the thermodynamics-based model proposed by Boyd and Lagoudas has been studied, to simulate the SMA response under capricious loading conditions. The constitutive model replicates the full transformation response of SMA satisfactorily, but is found to have limitations in accurately predicting the partial transformation response. Although a few modified approaches are prescribed in the literature, to address the same, each has its own set of shortcomings. Here, based on the well-established $\sigma - T$ phase diagram of SMA, a simple but effective methodology is proposed to mimic the partial phase transformation behaviour of SMA. Two new threshold parameters, 'Y_f', are introduced, which depend on the phase transformation evolution measures (ξ and ξ_r). The corresponding model parameters are evaluated following the newly introduced transformation criteria. A set of pseudoelastic cases with partial transformation during loading and unloading are simulated, using the modified model. The responses predicted by the new approach are then compared with those obtained from the existing models, and the former has been found to yield a more realistic response for partial transformation cases.

Chapter 3

Self-Sensing of SMA Wire Actuator Using an Extended Kalman Filter

3.1 Introduction

This chapter discusses the development of an Extended Kalman Filter (EKF) based estimation technique to explore the self-sensing feature of Shape Memory Alloys (SMA) wire actuators. An EKF is a tool that can be used to estimate the state of a system by utilising its dynamic model and employing some of the measured states of the system. During thermo-mechanical loading, SMA wires undergo phase transformation, resulting in the various material properties, like elastic modulus, electrical resistivity, thermal conductivity, etc., to vary as a function of martensite volume fraction (ξ). This yields a change in the electrical resistance of the wire, which can be used to estimate the SMA wire's state. Here, an EKF model has been developed to estimate the SMA wire actuator's response from the change in its electrical resistance during actuation. Firstly, the system model, required for the EKF is formulated. The necessary experimental setup is fabricated, and the developed EKF model is used to estimate the system response, offline, from the experimentally measured change in electrical resistance of the SMA wire during actuation.

3.2 Self-Sensing in SMA Wire Actuators

As a pre-strained SMA wire is heated by means of resistive heating (Joule's effect), the temperature increases and as it rises above the austenite start temperature, the SMA starts transforming from martensite state into the austenite phase. During this process, both the stress and temperature increase (refer Fig.3.1a) and the corresponding electrical resistance reduces due to the changes in the length of the SMA wire and the electrical resistivity of the material (refer Fig.3.1b). Upon cooling, the SMA traces back to its original state, albeit accompanied by a hysteresis behaviour. Various control mechanisms [66, 98, 99, 100] are proposed in the literature to control this highly non-linear behaviour of SMA. However, these feedback systems require external sensors, which makes the system bulky and costly. This can be avoided by utilizing the self-sensing behaviour of SMA, wherein the change in the electrical resistance of the SMA wire can be used to determine the system's state. In the literature, various empirical methodologies are proposed to harness the self-sensing feature of SMA wire actuators. However, these mechanisms are system-specific, requiring experimentally derived polynomial relations, which is unique to the given system undergoing a particular loading-unloading cycle. To obviate this, a robust estimation technique, which can be used under a varied set of loading conditions, has to be developed to predict the state of the SMA wire system, taking into account the change in the electrical resistance of SMA while actuating. For this purpose, Gurung and Banerjee proposed an Extended Kalman Filter (EKF) [84] and an Unscented Kalman Filter (UKF) [85] to estimate the SMA system's response. However, these filters are developed using phenomenological models [43, 44]. This class of models, are convenient to study and simulate a wide variety of SMA wire-based engineering applications due to their simplicity. However, they possess limited capability when SMA actuators are subjected to non-monotonic loading. The model proposed by Buravalla and Khandelwal [47] could be used in such loading cases. But in order to apply these models, the loading path must be known a-priori, which implies that the entire load history is to be known in the $\sigma - T$ phase diagram of SMA (Fig.1.1). The determination of the transformation status in the $\sigma - T$ diagram, for an arbitrary loading case, is discussed in [51], which involves

a complex algorithm. In this scenario, the thermodynamics-based models [52, 57] may be a better proposition for such loading conditions, as the transformation surface helps in identifying the status of SMA phase transformation even in non-proportional cases. Hence, the modified Boyd and Lagoudas model discussed in Chapter 2, affords to be a better choice for the state estimation of SMA wire actuators, for both proportional as well as non-proportional loading conditions. Hence, a state estimation technique following an Extended Kalman Filter has been developed based on the modified Boyd and Lagoudas model and is briefly outlined in the next section.

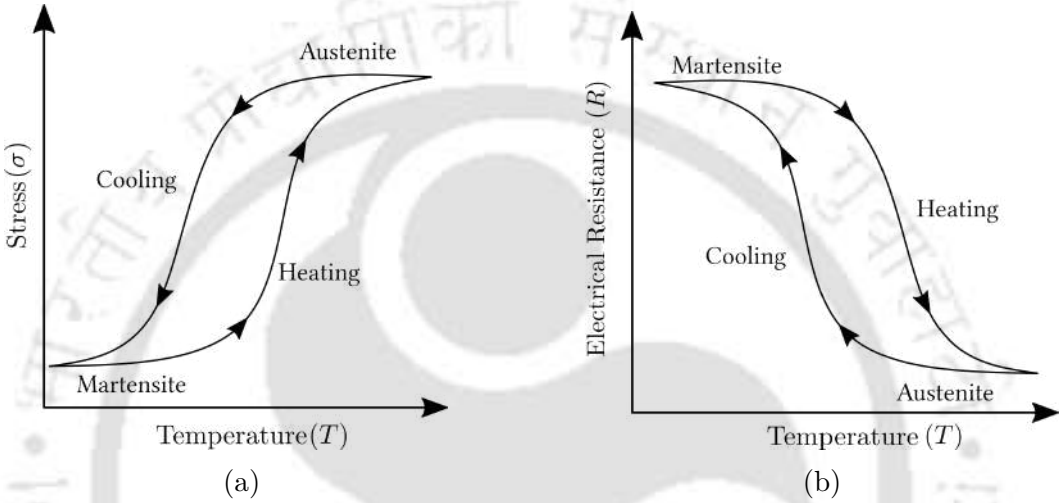

Figure 3.1: (a) Variation of stress, and the (b) corresponding change in electrical resistance of SMA wire actuator with its temperature [94].

3.3 Extended Kalman Filter

State estimation is the process of estimating the state variables of the dynamic model of a physical system, by utilizing the information of the system's behaviour till the previous instant. Various state estimation techniques are proposed in the literature; however, the Kalman filter (KF) is one of the most popular and optimal state estimators for a linear system. It is commonly used

- to estimate a system's state which cannot be measured directly, and
- to estimate the state of a system by combining the measurements from different sources which may contain noise.

The problem with linear systems is that they are seldom found in nature, and thus non-linear estimators are required. The Extended Kalman Filter (EKF) is basically a Kalman filter-based estimator, applied to a linearised version of a non-linear system. An EKF estimates the present state of a dynamic model by using,

- the non-linear system dynamics,
- the values of state variables at the previous state,
- the measurement values at the present state, and
- the process and measurement noises.

EKF-based algorithms are being developed [101] for intelligent electricity distribution grids, which play a major role in an energy-efficient future. EKFs are being used to accurately determine the state of charge (SoC) of Li-ion batteries [102, 103]. Navigation systems for micro-aerial vehicles (MAV) are developed based on EKFs, which combine the magnetometer and optical sensor data and estimate the velocity and altitude of the MAV [104]. In this case of evaluating the current state of an SMA system, a discrete-time EKF is used, which considers discrete-time system dynamics and measurements [105]. The following section discusses the basic steps involved in an EKF.

3.3.1 Discrete Non-Linear System Model

At any time t_{n+1}, the system model comprises of,

- **Process Model:** It defines a non-linear function which propagates the mean and covariance of the states through time. It can be represented in the discrete form as,

$$\boldsymbol{X}_{n+1} = \boldsymbol{f}(\boldsymbol{X}_n, \boldsymbol{u}_{n+1}) + \boldsymbol{w}_n, \tag{3.1}$$

  where, $\boldsymbol{X}$ denotes the state variable vector, $\boldsymbol{u}$ is the input vector and $\boldsymbol{w}$ refers the process noise. Here, subscripts $n+1$ and n denote the present state and the previous state, respectively.

- **Measurement Model:** It represents the output of the system ($\boldsymbol{Y}$) as a non-linear function of state variables ($\boldsymbol{X}$) and the measurement noise ($\boldsymbol{v}$) as,

$$\boldsymbol{Y}_{n+1} = \boldsymbol{g}(\boldsymbol{X}_{n+1}) + \boldsymbol{v}_{n+1}. \tag{3.2}$$

3.3.2 Noise Models

The noise models, $\boldsymbol{w}_n$ and $\boldsymbol{u}_n$ are both assumed to be white, having zero-mean and are uncorrelated with known covariances $\boldsymbol{Q}_n$ and $\boldsymbol{M}_n$, respectively. They are represented as,

$$\begin{aligned} \boldsymbol{w}_n &\sim (0, \boldsymbol{Q}_n), \\ \boldsymbol{v}_n &\sim (0, \boldsymbol{M}_n), \\ E(\boldsymbol{w}_n \boldsymbol{w}_q^T) &= \boldsymbol{Q}_n \delta_{n-q}, \\ E(\boldsymbol{v}_n \boldsymbol{v}_q^T) &= \boldsymbol{M}_n \delta_{n-q}, \\ E(\boldsymbol{v}_n \boldsymbol{w}_q^T) &= 0. \end{aligned} \tag{3.3}$$

Here, δ_{n-q} is Kronecker delta function, where δ_{n-q}=1, for $n = q$ and δ_{n-q}=0, for $n \neq q$. $\boldsymbol{Q}_n$ is the process noise covariance matrix and $\boldsymbol{M}_n$ denotes the measurement noise covariance matrix.

3.3.3 Algorithm

At each time step, EKF undergoes two processes, namely, the Time Update step and Measurement Update step. These are discussed below.

1. **Time Update:**

   In this step, the EKF predicts the present value (time instant '$n+1$') of the state variable ($\boldsymbol{X}$) from its corresponding values at the previous step (time instant 'n') and the current input ($\boldsymbol{u}$) using the process model, following,

$$\boldsymbol{X}_{n+1}^{-} = \boldsymbol{f}(\boldsymbol{X}_n^{+}, \boldsymbol{u}_{n+1}) + \boldsymbol{w}_n. \tag{3.4}$$

Here, the obtained state $\boldsymbol{X}_{n+1}^{-}$ is known as the a-priori state estimate. The state error covariance is denoted as $\boldsymbol{P} = \mathrm{E}[(\boldsymbol{X} - \bar{\boldsymbol{X}})(\boldsymbol{X} - \bar{\boldsymbol{X}})^{\mathrm{T}}]$ and is obtained for the present state following the equation,

$$\boldsymbol{P}_{n+1}^{-} = \boldsymbol{J}_n \boldsymbol{P}_n^{+} \boldsymbol{J}_n^{\mathrm{T}} + \boldsymbol{Q}_n. \tag{3.5}$$

Here $\boldsymbol{J}$ refers to the Jacobian of $\boldsymbol{f}$ and $\bar{\boldsymbol{X}}$ is the mean value of $\boldsymbol{X}$.

2. **Measurement Update:**

In this step, the a-priori state estimate and the state error covariance obtained in the Time Update step are updated by using the measurement data ($\boldsymbol{Y}$) at the present state. The a-priori state estimate is updated as,

$$\boldsymbol{X}_{n+1}^{+} = \boldsymbol{X}_{n+1}^{-} + \boldsymbol{K}_{n+1}(\boldsymbol{Y}_{n+1} - \boldsymbol{g}(\boldsymbol{X}_{n+1}^{-})). \tag{3.6}$$

Here, $\boldsymbol{X}_{n+1}^{+}$ is termed as the posteriori state estimate. This estimate is the weighted average of a-priori state estimate ($\boldsymbol{X}_{n+1}^{-}$) and the measurement residue ($\boldsymbol{Y}_{n+1} - \boldsymbol{g}(\boldsymbol{X}_{n+1}^{-})$), which is difference between the actual measurement ($\boldsymbol{Y}_{n+1}$) and the estimated output $\left(\boldsymbol{g}(\boldsymbol{X}_{n+1}^{-})\right)$. If the estimated output is closer to the measured value, the state estimated is accurate. But for large differences, the estimated state is inaccurate. Here, the Kalman gain determines the significance of both the a-priori estimate and the measurement in determining the posteriori state estimate. The Kalman gain $\boldsymbol{K}_{n+1}$ is defined as,

$$\boldsymbol{K}_{n+1} = \boldsymbol{P}_{n+1}^{-} \boldsymbol{N}_{n+1}^{\mathrm{T}} (\boldsymbol{N}_{n+1} \boldsymbol{P}_{n+1}^{-} \boldsymbol{N}_{n+1}^{\mathrm{T}} + \boldsymbol{M}_{n+1})^{-1}, \tag{3.7}$$

where, $\boldsymbol{N}$ is the Jacobian of $\boldsymbol{g}$. The Kalman gain is determined by using the state error covariance ($\boldsymbol{P}_{n+1}^{-}$) and the measurement noise covariance ($\boldsymbol{M}_{n+1}$). If the measurement data is very noisy, the Kalman gain is small due to a large $\boldsymbol{M}_{n+1}$. In such cases, more weightage is given to the a-priori state to determine the present state. In case of large state error covariance, the Kalman gain would have a higher value and more emphasis is given to the measurement data to estimate the present

state. Finally, the a-priori state error covariance is then updated following,

$$\boldsymbol{P}_{n+1}^{+} = (\mathbf{I} - \boldsymbol{K}_{n+1}\boldsymbol{N}_{n+1})\boldsymbol{P}_{n+1}^{-}. \tag{3.8}$$

3.4 SMA Wire Actuated Linear System

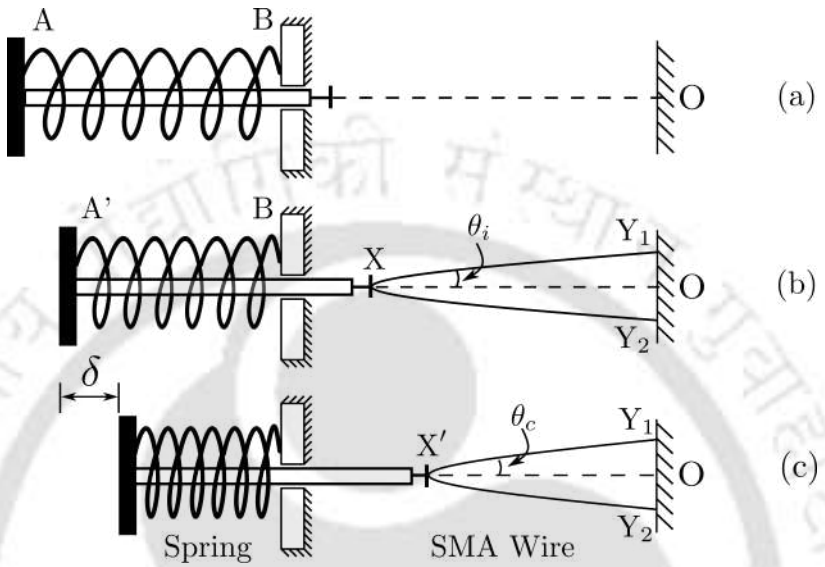

Figure 3.2: Schematic of a linear spring biased SMA wire actuator, illustrating (a) the initial configuration, (b) the initial pre-compressed configuration, and (c) an intermediate position while actuating.

A linear spring AB, shown in Fig.3.2a has been compressed and is then connected to an SMA wire ($Y_1 - X - Y_2$) and held between two fixed supports, as shown in Fig.3.2b. The wire at room temperature is hence loaded to a stress above σ_f^{cr} such that it is in a complete Detwinned Martensite state. Here, the spring will constrain the recovery of SMA wire, as it undergoes phase transformation during heating. In this arrangement, both the stress and strain in SMA will vary simultaneously with its temperature. As the SMA wire is heated by passing an electrical current through it, its temperature increases due to resistive heating, and reverse transformation sets in. The corresponding extent of transformation is exhibited through the change in length of the SMA wire; compressing the spring by δ, as shown in Fig.3.2c. Here, $Y_1 - X - Y_2$ is the initial pre-strained state of the SMA wire and $Y_1 - X' - Y_2$ is some intermediate state of the SMA wire during recovery, following reverse transformation upon heating. During reverse transformation,

the electrical resistance of the SMA wire reduces due to the decrement in its length and the drop in its electrical resistivity.

Upon reduction of electrical input, the SMA wire starts cooling due to convective heat loss with the environment. The forward transformation initiates as the temperature drops below the martensite start temperature. Due to the spring force, the austenite phase transforms back to the detwinned martensite phase, allowing the SMA wire to return to its initial length. During the forward transformation, the electrical resistance of the SMA wire gradually increases back to its initial value. The goal of the present study is to relate the change in length of the SMA wire with the change in electrical resistance of the same. For this purpose, the system model is formulated in the following section, which will be used in the EKF model.

3.5 Development of Process and Measurement Models

This section discusses the development of the heat balance equation governing the temperature variation in the SMA wire. It is followed by the derivation of the one-dimensional SMA constitutive model, to determine the state of the SMA wire, while subjected to strain and temperature increment. Finally, the relation between the strain in the wire and the stress governed by the force equilibrium equation, and the kinematic constraints are derived.

3.5.1 Heat Balance Equation

In practical applications, the temperature of an SMA wire is controlled through Joule's heating. For this, a voltage is applied across the thin SMA wire, and since the wire has a very large electrical resistance, resistive heating increases its temperature. Here, the SMA wire is modelled as a thin cylinder having uniform temperature, T and subjected to uniform resistive heating with convective heat loss to the ambience. The latent heat of absorption and emission during phase transformation are also considered. The governing

differential heat equation can be derived from energy conservation as,

$$C_v \frac{dT}{dt} = \frac{1}{v_m}\left(\frac{V(t)^2}{R_{sma}} - hA_{surf}(T - T_a)\right) + \lambda \frac{d\xi}{dt}. \tag{3.9}$$

Here, $V(t)$ denotes the applied voltage at any time instant 't'. R_{sma} is the electrical resistance of the SMA wire, A_{surf} represents the surface area of the SMA wire and T_a is the ambient temperature. λ refers to the latent heat of transformation, v_m is the volume of SMA wire, and C_v is the effective heat capacity of SMA. Like other material properties, the effective heat capacity is derived as a linear combination of the same at pure martensite and austenite state, following,

$$C_v(\xi) = C_v^A + \xi(C_v^M - C_v^A). \tag{3.10}$$

In the above equation, C_v^M and C_v^A are the heat capacity of SMA in complete martensite and austenite phases, respectively. Here, the heat transfer coefficient 'h' is taken as a quadratic function of temperature [84] as,

$$h = h_0 + h_1 T^2, \tag{3.11}$$

where, h_0 and h_1 are constants. The difference form of heat balance equation (Eqn.(3.9)) can be derived as,

$$C_v \Delta T = \frac{1}{v_m}\left(\frac{V(t)^2}{R_{sma}} - hA_{surf}(T - T_a)\right) \times \Delta t + \lambda \Delta \xi. \tag{3.12}$$

Eqn.(3.12) can be rewritten as,

$$C_v(T_{n+1} - T_n) = \frac{1}{v_m}\left(\frac{V_{n+1}^2}{R_{sma}} - hA_{surf}(T_{n+1} - T_a)\right) \times \Delta t + \lambda \Delta \xi_{n+1}. \tag{3.13}$$

Upon rearranging the above equation, one obtains,

$$T_{n+1}\left(C_v + \frac{hA_{surf}\Delta t}{v_m}\right) = C_v T_n + \frac{1}{v_m}\left(\frac{V_{n+1}^2}{R_{sma}} + hA_{surf}T_a\right) \times \Delta t + \lambda \Delta \xi_{n+1}. \tag{3.14}$$

Hence the expression for temperature at t_{n+1} time step is obtained as,

$$T_{n+1} = \left(\frac{1}{\mathrm{Z}}\right)\left\{(C_v v_m T_n) + \left(\frac{V_{n+1}^2}{R_{sma}} + hA_{surf}T_a\right) \times \Delta t + \left(\lambda v_m \Delta\xi_{n+1}\right)\right\}, \tag{3.15}$$

where, Z=$(C_v v_m + hA_{surf}\Delta t)$. Since ξ_{n+1} depends on T_{n+1} as well, during the transformation correction, the discretized form of temperature equation at $(k+1)^{th}$ iteration is written as,

$$T_{n+1}^{(k+1)} = \left(\frac{1}{\mathrm{Z}}\right)\left\{(C_v v_m T_n) + \left(\frac{V_{n+1}^2}{R_{sma}} + hA_{surf}T_a\right) \times \Delta t + \left(\lambda v_m \Delta\xi_{n+1}^{(k)}\right)\right\}. \tag{3.16}$$

3.5.2 One-Dimensional SMA Constitutive Model

In the case of a linear spring-biased SMA wire actuator, the SMA wire is taken as a one-dimensional element, assuming homogeneous material properties throughout the entire length. Hence, the 3-D constitutive model discussed in Chapter 2 is simplified to a 1-D model for this study. Only one stress component, and one strain component, carry relevant information, which are,

$$\sigma = \sigma_{11} \neq 0, \quad \varepsilon = \varepsilon_{11} \neq 0. \tag{3.17}$$

Thus, the fourth-order compliance tensors $\boldsymbol{S}^{(.)}$ and the second-order thermal expansion tensors $\boldsymbol{\alpha}^{(.)}$, reduce to scalars S and α. Any material properties 'X', are assumed to follow,

$$X(\xi) = X^A + \xi\left(X^M - X^A\right), \tag{3.18}$$

where, ξ denotes the current martensite volume fraction and X with superscripts M and A representing the same property in complete martensite and austenite phases, respectively. Following Eqn.(2.3), the one-dimensional form of the constitutive equation is obtained as,

$$\varepsilon = S\sigma + \alpha(T - T_0) + \varepsilon^t. \tag{3.19}$$

Consequently, the stress in SMA wire at any time, t_{n+1}, can expressed using,

$$\sigma_{n+1} = S_{n+1}^{-1} \left[\varepsilon_{n+1} - \alpha_{n+1}(T_{n+1} - T_0) - \varepsilon_{n+1}^{t}\right]. \tag{3.20}$$

The transformation tensor $\mathbf{\Lambda}$ in Eqn.(2.6) reduces to the scalar H in one dimensional case. Thus the equation for the evolution of transformation strain becomes,

$$\dot{\varepsilon}^t = H \mathrm{sgn}(\sigma)\dot{\xi}, \tag{3.21}$$

where, the sign function 'sgn' is defined as,

$$\mathrm{sgn}(\sigma) = \begin{cases} 1, & \text{if,} \quad \sigma \geq 0, \\ -1, & \text{if,} \quad \sigma \leq 0. \end{cases} \tag{3.22}$$

Following Eqn.(2.12), one obtains the 1-D thermodynamic force Θ as,

$$\begin{aligned} \Theta =& \sigma H + \frac{1}{2}\sigma^2 \Delta S + \sigma \Delta\alpha (T - T_0) - \rho \Delta C_v \left[(T - T_0) - T \ln\left(\frac{T}{T_0}\right)\right] \\ &+ \rho \Delta s_0 T - \rho \Delta u_0 - \frac{\partial h_f}{\partial \xi}. \end{aligned} \tag{3.23}$$

The transformation function (ϕ) defined in Eqn.(2.13), in conjunction with the Kuhn-Tucker conditions presented in Eqns.(2.14) and (2.15), dictate the forward and reverse transformation of SMA. For this study, the cosine hardening function defined in Eqn.(2.17), the modified yield parameter (Y_f) expressed in Eqn.(2.18) and the model parameters shown in Eqn.(2.19) are used.

Return Mapping Algorithm

For each time step, the stress (σ), the martensite volume fraction (ξ) and the transformation strain (ε^t) are calculated following the convex cutting return mapping algorithm, discussed in Section 2.5.1. At t_{n+1}, during the thermo-elastic predictor step, the stress (σ_{n+1}) and transformation function (ϕ_{n+1}) are calculated for the new values of strain (ε_{n+1}) and temperature (T_{n+1}), assuming martensite volume fraction $\xi_{n+1} = \xi_n$. If $\phi \leq 10^{-8}$,

the predicted state is taken as the final state, and one advances to the next time step ($t_{n+1} \rightarrow t_{n+2}$). If the condition is violated, the transformation correction step is summoned, and the martensite volume fraction and the transformation strain are corrected iteratively following,

$$\Delta\xi_{n+1}^{(k)} = \frac{\phi_{n+1}^{(k)}}{\left(\Delta S.\sigma_{n+1}^{(k)} + H\right)^2 - \left(\frac{2\rho\Delta s_0}{a_c^M.\sqrt{1-(2\xi-1)^2}}\right)}, \qquad \forall \quad \dot{\xi} > 0,$$
$$\Delta\xi_{n+1}^{(k)} = \frac{\phi_{n+1}^{(k)}}{-\left(\Delta S.\sigma_{n+1}^{(k)} + H\right)^2 - \left(\frac{-2\rho\Delta s_0}{a_c^A.\sqrt{1-(2\xi-1)^2}}\right)}, \qquad \forall \quad \dot{\xi} < 0, \tag{3.24}$$

$$\Delta\varepsilon_{n+1}^{t(k)} = H.\Delta\xi_{n+1}^{t(k)}, \tag{3.25}$$

$$\xi_{n+1}^{(k+1)} = \xi_{n+1}^{(k)} + \Delta\xi_{n+1}^{(k)}, \tag{3.26}$$

$$\varepsilon_{n+1}^{(k+1)} = \varepsilon_{n+1}^{(k)} + \Delta\varepsilon_{n+1}^{(k)}. \tag{3.27}$$

From the updated values of ξ and ε^t, the values of σ_{n+1} and ϕ_{n+1} are recalculated and this iterative procedure continues ($k \rightarrow k+1$) till the tolerance on ϕ is obtained, after which the following load step is continued.

3.5.3 Force Equilibrium and Kinematic Constraint

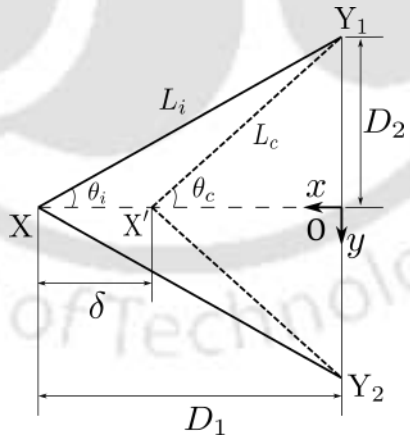

Figure 3.3: Schematic representation of SMA wire positions.

As the voltage is applied across the SMA wire, the temperature of the SMA wire increases, and the reverse transformation initiates. This changes the length of the SMA wire, compressing the spring by an amount 'δ'. Figure 3.3 depicts the two different con-

figurations of the SMA wire actuator, during the actuation of the system (refer Fig.3.2), with Y_1-X-Y_2 and $Y_1-X'-Y_2$ illustrating the initial pre-strained and the intermediate configurations during recovery of the SMA wire, respectively. The displacement of point X to X$'$ depicts the compression of the spring (δ). $2L_i$ and $2L_c$ represent the initial and current lengths of the SMA wire, respectively. Considering the force equilibrium at the current configuration, one gets,

$$2(\sigma - \sigma_i)A\cos\theta_c = K_s\delta, \tag{3.28}$$

where, σ depicts the recovery stress during actuation and σ_i represents the initial stress in the SMA wire. A is the cross-section of the SMA wire, and K_s models the spring stiffness. From geometry (Fig.3.3), one gets,

$$\cos\theta_c = \frac{D_1 - \delta}{\sqrt{(D_1-\delta)^2 + D_2^2}}, \tag{3.29}$$

where, D_1 and D_2 are the distances shown in Fig.3.3. Substituting Eqn.(3.29) into Eqn.(3.28), one obtains,

$$2(\sigma - \sigma_i)A \times \frac{D_1 - \delta}{\sqrt{(D_1-\delta)^2 + D_2^2}} = K_s\delta. \tag{3.30}$$

After rearranging Eqn.(3.30), the expression for the stress in the SMA wire can be obtained as,

$$\sigma = \sigma_i + \frac{K_s\delta\sqrt{(D_1-\delta)^2 + D_2^2}}{2A(D_1-\delta)}. \tag{3.31}$$

From the geometric stand-point, the current length of the SMA wire is expressed as,

$$L_c = \sqrt{(D_1-\delta)^2 + D_2^2} = L_0(1+\varepsilon). \tag{3.32}$$

Following Eqn.(3.32), for the spring compression, δ, the strain in the SMA wire can be

obtained as,

$$\varepsilon = \frac{\sqrt{(D_1 - \delta)^2 + D_2^2}}{L_0} - 1, \tag{3.33}$$

where, L_0 is the unstretched length of the SMA wire. Solving Eqns.(3.31) and (3.33), one relates the strain in SMA as a non-linear function of stress as,

$$\varepsilon = \psi(\sigma). \tag{3.34}$$

Substituting Eqn.(3.34) into Eqn.(3.20), the discretized form of the constitutive equation is written as,

$$\sigma_{n+1} = S_{n+1}^{-1} \left[\psi(\sigma_{n+1}) - \alpha_{n+1}(T_{n+1} - T_0) - \varepsilon_{n+1}^t\right]. \tag{3.35}$$

During the transformation correction, the discretized form of constitutive equation at $(k+1)^{th}$ iteration can be expressed as,

$$\sigma_{n+1}^{(k+1)} = S_{n+1}^{(k+1)^{-1}} \left[\psi(\sigma_{n+1}^{(k+1)}) - \alpha_{n+1}^{(k+1)}(T_{n+1}^{(k+1)} - T_0) - \varepsilon_{n+1}^{t\,(k+1)}\right]. \tag{3.36}$$

Upon solving the above equation, iteratively, one obtains the current stress at t_{n+1}.

3.5.4 Electrical Resistance of SMA Wire

The electrical resistance of any component is directly proportional to the length of the element and its electrical resistivity, and is inversely proportional to the area of the cross-section. Thus, the electrical resistance of the SMA wire (R_{sma}) can be expressed as,

$$R_{sma} = \frac{\rho L_c}{A}. \tag{3.37}$$

During the actuation process, the resistivity of SMA changes due to phase transformation from austenite to martensite and vice-versa. Following Eqn.(3.18), the resistivity of SMA can be expressed as,

$$\rho = \rho_A + \xi(\rho_M - \rho_A). \tag{3.38}$$

Here, ρ_M and ρ_A are the electrical resistivities of SMA in complete martensite and austenite phases, respectively. Equation (3.38) implies that the resistivity of SMA is a function of martensite volume fraction ξ, which in turn depends on temperature (T) and stress (σ) of SMA. Thus, the electrical resistivity of SMA is a non-linear function of σ and T. The current length of the SMA wire, L_c, can be written as,

$$L_c = L_0(1 + \varepsilon) = L_0(1 + \psi(\sigma)). \tag{3.39}$$

The change in the area of the cross-section of the SMA wire during actuation is neglected in this study. Following the load increment and transformation correction, the electrical resistance at t_{n+1}, is expressed as,

$$(R_{sma})_{n+1} = \frac{(\rho_A + \xi_{n+1}\ (\rho_M - \rho_A))\ \ L_0\ \ (1 + \psi(\sigma_{n+1}))}{A}. \tag{3.40}$$

The following section discusses the development of an EKF to estimate the outcome of the SMA wire actuator (δ), from the measured electrical signal of the same; by employing the constitutive model, the heat balance equation, the force equilibrium and the resistance-strain relation.

3.6 EKF for SMA Wire Actuator System

For any general loading condition, the state of SMA at any time instant can be completely defined by the stress (σ), temperature (T) and martensite volume fraction (ξ). As in the present system, the stress and strain of the SMA wire monotonically change with temperature; one can define the state of SMA using only the current stress and temperature while tracing the same from a completely known state following the thermo-mechanical path. Thus, the state vector of the system is represented as,

$$\boldsymbol{X} = [T \quad \sigma]^T. \tag{3.41}$$

According to Eqn.(3.1), one requires a system model, able to calculate the present state, $\boldsymbol{X}_{n+1}$, by using the previous state, $\boldsymbol{X}_n$, and the present input, $\boldsymbol{u}_{n+1}$. At time t_{n+1}, the temperature (T_{n+1}) and stress (σ_{n+1}) represent the state vector, $\boldsymbol{X}_{n+1}$. Following Eqns.(3.15) and (3.35), the process vector $\boldsymbol{f} = [f_1 \quad f_2]^T$ can be obtained as,

$$f_1 = \left(\frac{1}{\mathrm{Z}}\right)\left\{(C_v v_m T_n) + \left(\frac{V_{n+1}^2}{R} + hA_{surf}T_a\right)\Delta t + \left(\lambda v_m \Delta\xi_{n+1}\right)\right\}, \tag{3.42}$$

$$f_2 = S_{n+1}^{-1}\ \left[\psi(\sigma_{n+1}) - \alpha_{n+1}(T_{n+1} - T_0) - \varepsilon_{n+1}^t\right]. \tag{3.43}$$

Here, subscripts $(n+1)$ and (n) signify the corresponding parameter at t_{n+1} and t_n, respectively. In this application, the output displacement (δ) has to be estimated from the measured electrical resistance of SMA (R_{sma}). Hence, the measurement model comprises of only R_{sma}, *i.e.*,

$$\boldsymbol{Y}_{n+1} = (R_{sma})_{n+1}. \tag{3.44}$$

Following Eqns.(3.2) and (3.40), the non-linear measurement model g can be expressed as,

$$g = \frac{(\rho_A + \xi_{n+1}\ (\rho_M - \rho_A))\ \ L_0\ \ (1 + \psi(\sigma_{n+1}))}{A}. \tag{3.45}$$

The Jacobian $\boldsymbol{J}$ of the non-linear process function $\boldsymbol{f}$ is determined by differentiating it with the state variables, σ and T, and can be expressed as,

$$\boldsymbol{J} = \begin{bmatrix} \frac{df_1}{dT} & \frac{df_1}{d\sigma} \\ \\ \frac{df_2}{dT} & \frac{df_2}{d\sigma} \end{bmatrix}. \tag{3.46}$$

The Jacobian $\boldsymbol{J}$ at time step n are numerically calculated as,

$$\boldsymbol{J}_n = \begin{bmatrix} \dfrac{f_1'(T_n + \Delta T, \sigma_n) - f_1(T_n, \sigma_n)}{\Delta T} & \dfrac{f_1''(T_n, \sigma_n + \Delta\sigma) - f_1(T_n, \sigma_n)}{\Delta\sigma} \\ \\ \dfrac{f_2'(T_n + \Delta T, \sigma_n) - f_2(T_n, \sigma_n)}{\Delta T} & \dfrac{f_2''(T_n, \sigma_n + \Delta\sigma) - f_2(T_n, \sigma_n)}{\Delta\sigma} \end{bmatrix}. \tag{3.47}$$

Here f_1 and f_2 denote the numerical values obtained using Eqn.(3.42) and Eqn.(3.43), respectively, from the posteriori state, (T_n, σ_n). f_1' and f_2' represent the values of the same

equations determined at $(T_n + \Delta T, \sigma_n)$. Similarly, f_1'' and f_2'' are the solutions of the same, obtained at $(T_n, \sigma_n + \Delta\sigma)$. Here ΔT and $\Delta\sigma$ are very small values of temperature and stress, respectively. The Jacobian $\boldsymbol{N}$ of the measurement model g, with respect to the

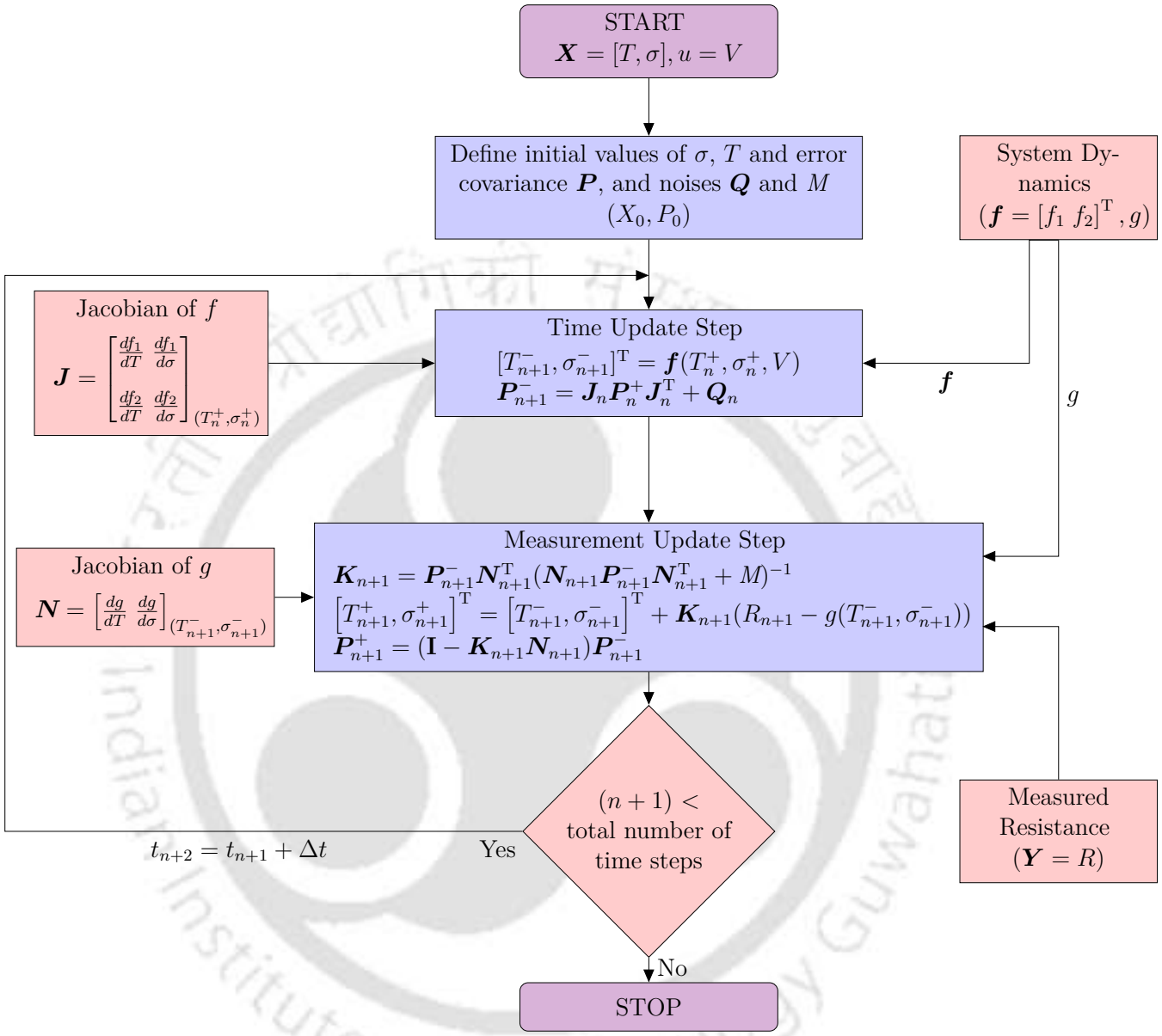

Figure 3.4: Flowchart of the developed EKF

state variables is obtained as,

$$\boldsymbol{N} = \begin{bmatrix} \frac{dg}{dT} & \frac{dg}{d\sigma} \end{bmatrix}. \tag{3.48}$$

It is calculated numerically following,

$$\boldsymbol{N}_{n+1} = \begin{bmatrix} \frac{g'(T_{n+1} + \Delta T, \sigma_{n+1}) - g(T_{n+1}, \sigma_{n+1})}{\Delta T} & \frac{g''(T_{n+1}, \sigma_{n+1} + \Delta\sigma) - g(T_{n+1}, \sigma_{n+1})}{\Delta\sigma} \end{bmatrix}. \tag{3.49}$$

Here g is the numerical value of Eqn.(3.45) determined using the a-priori values of the present step, $(T^-_{n+1}, \sigma^-_{n+1})$. g' and g'' are the numerical values of the same equation determined at $(T^-_{n+1} + \Delta T, \sigma^-_n)$ and $(T^-_{n+1}, \sigma^-_{n+1} + \Delta\sigma)$, respectively. The flowchart of the developed EKF is illustrated in Fig.3.4.

3.7 Validation of the Developed EKF

Table 3.1: Geometric parameters of the system

Geometric parameter	Value
Diameter of SMA wire, d	0.125 mm
Initial Length of SMA wire	540 mm
Initial pre-strain, e_0	0.03757
Spring Stiffness, K_s	334.5 N m^{-1}

Table 3.2: Material parameters of SMA wire [84]

Parameter	Value	Parameter	Value
E^A	75 GPa	E^M	28 GPa
α_A	22×10^{-6} °C^{-1}	α_M	22×10^{-6} °C^{-1}
C_A	12 MPa K^{-1}	C_M	10 MPa K^{-1}
C_v^A	5.92×10^6 J K^{-1} m^{-3}	C_v^M	4.506×10^6 J K^{-1} m^{-3}
ρ_A	9.47 ×10^{-7} Ω m	ρ_M	11.103 ×10^{-7} Ω m
A_s	312 K	A_f	319 K
M_s	300 K	M_f	293 K

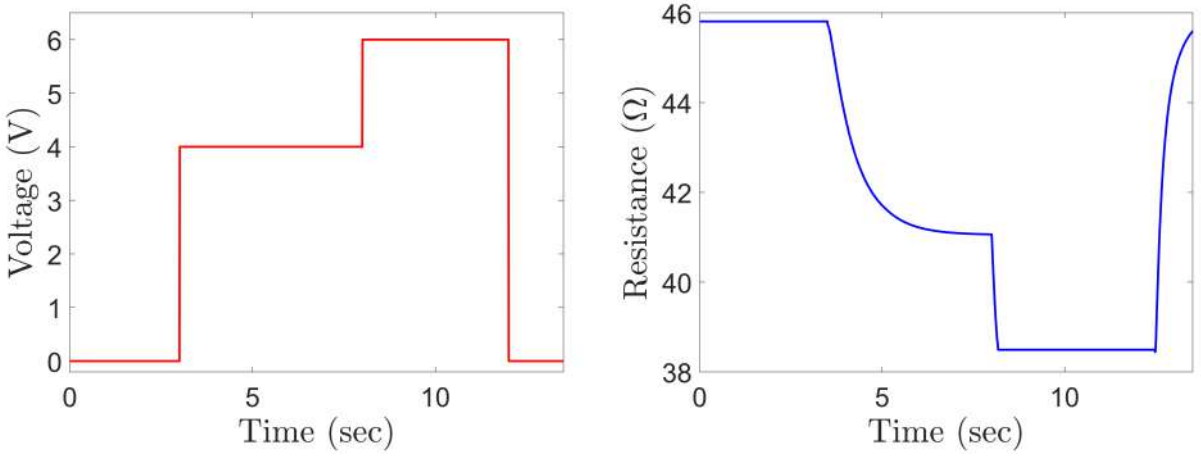

(a) (b)

Figure 3.5: (a) Voltage input applied across SMA wire, and (b) corresponding electrical resistance variation in SMA wire calculated using the modified model.

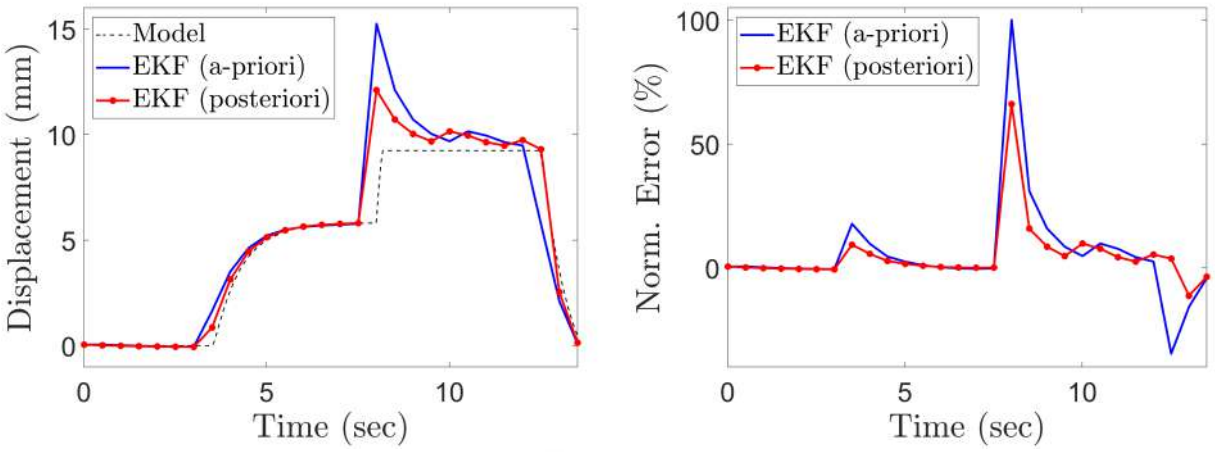

(a) (b)

Figure 3.6: Comparison of (a) displacement obtained from the model, a-priori and posteriori estimated displacement obtained from EKF, and (b) the normalised error in estimated displacements w.r.t to the one obtained from the modified model.

Following the flowchart depicted in Fig.3.4, an EKF model is developed in MATLAB R2019a © Mathworks Inc., to estimate the system response from the change in electrical resistance of the SMA wire actuator. To validate the developed EKF, the system response estimated by the EKF, is compared with the one obtained from the modified SMA model discussed in Chapter 2. The SMA wire actuated linear spring discussed in Section 3.4 is simulated in a manner that it undergoes a combination of partial and complete phase transformation. In that case, we need to solve Eqns.(3.15), (3.20), (3.40), to obtain the displacement and electrical resistance variation of the SMA wire for a given voltage signal. The simulated electrical resistance variation of SMA during actuation is evaluated and has been used as the measurement data in the EKF ($\boldsymbol{Y}$ in Eqn.(3.6)), to estimate the state of the actuator. The assumed initial condition, geometric and material parameters of the SMA wire, are illustrated in Tables 3.1 and 3.2, respectively.

For the input voltage, shown in Fig.3.5a, the system model is integrated with very small time steps (0.01s), to calculate the spring displacement and the corresponding variation in electrical resistance of the SMA wire, and is illustrated in Fig.3.6a (black dotted lines) and Fig.3.5b, respectively. To evaluate the performance of the developed EKF, large time steps (0.5s) are taken in the time update step of the EKF (Eqn.(3.4)), to intentionally introduce error in the a-priori state estimate ($\boldsymbol{X}_{n+1}^{-}$ in Eqn.(3.4)). The spring displacement is computed based on the a-priori estimate and is compared against the same obtained

from the modified model, simulated with the small time step, and is illustrated as the blue curve in Fig.3.6a. Following the measurement update equation (Eqn.(3.6)), the posteriori state of the system ($\boldsymbol{X}_{n+1}^{+}$) has been estimated by the EKF using the a-priori state estimate ($\boldsymbol{X}_{n+1}^{-}$), and the simulated electrical resistance of SMA illustrated in Fig.3.5b. The spring displacement corresponding to the posteriori estimate is calculated and is denoted in red in Fig.3.6a. The error in a-priori and posteriori estimates of spring displacement, in comparison to the same obtained from the model, normalised against the maximum displacement, are depicted in Fig.3.6b. Here, one can observe that the a-priori estimate contains a significant error in comparison to the posteriori one. It is especially true when there is a sudden change in the input voltage during which the electrical resistance of SMA corrects the a-priori state estimate of EKF. This reveals that the use of electrical resistance (R_{sma}) information in the measurement step of the developed EKF has the potential to amend the a-priori estimate and provide a more accurate estimate of the system response.

3.8 Experimental Details

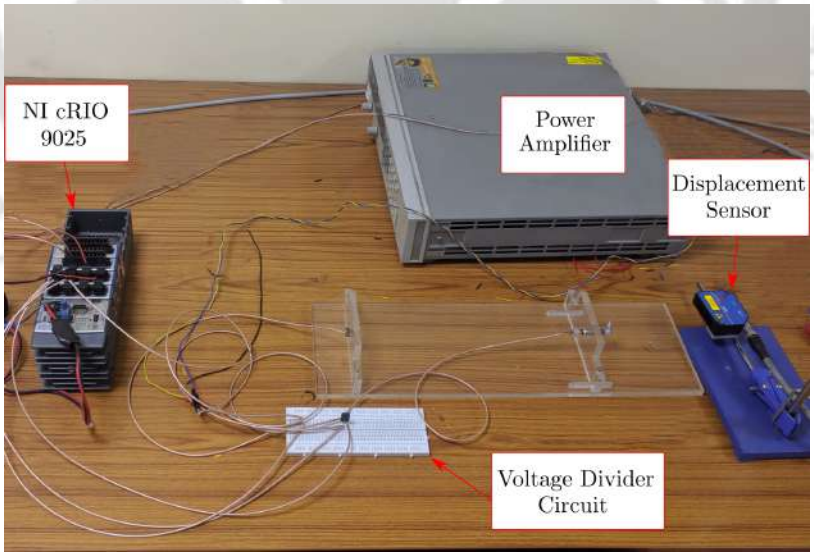

Figure 3.7: Experimental setup.

An experimental setup, shown in Fig.3.7, is developed, to evaluate the performance of the proposed EKF. It comprises of the spring-biased SMA wire actuator, a real-time controller, a programmable power supply, a laser displacement sensor, and a voltage

divider circuit. A detailed description of each of the components is discussed below.

(a) **SMA wire actuated linear spring:** A spring of stiffness K_s = 334.5 N/m is connected to a 125 μm SMA wire of 540 mm length. It is held at both ends to form a V-shape, as shown in Fig.3.8. When a voltage is applied across the SMA wire, its temperature increases and the SMA wire contracts, compressing the linear spring attached on the left end. Upon reduction of the applied voltage, the temperature reduces, and the system returns to its initial configuration, due to the biasing force provided by the spring. An E-type fine wire (50 μm diameter) thermocouple from Omega, CHCO-002, has been held in contact with the fixed end of the SMA wire 'Y_2', to measure the change in the temperature of the same.

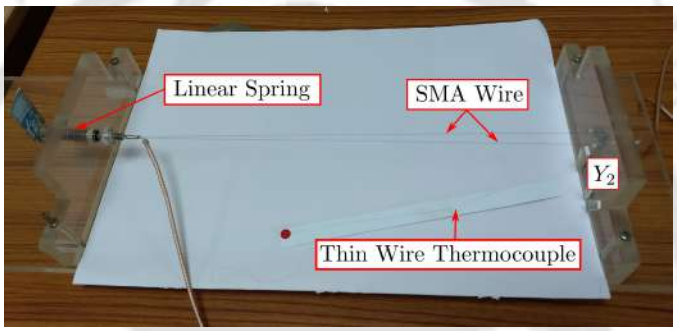

Figure 3.8: SMA wire-spring actuator system.

(b) **NI cRIO-9025:** Figure 3.9 depicts the real-time NI cRIO-9025 controller used to control and monitor the I/P and O/P to and from the system. Two modules, namely NI-9263 and NI-9219, are connected to the cRIO for performing the data acquisition operations. NI-9263 is a universal analog output module, able to provide voltage signals of up to 10V. In this setup, it is used to supply the input voltage signals required to activate the SMA wire actuator. The latter is a universal analog input module, for acquiring analog signals from various sensors, e.g., thermocouples, displacement sensors, strain gauges etc. Here it has been used to measure the voltage across multiple points in the circuit and the voltage signal from the laser displacement sensor.

(c) **Programmable power supply:** A 200W power supply, 6642A from Agilent, as shown in Fig.3.10, is used to supply the voltage across the SMA wire and the fixed

Figure 3.9: NI cRIO-9025.

resistor $R_0 = 5\Omega$. The power supply can provide 0-20V and 0-10A. During the experiment, the maximum operational current is kept fixed, and the voltage signal obtained from NI-9263 is amplified with a gain factor of four and applied across the SMA wire system.

Figure 3.10: Agilent 6642A power supply.

(d) **Laser displacement sensor:** A laser displacement sensor, optoNCDT-1402 from Micro-Epsilon, as shown in Fig.3.11, is used to measure the change in the length of the spring (δ). It has a measuring range of 100 mm, with a resolution of 10 μm, and yields an analog signal of $0-5$V. The output signal is acquired using NI-9219, and the corresponding displacement is calculated following,

$$\delta = 25(V_{out} - V_i), \tag{3.50}$$

where, V_{out} and V_i are the measured output voltages corresponding to the displacement of the spring 'δ', and the same at the initial configuration of the system, respectively.

(e) **Voltage divider circuit:** A simple voltage divider circuit has been devised to measure the electrical resistance of the SMA wire. The schematic of the same is shown in Fig.3.12. Here, a fixed resistor of $R_0 = 5\Omega$ is connected in series with the SMA wire. The total voltage drop (V_t) across the SMA wire (R_{sma}) and R_0, and the

Figure 3.11: Laser displacement sensor.

voltage drop (V_r) across only R_0, are acquired using the analog input module NI-9219. Subsequently, the electrical resistance of the SMA wire is calculated following,

$$R_{sma} = \frac{(V_t - V_r) \times 5}{V_r}. \tag{3.51}$$

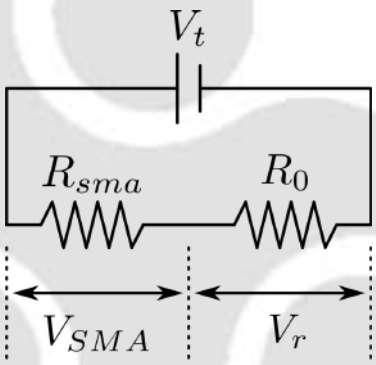

Figure 3.12: Voltage Divider Circuit

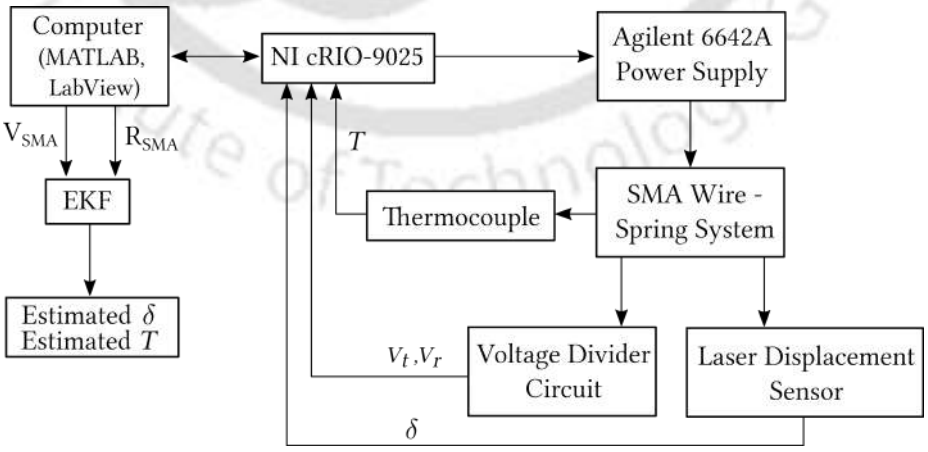

Figure 3.13: Flow diagram of the entire procedure.

3.8.1 Experimental Procedure

The schematic of the entire experimental setup is presented in Fig.3.13. The desired voltage signal is designed in LabVIEW 2019, which is then converted into an analog signal using NI-9263, and is amplified using the power amplifier. This amplified voltage is then applied across the SMA wire and the fixed resistor R_0. As the voltage increases, the temperature of the SMA wire increases, ensuing actuation. The temperature data is acquired from the thermocouple and the analog module NI-9219. The output voltage from the laser displacement sensor, V_{out}, is used to evaluate the spring displacement following Eqn.(3.50). Simultaneously, the voltage drops V_t and V_r are acquired by the analog input module NI-9219 and the change in the electrical resistance of the SMA wire (R_{sma}) is calculated following Eqn.(3.51). Now, the voltage drop across the SMA wire, $V_{SMA} = V_t - V_r$, is employed as the input data ($\boldsymbol{u}$ in Eqn.(3.1)), and the acquired resistance, R_{sma}, is fed as the measured data ($\boldsymbol{Y}$ in Eqn.(3.2)), into the developed EKF; to estimate the stress and temperature of the SMA wire, as the input voltage varies.

3.9 Results and Discussions

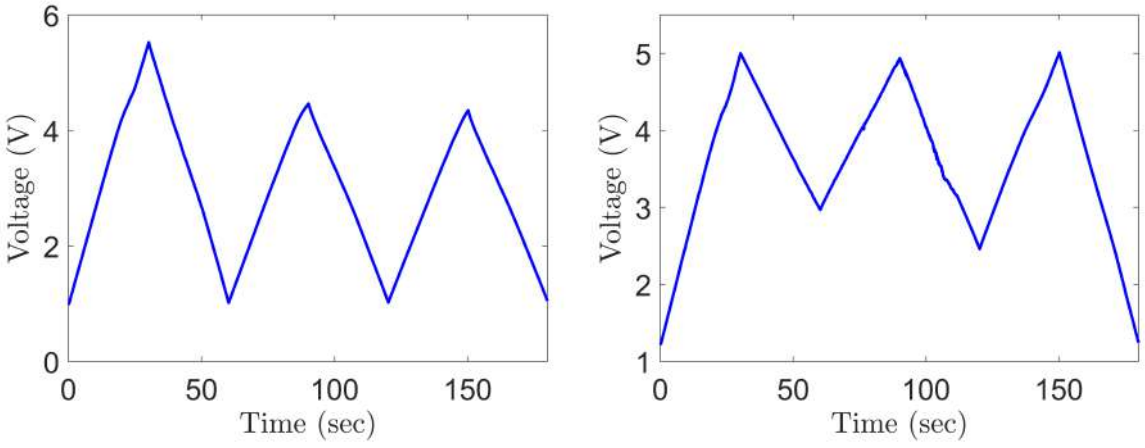

(a) (b)

Figure 3.14: Input voltage measured across the SMA wire, in case of, (a) partial heating, and (b) partial cooling.

An EKF model is developed in MATLAB R2019a © Mathworks Inc., and has been validated by comparing the system response estimated by the EKF against the same

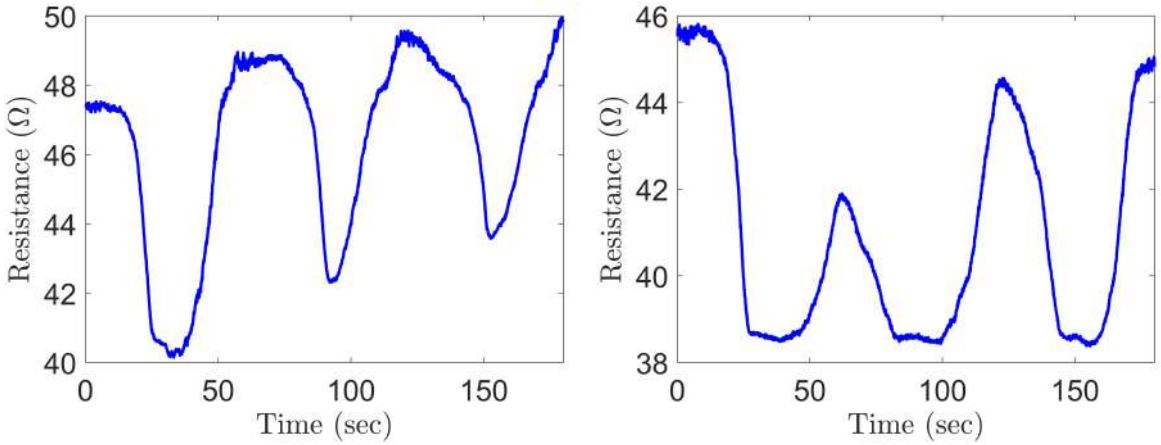

(a) (b)

Figure 3.15: Measured electrical resistance of SMA wire, in case of, (a) partial heating, and (b) partial cooling.

obtained from the modified SMA model, for the SMA wire actuator undergoing a combination of partial and complete transformation cycles. During the experiment, two different voltage signals, shown in Figs.3.14a and 3.14b, are applied across the SMA wire actuator. These are devised to attain partial transformations, both during heating and cooling, respectively. The corresponding variation in electrical resistance of the SMA wire, as measured during the experiment, are shown in Figs.3.15a and 3.15b. Using the electrical resistance as the measured data ($\boldsymbol{Y}$ in Eqn.(3.2)) and the voltage signal as input ($\boldsymbol{u}$ in Eqn.(3.1)), the proposed EKF is used to estimate the stress and temperature of the SMA wire. The spring displacement, 'δ', has been evaluated from the estimated stress, following Eqn.(3.28). The assumed initial condition, geometric and material parameters of the SMA wire are illustrated in Tables 3.1 and 3.2, respectively. The estimated data are then compared with the corresponding measured ones and are presented in Figs.3.16 and 3.17, for partial heating and cooling cases, respectively. Furthermore, for the same inputs, the estimated displacement and temperature obtained using the EKF developed by Gurung and Banerjee [84] are also plotted in the same figures.

As seen in Fig.3.16, both the EKF models estimate the temperature with a similar accuracy of less than $\pm 5^{\circ}$C. However, the displacements estimated by the EKF models differ slightly (refer Fig.3.17). Here, one can observe that the estimated displacements are pretty close in the full transformation case for both the EKF models, having a maximum

error of less than 5%. However, with the proposed approach, a maximum estimation error of less than 15% (1.5mm) is observed in partial transformation. In contrast, the other EKF [84] renders a maximum error of around 22% (2.2mm). To quantify the error in the whole response, an RMS error is defined following,

$$e_{RMS} = \frac{\sum_{i=1}^{n} \left(\delta_{est}(t_i) - \delta_{exp}(t_i)\right)^2}{n}. \tag{3.52}$$

Here, δ_{exp} is the experimental displacement and δ_{est} represents the displacement obtained from the respective EKFs, at every time step, t_i. The RMS error (e_{RMS}) calculated from the proposed EKF and the same based on [84] are found to be 0.7467 mm (8.36% δ_{max}) and 1.2464 mm (13.96% δ_{max}), respectively. It reveals that the present EKF performs better in comparison to its earlier version.

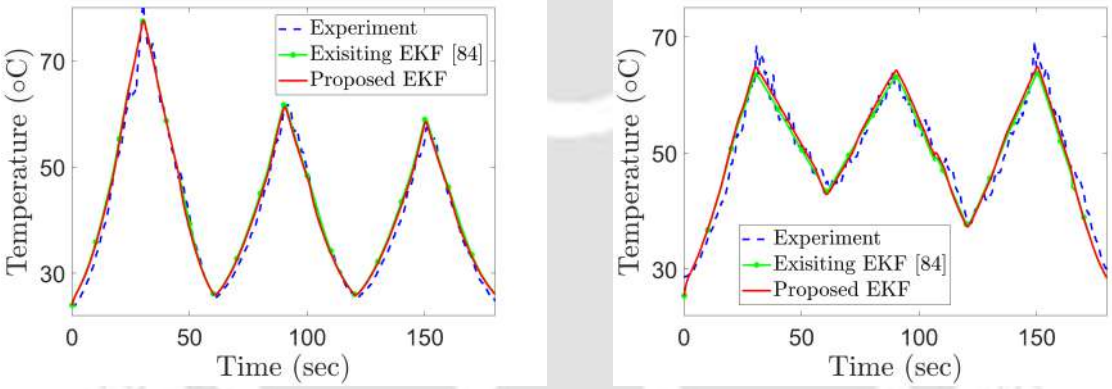

Figure 3.16: Comparison between the estimated and measured temperature for, (a) partial heating, and (b) partial cooling cases.

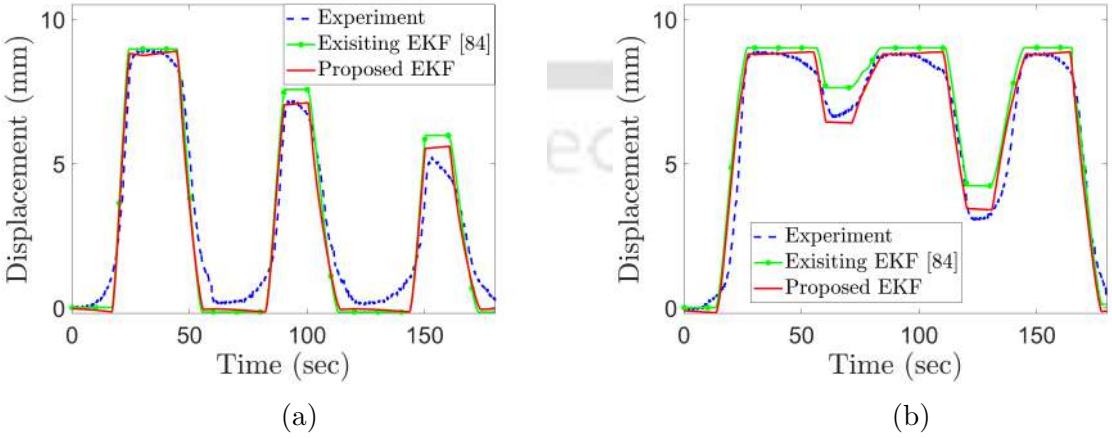

Figure 3.17: Comparison between the estimated and measured displacement for, (a) partial heating, and (c) partial cooling cases.

3.10 Conclusions

In this chapter, an Extended Kalman Filter (EKF) has been developed based on the modified constitutive model discussed in the previous chapter, to harness the self-sensing feature of an SMA wire actuator. The discretized form of the heat balance equation, the constitutive model, force equilibrium and kinematic constraints are derived, to form the system model, as required for the EKF. The output from the proposed EKF is then compared with the model response, to demonstrate its effectiveness. An experimental setup has been developed, to measure the change in electrical resistance of the SMA actuator, while undergoing varied degrees of actuation. The applied voltage and measured resistance signals are used in the developed EKF, to estimate the system responses in terms of displacement and temperature of the SMA. These estimated responses are then compared with the corresponding measured ones. The performance of the present EKF is found to be better, in comparison to the existing models, particularly in partial transformation cases, thus revealing the potential of the developed EKF in the self-sensing application of SMA.

Chapter 4

Particle Filter Based Self-Sensing Shape Memory Alloy Wire Actuator Under External Cooling

4.1 Introduction

In the previous chapter, an Extended Kalman Filter (EKF) based state estimation technique has been developed to assess the response of the SMA wire actuated linear system. Although the proposed technique, qualitatively traces the experimental response for a set of varied voltage input signals, quantitative discrepancies are found to be around 10-15%. These may be attributed to inaccuracies in the system model, parametric and experimental uncertainties. Additionally, unwanted cooling is a major concern in real-world applications involving electrically heated SMA wire actuators, where maintaining constant ambient conditions or providing ideal thermal insulation may not always be feasible. Estimating the response of SMA wire actuators, operating under such an environment, is a significant challenge. To obviate these, a particle filter (PF) based state estimation technique has been explored. A particle filter (PF) is a non-linear state estimator based on Bayes' rule in probability theory [105]. In this chapter, a PF has been developed to estimate the level of actuation in the SMA wire actuated system from the change in the electrical resistance of the SMA wire. Firstly, a brief introduction of the

PF is discussed, followed by the development of the PF model for the SMA wire actuated linear system. An experimental setup with necessary arrangements to introduce forced cooling during actuation, has been designed and fabricated, and the filter's effectiveness under practical loading conditions has been examined.

4.2 Convective Cooling of SMA Wire Actuator

Generally, an SMA wire actuator is heated by resistive heating and is cooled using natural or forced convection. It has been found that the effect of the heat transfer coefficient (h) on the temperature variation of a thin SMA wire is very prominent. For a slight change in the value of the heat transfer coefficient, the temperature of the SMA wire varies significantly [94]. This can lead to an incorrect prediction of SMA's transformation state. This is especially true in practical cases, wherein unwanted cooling can occur due to improper insulation or forced cooling, leading to a drop in the displacement generated by an SMA wire [96]. Recently, Theodore and Bishay [97] studied the effect of the convective boundary condition on the actuation generated by a flexible laminate embedded with SMA wire, wherein the removal of a blowing fan led to a significant increase in the tip deflection. In the literature, a wide range of heat transfer coefficient values are reported while modelling the temperature variation in SMA wire. Different relationships starting from linear [73], quadratic [65] to quartic variation [95] of 'h' with temperature are promulgated. The heat transfer coefficient of a wire has also been reported to be evaluated from the Nusselt number relation for a cylindrical cross-section [87]. Bhattacharyya *et al.* [106] had taken the heat transfer coefficient of a 1mm thick SMA plate as $h = 25$ W/m^2K and $h = 200$ W/m^2K for free and forced convection cases, respectively. In case of a Ni-Ti wire of diameter, $d = 0.38$mm, the value of h has been reported as 61 W/m^2K [107]. In [108], the value h for Ni-Ti polycrystals is stated as 93 W/m^2K. Using either of these values of h yields a widely different response. To address this issue, in this study, the heat transfer coefficient has been estimated following the parameter estimation technique. In literature, parameter estimation has been used for fault detection in aircraft engines, and turbofan [109, 110]. The same technique has been explored here to estimate the convective

heat transfer coefficient, while predicting the state of the SMA wire actuated system, from the measured electrical resistance variation of the SMA wire. In what follows is a brief discussion about the particle filter and then the derivation of the process model required for the same.

4.3 Particle Filter

A PF is a Bayesian filter that estimates a system's state based on the non-linear system model. In the case of an EKF and a UKF, the non-linear system model is approximated as first-order or higher-order equations. This gives satisfactory estimates for most systems, except those with very high non-linearity. However, a PF estimates any entity based on its probability distribution. Here, the key idea is to depict the *pdf* as a collection of random samples, with associated weight based on the measured state. The propagated states are estimated based on the samples' weights [111]. Several applications of PF have been proposed in the literature. PF has been used in wireless communications [112] and robotic localization [113] applications. Ohlmeyer and Menon [114] studied the application of PF in multi-body tracking systems, where the PF has to estimate the position of an air vehicle in the presence of several tracking decoys. Oppenheim *et al.* [115] discussed the implementation of PF in chemo-metrics to estimate the amount of bacterial concentration during wastewater treatment in a bioreactor. Tirri *et al.* [116] presented a PF for the obstacle detection and tracking function of an Unmanned Aircraft System (UAS). PF has also been used in weather prediction and for real-time storm forecasting systems at NOAA [117]. Dyrmishi *et al.* [118] proposed a PF for trajectory reconstruction and positioning by utilizing the mobile data details, including the time stamp and geo-location information.

Here, the basic steps of a particle filter are discussed briefly. At the initiation of the estimation problem, N state vectors are generated based on the initial *pdf*, $p(x_0)$. These state vectors are known as particles. One propagates these N particles at each instant to the next time step, based on the system model. Next, the relative likelihood of each particle is determined based on the measured state. Finally, a resampling procedure is carried out in accordance with the relative likelihood, for expediting convergence. The

detailed steps involved in a PF are discussed below.

4.3.1 System Model

At any instant 't_{n+1}', the discrete non-linear process model is defined as,

$$\boldsymbol{X}_{n+1} = \boldsymbol{f}(\boldsymbol{X}_n, \boldsymbol{u}_{n+1}, \boldsymbol{w}_n), \tag{4.1}$$

and the measurement model is outlined as,

$$\boldsymbol{Y}_{n+1} = \boldsymbol{g}(\boldsymbol{X}_{n+1}, \boldsymbol{v}_{n+1}), \tag{4.2}$$

respectively. Here, $\boldsymbol{X}$ refers to the system's state vector, and $\boldsymbol{f}$ is the non-linear state propagation function. The input vector is illustrated as $\boldsymbol{u}$. Further, $\boldsymbol{Y}$ represents the measurement variable and $\boldsymbol{g}$ is the non-linear observation function. Here, $\boldsymbol{w}_{n+1}$ and $\boldsymbol{v}_{n+1}$ are the process noise and measurement noise, with $\boldsymbol{Q}_{n+1}$ and $\boldsymbol{M}_{n+1}$ being their respective covariances.

4.3.2 Algorithm

- In the beginning, *i.e.*, at time step $n = 0$, one generates a set of N random particles based on the initial known *pdf*, $p(x_0)$. These are denoted as $\boldsymbol{X}_{0,i}$, with, $i = 1, 2, ..., N$, denoting the respective particle number.

- Say, at any time instant t_{n+1}, all the particles are propagated across time, following the process model (Eqn.(4.1)), to obtain,

$$\boldsymbol{X}^{-}_{n+1,i} = \boldsymbol{f}(\boldsymbol{X}^{+}_{n,i}, \boldsymbol{u}_{n+1}, \boldsymbol{w}_n). \tag{4.3}$$

  Here, $\boldsymbol{X}^{-}_{n+1,i}$ denotes the a-priori state estimate of the i^{th} particle at time t_{n+1}.

- After obtaining the measurement value $\hat{\boldsymbol{Y}}_{n+1}$ at t_{n+1}, one evaluates the conditional probability of the measured state with respect to each of the particles. It is expressed

as,

$$q_i^{'} \sim \frac{1}{(2\pi)^{m/2}|\boldsymbol{M}_{n+1}|^{1/2}} \exp\left(\frac{-\left[\hat{\boldsymbol{Y}}_{n+1} - \boldsymbol{g}(\boldsymbol{X}^{-}_{n+1,i})\right]^{\mathrm{T}} \boldsymbol{M}^{-1}_{n+1} \left[\hat{\boldsymbol{Y}}_{n+1} - \boldsymbol{g}(\boldsymbol{X}^{-}_{n+1,i})\right]}{2}\right). \tag{4.4}$$

- Then the obtained probabilities of each particle is normalized, to obtain the respective relative likelihood or weight following,

$$q_i = \frac{q_i^{'}}{\sum_{j=1}^{N} q_j^{'}}. \tag{4.5}$$

  This ensures the sum of the weights equals 1.

- Next, the resampling step is carried out to obtain the posterior estimate $\boldsymbol{X}^{+}_{n+1,i}$ of the state variables. The resampling is carried out as follows.
  - For any particle i, firstly generate a number n_r, which is uniformly distributed between 0 and 1.
  - Next, summate the obtained weights (q_i's) of each particle, one after another, until the cumulative weight is greater than the number, n_r. If, $\sum_{j=1}^{m-1} q_j < n_r$ and $\sum_{j=1}^{m} q_j \geqslant n_r$, then the value of state variables of the m^{th} particle becomes the posteriori value of i^{th} particle, *i.e.*, $\boldsymbol{X}^{+}_{n+1,i} = \boldsymbol{X}^{-}_{n+1,m}$.

  The above two steps are repeated for each of the N particles.

- Finally, one can calculate the mean and variance of the obtained particles, following standard practices and then move on to the next time step ($t_{n+1} \rightarrow t_{n+2}$).

4.4 System Description

The SMA wire actuated system discussed in Chapter 3 has also been considered in this study, and for the convenience of the readers, the schematic of the same is depicted in Fig.4.1. Here, $\mathrm{Y}_1 - \mathrm{X} - \mathrm{Y}_2$ is the initial pre-stretched configuration of the SMA wire, and $\mathrm{Y}_1 - \mathrm{X}' - \mathrm{Y}_2$ represents any of its intermediate states while undergoing actuation. The

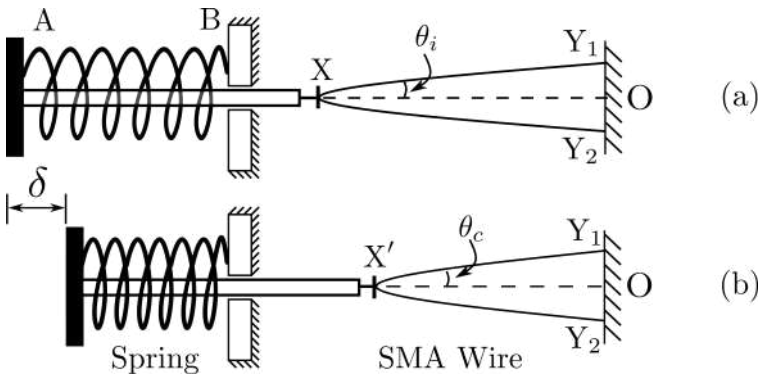

Figure 4.1: V- shaped SMA wire actuator system

spring AB is connected to the SMA wire representing a linear system. This also provides the required restoration force, *i.e.*, to drive the system back to its original state during cooling. In this arrangement, the SMA wire is heated using resistive heating (Joule's effect) by passing an electric current through the wire. During voltage increment, the temperature of the wire increases. At a temperature above the austenite start temperature (A_s), the reverse transformation initiates, during which the martensite (detwinned) transforms into austenite. As the SMA wire is constrained by the spring, the stress in the wire rises as the wire length decreases due to phase transformation. This is considered the loading phase of the SMA actuator. Now, as the applied voltage is reduced, the temperature of the wire drops due to natural or forced convection, rendering the formation of detwinned martensite from austenite, known as the forward transformation. As a result, the stress in the wire drops and this phase of the response is termed as the unloading phase. The objective of the present study is to determine the amount of actuation generated by the SMA wire actuator, by observing the electrical resistance variation of the SMA wire. For this purpose, a particle filter has been developed, to harness the self-sensing capability of SMA, wherein the SMA wire acts both as a sensor and an actuator.

4.5 System Modeling

The present work aims to determine the state of the SMA wire-actuated system by utilizing the change in its electrical resistance. The modified Boyd and Lagoudas model, discussed in Chapter 2, has been used in this study. Here, the heat balance equation, along with the quadratic heat transfer model (Eqn.(3.11)), governing the variation of

temperature of the SMA wire, is considered. The force equilibrium equation examined in Section 3.5.3 is used. Here, only the modified hardening function and the modified equation for electrical resistance are elucidated.

4.5.1 1-D SMA Constitutive Model

The 1-D constitutive model relating the stress (σ) of SMA with its strain (ε) and temperature (T), and the transformation function (Θ) follow Eqns.(3.20) and (3.23), respectively, as previously discussed in Section 3.5.2. The modified yield parameter (Y_f) depicted in Eqn.(2.20) has been considered. Here, a new smooth hardening function is used to accurately trace the smooth and gradual transition of the response, particularly at the beginning and end of phase transformation. The smooth hardening function is expressed as,

$$h_f(\xi) = \begin{cases} \frac{1}{2}a_1\left[\frac{\xi^{n_1+1}}{n_1+1} + \frac{(1-\xi)^{n_2+1}}{n_2+1}\right] + (a_3+a_4)\xi & \forall \quad \dot{\xi} > 0 \\ \frac{1}{2}a_2\left[\frac{\xi^{n_3+1}}{n_3+1} + \frac{(1-\xi)^{n_4+1}}{n_4+1}\right] + (a_3-a_4)\xi & \forall \quad \dot{\xi} < 0 \end{cases} \tag{4.6}$$

The associated model parameters are derived by following the procedure described in Section 2.4, and are shown below.

$$\begin{aligned}
\rho\Delta s_0 &= -CH, \\
\rho\Delta u_0 &= \frac{\rho\Delta s_0}{2}(M_s + A_f), \\
a_1 &= \rho\Delta s_0(M_f - M_s), \\
a_2 &= \rho\Delta s_0(A_s - A_f), \\
a_3 &= \frac{\rho\Delta s_0\left(-M_s + M_f + A_s - A_f\right)}{4} + \frac{\left(\sigma_{M_s}^2 + \sigma_{A_f}^2 + \sigma_{M_f}^2 + \sigma_{A_s}^2\right)\Delta S}{8}, \\
a_4 &= \frac{a_2}{4}\left[\frac{\xi_r^{n_3}}{n_3+1} + \frac{(1-\xi_r)^{n_4+1}}{\xi_r(n_4+1)}\right] - \frac{a_1}{4}\left[\frac{\xi_r^{n_1}}{n_1+1} + \frac{(1-\xi_r)^{n_2+1}}{\xi_r(n_2+1)}\right], \\
Y_1 &= \frac{\rho\Delta s_0}{4}\left(M_s + M_f - A_s - A_f\right) - a_4, \\
Y_2 &= \frac{-a_1\left[1 + \xi_r^{n_1} - (1-\xi_r)^{n_2}\right]}{2\xi_r\left(e^{\gamma(1-\xi_r)} - 1\right)}, \\
Y_3 &= \frac{-a_2\left[1 - \xi_r^{n_3} + (1-\xi_r)^{n_4}\right]}{2(1-\xi_r)\left(e^{\gamma\xi_r} - 1\right)}.
\end{aligned} \tag{4.7}$$

The detailed derivation of the model parameters is presented in Appendix C. The modified model is implemented following the return mapping algorithm, presented in Section 2.5.

4.5.2 Electrical Resistance Variation of SMA Wire

As discussed in Section 3.5.4, following Eqn.(3.40), the electrical resistance of SMA wire can be written as,

$$R_{sma} = \frac{(\rho_A + \xi\ (\rho_M - \rho_A))\ L_0\ (1 + \psi(\sigma))}{A}, \tag{4.8}$$

with, ρ_M and ρ_A representing the individual electrical resistivities of martensite and austenite phases, respectively. Previously, the resistivities are considered as constants. Here, the resistivity of the individual phases are modelled as a function of temperature [74] to better delineate the change in the electrical resistance of SMA while undergoing actuation, and can expressed as,

$$\rho_M = \rho_{M0} + \rho_{M1}(T - T_a), \quad \text{and} \tag{4.9}$$

$$\rho_A = \rho_{A0} + \rho_{A1}(T - A_f), \tag{4.10}$$

where, ρ_{M0}, ρ_{M1} and ρ_{A0}, ρ_{A1} are constants corresponding to complete Martensite and Austenite phases, respectively.

The next section, discusses the development of the PF based on the system model, comprising of the heat balance equation (Eqn.(3.9)), the constitutive model (Eqn.(3.20)), the force equilibrium equations (Eqn.(3.28)), and the resistance-strain expression (Eqn.(4.8)).

4.6 Particle Filter for SMA Wire System

The motivation of this section is to derive the state propagation, and observation relations for the SMA wire actuated system. For an SMA wire actuated system, one can estimate the state of SMA by utilizing its temperature (T), stress (σ) and martensite volume fraction (ξ). However, in the case of a monotonically loaded spring-SMA system, one can evaluate the system's current state by using the known stress and temperature at the previous time instant. Hence, the state vector $\boldsymbol{X}$ of the SMA wire actuated system

comprises of,

$$\boldsymbol{X} = [T \quad \sigma]^{\mathrm{T}}. \tag{4.11}$$

Following Eqn.(4.3), at any time instant, t_{n+1}, one can estimate the state of the system $\boldsymbol{X}_{n+1}$ (σ_{n+1} and T_{n+1}) by employing the known values at the previous state $\boldsymbol{X}_n$ (σ_n and T_n) and present input voltage, V_{n+1}. Using the constitutive relation (Eqn.(3.20)) and stress-strain relation (Eqn.(3.34)), the stress equation at t_{n+1} can be written as,

$$\sigma_{n+1} = S_{n+1}^{-1}\left(\psi(\sigma_{n+1}) - \alpha_{n+1}(T_{n+1} - T_0) - \varepsilon_{n+1}^{t}\right). \tag{4.12}$$

Similarly, the heat balance equation (Eqn.(3.9)) can be rewritten to obtain the temperature of SMA at t_{n+1} as,

$$T_{n+1} = \left(\frac{1}{\mathrm{Z}}\right)\left\{(C_v v_m T_n) + \left(\frac{V_{n+1}^2}{R} + hA_{surf}T_a\right)\Delta t + \left(\lambda v_m \Delta\xi_{n+1}\right)\right\}, \tag{4.13}$$

where, $\mathrm{Z} = (C_v v_m + hA_{surf}\Delta t)$ and $\Delta\xi_{n+1} = \left(\xi_{n+1} - \xi_n\right)$. Hence, the non-linear state propagation function $\boldsymbol{f}$ (in Eqn.(4.1)) can be obtained as,

$$\begin{bmatrix} T_{n+1} \\ \sigma_{n+1} \end{bmatrix} = \begin{bmatrix} \left(\frac{1}{\mathrm{Z}}\right)\left\{(C_v v_m T_n) + \left(\frac{V_{n+1}^2}{R} + hA_{surf}T_a\right)\Delta t + \left(\lambda v_m \Delta\xi_{n+1}\right)\right\} \\ S_{n+1}^{-1}\left(\psi(\sigma_{n+1}) - \alpha_{n+1}(T_{n+1} - T_0) - \varepsilon_{n+1}^{t}\right) \end{bmatrix}. \tag{4.14}$$

In the present system, the initial state of the SMA wire, *i.e.*, the initial temperature (T_i) and stress (σ_i), are the known measurands. The initial temperature (T_i = 296.68 K) is measured using a fine wire thermocouple, and the initial stress (σ_i = 109.05 MPa) is evaluated using the static equilibrium equation at the initial configuration. As illustrated in Algorithm 1, a white process noise is added to the known initial state ($\boldsymbol{X}_i$) to generate a set of initial particles ($\hat{\boldsymbol{X}}_i$), required for the particle filter. The process noise model $\boldsymbol{w}$ is assumed to follow a Gaussian distribution with zero mean and covariance $\boldsymbol{Q}$ as,

$$\boldsymbol{Q} = 10^{-6} \times \begin{bmatrix} T_i & 0 \\ 0 & \sigma_i \end{bmatrix}. \tag{4.15}$$

Algorithm 1 generates 'N' state vectors by drawing a random scalar from the standard

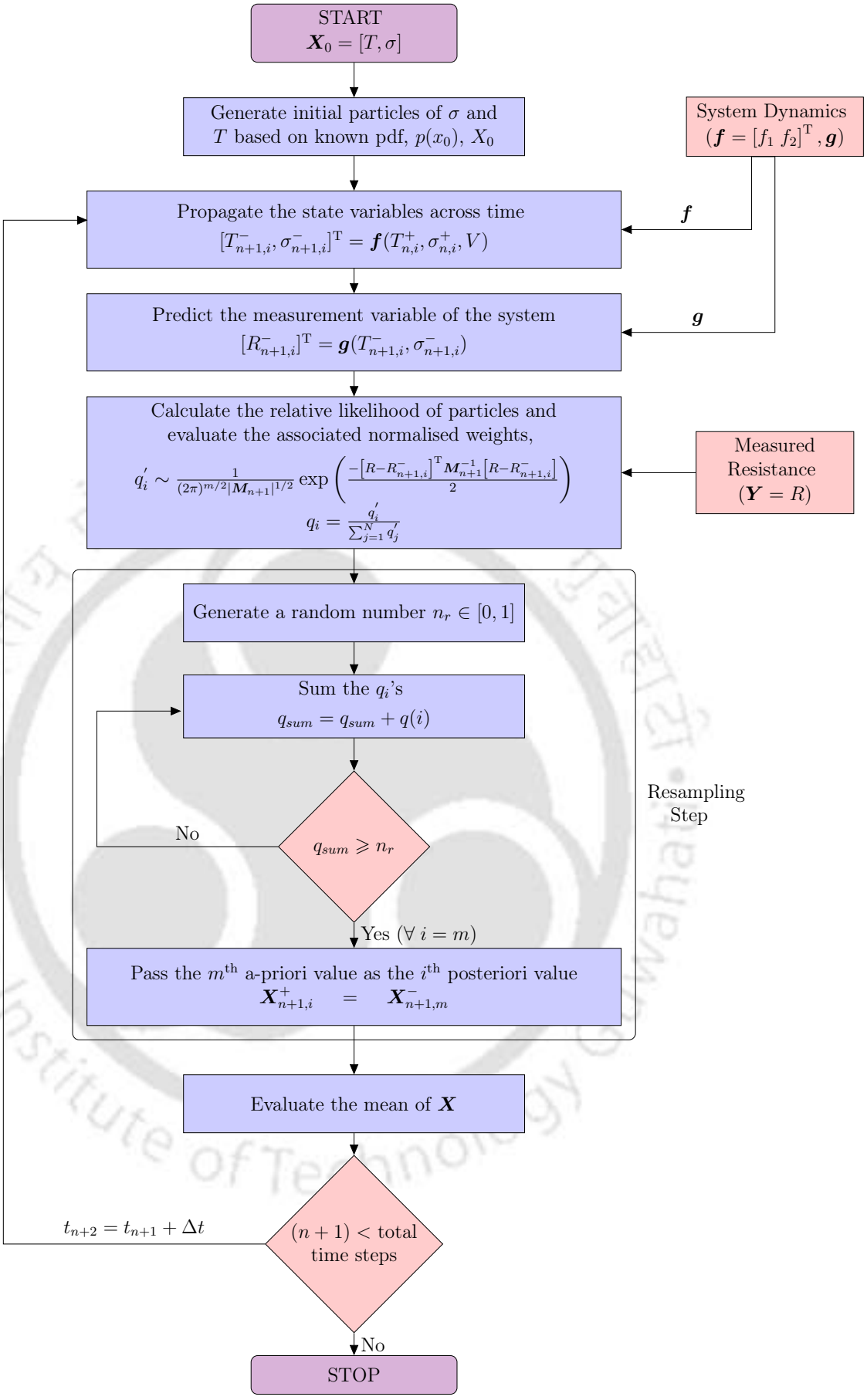

Figure 4.2: Flowchart of the developed PF

normal distribution $\mathcal{N}(0,\ 1)$, referred to as *randn* function here. This populates 'N' unique initial state vectors about the known mean values (T_i, σ_i), with a small degree of scatter. The objective of the present study is to evaluate the extent of actuation from the change

Algorithm 1: An algorithm for initializing the particle filter

Input: $T_i,\ \sigma_i,\ N$
Initial state: $\boldsymbol{X}_i = [T_i\ ;\ \sigma_i]$
Process Noise Covariance: $\boldsymbol{Q} = diag\ (\ [T_i\ \sigma_i]\ ) \times 10^{-6}$
for $n = 1 : N$ **do**
  $\hat{\boldsymbol{X}}_i(:, n) = \boldsymbol{X}_i + sqrt(Q) \times [randn;\ randn]$;
end

in the SMA wire's electrical resistance. Hence the electrical resistance of SMA, R_{sma}, is taken as the measurement variable $\boldsymbol{Y}_{n+1}$ (see Eqn.(4.2)). Following Eqn.(4.8), one can obtain the non-linear observation function $\boldsymbol{g}$ as,

$$g = \frac{(\rho_A + \xi_{n+1}\ (\rho_M - \rho_A))\ \ l_0\ \ (1 + \psi(\sigma_{n+1}))}{A} \tag{4.16}$$

The flowchart illustrating the steps involved in the proposed PF is presented in Fig.4.2.

4.7 Experimental Details

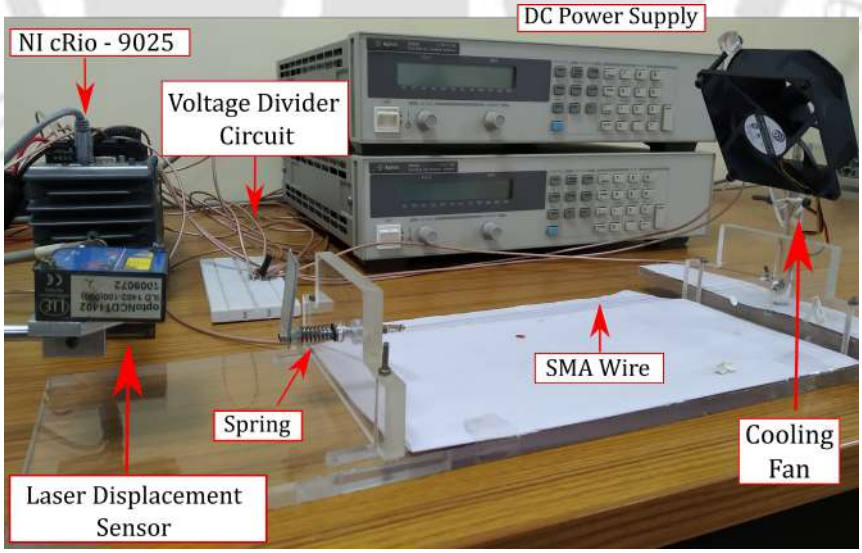

Figure 4.3: Experimental setup developed for external cooling of SMA wire actuator.

As the purpose is to estimate the displacement of the SMA wire actuated system from the measured electrical resistance of the SMA wire, an experimental setup has been

fabricated to obtain this change in electrical resistance of the SMA wire; while it is subjected to different voltage signals and different levels of cooling. Figure 4.3 shows the details of the experimental setup. It comprises of an SMA wire actuated spring (refer Fig.3.8), a data acquisition system (refer Fig.3.9), DC power supply (refer Fig.3.10), a laser displacement sensor (refer Fig.3.11) and a voltage divider circuit (refer Fig.3.12), with all the components performing their respective tasks as discussed in Section 3.8. Here, a fan (refer to Fig.4.4) is used to cool the SMA wire intermittently at regular intervals. The brushless fan from Glacial Tech has an operating DC voltage of 12V and a current of 0.17A. In the present study, the fan is switched ON and OFF at specific zones of actuation for a different duration. Additionally, the fan is also run at different speeds, by changing the input voltage supplied to it. This is controlled by regulating the voltage signal using LabVIEW 2019 and NI cRiO-9025. This voltage signal is then amplified and applied through the programmable DC power supply across the input terminals of the fan.

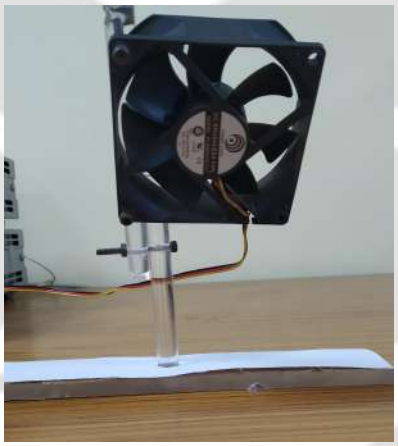

Figure 4.4: External fan used for forced cooling of SMA wire.

Two modules, namely, NI-9219 and NI-9263, are connected to the cRIO to control and acquire the inputs and output signals. The system comprises a 540 mm long SMA wire of diameter 125 μm, held in a V-shape, and is connected to a linear spring, as seen in Fig.3.8. A set of pre-defined voltage signals are defined in LabVIEW 2019 and is applied across the SMA wire and a known resistance ($R_0 = 5\Omega$) using the DC power supply and cRIO. The flow diagram of the experimental procedure is depicted in Fig.4.5. Figures 4.6a and 4.6b illustrate the voltage input applied across the SMA wire-actuated

system. They are referred to as the partial heating and the partial cooling cases, since it is designed to achieve one complete transformation cycle and two partial transformations during heating and cooling, respectively. The temperature of the SMA wire is controlled using these voltage signals, which in turn yields actuation. The laser displacement sensor is used to measure the change in the length of the linear spring 'δ'. During actuation, the electrical resistance of the SMA wire (R_{sma}) is evaluated using the voltage divider circuit following Eqn.(3.51). Using the calculated electrical resistance (R_{sma}) as the measured data and the voltage across SMA (V_{SMA}) as input data, the spring displacement (δ) is estimated using the developed PF and compared against the measured displacement.

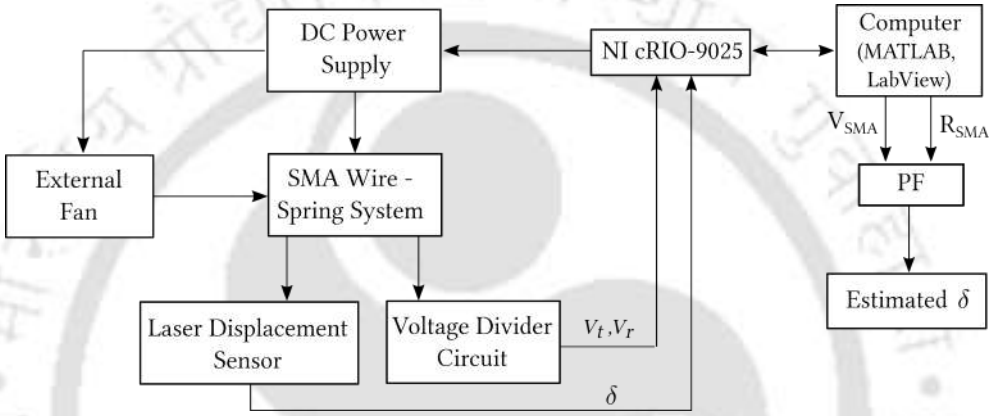

Figure 4.5: Flow diagram of the entire procedure

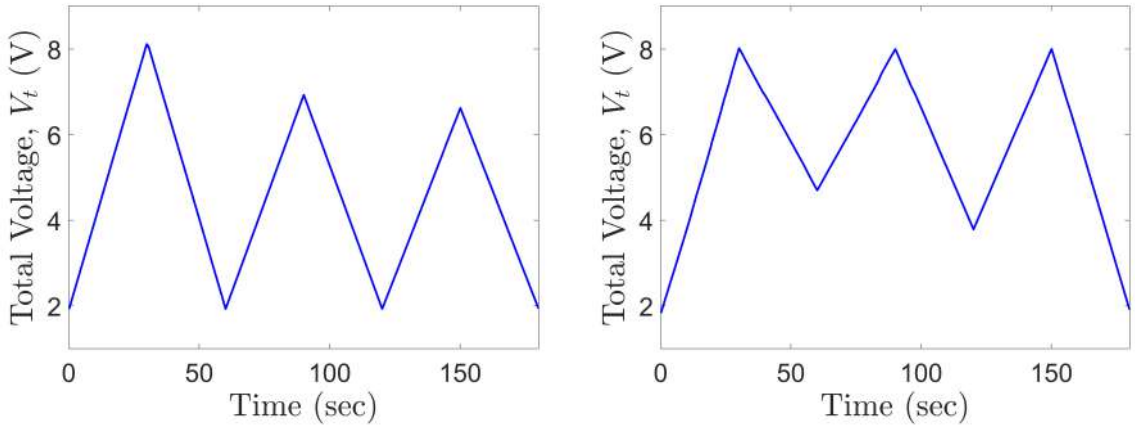

Figure 4.6: Total voltage applied across the SMA wire actuator system, in case of, (a) partial heating, and (b) partial cooling.

Here, the experiments are carried out to determine the efficacy of the proposed PF under arbitrary loading conditions. During the experiment, the SMA wire is intentionally

	Max/Min Zone	Transient Zone	Boundary Zone
$t_c = 1s$	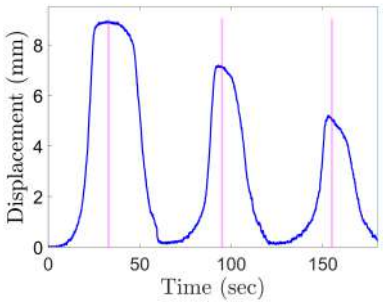 Case PH(L)-I	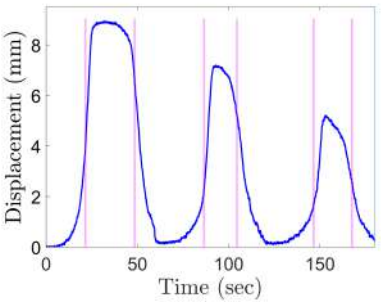 Case PH(L)-IV	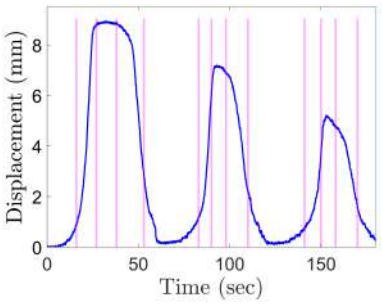 Case PH(L)-VII
$t_c = 3s$	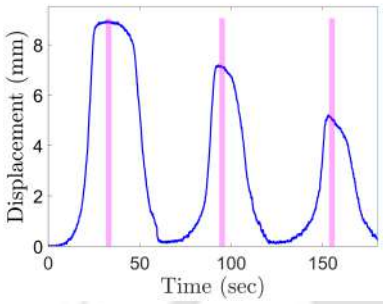 Case PH(L)-II	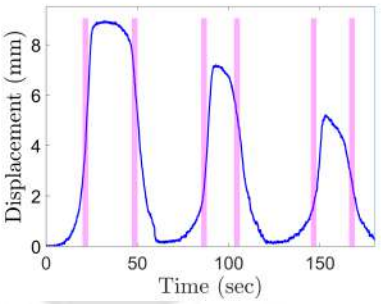 Case PH(L)-V	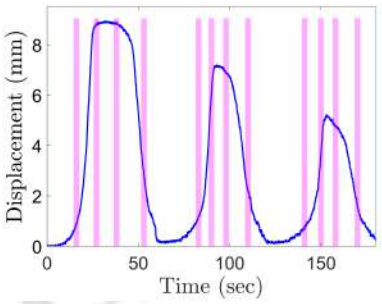 Case PH(L)-VIII
$t_c = 5s$	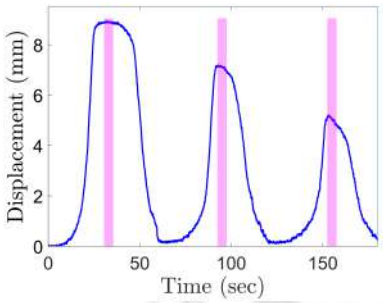 Case PH(L)-III	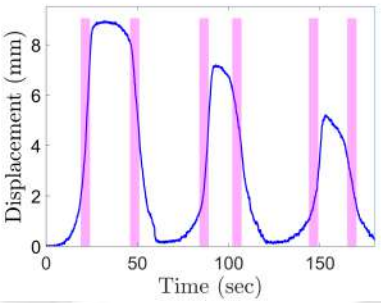 Case PH(L)-VI	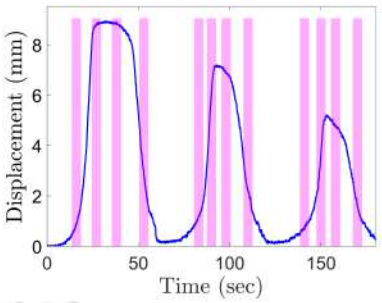 Case PH(L)-IX

Table 4.1: Pictorial representation of the set of sudden cooling experiments carried out in the study, during partial heating condition, with respect to the system response under natural cooling, while subjected to the voltage signal shown in Fig.4.6a.

cooled using an external fan to simulate practical loading situations. The speed, timing and duration of the fan in its ON position are controlled by the cRIO. Table 4.1 and Table 4.2 illustrate the various forced cooling cases carried out in this study during partial heating (Fig.4.6a) and partial cooling (Fig.4.6b) conditions, respectively. In these tables, the shaded vertical bars in each of the figures represent the forced cooling zones during

	Max/Min Zone	Transient Zone	Boundary Zone
$t_c = 1s$	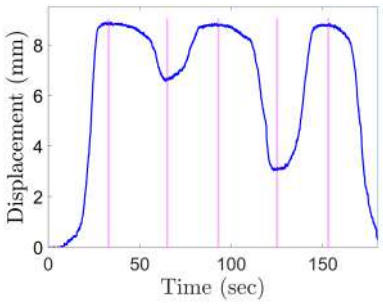 Case PC(L)-I	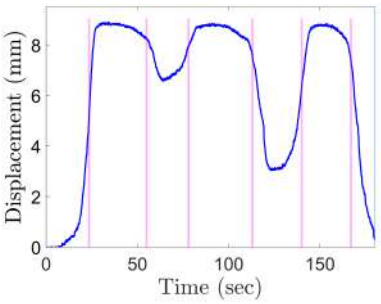 Case PC(L)-IV	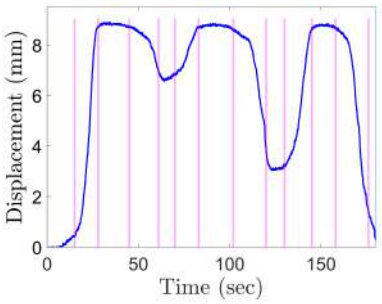 Case PC(L)-VII
$t_c = 3s$	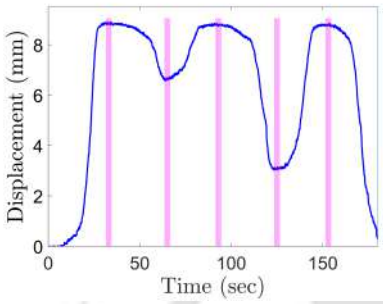 Case PC(L)-II	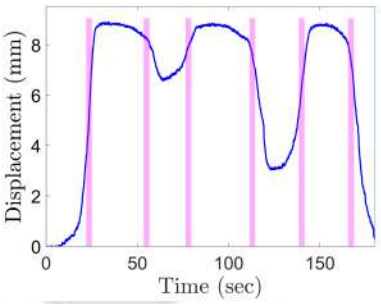 Case PC(L)-V	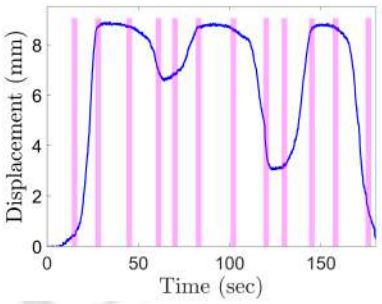 Case PC(L)-VIII
$t_c = 5s$	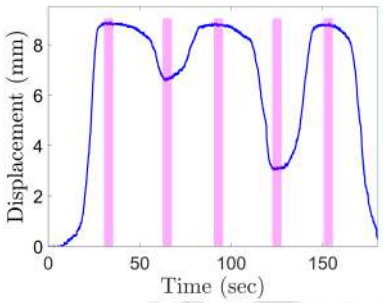 Case PC(L)-III	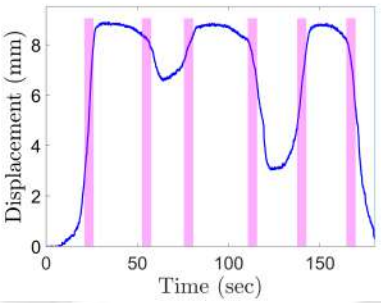 Case PC(L)-VI	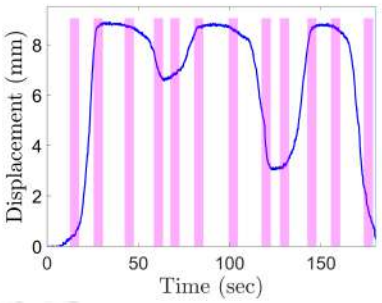 Case PC(L)-IX

Table 4.2: Pictorial representation of the set of sudden cooling experiments carried out in the study, during partial cooling condition, with respect to the system response under natural cooling, while subjected to the voltage signal shown in Fig.4.6b.

actuation, superimposed over the experimental responses of an SMA actuated system undergoing only natural convection, while subjected to the same voltage inputs as shown in Figs.4.6a and 4.6b. Then, the fan is switched ON for increasing cooling durations, *i.e.*, for 1s, 3s and 5s, to simulate quick as well as prolonged cooling conditions. They are presented in the rows of both tables. In each of these cases, cooling is carried out at three

different stages of actuation, *i.e.*, forced cooling is introduced (i) while the displacement is either maximum or minimum, referred the max/min position, (ii) while the SMA is undergoing phase transformation, called as transient position, and (iii) while the state of SMA is at the boundary between the peak and the transient position, denoted as boundary position. These are depicted in each of the columns of Tables 4.1 and 4.2. Further, each of these cooling experiments is also carried out at three different cooling intensities; *i.e.*, by controlling the speed of the fan by altering the voltage supplied to it. The 12V fan is run at three different input voltage levels of 4V, 8V and 12V, and are correspondingly dubbed as *low level*, *medium level* and *high level* of cooling, respectively, in this study. The corresponding speeds of rotation are found to be 860 rpm, 1778 rpm and 2637 rpm, respectively. The measured displacement for each case is then compared against the same estimated from the PF and are illustrated in the following section.

4.8 Comparison of Performance Between the Developed PF and EKF

Table 4.3: Material parameters of SMA wire

Parameter	Value	Parameter	Value
E^A	75 GPa	E^M	28 GPa
α_A	22×10^{-6} K^{-1}	α_M	22×10^{-6} K^{-1}
C_A	12×10^{6} Pa K^{-1}	C_M	10×10^{6} Pa K^{-1}
C_v^A	5.92×10^{6} J K^{-1} m^{-3}	C_v^M	4.506×10^{6} J K^{-1} m^{-3}
ρ_{A0}	10.5×10^{-7} Ω m	ρ_{M0}	11.2×10^{-7} Ω m
ρ_{A1}	1.43×10^{-9} Ω m K^{-1}	ρ_{M1}	1.43×10^{-10} Ω m K^{-1}
A_s	330 K	A_f	351 K
M_s	326 K	M_f	305 K
λ	5 kJ kg^{-1}	H	0.034
h_0	160 W m^{-2} K^{-1}	h_1	0.02 W m^{-2} K^{-3}
n_1	2	n_2	10
n_3	5	n_4	2

To verify the effectiveness of the proposed PF, two input voltage signals, shown in Figs.4.6a and 4.6b, are considered to activate the SMA wire. The external fan is switched OFF during these experiments and thus can be referred to as the natural cooling experiment, similar to the ones conducted in Chapter 3. In the developed PF, the electrical

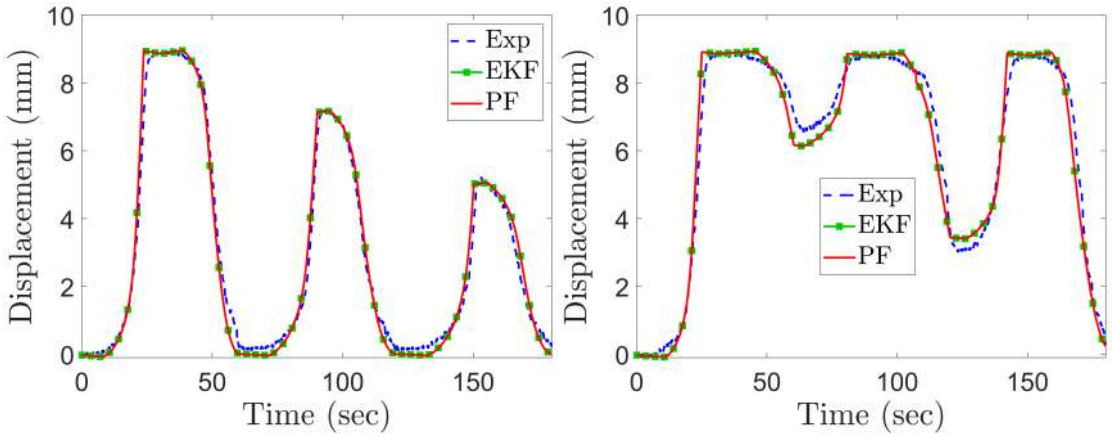

Figure 4.7: Comparison between the displacement estimated by the EKF and PF against the measured displacement for, (a) partial heating, and (c) partial cooling cases

resistance of the SMA wire, obtained using the voltage divider circuit, is used as the measured data ($\boldsymbol{Y}$ in Eqn.(4.2)), and the applied voltage signal is used as input ($\boldsymbol{u}$ in Eqn.(4.1)). The number of particles is taken as N=20. The estimated displacement (δ) is computed from the estimated stress, following Eqn.(3.28), and the same has been compared against the one obtained experimentally and is shown in Fig.4.7. Additionally, for the same inputs, the displacement estimated by the Extended Kalman filter (EKF) proposed in Chapter 3, with the modified hardening function (Eqn.(4.6)), are shown in the same figures. The geometric and material parameters used, are shown in Tables 3.1 and 4.3, respectively. Figures 4.7a and 4.7b show that the developed PF has estimated the state of SMA wire with significant accuracy, and is found to be quite effective in harnessing the self-sensing capability of SMA wire. However, both estimators performed quite satisfactorily. The improvement in estimation accuracy of the EKF, compared to the same depicted in Fig.3.17, may be attributed to the newly proposed smooth hardening function and its associated model parameters. To quantify the error in the estimation of the developed PF and the EKF, the RMS error (e_{RMS}) of the respective filter with respect to the experimental displacement is evaluated following Eqn.(3.52) and are listed in Table 4.4. The maximum errors as a percentage of maximum displacement (δ_{max}) are calculated and illustrated in the same table. The test cases are simulated in MATLAB R2021a ©MathWorks Inc. in an Intel i5-10400 (@ 2.90 GHz) desktop running Microsoft

	RMS Error		Maximum Error		Computational Time	
	EKF	**PF**	**EKF**	**PF**	**EKF**	**PF**
Partial Heating	0.3596 mm (3.67% of δ_{max})	0.3593 mm (3.67% of δ_{max})	0.9130 mm (9.32% of δ_{max})	0.9122 mm (9.31% of δ_{max})	0.1401 s	0.5942 s
Partial Cooling	0.4479 mm (4.57% of δ_{max})	0.4479 mm (4.57% of δ_{max})	1.3690 mm (13.97% of δ_{max})	1.3612 mm (13.89% of δ_{max})	0.1322 s	0.5751 s

Table 4.4: RMS error, maximum error and computational time for both the PF and EKF under partial heating and cooling condition.

Windows 10, and the corresponding computational time are also illustrated in Table 4.4. Here, one can observe that both the PF and EKF yield results with comparable accuracy for either loading conditions. However, the PF is found to consume more computational time than the EKF, thus negating the need for a computationally intense model like PF for the aforestated monotonic loading conditions.

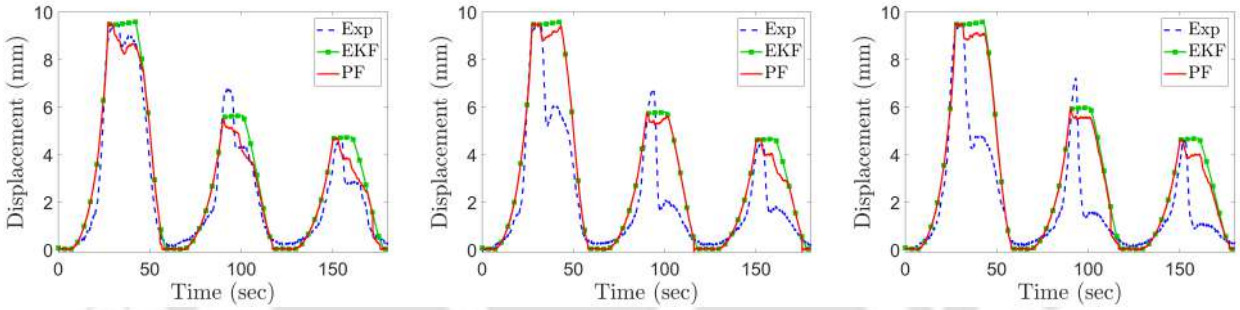

Figure 4.8: Comparison among the displacement estimated by the EKF, PF and the measured displacement for *medium level* forced cooling cases, (a) PH(L)-I, (b) PH(L)-II, and (c) PH(L)-III.

To simulate practical loading situations, the response of the system while the SMA wire actuator is subjected to undesired forced cooling, is estimated from both the PF and EKF and compared against the experimental one. Here, the SMA wire is cooled, using an external fan as discussed in Section 4.7. The fan is switched ON at the *medium level*, with increasing cooling time of t_c=1s, t_c=3s and t_c=5s, presented as the forced cooling cases PH(L)-I, PH(L)-II and PH(L)-III in Table 4.1, respectively. For the input voltage signal depicted in Fig.4.6a and using the technique discussed in Section 4.6, the displacement is estimated by both the EKF and the PF and depicted in Fig.4.8. The associated maximum and RMS errors are reported in Table 4.5. Here, one can observe that the displacement

	RMS Error		Maximum Error		Computational Time	
	EKF	**PF**	**EKF**	**PF**	**EKF**	**PF**
PH(L)-I	0.7770 mm (7.92% of δ_{max})	0.6261 mm (6.38% of δ_{max})	1.9655 mm (20.05% of δ_{max})	1.7738 mm (18.10% of δ_{max})	0.2450 s	0.5754 s
PH(L)-II	1.6001 mm (16.32% of δ_{max})	1.4468 mm (14.76% of δ_{max})	4.2955 mm (43.83% of δ_{max})	3.7726 mm (38.49% of δ_{max})	0.2125 s	0.4913 s
PH(L)-III	1.9758 mm (20.16% of δ_{max})	1.7565 mm (17.92% of δ_{max})	5.2867 mm (53.94% of δ_{max})	4.7540 mm (48.51% of δ_{max})	0.2201 s	0.5113 s

Table 4.5: RMS error, maximum error and computational time for both the PF and EKF corresponding to forced cooling cases PH(L)-I, PH(L)-II and PH(L)-III.

estimated by the PF is marginally better than the one estimated by the EKF. The RMS error in case of the PF ranges from 6-18% compared to 8-20% for the EKF. In the case of 5s cooling duration (PH(L)-III), the maximum error for the PF and EKF are found to be around 48% and 54% of the maximum displacement, respectively. Hence, one can infer that the PF captures a larger drop in actuation level during cooling in comparison to the EKF. This could be due to the probability-based estimation technique of the PF, but the accuracy is still inadequate. This inaccuracy can be attributed to the quadratic heat transfer model (Eqn.(3.11)) assumed in the study, which doesn't account for the necessary change in the heat transfer coefficient to accommodate the forced cooling. To obviate this, the heat transfer coefficient has also been estimated along with the stress and temperature of the SMA, and is discussed in the next section.

4.9 State Estimation Using Modified PF

In real-world applications, it is assumed that the state estimation of a physical problem provides an adequate measure of the system's output. However, practical cases often involve many time-varying parameters that govern a system's state. In literature, Kalman filters have been used to estimate the parameters of a dynamic system, in addition to its state variables [109, 110]. Following the same principle, in this study, the developed PF has been modified to estimate the heat transfer coefficient, expecting to improve the estimation accuracy.

4.9.1 Modified PF for SMA Wire Actuated System

The non-linear system dynamics, dependent on any set of unknown parameter '$\boldsymbol{p}$' can be expressed as,

$$\boldsymbol{X}'_{n+1} = \boldsymbol{f}_p(\boldsymbol{X}'_n, \boldsymbol{u}_{n+1}, \boldsymbol{w}_n, \boldsymbol{p}), \tag{4.17}$$

$$\text{and,} \quad \boldsymbol{Y}_{n+1} = \boldsymbol{g}(\boldsymbol{X}_{n+1}, \boldsymbol{v}_{n+1}), \tag{4.18}$$

Here, $\boldsymbol{X'}$ represents the modified state vector of the system comprising of the state variables and the unknown parameter vector '$\boldsymbol{p}$', and $\boldsymbol{f}_p$ is the modified non-linear state model. The other terms bear the same definition as discussed in Section 4.3.1. In this study, the heat transfer coefficient 'h' has been estimated in addition to the state variables, temperature (T) and stress (σ). Thus, the modified state vector appears as,

$$\boldsymbol{X'} = \begin{bmatrix} \boldsymbol{X} \\ \boldsymbol{p} \end{bmatrix} = \begin{bmatrix} T \\ \sigma \\ h \end{bmatrix} \tag{4.19}$$

The heat transfer coefficient is modeled as,

$$h_{n+1} = h_n + \zeta_{n+1}, \tag{4.20}$$

where, $\zeta_{n+1} \sim (0, \boldsymbol{B}_{n+1})$ is assumed as white Gaussian noise having covariance $\boldsymbol{B}_{n+1}$. A small random noise has been added to diversify the parameter and avoid degeneration. The updated non-linear function, $\boldsymbol{f}_p$ in Eqn.(4.17), can now be expressed as,

$$\boldsymbol{f}_p = \begin{bmatrix} T_{n+1} \\ \sigma_{n+1} \\ h_{n+1} \end{bmatrix} = \begin{bmatrix} \left(\frac{1}{\mathrm{Z}}\right)\left\{(C_v v_m T_n) + \left(\frac{V_{n+1}^2}{R} + h_{n+1} A_{surf} T_a\right)\Delta t + \left(\lambda v_m \Delta\xi_{n+1}\right)\right\} \\ S_{n+1}^{-1}\left(\psi(\sigma_{n+1}) - \alpha_{n+1}(T_{n+1} - T_0) - \varepsilon_{n+1}^t\right) \\ h_n \end{bmatrix} \tag{4.21}$$

The steps involved in the modified PF are the same as that discussed in Sections 4.3.2 and 4.6, and the flowchart, as shown in Fig.4.2. The only difference is that the Eqn.(4.21) is used for state propagation, instead of Eqn.(4.14). Further, a modified EKF has also

been developed in this study by utilizing Eqns.(4.16), (4.19) and (4.21), and following the methodology discussed in Chapter 3. In the next section, the displacement of the SMA wire actuated system is estimated from the experimentally measured electrical resistance of the SMA wire under forced cooling conditions illustrated in Tables 4.1 and 4.2. Further, the system response estimated using the modified PF and the modified EKF models are compared with the experimentally obtained displacement.

4.10 Results and Discussions

Figures 4.6a and 4.6b show the voltage signals applied across the SMA wire actuator depicted in Fig.3.8. During the actuation process, the SMA wire is intermittently cooled at various stages of actuation, to varying extent and magnitude, as illustrated in Tables 4.1 and 4.2. These test cases provide a holistic understanding of the SMA wire actuator's behaviour under diverse ambient conditions. During the experiment, the change in the electrical resistance of the SMA wire (R_{sma}) is evaluated from measured voltage signals using Eqn.(3.51). One has to note that during forced cooling, the electrical resistance of the SMA wire varies abruptly, which is harnessed to determine the change in the level of actuation. Using the voltage applied across the SMA ($V_{SMA} = V_t - V_r$) as the input data ($\boldsymbol{u}$ in Eqn.(4.1)) and the acquired electrical resistance (R_{sma}) as the measured data ($\boldsymbol{Y}$ in Eqn.(4.2)), the state of the system is estimated using both the modified PF and the modified EKF, as discussed in Section 4.9.1. The displacement is obtained from the estimated stress, following Eqn.(3.28) and is compared against the measured displacement; for each of the cases depicted in Tables 4.1 and 4.2, and are presented below.

Figures 4.9, 4.10 and 4.11 present the displacement estimated by the modified PF and the modified EKF against the experimental one for the partial heating case, *i.e.*, for the input voltage signal shown in Fig.4.6a, enduring *low level*, *medium level* and *high level* forced cooling, respectively. Here, the sub-figures (a), (b) and (c) represent three different cooling cases, referred to as cases PH(L)-I, PH(L)-II and PH(L)-III, in Table 4.1, respectively. These depict the corresponding system response for cooling durations of 1s, 3s and 5s, respectively. Here, one can observe that the displacement estimated by

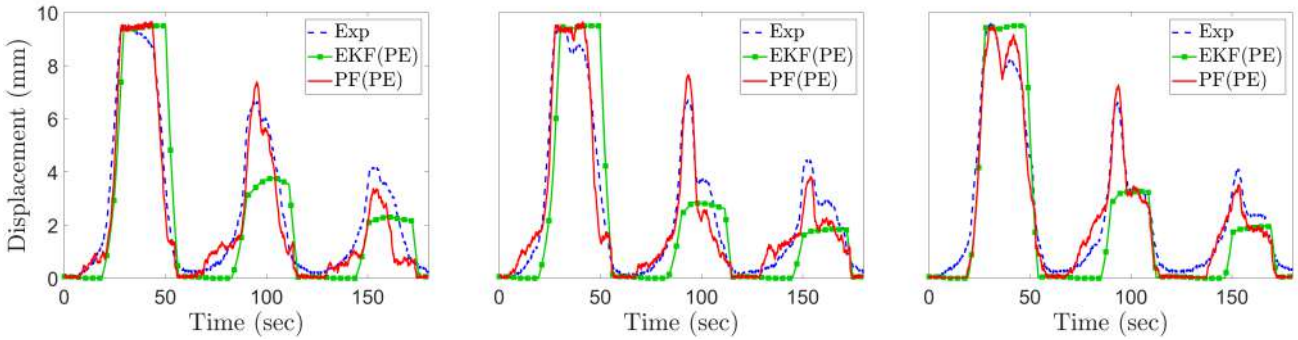

(a) (b) (c)

Figure 4.9: Comparison among the displacement estimated by the modified EKF, modified PF and the measured displacement for *low level* forced cooling cases, (a) PH(L)-I, (b) PH(L)-II, and (c) PH(L)-III.

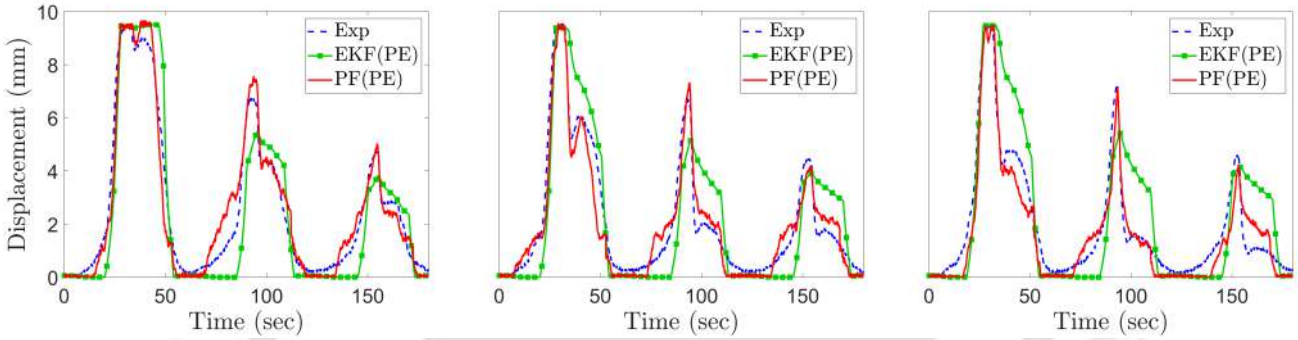

(a) (b) (c)

Figure 4.10: Comparison among the displacement estimated by the modified EKF, modified PF and the measured displacement for *medium level* forced cooling cases, (a) PH(L)-I, (b) PH(L)-II, and (c) PH(L)-III.

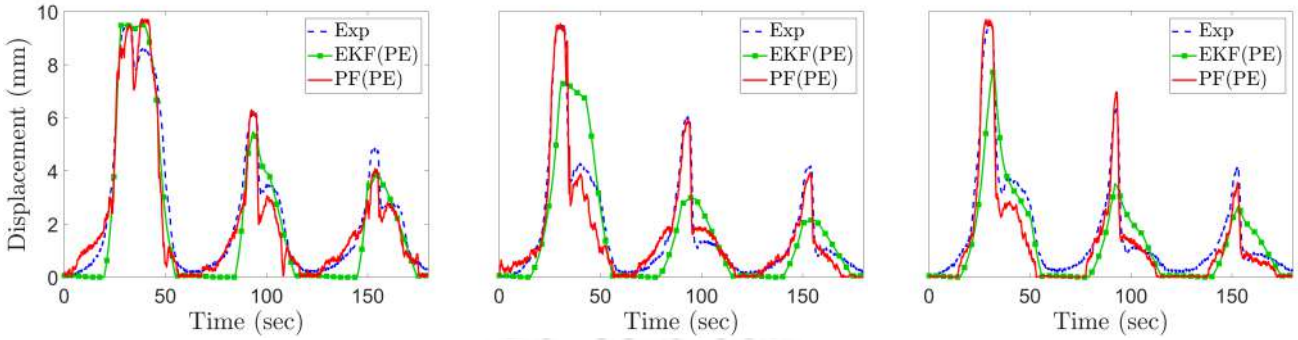

(a) (b) (c)

Figure 4.11: Comparison among the displacement estimated by the modified EKF, modified PF and the measured displacement for *high level* forced cooling cases, (a) PH(L)-I, (b) PH(L)-II, and (c) PH(L)-III.

the modified PF is closer to the experimental one for all test cases, with a maximum estimation error of about 2.3 mm (23.5% of δ_{max}); in comparison to a maximum error of 4.3 mm (44% of δ_{max}) obtained using the modified EKF. Note that the modified PF filter

nicely captures the sudden change in displacement when forced cooling is introduced. One can infer that the approach of parametric estimation of the heat transfer coefficient 'h', has improved the estimation accuracy significantly. This is because the value of h is corrected based on the change in the measured electrical resistance of the SMA wire during forced cooling. Some improvement can also be seen in the responses estimated by the modified EKF; however, it is still unable to delineate the sudden drop in actuation during cooling, resulting in a higher estimation error. The corresponding changes in heat transfer coefficients as estimated by the modified PF and the modified EKF are shown in Figures 4.12, 4.13 and 4.14. Here, the heat transfer coefficient h has been normalized against the initial value (h_i) assumed in the study. One can witness the spontaneous change in the value of h, particularly while forced cooling is introduced. Moreover, as the forced cooling is stopped, the value of h tends to recover back to the nominal value, representing slower cooling during natural convection. The higher accuracy in the case of PF can be attributed to the faster modifications of h depending on the measured changes in R_{sma}. Table 4.6 illustrates the RMS error, maximum error and the computational time required for both the modified EKF and PF, across the aforementioned 9 test cases. Here, one can observe that the modified PF has a lesser estimation error in comparison to the modified EKF, across all forced cooling cases, but consumes higher computational time. This is due to the repetition of the same estimation steps for each of the particles.

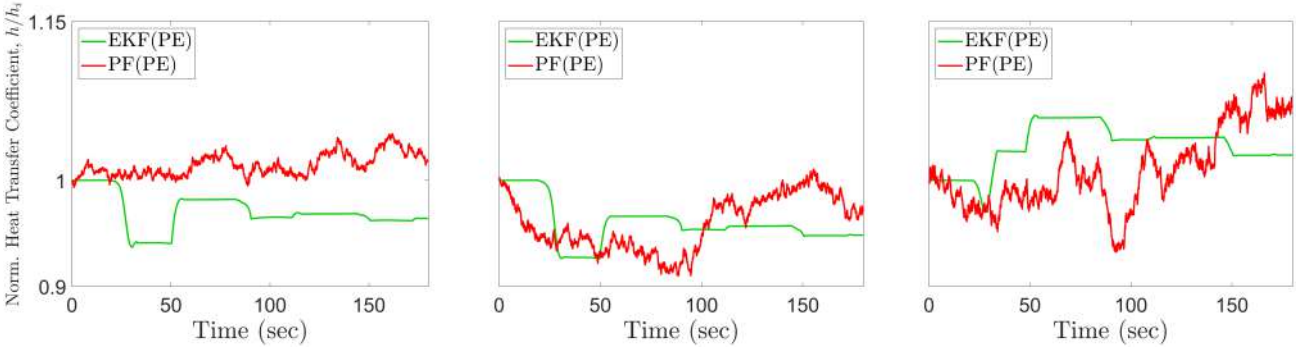

Figure 4.12: Normalized heat transfer coefficient estimated by the modified PF for *low level* forced cooling cases, (a) PH(L)-I, (b) PH(L)-II, and (c) PH(L)-III.

Figures 4.15, 4.16 and 4.17 depict the estimated displacement for *low level*, *medium level* and *high level* cooling cases, respectively. Each subfigure corresponds to different

Cooling case	RMS Error		Maximum Error		Computational Time	
	EKF	**PF**	**EKF**	**PF**	**EKF**	**PF**
PH(L)-I, (Low)	1.459 mm (14.88% of δ_{max})	0.560 mm (5.72% of δ_{max})	4.319 mm (44.07% of δ_{max})	1.809 mm (18.46% of δ_{max})	0.169 s	5.18 s
PH(L)-II (Low)	1.574 mm (16.06% of δ_{max})	0.639 mm (6.52% of δ_{max})	4.146 mm (42.31% of δ_{max})	2.186 mm (22.31% of δ_{max})	0.188 s	5.164 s
PH(L)-III (Low)	1.260 mm (12.86% of δ_{max})	0.578 mm (5.90% of δ_{max})	3.753 mm (38.29% of δ_{max})	1.782 mm (18.18% of δ_{max})	0.169 s	5.107 s
PH(L)-I (Medium)	1.405 mm (14.33% of δ_{max})	0.584 mm (5.96% of δ_{max})	3.318 mm (33.86% of δ_{max})	1.818 mm (18.56% of δ_{max})	0.178 s	5.207 s
PH(L)-II (Medium)	1.289 mm (13.15% of δ_{max})	0.649 mm (6.63% of δ_{max})	3.289 mm (33.56% of δ_{max})	2.297 mm (23.44% of δ_{max})	0.168 s	5.173 s
PH(L)-III (Medium)	1.281 mm (13.07% of δ_{max})	0.656 mm (6.69% of δ_{max})	2.927 mm (29.87% of δ_{max})	1.968 mm (20.08% of δ_{max})	0.166 s	5.071 s
PH(L)-I (High)	0.903 mm (9.21% of δ_{max})	0.544 mm (5.55% of δ_{max})	2.804 mm (28.61% of δ_{max})	1.762 mm (17.98% of δ_{max})	0.166 s	5.143 s
PH(L)-II (High)	0.861 mm (8.79% of δ_{max})	0.599 mm (6.11% of δ_{max})	3.394 mm (34.63% of δ_{max})	2.383 mm (24.32% of δ_{max})	0.159 s	5.088 s
PH(L)-III (High)	0.949 mm (9.69% of δ_{max})	0.564 mm (5.76% of δ_{max})	3.068 mm (31.31% of δ_{max})	1.654 mm (16.88% of δ_{max})	0.153 s	5.127 s

Table 4.6: RMS error, maximum error and computational time for both the PF and EKF undergoing forced cooling cases PH(L)-I, PH(L)-II and PH(L)-III.

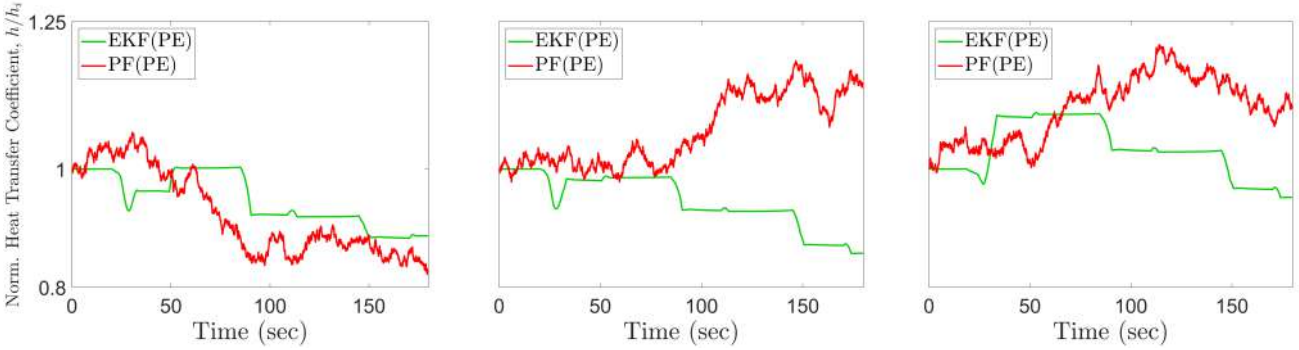

Figure 4.13: Normalized heat transfer coefficient estimated by the modified PF for *medium level* forced cooling cases, (a) PH(L)-I, (b) PH(L)-II, and (c) PH(L)-III.

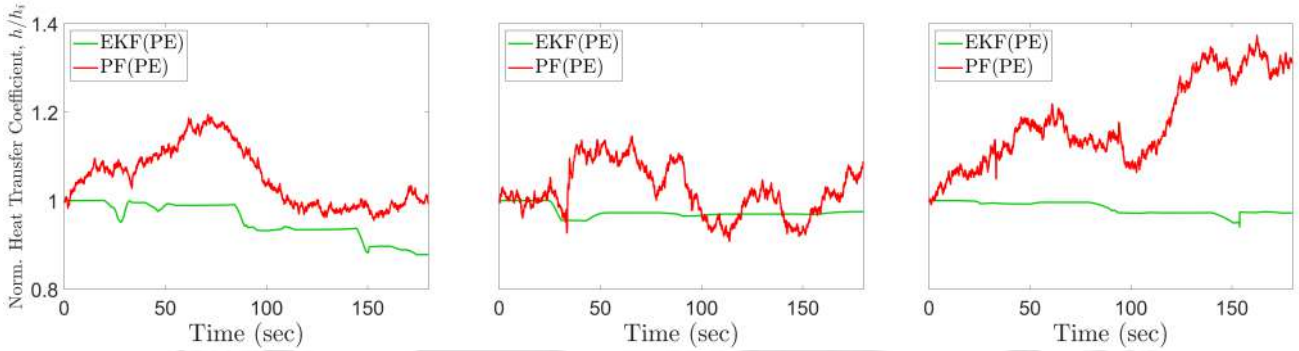

Figure 4.14: Normalized heat transfer coefficient estimated by the modified PF for *high level* forced cooling cases, (a) PH(L)-I, (b) PH(L)-II, and (c) PH(L)-III.

cooling durations, *i.e.*, 1s, 3s, and 5s. The external cooling transpires while SMA undergoes phase transformation, as illustrated in PH(L)-IV, PH(L)-V and PH(L)-VI, in Table 4.1. Here, one can observe that the modified PF is better equipped to decipher the external cooling situations, as depicted by the sharp change in the estimated displacement during the phase transformation. The maximum estimation error of the modified PF and the EKF are around 2.5 mm (25.5% of δ_{max}) and 4.7 mm (47.9% of δ_{max}), respectively. Figure 4.18 depicts the resistance estimated by the modified PF for the corresponding *low level* cooling cases shown in Fig.4.15. Here, one can clearly observe the notch in the electrical resistance variation when the external cooling is introduced. The corresponding drops in the actuation level are evident in Fig.4.15. This detection of the sudden change in measured resistance by the filter, and the corresponding rapid modification of the heat transfer coefficient, results in the improved estimation accuracy in the case of both the EKF and PF. The parameter h estimated by the modified EKF and modified PF, showed

similar variation, in both its nature and magnitude, as observed in Figs.4.12, 4.13 and 4.14. Hence, for the sake of brevity, these plots are omitted.

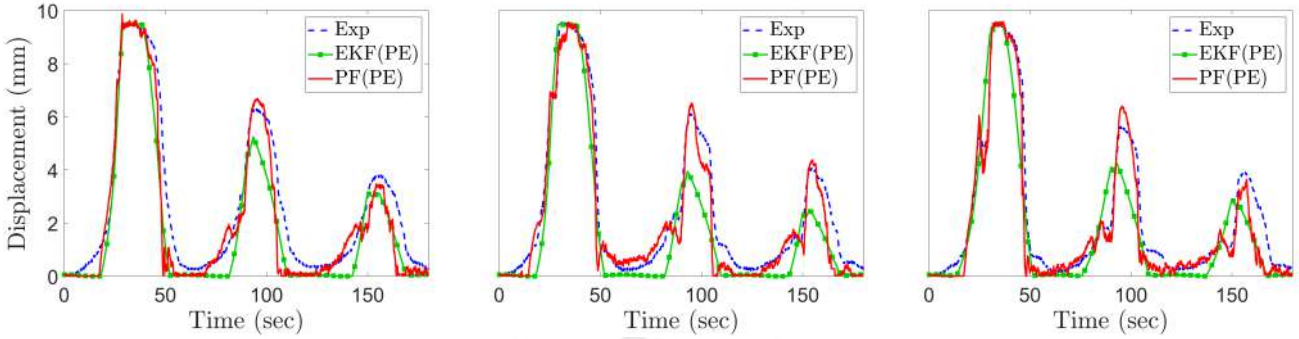

(a) (b) (c)

Figure 4.15: Comparison among the displacement estimated by the modified EKF, modified PF and the measured displacement for *low level* forced cooling cases, (a) PH(L)-IV, (b) PH(L)-V, and (c) PH(L)-VI.

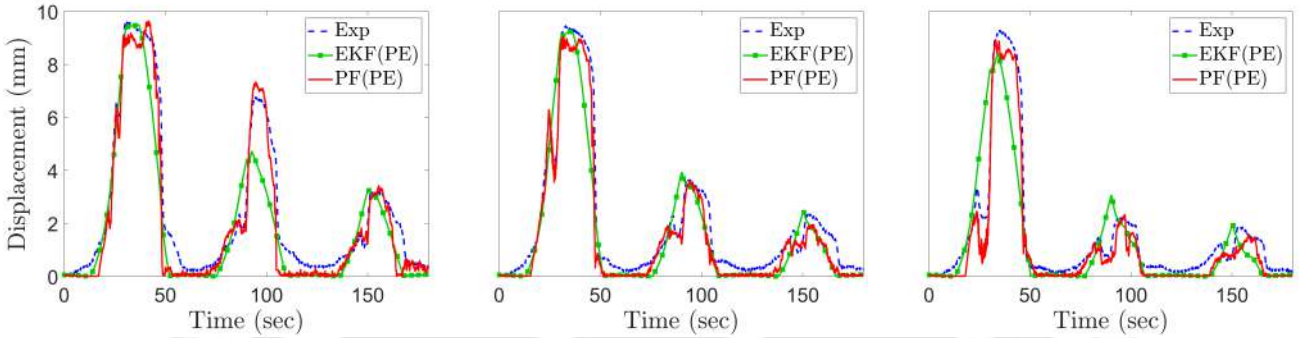

(a) (b) (c)

Figure 4.16: Comparison among the displacement estimated by the modified EKF, modified PF and the measured displacement for *medium level* forced cooling cases, (a) PH(L)-IV, (b) PH(L)-V, and (c) PH(L)-VI.

Figures 4.19, 4.20 and 4.21 illustrate the system response for the abruptly cooled SMA wire actuated system for *low level*, *medium level* and *high level* cooling, respectively, described as cases PH(L)-VII, PH(L)-VIII and PH(L)-IX, in Table 4.1, respectively. The system response estimated by the modified PF is significantly better than the modified EKF across most cases. The maximum error of the modified PF is around 2.9 mm (29.6% of δ_{max}), and that of EKF is 3.5 mm (35.7% of δ_{max}). However, in some cases, where the external cooling time is 1s, the EKF seems to give slightly better results than PF, although it cannot detect the sudden drops in displacement as the cooling initiates. Here, one can also notice that the estimation error is low for prolonged cooling cases, as it allows

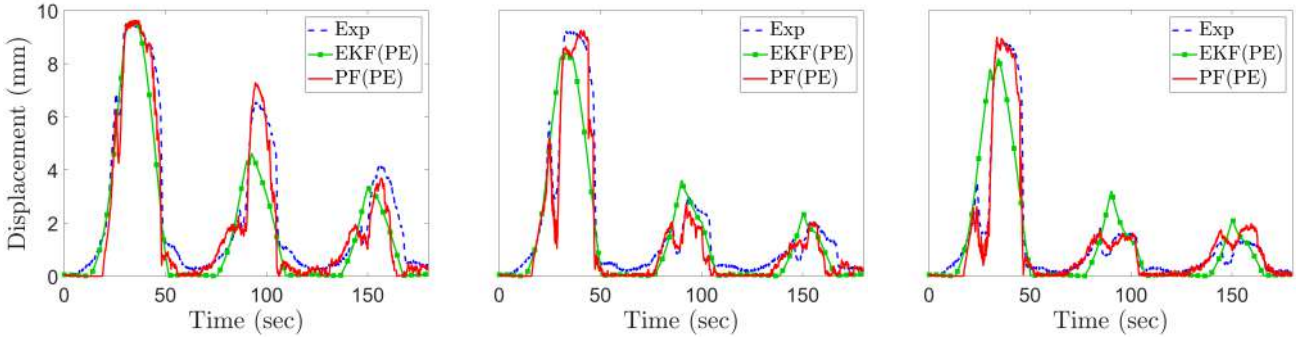

(a) (b) (c)

Figure 4.17: Comparison among the displacement estimated by the modified EKF, modified PF and the measured displacement for *high level* forced cooling cases, (a) PH(L)-IV, (b) PH(L)-V, and (c) PH(L)-VI.

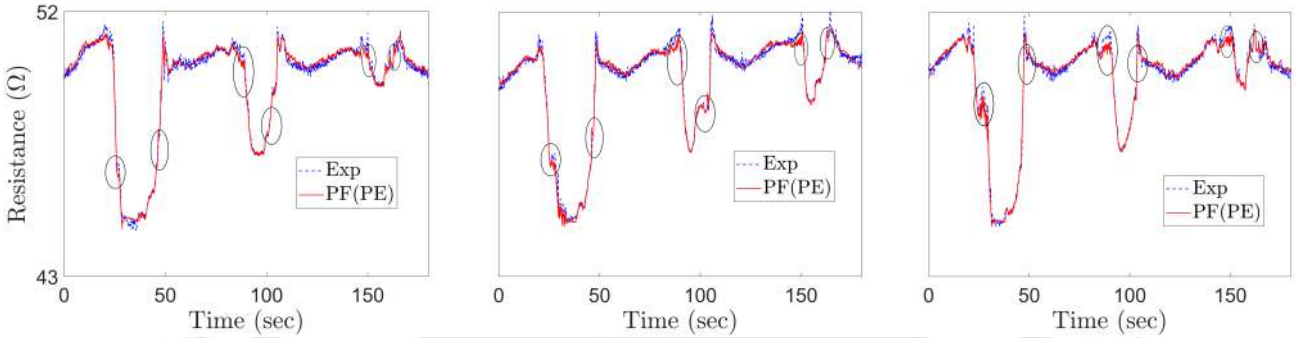

(a) (b) (c)

Figure 4.18: Comparison among the resistance estimated by the modified PF and the measured resistance for *low level* forced cooling cases, (a) PH(L)-IV, (b) PH(L)-V, and (c) PH(L)-VI.

ample time for the estimator to predict the state of SMA accurately. Further, the heat transfer coefficient plots of the same showed discernible changes as the forced cooling was initiated, akin to Figs.4.12, 4.13 and 4.14 and have therefore been elided.

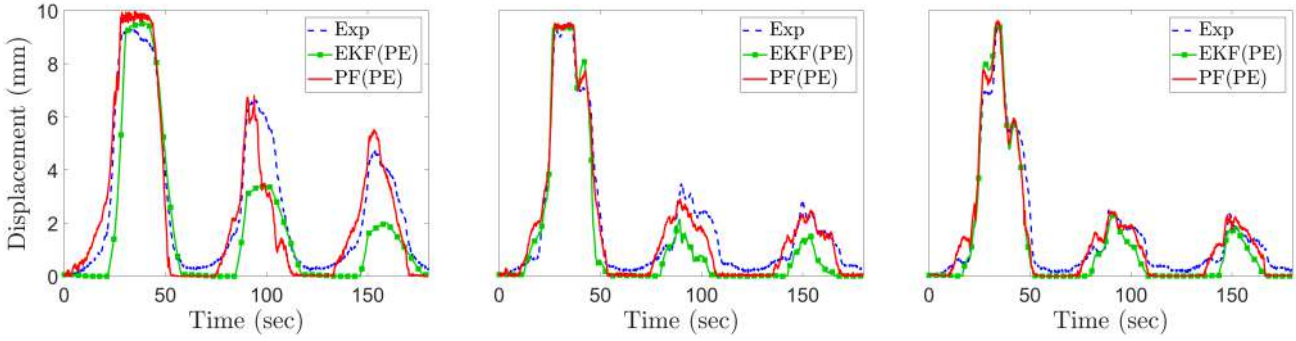

(a) (b) (c)

Figure 4.19: Comparison among the displacement estimated by the modified EKF, modified PF and the measured displacement for *low level* forced cooling cases, (a) PH(L)-VII, (b) PH(L)-VIII, and (c) PH(L)-IX.

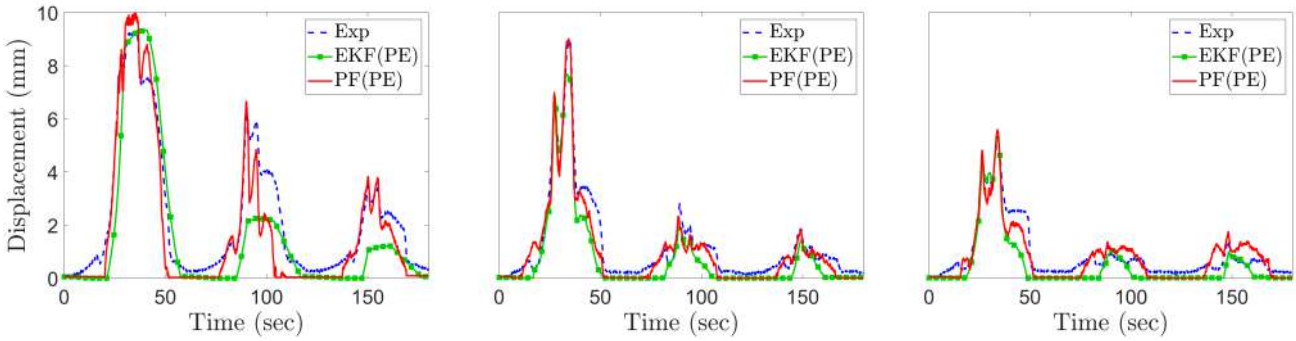

(a) (b) (c)

Figure 4.20: Comparison among the displacement estimated by the modified EKF, modified PF and the measured displacement for *medium level* forced cooling cases, (a) PH(L)-VII, (b) PH(L)-VIII, and (c) PH(L)-IX.

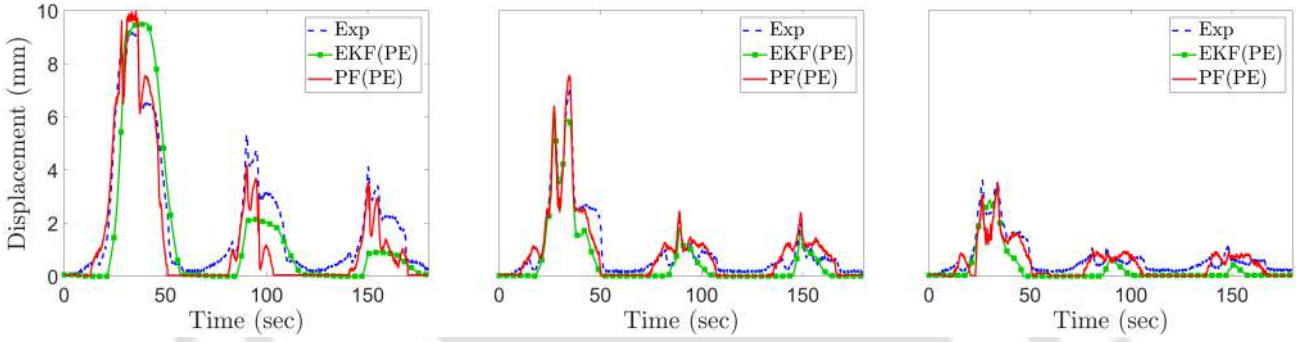

(a) (b) (c)

Figure 4.21: Comparison among the displacement estimated by the modified EKF, modified PF and the measured displacement for *high level* forced cooling cases, (a) PH(L)-VII, (b) PH(L)-VIII, and (c) PH(L)-IX.

A similar study has been carried out for the SMA wire actuated system under partial cooling conditions, achieved while applying a voltage signal shown in Fig.4.6b. As in earlier cases, the SMA wire is intermittently cooled at different stages of actuation, for increasing time durations and intensity, as depicted in Table 4.2. Figures 4.22, 4.23 and 4.24 illustrate the displacement predicted by the modified EKF and PF for *low level*, *medium level* and *high level* cooling, respectively, while the SMA wire is subjected to forced cooling cases PC(L)-I, PC(L)-II and PC(L)-III shown in Table 4.2. These are designated as sub-figures (a), (b) and (c), respectively. Here, one can perceive the modified PF's improved estimation accuracy compared to the modified EKF. The PF satisfactorily captures the sudden fall in actuation due to forced convection. The EKF outlines the SMA response obtained from the system, albeit at a lower accuracy. This is especially true in

areas of sudden cooling. The maximum estimation error of the modified PF and EKF are found to be around 1.6 mm (16.3% of δ_{max}) and 2.9 mm (30% of δ_{max}), respectively. The corresponding changes in h are illustrated in Figs.4.25, 4.26 and 4.27 depicting the abrupt change in the value of the heat transfer coefficient as the forced cooling initiates. Table 4.7 presents the RMS and maximum errors and the computational time of both the modified EKF and PF across the above-mentioned 9 test cases. Here, one can discern that the modified PF provides a more accurate estimate of the response in comparison to the modified EKF, across all test cases. However, the modified PF consumes more computational time than the modified EKF, owing to the recurrent calculations involved in PF.

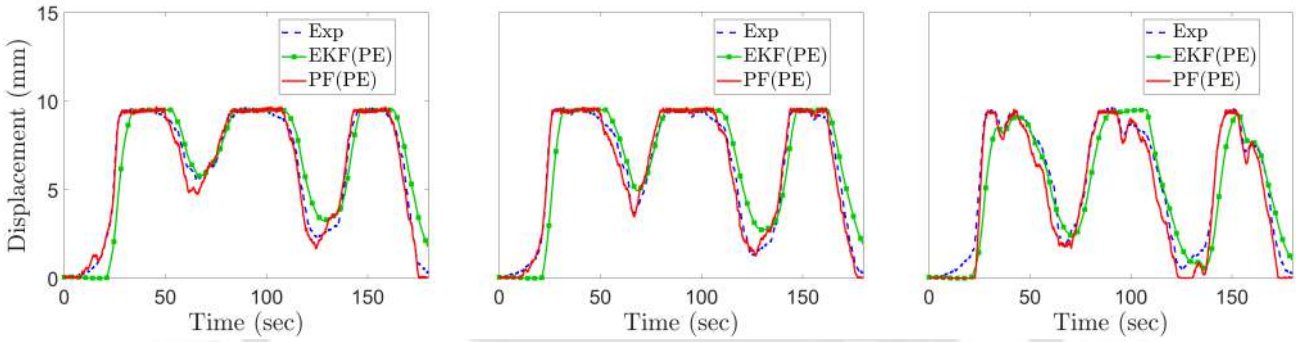

Figure 4.22: Comparison among the displacement estimated by the modified EKF, modified PF and the measured displacement for *low level* forced cooling cases, (a) PC(L)-I, (b) PC(L)-II, and (c) PC(L)-III.

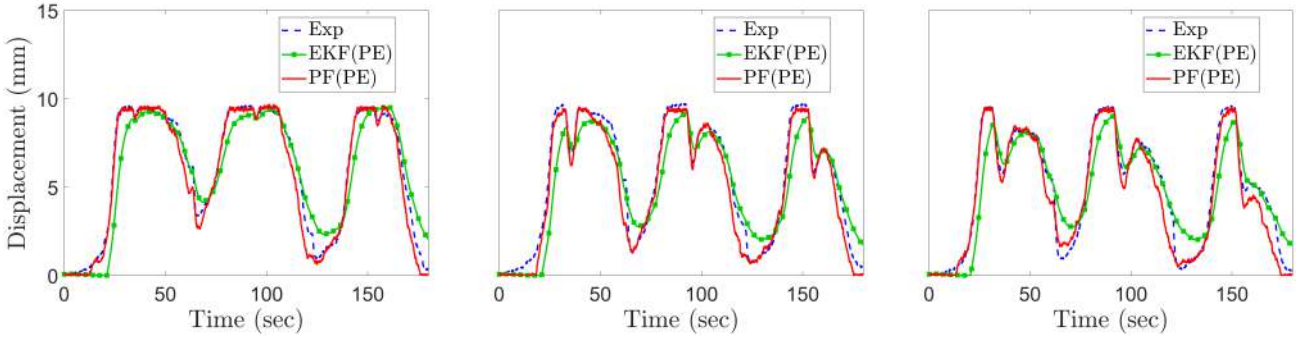

Figure 4.23: Comparison among the displacement estimated by the modified EKF, modified PF and the measured displacement for *medium level* forced cooling cases, (a) PC(L)-I, (b) PC(L)-II, and (c) PC(L)-III.

Figures 4.28, 4.29 and 4.30 illustrate the displacement response of SMA wire actuator undergoing *low level*, *medium level* and *high level* cooling during A-M phase transforma-

Cooling case	RMS Error		Maximum Error		Computational Time	
	EKF	**PF**	**EKF**	**PF**	**EKF**	**PF**
PC(L)-I (Low)	0.975 mm (9.95% of δ_{max})	0.551 mm (5.62% of δ_{max})	2.686 mm (27.41% of δ_{max})	0.996 mm (10.16% of δ_{max})	0.138 s	5.339 s
PC(L)-II (Low)	1.074 mm (10.96% of δ_{max})	0.543 mm (5.54% of δ_{max})	2.323 mm (23.71% of δ_{max})	1.013 mm (10.33% of δ_{max})	0.144 s	5.318 s
PC(L)-III (Low)	1.168 mm (11.91% of δ_{max})	0.650 mm (6.64% of δ_{max})	1.617 mm (16.50% of δ_{max})	0.967 mm (9.87% of δ_{max})	0.142 s	5.231 s
PC(L)-I (Medium)	1.041 mm (10.62% of δ_{max})	0.555 mm (5.67% of δ_{max})	1.997 mm (20.38% of δ_{max})	0.922 mm (9.41% of δ_{max})	0.141 s	5.217 s
PC(L)-II (Medium)	1.189 mm (12.13% of δ_{max})	0.646 mm (6.59% of δ_{max})	2.217 mm (22.62% of δ_{max})	1.189 mm (12.14% of δ_{max})	0.144 s	5.303 s
PC(L)-III (Medium)	1.243 mm (12.68% of δ_{max})	0.673 mm (6.87% of δ_{max})	3.003 mm (30.64% of δ_{max})	1.398 mm (14.27% of δ_{max})	0.128 s	5.299 s
PC(L)-I (High)	1.014 mm (10.35% of δ_{max})	0.639 mm (6.53% of δ_{max})	2.121 mm (21.64% of δ_{max})	1.091 mm (11.13% of δ_{max})	0.142 s	5.306 s
PC(L)-II (High)	1.344 mm (13.72% of δ_{max})	0.652 mm (6.65% of δ_{max})	2.898 mm (29.57% of δ_{max})	1.669 mm (17.03% of δ_{max})	0.179 s	5.383 s
PC(L)-III (High)	1.376 mm (14.04% of δ_{max})	0.628 mm (6.41% of δ_{max})	2.458 mm (25.08% of δ_{max})	1.092 mm (11.14% of δ_{max})	0.149 s	5.254 s

Table 4.7: RMS error, maximum error and computational time for both the PF and EKF undergoing forced cooling cases PC(L)-I, PC(L)-II and PC(L)-III.

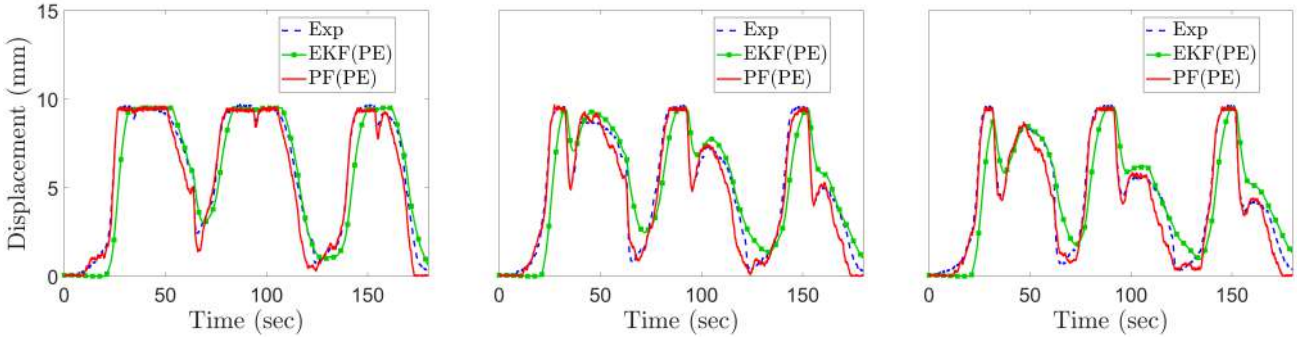

(a) (b) (c)

Figure 4.24: Comparison among the displacement estimated by the modified EKF, modified PF and the measured displacement for *high level* forced cooling cases, (a) PC(L)-I, (b) PC(L)-II, and (c) PC(L)-III.

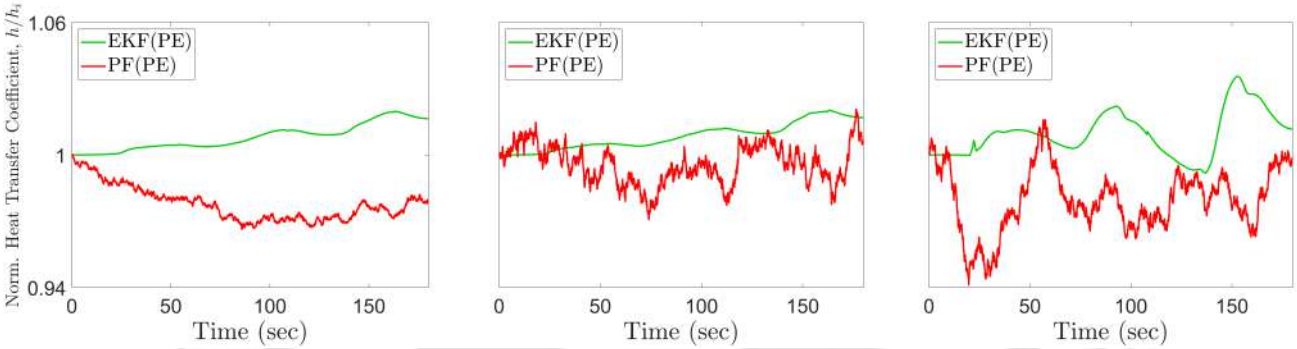

(a) (b) (c)

Figure 4.25: Normalized heat transfer coefficient estimated by the modified PF for *low level* forced cooling cases, (a) PC(L)-I, (b) PC(L)-II, and (c) PC(L)-III.

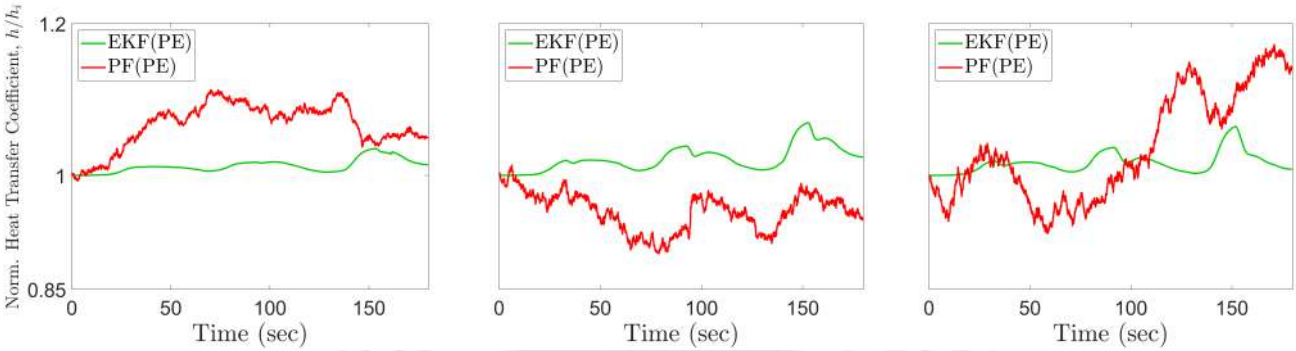

(a) (b) (c)

Figure 4.26: Normalized heat transfer coefficient estimated by the modified PF for *medium level* forced cooling cases, (a) PC(L)-I, (b) PC(L)-II, and (c) PC(L)-III.

tion. The sub-figures (a), (b) and (c) depict the cooling instances PC(L)-IV, PC(L)-V and PC(L)-VI, respectively, in Table 4.2. Here as well, the modified PF is superior to the modified EKF, in delineating the abrupt drop in the system response, upon forced cooling. The modified PF's maximum error is around 2 mm (20.4% of δ_{max}), whereas the maximum error of the modified EKF is about 3 mm (30.6% of δ_{max}). The related heat

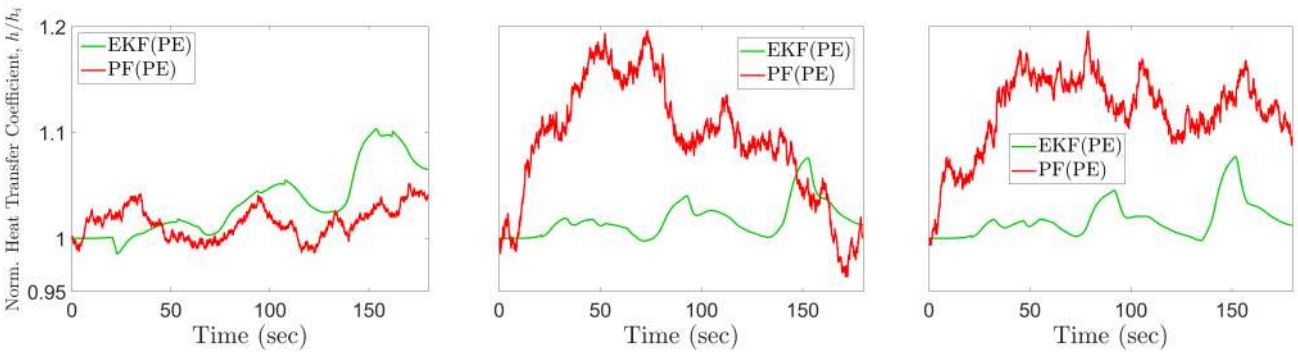

(a) (b) (c)

Figure 4.27: Normalized heat transfer coefficient estimated by the modified PF for *high level* forced cooling cases, (a) PC(L)-I, (b) PC(L)-II, and (c) PC(L)-III.

transfer coefficient estimated by both the modified EKF and PF showed a similar order of variation upon forced cooling, congruent to the same observed in Figs.4.25, 4.26 and 4.27. Hence, the h-plots have not been reported for the sake of conciseness.

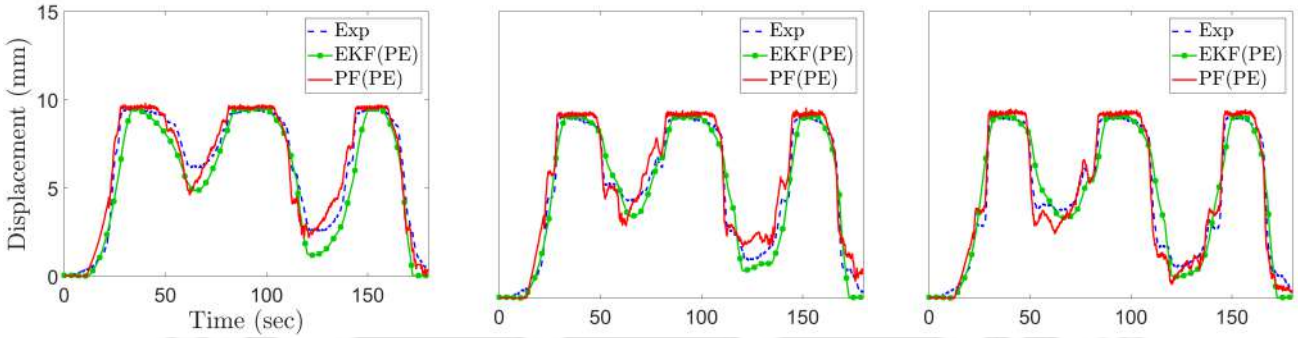

(a) (b) (c)

Figure 4.28: Comparison among the displacement estimated by the modified EKF, modified PF and the measured displacement for *low level* forced cooling cases, (a) PC(L)-IV, (b) PC(L)-V, and (c) PC(L)-VI.

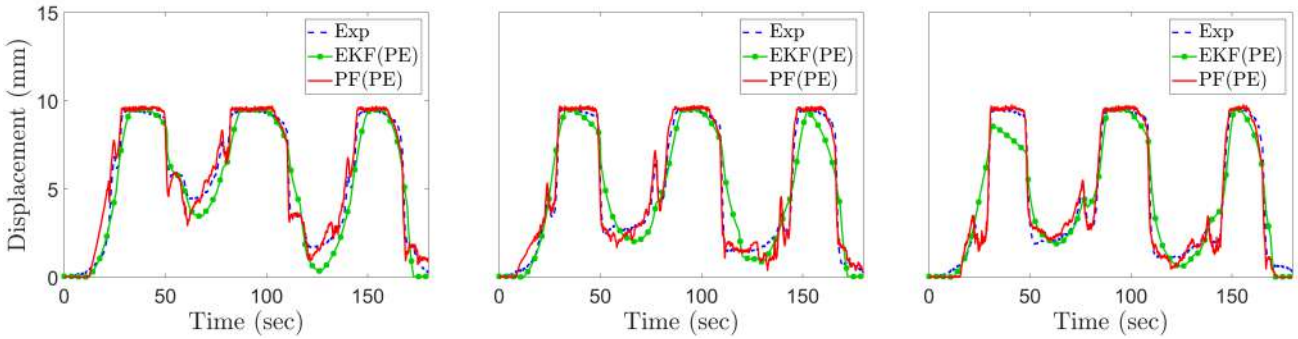

(a) (b) (c)

Figure 4.29: Comparison among the displacement estimated by the modified EKF, modified PF and the measured displacement for *medium level* forced cooling cases, (a) PC(L)-IV, (b) PC(L)-V, and (c) PC(L)-VI.

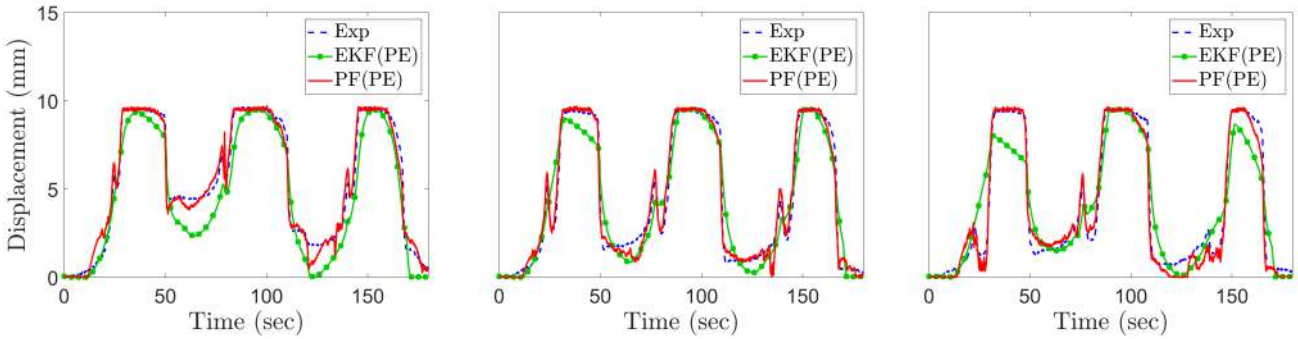

(a) (b) (c)

Figure 4.30: Comparison among the displacement estimated by the modified EKF, modified PF and the measured displacement for *high level* forced cooling cases, (a) PC(L)-IV, (b) PC(L)-V, and (c) PC(L)-VI.

Further, the displacement estimate of the system corresponding to cooling cases PC(L)-VII, PC(L)-VIII and PC(L)-IX in Table 4.2, for *low level*, *medium level* and *high level* cooling are shown in Figs.4.31, 4.32 and 4.33, respectively. The displacement curves show that the modified PF estimate is quantitatively better in comparison to the EKF one, for all cooling cases. The heat transfer coefficient plots showed a significant change in h as the transformation progresses under forced cooling conditions, analogous to the trend realized in Figs.4.25, 4.26 and 4.27, and are thus excluded. One can infer that the non-linear estimation methodology utilizing the probabilistic technique results in a swift and scrupulous variation of h in the modified PF estimator, thus rendering a displacement estimate of higher accuracy in comparison to that of the modified EKF. These responses illustrate the true potential of the proposed modified PF in estimating the system response of a suddenly cooled SMA wire actuated system.

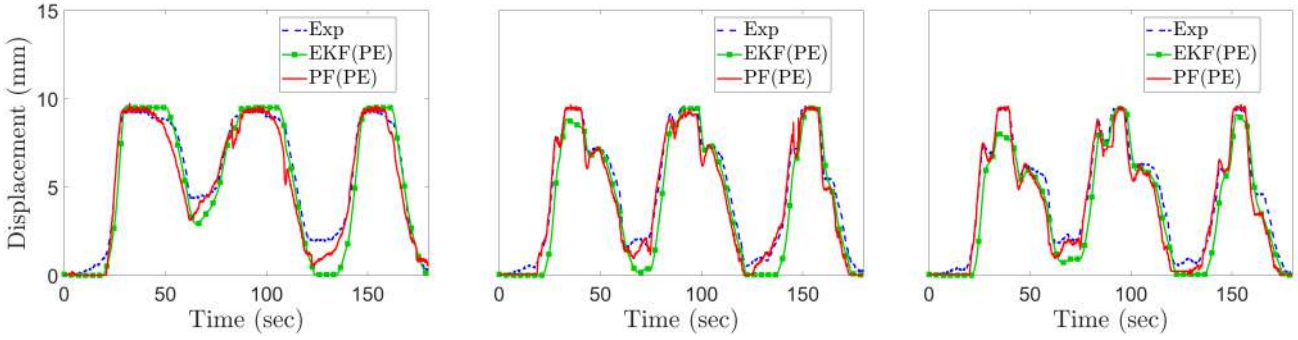

(a) (b) (c)

Figure 4.31: Comparison among the displacement estimated by the modified EKF, modified PF and the measured displacement for *low level* forced cooling cases, (a) PC(L)-VII, (b) PC(L)-VIII, and (c) PC(L)-IX.

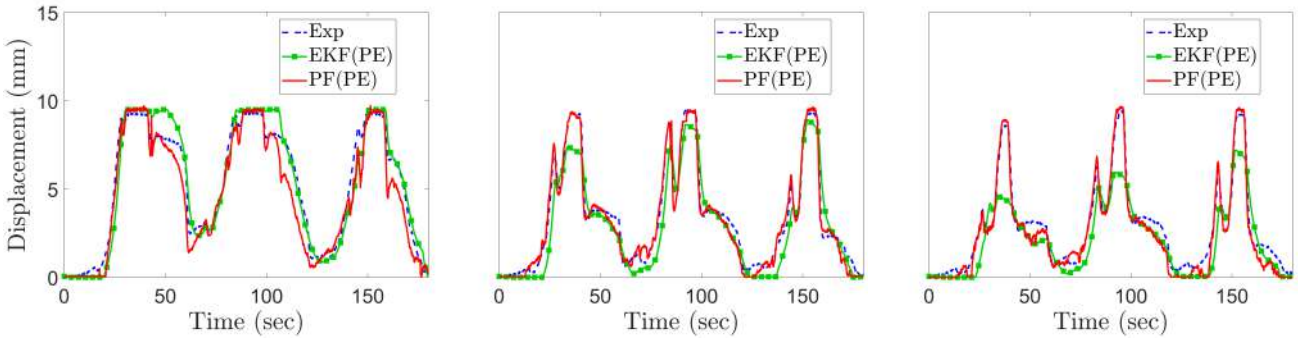

(a) (b) (c)

Figure 4.32: Comparison among the displacement estimated by the modified EKF, modified PF and the measured displacement for *medium level* forced cooling cases, (a) PC(L)-VII, (b) PC(L)-VIII, and (c) PC(L)-IX.

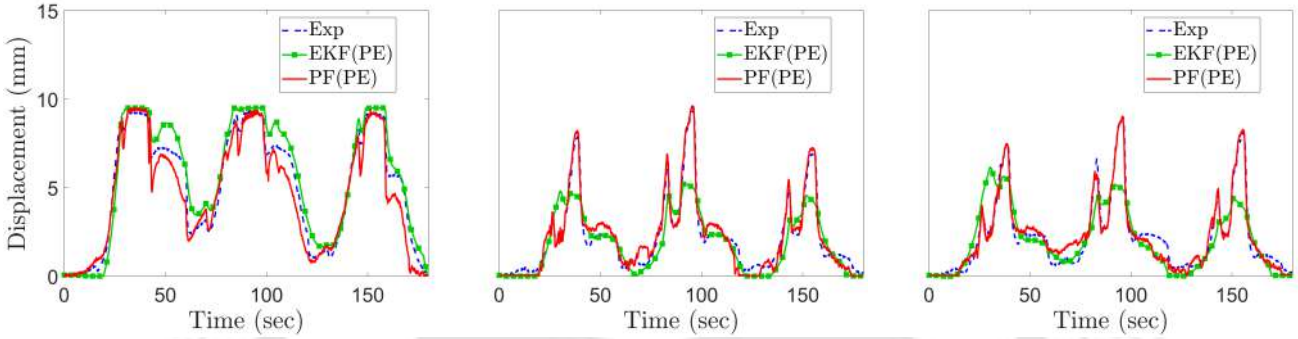

(a) (b) (c)

Figure 4.33: Comparison among the displacement estimated by the modified EKF, modified PF and the measured displacement for *high level* forced cooling cases, (a) PC(L)-VII, (b) PC(L)-VIII, and (c) PC(L)-IX.

4.11 Conclusions

In this chapter, a Particle Filter (PF) has been developed to estimate the SMA wire actuated system response using the measured electrical resistance variation of the SMA wire. The discretized form of both the heat balance equation and the modified constitutive model of SMA are derived, representing the system model required for the PF. Using the voltage applied across the SMA as the input data and the experimentally determined electrical resistance of SMA as the measured data, the developed PF has been used to estimate the level of actuation of the SMA wire actuator. For an SMA wire system enduring actuation under natural cooling, it is found that the displacement estimated by the PF closely follows the same obtained experimentally with an RMS error of about 0.4mm, exhibiting the efficacy of the proposed PF. Here, one can observe that the modified version

of the previously proposed EKF also predicts the response with comparable accuracy as that of PF. However, the computational time consumed by the PF is significantly larger than that of the EKF, thus making the EKF-based estimation better suited for natural cooling cases.

Furthermore, a new set of experiments are carried out with the SMA actuator undergoing forced cooling of different durations and intensities. Here, the displacement estimated by the proposed PF is slightly better than the existing estimation models, but the improvement is inadequate for practical actuation purposes. To obviate it, a modified PF has been proposed, wherein the heat transfer coefficient is estimated in addition to the stress and temperature of the SMA wire. Next, the performance of the modified PF is assessed when the actuation undergoes in the presence of forced cooling. The system response evaluated by the modified PF has dramatically improved, while the heat transfer coefficient of the SMA wire is estimated along with the other state variables. In most cases, it has been observed that the value of the normalized h increases as soon as forced cooling is introduced, and it gradually recedes with the abatement of forced cooling. However, there is no general trend in the variation of normalized h. This may be because the modified approach is also trying to bridge some modelling ambiguities during the state estimation. In the case of the partial heating condition (PH(L)-I, PH(L)-II, PH(L)-III), the RMS error of the modified PF is found to be around 6% of the maximum displacement (δ_{max}) and that of the modified EKF was found to be around 9-15% of δ_{max}. Additionally, in the case of the partial cooling condition (PC(L)-I, PC(L)-II, PC(L)-III), the RMS error of the modified PF is also around 6% of δ_{max}, compared to 10-14% of δ_{max} in case of the modified EKF. Here, one can observe that the modified PF has perceptibly better accuracy than that of the modified EKF across all the test cases, albeit at the cost of larger computational time. The improvement in the estimation accuracy with the modified PF approach reveals its true potential as a self-sensing tool in real-life applications.

Chapter 5

Self-Sensing of a Shape Memory Alloy Wire Actuator Undergoing Non-Proportional Loading

5.1 Introduction

In literature, all self-sensing applications are developed for linear systems, where the SMA wire actuators undergo a monotonic variation of stress and temperature, referred to as proportional loading. However, non-proportional loading situations are often encountered in practice [49]. To address these situations, a robust estimation technique has to be developed, which not only depends on experimental data, but is also based on the system model. Moreover, none of the existing self-sensing approaches address the effect of abrupt, forced cooling of SMA wire actuators, which is very likely in practical SMA wire-based applications. In this chapter, the response of an SMA wire actuated non-linear system is estimated under proportional as well as non-proportional loading conditions. Following a similar strategy discussed in Chapter 4, a PF has been developed for this purpose. Subsequently, an experimental setup is fabricated, and using the measured electrical resistance of SMA, the PF estimates the link position, while actuating, and its effectiveness in harnessing the self-sensing ability of the SMA wire actuator is demonstrated.

5.2 System Description

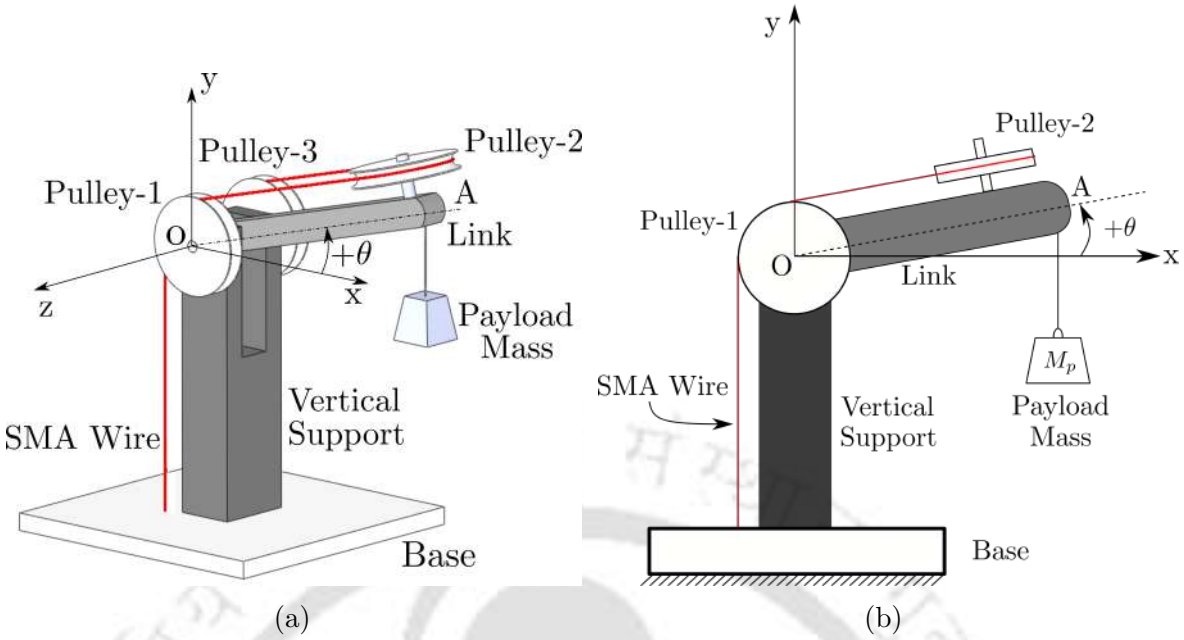

Figure 5.1: (a) SMA wire actuated manipulator, and (b) its schematic representation.

The SMA wire actuated 1-DOF manipulator considered in this study, and its schematic representation are illustrated in Figs.5.1a and Fig.5.1b. A pre-strained SMA wire, wound over a series of 3 pulleys, is fixed to the base, as depicted by the red curve in Fig.5.1a. Pulley-1 is attached to the link such that its axis of rotation is parallel to the base. The Pulley-2 is placed such that its axis remains perpendicular to that of the link. Pulley-3 is placed on the same axis as that of Pulley-1 and is on the opposite side of the link (refer Fig.5.1a). The manipulator system having a link of mass M_l, carries a payload mass (M_p). A torsional spring provides the bias force on the SMA wire actuator. The SMA wire's temperature is controlled using resistive heating, by applying a voltage across the same. When the voltage increases, the temperature increases and the reverse transformation initiates as it goes above the austenite start temperature (A_s). The resulting recovery stress pulls the link in the counter-clockwise direction ($+\theta$). While the applied voltage is reduced, the SMA wire cools due to convective heat loss. As the temperature drops below the martensite start temperature (M_s), the forward transformation initiates in the presence of payload and spring force, and the link returns to its initial configuration.

In this study, the present system undergoes two different non-proportional loading cases. In the first one, during actuation, the SMA wire is abruptly cooled for short dura-

tions. This mimics practical situations, wherein an unwanted external cooling might lead to a drop in actuation. In the same system, with a slight change in the initial orientation, one can achieve another situation, as illustrated in Fig.5.2a. Here, as the link continuously rises due to actuating force of the SMA wire, the stress in the wire increases gradually. Upon crossing the horizontal position (point a), the stress in the SMA wire reaches its maximum value (σ_{max}) at point b, and then subsequently reduces. However, the temperature of the wire keeps increasing monotonically (red line in Fig.5.2b), resulting in a loading situation wherein the stress and temperature in the wire vary non-monotonically. This results in a sudden reduction in the transformation boundaries and hence the transformation temperatures, leading to a quick completion of the ongoing reverse phase transformation, as illustrated in Fig.5.2b. To estimate the system response under these situations, a PF is developed, and its effectiveness is demonstrated by comparing the outcomes of the PF with the corresponding experimental observations.

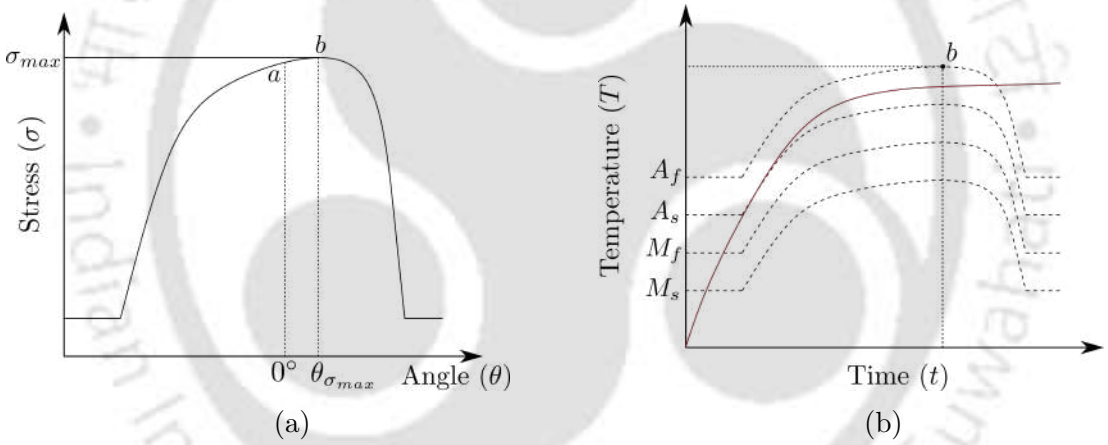

Figure 5.2: (a) Variation of stress, and (b) temperature in the SMA wire.

The objective of the present study is to estimate the angular position of the link (θ), using the measured change in the electrical resistance of the SMA wire, for a varied set of loading conditions, eliminating the need for a rotary encoder. The same has been achieved by employing a PF-based state estimation approach, a detailed description of which can be found in Section 4.3. To develop a PF for the SMA wire actuated manipulator system, one has to define the set of equations, representing the process and measurement models and their output. For this purpose, the discrete form of the constitutive model of SMA, system kinematics, equation of motion and heat balance equations are derived in the

following section.

5.3 System Modeling

The governing equations for the SMA wire actuated manipulator comprise of the SMA constitutive model, heat balance equation, kinematic constraints, equation of motion and the relation between the strain and the electrical resistance of the SMA wire.

5.3.1 1-D SMA Constitutive Model

This study uses the modified form of the Boyd and Lagoudas model, as discussed in Chapter 4, to simulate the SMA response. The 1-D constitutive equation, relating the stress (σ), strain (ε) and temperature (T) of the SMA wire, is expressed as,

$$\sigma = S^{-1}\left(\varepsilon - \alpha(T - T_0) - \varepsilon^t\right). \tag{5.1}$$

Here, S denotes the compliance, and α defines the thermal expansion coefficient. Also, the rate of change of the transformation strain (ε^t) is related to the rate of change of martensite volume fraction ($\dot{\xi}$) following, $\dot{\varepsilon}^t = H\dot{\xi}$. Here, H refers to the maximum transformation strain in SMA. The transformation function (ϕ) is defined following Eqns.(2.12) and (2.13) as,

$$\begin{aligned}\phi(\sigma, T, \xi) = \pm\Bigg\{&\sigma H + \sigma\Delta\alpha(T - T_0) + \frac{1}{2}\sigma^2\Delta S + \rho\Delta s_0 T - \rho\Delta u_0 \\ &+ \rho\Delta C_v\left[T\ln\left(\frac{T}{T_0}\right) - (T - T_0)\right] - \frac{\partial h_f}{\partial \xi}\Bigg\} - Y_f.\end{aligned} \tag{5.2}$$

Here, C_v defines the specific heat, and s_0 and u_0 are the entropy and internal energy at the reference state, respectively. Also, $h_f(\xi)$ and $Y_f(\xi)$ denote the exponential hardening function and the threshold value of thermodynamic force at yield, and are expressed as,

$$h_f(\xi) = \begin{cases} \frac{1}{2}a_1\left[\frac{\xi^{n_1+1}}{n_1+1} + \frac{(1-\xi)^{n_2+1}}{n_2+1}\right] + (a_3 + a_4)\xi & \forall \quad \dot{\xi} > 0 \\ \frac{1}{2}a_2\left[\frac{\xi^{n_3+1}}{n_3+1} + \frac{(1-\xi)^{n_4+1}}{n_4+1}\right] + (a_3 - a_4)\xi & \forall \quad \dot{\xi} < 0. \end{cases} \tag{5.3}$$

$$Y_f(\xi) = \begin{cases} Y_1 + Y_2\xi_r \left(e^{\gamma(1-\xi)} - 1\right), & \forall \quad \dot{\xi} > 0 \\ Y_1 + Y_3(1-\xi_r)\left(e^{\gamma\xi} - 1\right), & \forall \quad \dot{\xi} < 0 \end{cases} \tag{5.4}$$

The associated model parameters $Y_1, Y_2, Y_3, a_1, a_2, a_3$ and a_4 are taken from Eqn.(4.7). The modified constitutive model is implemented following the convex cutting return mapping algorithm [56] discussed in Section 2.5.

5.3.2 Heat Balance Equation

The heat balance equation considering the resistive heating, convective heat loss and latent heat of transformation can be expressed as,

$$C_v v_m \frac{dT}{dt} = \frac{V(t)^2}{R_{sma}} + \lambda v_m \frac{d\xi}{dt} - hA_{surf}(T - T_a). \tag{5.5}$$

Here, $V(t)$ is the input voltage, C_v denotes the heat capacity of SMA, R_{sma} stands for the electrical resistance, v_m and A_{surf} represent the volume and surface area of the SMA wire, and λ denotes the latent heat of SMA. Further, h refers to the convective heat transfer coefficient, which has been estimated following the parameter estimation technique, as discussed in Section 5.5.

5.3.3 Kinematic Relations

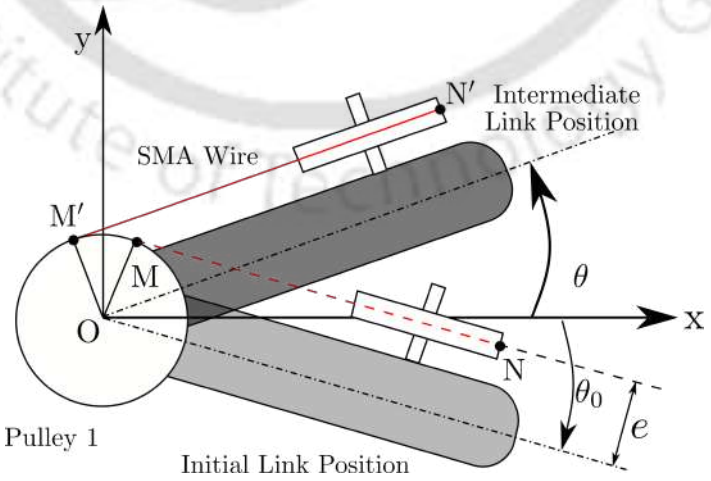

Figure 5.3: Schematic showing the motion of the link in the SMA wire manipulator

Two configurations of the SMA wire actuated manipulator are shown in Fig.5.3. Here, MN and M′N′ represent the SMA wire's initial and an intermediate orientation during actuation, respectively. The link subtends angles of θ_0 and θ with the horizontal axis at its initial and intermediate positions, respectively. With the application of voltage, the SMA wire contracts, pulling the link in the counter-clockwise direction from its initial configuration of MN to M′N′. Here, the contraction in the SMA wire (ΔL) is the same as that of the arc length MM′ and is calculated as,

$$\Delta L = R_p \Delta\theta. \tag{5.6}$$

This can be rewritten as,

$$L_0(1+\varepsilon_0) - L_0(1+\varepsilon) = R_p(\theta - \theta_0), \tag{5.7}$$

where, L_0 is the unstretched length of the SMA wire, R_p denotes the radius of the pulley and ε_0 represents the initial strain. Since the wire is wrapped around both Pulley-1 and Pulley-3, Eqn.(5.7) can be expressed as,

$$L_0(1+\varepsilon_0) - L_0(1+\varepsilon) = 2R_p(\theta - \theta_0). \tag{5.8}$$

Rearranging Eqn.(5.8), the strain in the SMA wire (ε) corresponding to the intermediate position of the link (θ) can be obtained as,

$$\varepsilon = \frac{2R_p}{L_0}(\theta - \theta_0) + \varepsilon_0. \tag{5.9}$$

5.3.4 Equation of Motion

Considering moment equilibrium of the link about the axis of the Pulley-1 or Pulley-3 (refer Fig.5.1a), one gets,

$$I_l\ddot{\theta} + K_\theta(\theta - \theta_0) + c\dot{\theta} + \left(M_p + \frac{M_l}{2}\right) g L_l \cos\theta = \sigma A e. \tag{5.10}$$

Here, I_l denotes the second moment of inertia of the link about point O, K_θ is the torsional stiffness of the spring, c represents the damping coefficient, M_p is the payload mass, M_l refers to the mass of the link, g is the acceleration due to gravity, and L_l stands for the effective length of the link, σ denotes stress in the SMA wire. A is the cross-sectional of the SMA wire, and e refers to the offset distance of the SMA wire from the centre line of the link.

5.3.5 Electrical Resistance of SMA Wire

During actuation, the electrical resistance of the SMA wire varies because of its change in length and cross-sectional area, and due to varying electrical resistivity during phase transformation. This change in electrical resistivity of SMA is modelled as, $\rho = \rho_A + \xi(\Delta\rho)$. Here, $\Delta\rho = (\rho_M - \rho_A)$, where ρ_M and ρ_A denote the electrical resistivities of SMA in complete M-phase and A-phase, respectively. During actuation, the current length of the SMA wire is calculated as, $l_c = l_0(1 + \varepsilon)$. Finally, the electrical resistance of the SMA wire can be expressed as,

$$R_{sma} = \frac{(\rho_A + \xi\ (\Delta\rho))\ \ l_0\ \ (1 + \varepsilon)}{A}. \tag{5.11}$$

The following section discusses the algorithm to simulate the coupled thermo-mechanical response of the manipulator using Eqn.(5.1), Eqn.(5.5), Eqn.(5.9) and Eqn.(5.10).

5.4 Algorithm for the Coupled Thermo-Mechanical Model

The strain (ε) and the current angular position (θ) are calculated from the system kinematics (Eqn.(5.9)) and the equation of motion (Eqn.(5.10)), by utilizing the velocity ($\dot{\theta}$) and acceleration ($\ddot{\theta}$) at the previous converged time step. This requires stress (σ), which alongside the internal material variables (ξ, ε^t) are obtained from the material model (Eqn.(5.1)). The constitutive equation requires the temperature (T) of the wire, which is computed from the heat balance equation (Eqn.(5.5)), which in turn is related

to the change in martensite volume fraction (ξ). This simulation demands an iterative approach, which is explained below in a step-by-step manner and is also illustrated using the flowchart in Fig.5.4.

Step 1: At any time step, t_{n+1}, one assumes at the outset, *i.e.*, iteration number $k = 0$, $T_{n+1}^{(0)} = T_n$, $\sigma_{n+1}^{(0)} = \sigma_n$, $\xi_{n+1}^{(0)} = \xi_n$, $\varepsilon_{n+1}^{t^{(0)}} = \varepsilon_n^t$, $\theta_{n+1}^{(0)} = \theta_n$, and $\dot{\theta}_{n+1}^{(0)} = \dot{\theta}_n$.

Step 2: The equation of motion is solved following Newmark's method [119], based on the trial stress $\sigma_{n+1}^{(k)}$, the link position $\theta_{n+1}^{(k)}$ and velocity $\dot{\theta}_{n+1}^{(k)}$, to obtain the new angular position, $\theta_{n+1}^{(k+1)}$. The detailed description of this iterative scheme is discussed in Section 5.4.1.

Step 3: Subsequently, the corresponding strain $\varepsilon_{n+1}^{(k+1)}$ in the SMA wire is determined from Eqn.(5.9).

Step 4: Simultaneously, the heat balance equation is solved using *ode45* (MATLAB R2021a © MathWorks), for the current voltage input, V_{n+1}, and using the material parameters corresponding to $\xi_{n+1}^{(k)}$, to obtain the new temperature, $T_{n+1}^{(k+1)}$.

Step 5: Next, using the strain ($\varepsilon_{n+1}^{(k+1)}$) and temperature ($T_{n+1}^{(k+1)}$), the corrected stress $\sigma_{n+1}^{(k+1)}$ and the corresponding internal material variables ($\xi_{n+1}^{(k+1)}$, $\varepsilon_{n+1}^{t^{(k+1)}}$), are calculated following return mapping algorithm, discussed in Section 2.5.

Step 6: If $\left|\sigma_{n+1}^{(k+1)} - \sigma_{n+1}^{(k)}\right| < 10^{-6}$, then the iterative procedure is stopped. Else, put $k = k+1$ and follow step-2 to step-6, till convergence criteria is satisfied.

5.4.1 Newmark's Method for Non-Linear Systems

The equation of motion (Eqn.(5.10)) of the link is non-linear in nature and thus necessitates an efficient numerical scheme to obtain a stable and accurate solution. Here, Newmark's method is used to solve the equation of motion, which involves an iterative procedure, wherein the residual force is reduced to zero to satisfy equilibrium [119]. For a single DOF system, having mass, 'm', and damping, 'c', the equation of motion can be

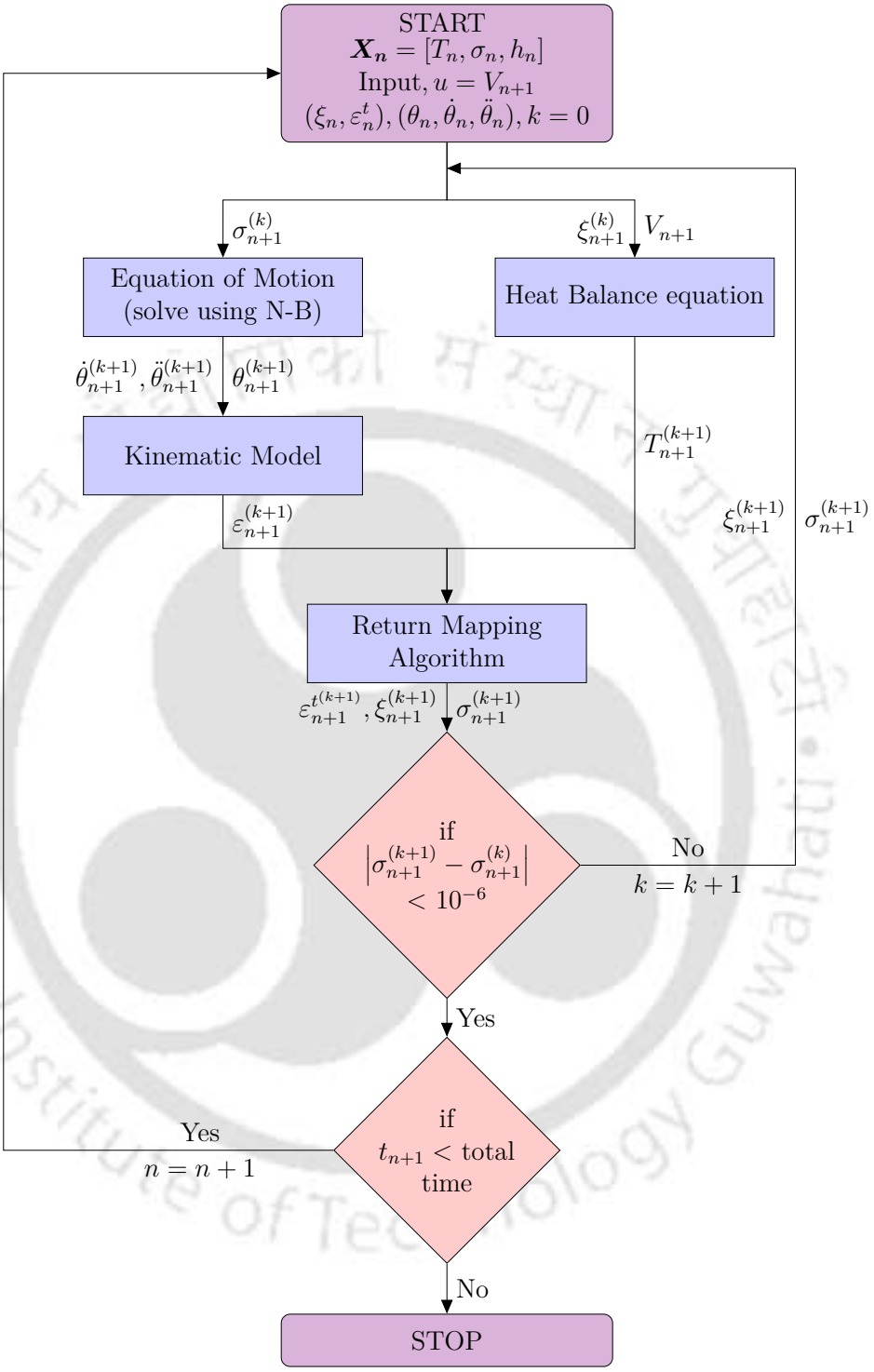

Figure 5.4: Flowchart of the coupled thermo-mechanical model of SMA wire manipulator

written as,

$$m\ddot{u} + c\dot{u} + f_s(u) = p. \tag{5.12}$$

Here, 'p' denotes the external force, and $f_s(u)$ represents the non-linear stiffness force. The residual force $\hat{R}$ at any time instant t_{n+1}, and j^{th} iteration can be expressed as,

$$\hat{R}_{n+1}^{(j)} = \hat{p}_{n+1} - (f_s)_{n+1}^{(j)} - a_1 u_{n+1}^{(j)}, \tag{5.13}$$

where,

$$\hat{p}_{n+1} = p_{n+1} + a_1 u_n + a_2 \dot{u}_n + a_3 \ddot{u}_n, \tag{5.14}$$

$$a_1 = \frac{1}{\beta(\Delta t)^2} m + \frac{\gamma}{\beta \Delta t} c, \tag{5.15}$$

$$a_2 = \frac{1}{\beta \Delta t} m + \left(\frac{\gamma}{\beta} - 1\right) c, \tag{5.16}$$

$$a_3 = \left(\frac{1}{2\beta} - 1\right) m + \Delta t \left(\frac{\gamma}{2\beta} - 1\right) c. \tag{5.17}$$

The displacement, velocity and acceleration of the previously converged time step are utilized as the initial condition for the next time step, *i.e.*, $u_{n+1}^{(0)} = u_n$, $\dot{u}_{n+1}^{(0)} = \dot{u}_n$ and $\ddot{u}_{n+1}^{(0)} = \ddot{u}_n$. The incremental displacement is calculated from the residual force as,

$$\Delta u^{(j)} = \hat{R}_{n+1}^{(j)} \left(\hat{k}_T^{(j)}\right)_{n+1}^{-1}, \tag{5.18}$$

where,

$$\left(\hat{k}_T^{(j)}\right)_{n+1} = \left(k^{(j)}\right)_{n+1} + a_1. \tag{5.19}$$

Here, $\hat{k}_T$ is referred as the tangent stiffness. The displacement and stiffness are updated following,

$$u_{n+1}^{(j+1)} = u_{n+1}^{(j)} + \Delta u^{(j)}, \tag{5.20}$$

$$\left(k^{(j+1)}\right)_{n+1} = \left.\frac{\partial f_s}{\partial u}\right|_{u_{n+1}^{(j+1)}}. \tag{5.21}$$

At each iteration, the residual force is checked, and the iteration is terminated when its value becomes less than a tolerance value. Upon convergence, one obtains the final

displacement, u_{n+1}. Finally, the corresponding velocity and acceleration are determined following,

$$\dot{u}_{n+1} = \frac{\gamma}{\beta\Delta t}\left(u_{n+1} - u_n\right) + \left(1 - \frac{\gamma}{\beta}\right)\dot{u}_n + \Delta t\left(1 - \frac{\gamma}{2\beta}\right)\ddot{u}_n, \tag{5.22}$$

and

$$\ddot{u}_{n+1} = \frac{1}{\beta(\Delta t)^2}\left(u_{n+1} - u_n\right) - \frac{1}{\beta\Delta t}\dot{u}_n + \left(1 - \frac{1}{2\beta}\right)\ddot{u}_n \tag{5.23}$$

respectively. The steps involved in the Newmark's scheme is shown in Algorithm 2.

Algorithm 2: An algorithm for Newmark's method

Input: $\gamma = \frac{1}{2}$, $\beta = \frac{1}{4}$, u_n, $\dot{u}_n$, $\ddot{u}_n$

Initial Calculations: Calculate a_1, a_2, a_3 following Eqns.(5.15), (5.16) and (5.17)

At j=0: Initialize, $u_{n+1}^{(j)} = u_n$, $\dot{u}_{n+1}^{(j)} = \dot{u}_n$, $\ddot{u}_{n+1}^{(j)} = \ddot{u}_n$, $(f_s^{(j)})_{n+1}$ and $(k^{(j)})_{n+1}$, and evaluate $\hat{p}_{n+1}$ and $\hat{R}_{n+1}^{(j)}$ following Eqns.(5.14) and (5.13)

while $\hat{R}_{n+1}^{(j)} > 10^{-6}$ **do**

  Determine $\left(\hat{k}_T^{(j)}\right)_{n+1}$ and $\Delta u^{(j)}$ following Eqns.(5.19) and (5.18)

  Update $u_{n+1}^{(j+1)}$ and $\left(k^{(j+1)}\right)_{n+1}$ using Eqns.(5.20) and (5.21)

  Evaluate $\hat{R}_{n+1}^{(j)}$ following Eqn.(5.13)

end

Final Calculations: Obtain the values of velocity ($\dot{u}_{n+1}$) and acceleration ($\ddot{u}_{n+1}$) from Eqns.(5.22) and (5.23), respectively.

In the following section, a particle filter has been developed, based on the process model comprising of the iterative method presented in Fig.5.4 and Algorithm 2, whereas the measurement model consists of the relation governing the variation of electrical resistance of the SMA wire as presented in Eqn.(5.11).

5.5 State Estimation of SMA Wire Actuated Manipulator

Here, the state vector for the SMA wire actuator comprises of,

$$\boldsymbol{X} = [T \quad \sigma]^T. \tag{5.24}$$

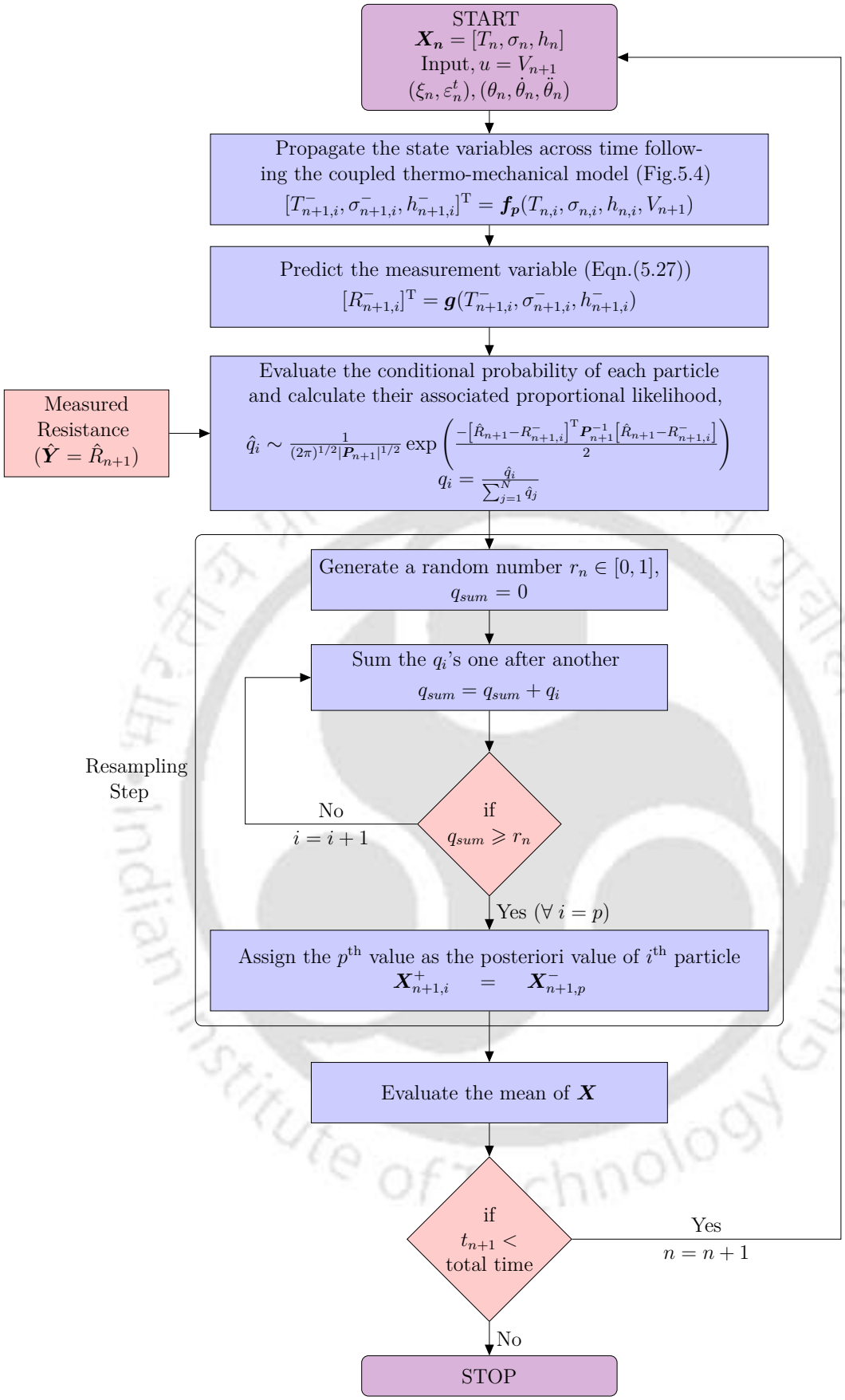

Figure 5.5: Flowchart of the developed PF

Though this approach yields satisfactory estimation for natural convective cooling, under forced or uncontrolled cooling situations, this offers poor estimation, as seen in the case of a linear system in Chapter 4. Since the variation in convective heat transfer coefficient during forced cooling is difficult to mimic, in this study, h is also estimated alongside the state of the SMA wire actuator using the PF. In that case, the modified state vector is expressed as,

$$\boldsymbol{X} = [T \quad \sigma \quad h]^T. \tag{5.25}$$

Following the discussion in Section 4.3.1, one can infer that at any instant t_{n+1}, the present state of the system $\boldsymbol{X}_{n+1} = [T_{n+1}, \sigma_{n+1}, h_{n+1}]^T$ can be estimated from the previous state $\boldsymbol{X}_n = [T_n, \sigma_n, h_n]^T$ and the present input $\boldsymbol{u}_{n+1} = V_{n+1}$, by employing the process model, *i.e.*, by solving Eqns.(5.1), (5.5) and (5.10), following the algorithm discussed in Section 5.4. Additionally, the heat transfer coefficient at t_{n+1} is modelled as,

$$h_{n+1} = h_n + \zeta_{n+1}, \tag{5.26}$$

where, $\zeta_{n+1} \sim (0, \boldsymbol{B}_{n+1})$ is a white Gaussian noise with covariance $\boldsymbol{B}_{n+1}$. In this application, the angular position of the link (θ) needs to be estimated from the variation of electrical resistance of SMA (R_{sma}). Hence, the measurement model is defined as, $\boldsymbol{Y} = R_{sma}$. Following Eqn.(5.11), the non-linear measurement model $\boldsymbol{g}$ can be expressed as,

$$\boldsymbol{g} = \frac{(\rho_A + \xi_{n+1}\,(\Delta\rho))\;\; l_0 \;\; (1 + \varepsilon_{n+1})}{A}. \tag{5.27}$$

The flowchart illustrating the steps involved in the proposed PF is presented in Fig.5.5.

5.6 Experimental Details

To study the effectiveness of the developed PF model, an experimental setup is developed, as shown in Fig.5.6. It comprises of the SMA wire actuated single DOF manipulator, a real-time controller NI cRIO-9025, a DC power supply from Agilent 6642A, a voltage divider circuit, a fan for external cooling, a rotary encoder and a force sensor. Except for the encoder and the force sensor, the other components of the experimental setup are

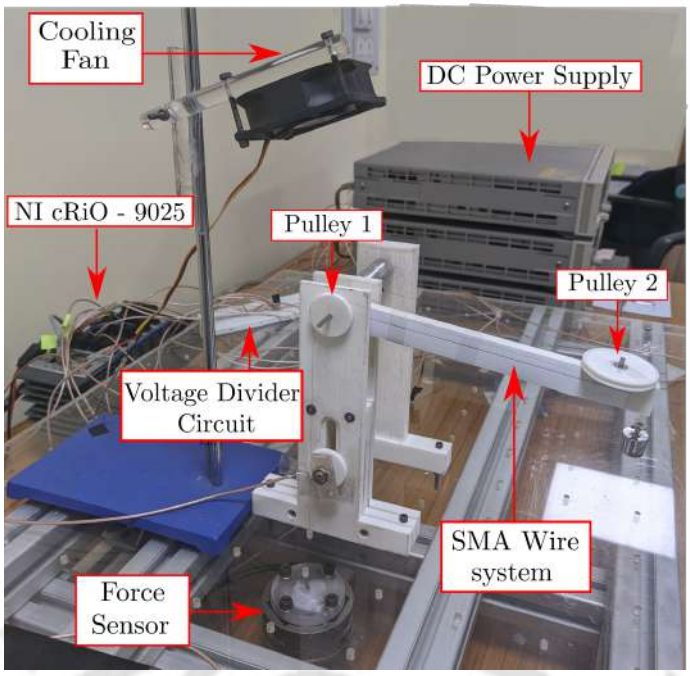

Figure 5.6: Experimental setup developed for the SMA wire actuated 1-DOF manipulator.

introduced in Sections 3.8 and Section 4.7. A detailed description of the manipulator, the encoder and the force sensor are provided below.

- **1-DOF SMA wire actuated manipulator:** Figures 5.6 and 5.7 show the SMA wire actuated rotary manipulator. It comprises a 720 mm long SMA wire with a diameter of 125 μm, wound over a set of three pulleys. The wire is held parallel to the link, as seen in the figure. Pulley 2 is held in a manner such that its axis is always perpendicular to the rotating link, and the Pulley 3 is placed in an axis that is parallel to the base, as shown in Fig.5.7. Pulley 1, shown in Fig.5.6, is held on the same axis as that of Pulley 3, but is on the other side of the link. A torsional spring is attached between the link and vertical support, rendering the bias force on the SMA wire. With the application of a voltage across the SMA wire, the temperature of the wire increases, rotating the link in the $+\theta$ direction, thus lifting the payload mass (M_p). As the voltage drops, the bias spring and the payload mass help the link return to its initial configuration. The encoder is connected to the axis of Pulleys 1 and 3, to measure the angle of rotation of the link.

- **Rotary Encoder:** A rotary encoder JT22-320-500 from Nidec Copal Electronics

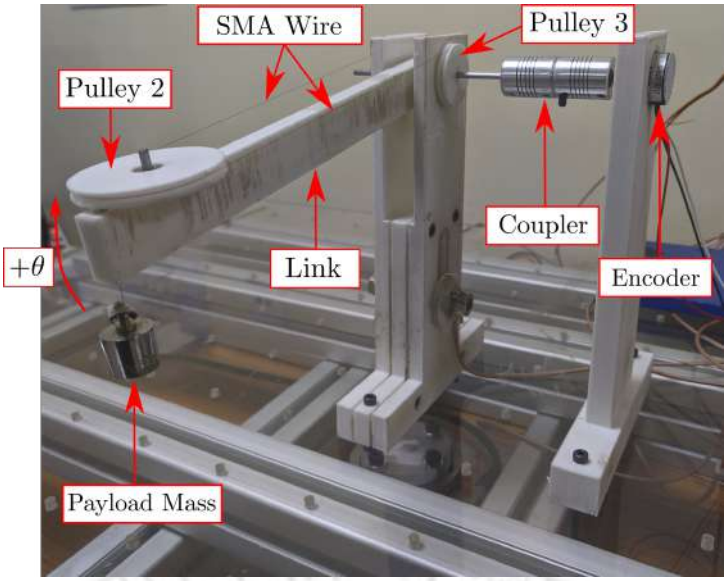

Figure 5.7: SMA wire actuated 1-DOF manipulator.

(refer to Fig.5.8) is used to measure the angle of rotation of the link. A DC power supply (Agilent 6642A) provides the required input voltage of 5V. It has an effective measuring range of $0° - 320°$, which is linearly proportional to the output voltage of $0.5\text{V} - 4.5\text{V}$. When the link rotates, the motion is transmitted to the shaft of the rotary encoder, yielding a change in the output voltage, which is acquired by NI 9219. The corresponding angle of rotation is calculated following,

$$\theta = 80(V_{out}^r - V_i^r), \tag{5.28}$$

where, V_{out}^r and V_i^r are the measured output voltages corresponding to angle 'θ' and the initial position of the link, 'θ_i'.

Figure 5.8: Rotary Encoder.

- **Force Sensor:** Figure 5.9 shows Gamma-SI-65-5, a 6-axis force sensor from ATI. It is kept directly below the manipulator to measure force in the SMA wire. The sensor is powered by another DC power supply (Agilent 6642A). The sensor yields six analog voltage signals, from which the three force and the three moment components are calculated using the calibration matrix. The analog voltage signals are acquired using NI 9219, and the force along the SMA wire is obtained. In the present system, the force sensor is kept in a manner, such that only the z-component of the force represents the same acting on the SMA wire.

Figure 5.9: Force sensor.

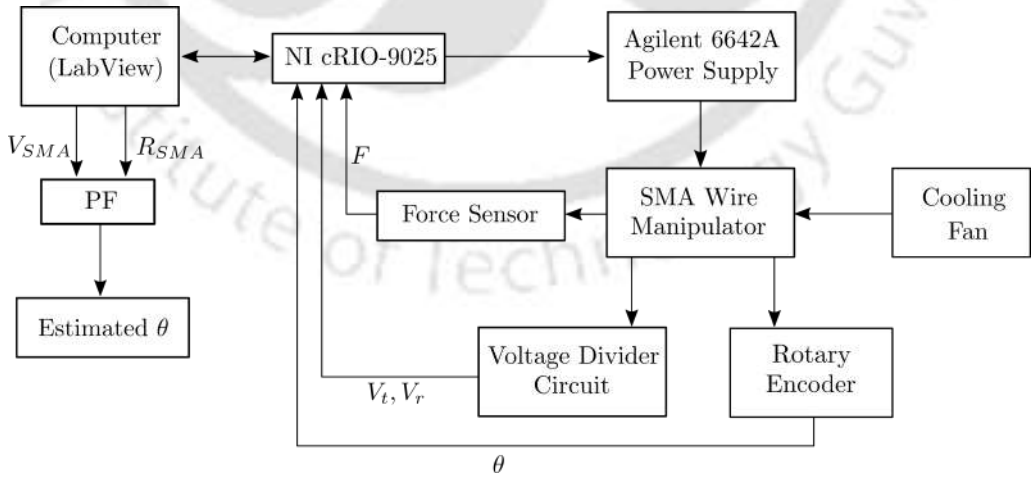

Figure 5.10: Schematic representation of entire procedure

A set of voltage input signals are designed in LabVIEW 2019, then amplified by another DC programmable power supply (Agilent 6642A), and is applied across the SMA

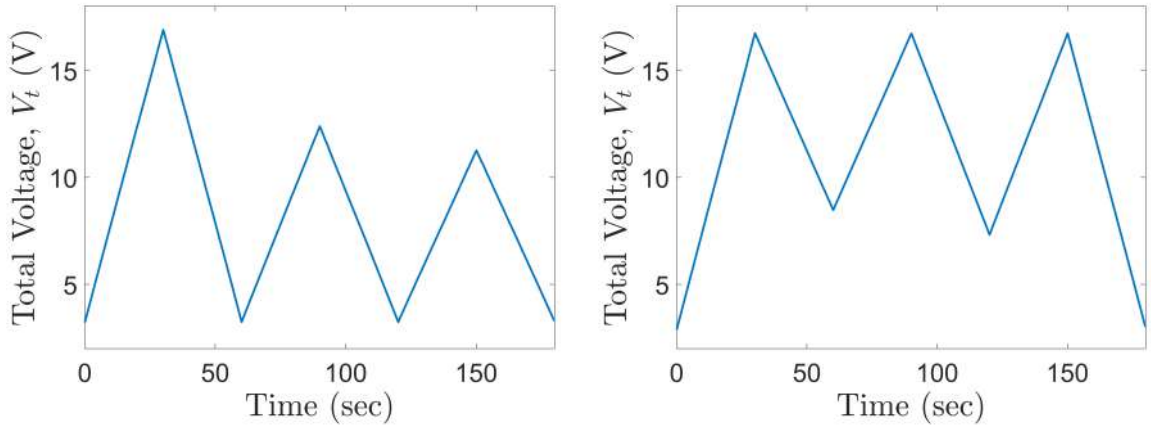

Figure 5.11: Total voltage applied across the SMA wire actuated manipulator, when subjected to, (a) partial heating, and (b) partial cooling condition.

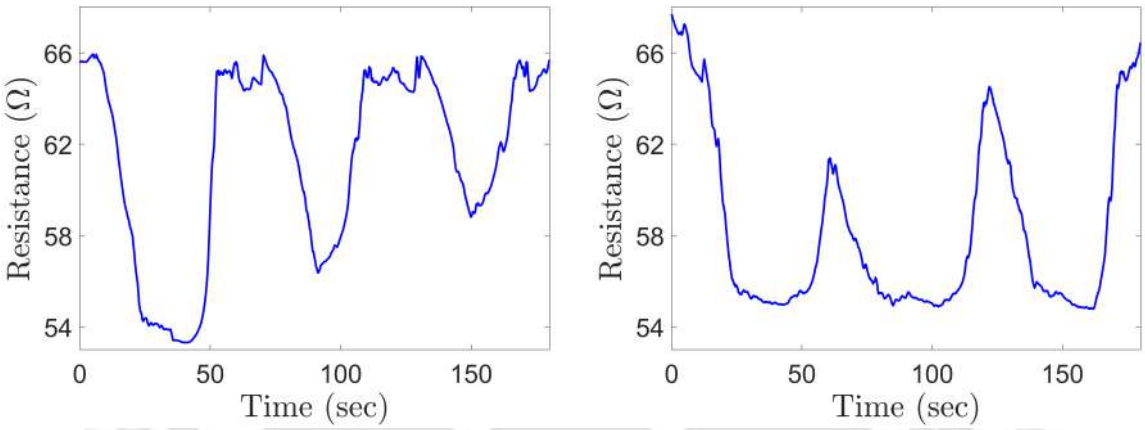

Figure 5.12: Measured electrical resistance of SMA wire, in case of, (a) partial heating, and (b) partial cooling.

wire and fixed resistor $R_0 = 5\Omega$. The NI cRIO-9025, a real-time controller, is engaged to control and acquire the I/P-O/P signals. The schematic of the entire experimental procedure is presented in Fig.5.10. Figures 5.11a and 5.11b illustrate the two triangular voltage inputs, applied across the SMA wire to actuate the link of the manipulator. These are designed so as to achieve partial phase transformations in the SMA wire during heating and cooling, and are referred to as partial heating and partial cooling cases, respectively. Upon application of the voltage signals, the temperature of the SMA wire increases, which in turn actuates the payload mass and is manifested by the rotation of the link. The corresponding variation in the electrical resistance of the SMA wire is measured using

	Max/Min Response	Transient Response
$t_c = 1s$	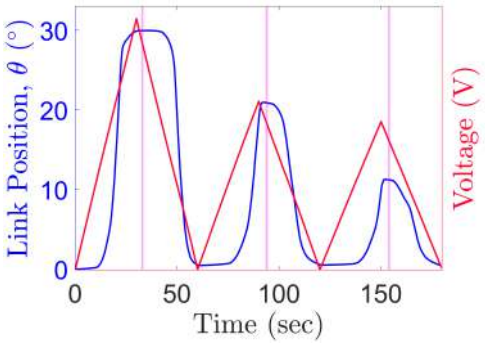 Case PH(NL)-I	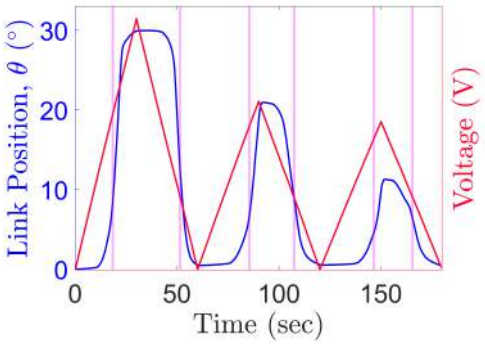 Case PH(NL)-IV
$t_c = 3s$	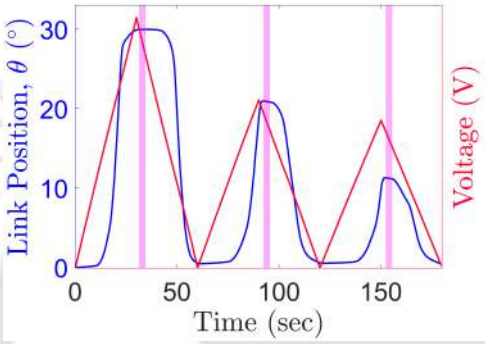 Case PH(NL)-II	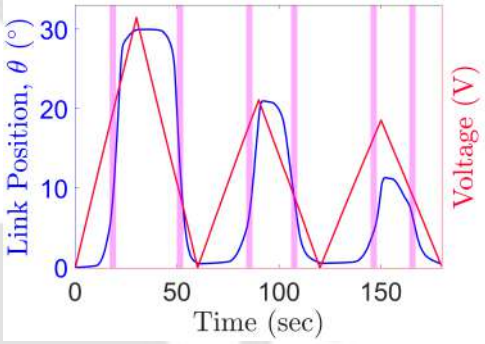 Case PH(NL)-V
$t_c = 5s$	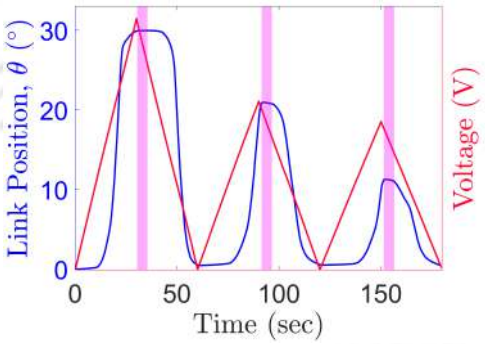 Case PH(NL)-III	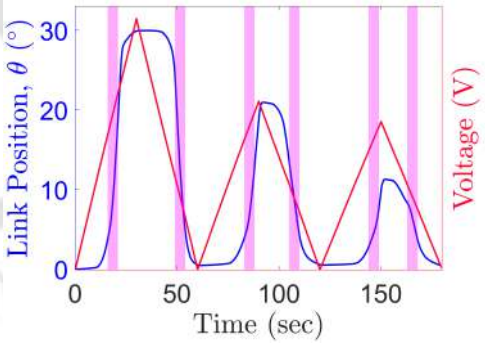 Case PH(NL)-VI

Table 5.1: Location and duration of forced cooling during partial heating case, shown with respect to the response of the system under natural cooling

	Max/Min Response	Transient Response
$t_c = 1s$	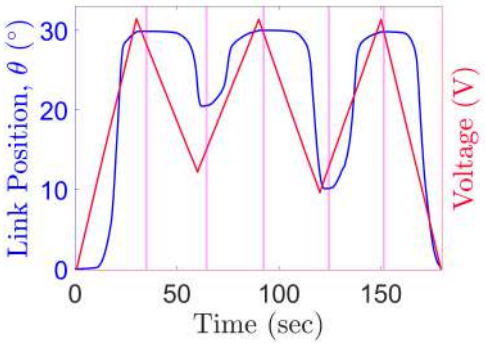 Case PC(NL)-I	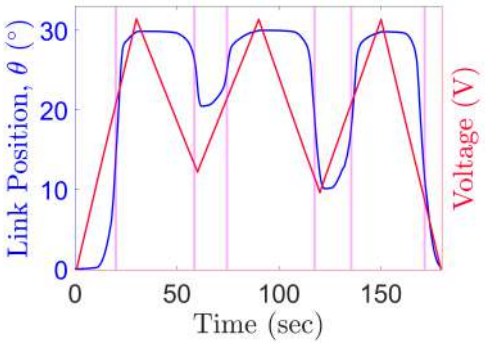 Case PC(NL)-IV
$t_c = 3s$	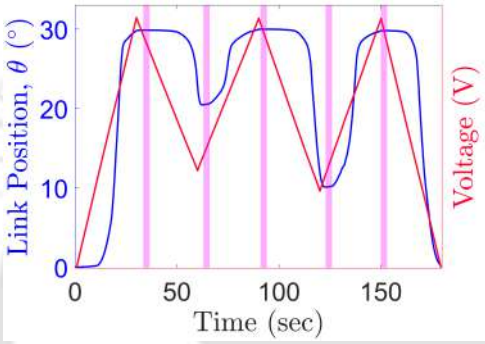 Case PC(NL)-II	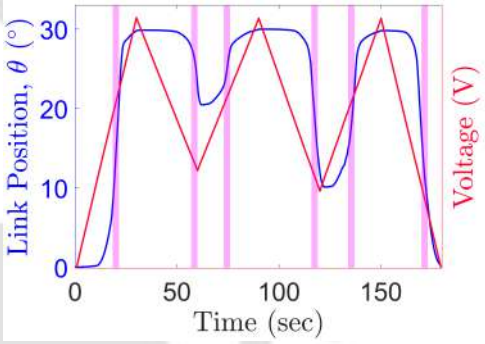 Case PC(NL)-V
$t_c = 5s$	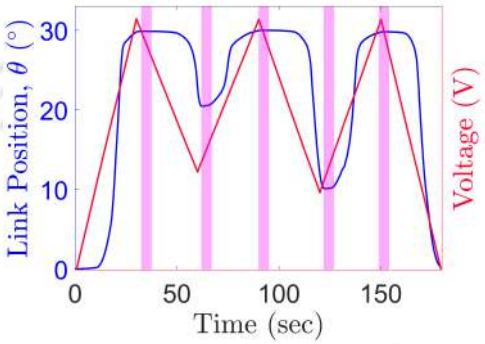 Case PC(NL)-III	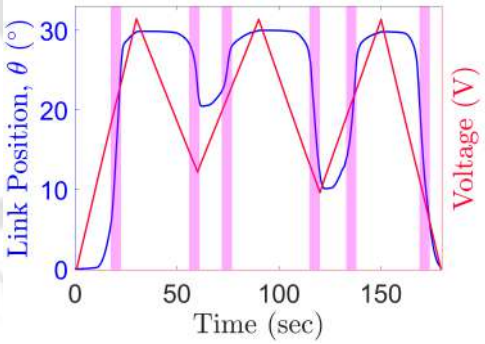 Case PC(NL)-VI

Table 5.2: Location and duration of forced cooling during partial cooling case, shown with respect to the response of the system under natural cooling

the voltage-divider circuit following Eqn.(3.51) and are shown in Fig.5.12. Next, using R_{sma} as the measured data and V_{SMA} as input data, the angle of rotation of the link is evaluated by using the developed filter and is compared against the one obtained from the encoder.

Another set of experiments are performed for the same set of voltage inputs to evaluate the proposed PF's performance under forced cooling conditions. The SMA wire is intermittently cooled by using a 12V/0.17A DC brush-less fan (shown in Fig.5.6), to simulate forced cooling situations. The fan is powered by another DC power supply and is controlled by the NI cRIO. Here, Tables 5.1 and 5.2 represent the diverse set of forced cooling test cases performed in this study, when the SMA wire actuated manipulator actuates under partial heating (Fig.5.11a) and partial cooling (Fig.5.11b) conditions, respectively. In the tables, the shaded regions illustrate the time durations where the forced cooling is introduced and are superposed over the response of the SMA wire actuated manipulator under the same voltage but under natural cooling conditions. Three aspects of forced cooling, that generally affect the SMA wire actuators' response, are investigated in this study. The first is the duration of cooling, the second is the state of SMA during cooling, and the third is the magnitude or intensity of cooling. In the 1^{st} case, the fan is kept ON for increasing time-spans (t_c) of 1s, 3s and 5s to simulate the effects of small, medium and large cooling durations. They are represented along the rows of Tables 5.1 and 5.2. The second factor is considered by introducing cooling at two different stages of the SMA actuation process, namely, (i) while the response is at its maximum or minimum, and (ii) while the response is in the transient state, and are presented along the columns of Tables 5.1 and 5.2. To mimic various cooling intensities, the fan is operated at three voltage levels of 4V, 8V and 12V, and the corresponding speeds of rotation are measured to be 860 rpm, 1778 rpm and 2637 rpm, respectively. They are dubbed as *low level*, *medium level* and *high level* of cooling, respectively, in this study. For each of these cases, the corresponding angle of rotation of the link is obtained from the encoder and are compared against the PF estimated responses, and are presented in the next section.

5.7 Results and Discussions

Here, three sets of test cases have been studied. In the first one, the system actuates under natural convection, whereas, the same is subjected to forced cooling in the second one. The link orientation estimated from the developed PF is compared against the same obtained experimentally. Finally, the performance of the proposed filter in non-proportional loading condition has also been examined and discussed.

5.7.1 Natural Cooling Case

Table 5.3: Geometric Parameters of manipulator system

Parameter	Value	Parameter	Value
M_l	34.43×10^{-3} Kg	M_p	20×10^{-3} Kg
L_l	0.21 m	e	0.014 m
I_l	5.06×10^{-4} Kg m^4	K_θ	0.0201 N m rad^{-1}
c	0.01 N m s rad^{-1}	g	9.81 m s^{-2}
L_0	0.728 m	R_p	0.0125 m

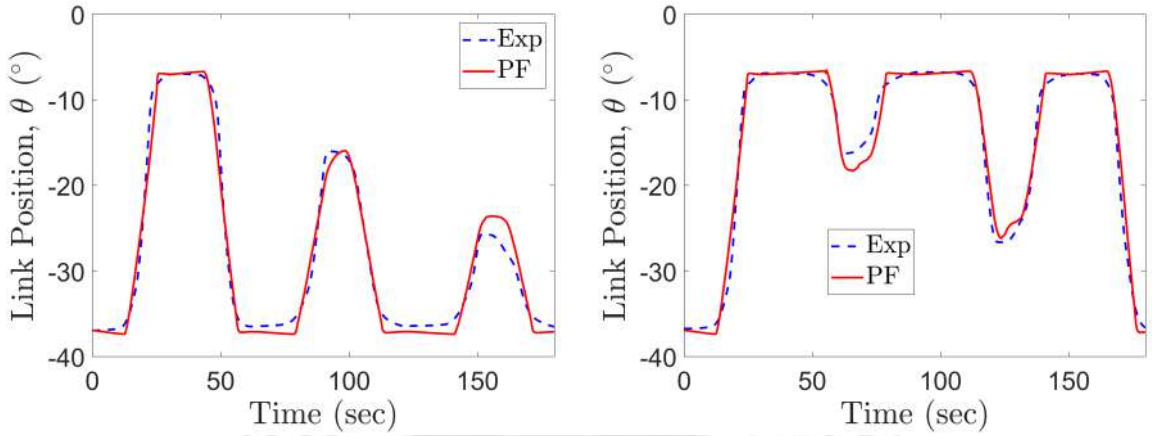

Figure 5.13: Comparison among the angle of rotation estimated by the PF and the experimental one for (a) partial heating, and (b) partial cooling loading case, under natural cooling.

In this case, the entire setup is kept inside a large transparent chamber, to avoid any form of unwanted forced cooling. Also, the cooling fan is switched OFF during this set of experiments. Using the voltage signals, depicted in Figs.5.11a and 5.11b as inputs and the corresponding measured electrical resistance of the SMA wire as the measured data, the

orientation of the link as estimated from the proposed PF, are shown in Fig.5.13. Here, the state vector illustrated in Eqn.(5.24) is used in the PF. The geometric parameters of the manipulator are detailed in Table 5.3, and the material properties of the SMA wire are reported in Table 4.3. Here, the manipulator is held at an initial orientation of $\theta = -37°$. As seen in Fig.5.13a, upon heating, the SMA wire contracts, lifting the payload mass. This rotates the link in the counter-clockwise direction, with the full transformation concluding at $\theta = -7°$. With decrement in applied voltage, the SMA wire cools due to natural cooling, and the biasing force applied by the spring and payload mass restores the link to its original configuration. Next, the wire is partially heated with voltage signals of decreasing magnitudes. A similar study was carried out, wherein the SMA wire is partially cooled for increasing magnitudes and then heated back to attain the highest link orientation ($\theta = -7°$), shown in Fig.5.13b. The orientation of the link estimated by the PF are also shown in the same figures. Here one can observe that the proposed filter has estimated the response with remarkable accuracy, during both partial heating and cooling cases. The estimation errors in the case of the filter are quantified using the following definition of RMS error.

$$\epsilon_{RMS} = \frac{\sum_{i=1}^{n} (\theta_{est}(t_i) - \theta_{exp}(t_i))^2}{n}. \tag{5.29}$$

Here, θ_{est} and θ_{exp} denote the link position estimated by the filter and the same obtained experimentally, at any time instant t_i, and n refers to the total time steps. Here, a maximum error of approximately 10% of the complete span of rotation of the link (θ_{span},) is observed. The RMS error is found to be 4.75% of θ_{span}, thus demonstrating the efficacy of the proposed PF in natural cooling conditions.

5.7.2 Forced Cooling Cases

Figures 5.11a and 5.11b depict the input voltage signals employed across the SMA wire to actuate the manipulator illustrated in Fig.5.7. With an increment in applied voltage, the temperature of the SMA wire increases, rotating the link counter-clockwise by an angle, θ. During the rotation, the SMA wire is cooled by means of forced convection with

varying magnitudes, durations, and at different stages of actuation. During cooling, the temperature of the SMA wire reduces abruptly, resulting in a drop in the level of actuation. The accompanying variation in electrical resistance is harnessed to estimate the position of the link using both the simple PF (using state vector presented in Eqn.(5.24)) and the modified PF (with state vector shown in Eqn.(5.25)), following the procedure discussed in Section 5.5. The link orientation estimated by the filters is compared against the same obtained from the encoder, and is presented below. Here, the simple PF and the modified PF are referred to as 'PF' (shown in green) and 'PF(PE)' (illustrated in red), respectively, in the subsequent figures.

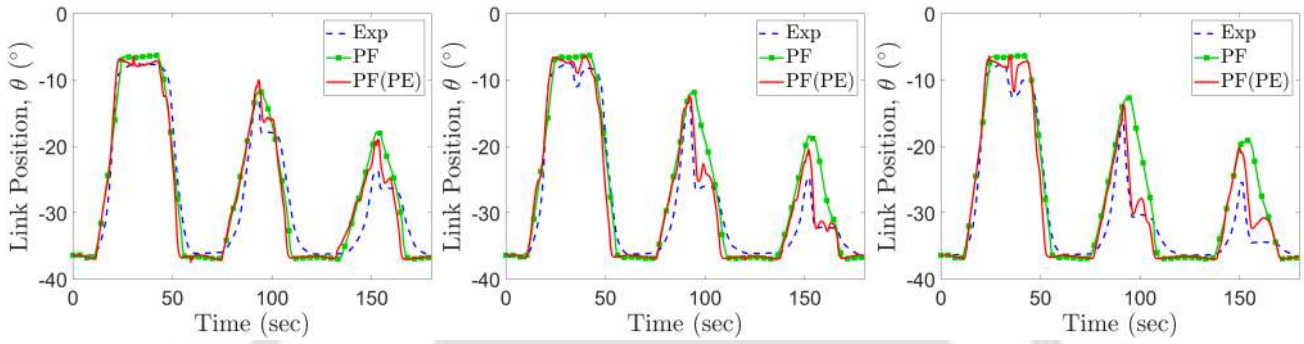

(a) (b) (c)

Figure 5.14: Angular position of the link estimated using the simple PF, the modified PF and the measured one, corresponding to (a) PH(*NL*)-I, (b) PH(*NL*)-II, and (c) PH(*NL*)-III, subjected to *High level* forced cooling.

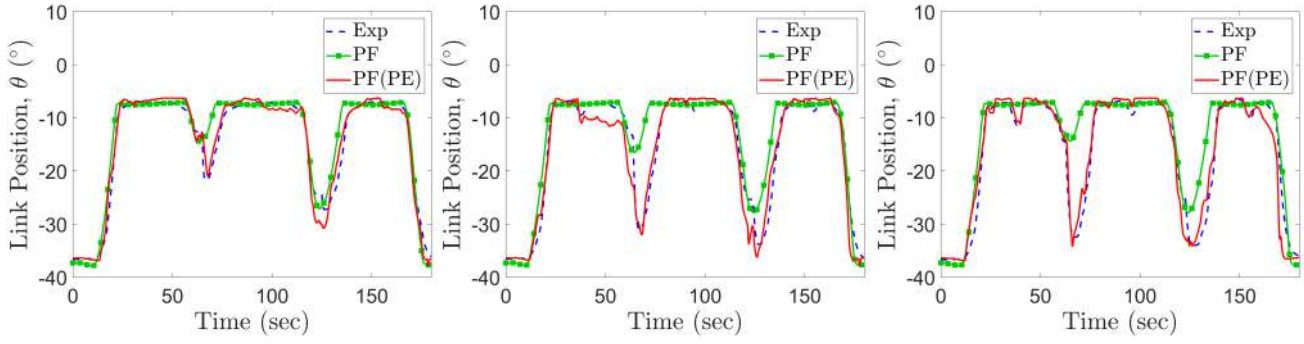

(a) (b) (c)

Figure 5.15: Angular position of the link estimated using the simple PF, the modified PF and the experimental one, corresponding to (a) PC(*NL*)-I, (b) PC(*NL*)-II, and (c) PC(*NL*)-III, subjected to *High level* forced cooling.

Forced cooling experiments, referred to as PH(*NL*)-I, PH(*NL*)-II and PH(*NL*)-III in Table 5.1, and PC(*NL*)-I, PC(*NL*)-II and PC(*NL*)-III in Table 5.2, are carried out to

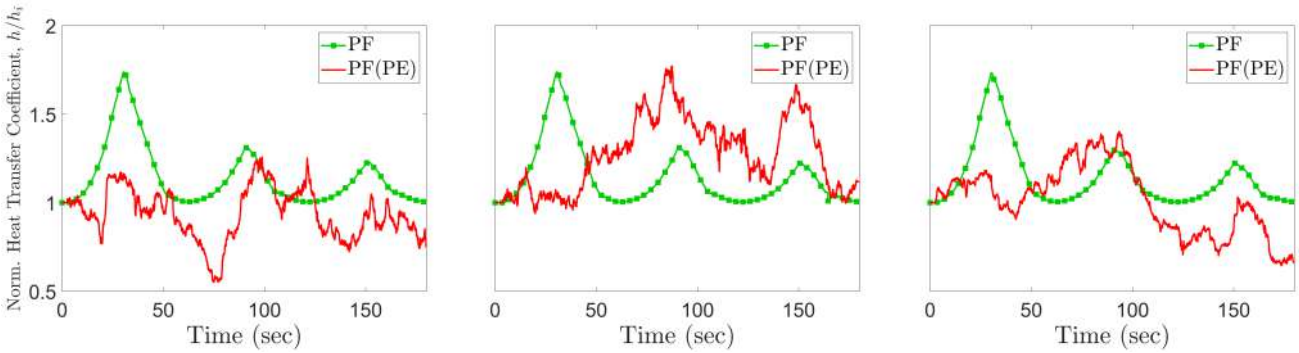

(a) (b) (c)

Figure 5.16: Normalized h of the simple PF and the same estimated by modified PF, corresponding to (a) PH(NL)-I, (b) PH(NL)-II, and (c) PH(NL)-III, subjected to *high level* forced cooling.

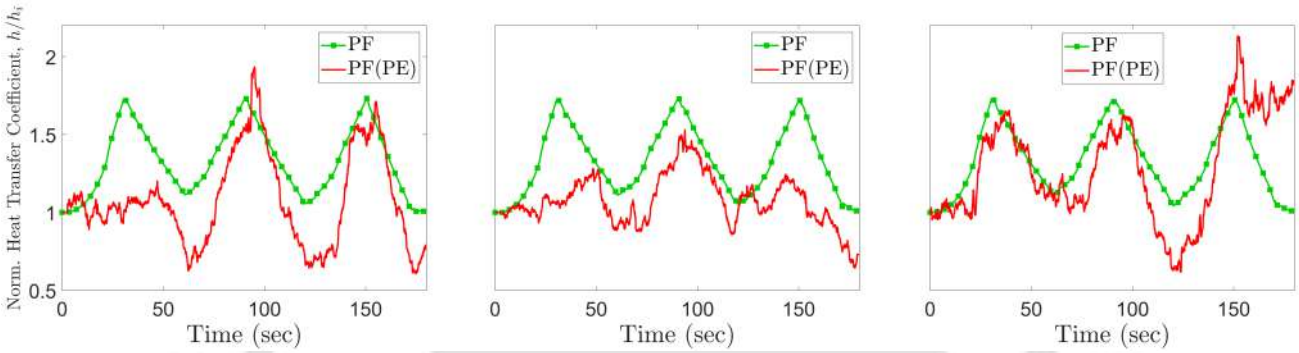

(a) (b) (c)

Figure 5.17: Normalized h of the simple PF and the same estimated by modified PF, corresponding to (a) PC(NL)-I, (b) PC(NL)-II, and (c) PC(NL)-III, subjected to *high level* forced cooling.

evaluate the performance of the proposed filters, and are depicted in Figs.5.14 and 5.15, respectively. During these experiments, the fan is switched ON at maximum speed, denoted as *high level* cooling. The responses of the manipulator are estimated by both the simple and the modified particle filters, and are compared with the corresponding experimental responses and are presented in the same figure. Sub-figures (a), (b), and (c) depict the system's response for increasing cooling periods of 1s, 3s and 5s, respectively. In the case of the simple PF, the value of h has been considered as a quadratic function of temperature (Eqn.(3.11)). In the modified approach, the value of h is estimated by the modified PF. The corresponding changes in the values of h obtained from both filters are shown in Figs. 5.16 and 5.17, respectively. Here, the value of h is normalized against the assumed initial value, h_i.

Cooling case	RMS Error		Maximum Error	
	Simple PF	**Modified PF**	**Simple PF**	**Modified PF**
PH(NL)-I (High)	3.338° (11.13% of θ_{span})	3.120° (10.41% of θ_{span})	10.714° (35.73% of θ_{span})	9.503° (31.71% of θ_{span})
PH(NL)-II (High)	3.989° (13.30% of θ_{span})	2.899° (9.67% of θ_{span})	13.486° (44.98% of θ_{span})	8.759° (29.23% of θ_{span})
PH(NL)-III (High)	4.768° (15.90% of θ_{span})	2.982° (9.95% of θ_{span})	15.572° (51.94% of θ_{span})	9.205° (30.71% of θ_{span})
PC(NL)-I (High)	2.930° (9.77% of θ_{span})	1.727° (5.76% of θ_{span})	10.030° (33.45% of θ_{span})	5.705° (19.03% of θ_{span})
PC(NL)-II (High)	4.881° (16.28% of θ_{span})	2.598° (8.67% of θ_{span})	13.657° (45.55% of θ_{span})	9.449° (31.53% of θ_{span})
PC(NL)-III (High)	5.959° (19.87% of θ_{span})	2.807° (9.36% of θ_{span})	15.254° (50.88% of θ_{span})	10.707° (35.73% of θ_{span})

Table 5.4: Maximum and RMS errors for the simple PF and modified PF undergoing forced cooling cases PH(NL)-I, PH(NL)-II, PH(NL)-III, PC(NL)-I, PC(NL)-II and PC(NL)-III.

Here, one can observe that the modified PF provides a much superior estimate than the simple PF. The modified PF shows a higher drop in the generated actuation, particularly in the forced cooling regions, and it captures the response with higher accuracy. The inaccuracy observed in the case of simple PF may be ascribed to the polynomial model of the heat transfer coefficient (Eqn.(3.11)), which doesn't take into account the sudden modification in the value of h when subjected to forced cooling, and is evident in Figs. 5.16 and 5.17. The RMS errors in the case of each of the filters are evaluated using Eqn.5.29. Table 5.4 illustrates the RMS and maximum errors for the simple PF and modified PF for the aforestated six *high level* forced cooling cases. The errors are expressed as a percentage of the total span of rotation, θ_{span}. Here, the modified PF has a significantly lower computational error compared to that of the simple PF, across all cases. For partial heating (PH(NL)-I, PH(NL)-II and PH(NL)-III), the modified PF has an RMS error of around 9% of the complete span of link rotation (θ_{span}) compared to 16% of θ_{span} in case of the simple PF. During partial cooling conditions (PC(NL)-I, PC(NL)-II, PC(NL)-III), the RMS error of the modified PF and simple PF are around 6-9% of θ_{span} and 16-19%

of θ_{span}, respectively. One can also observe that the simple PF has comparatively lower estimation error during 1s (PH(NL)-I, PC(NL)-I) forced cooling as compared to prolonged cooling cases, although modified PF has a lower error in all cases. This lower error at 1s cooling may be due to the lesser change in the actual value of heat transfer coefficient h. Hence, in the case of 1s cooling, the divergence in the estimated response for the simple and the modified PF will be less. However, when the system is subjected to prolonged cooling, a significant change in heat transfer will occur, which is being estimated by the modified PF based on the change in R_{sma}, and therein corrects the estimated response; the same is not possible in the case of regular PF which follows a pre-defined polynomial of h (Eqn.(3.11)). Hence, for the remaining part of this study, the modified PF has been utilized to estimate the link position of the SMA wire actuated manipulator, while subjected to forced cooling.

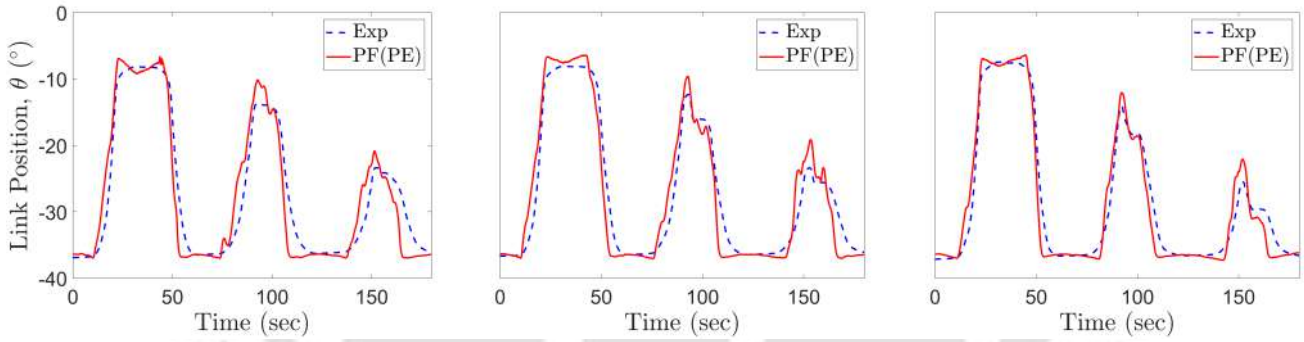

Figure 5.18: Angular position of the link estimated using the modified PF and the experimental one, corresponding to (a) PH(NL)-I, (b) PH(NL)-II, and (c) PH(NL)-III, subjected to *Low level* forced cooling.

For the applied voltage signal depicted in Fig.5.11a, the estimated link positions obtained using the modified PF, as compared to the experimental one, are illustrated in Figs. 5.18 and 5.19 for *low level* and *medium level* forced cooling cases, respectively. The system response for the cooling intervals of 1s, 3s and 5s, dubbed as cases PH(NL)-I, PH(NL)-II and PH(NL)-III, in Table 5.1 are depicted as the sub-figures (a), (b) and (c), respectively. Here, the link position predicted by the modified PF is qualitatively following the measured response, across all forced cooling cases. The maximum estimation error is found to be below 10% except for a few instances. The corresponding estimated

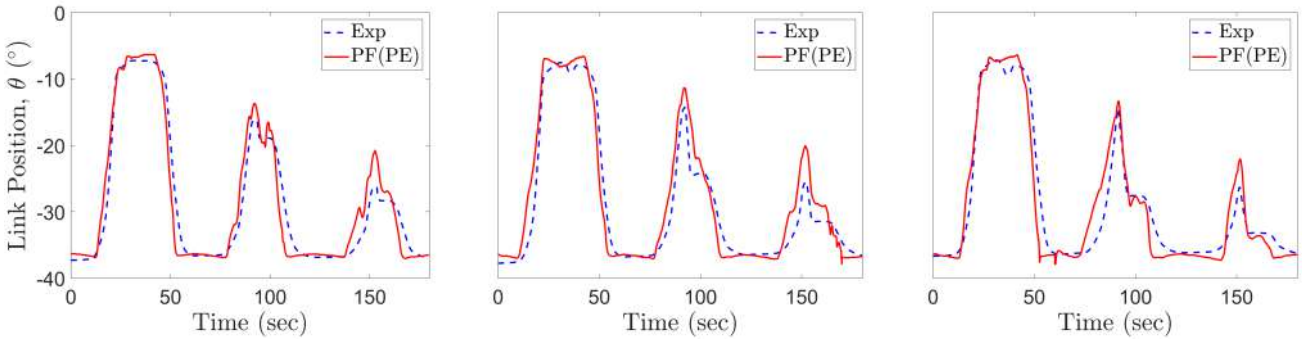

(a) (b) (c)

Figure 5.19: Angular position of the link estimated using the modified PF and the experimental one, corresponding to (a) PH(*NL*)-I, (b) PH(*NL*)-II, and (c) PH(*NL*)-III, subjected to *Medium level* forced cooling.

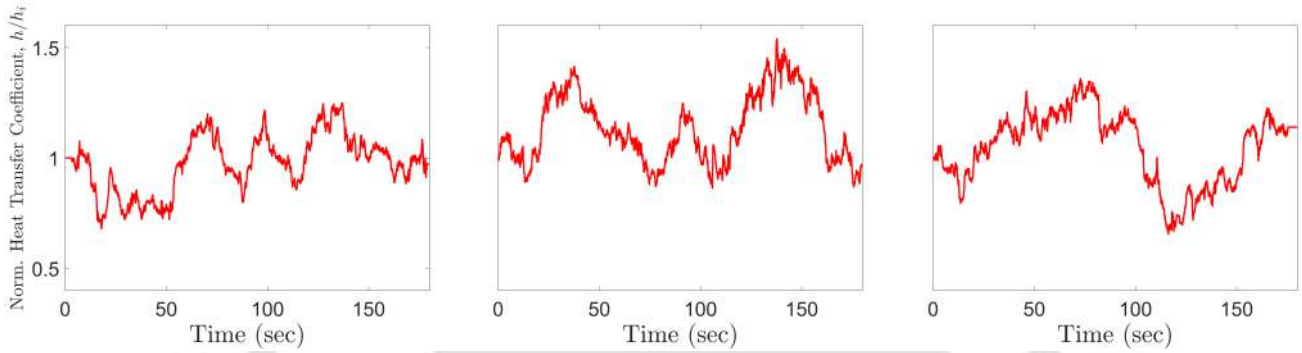

(a) (b) (c)

Figure 5.20: Normalized h estimated by the modified PF, corresponding to (a) PH(*NL*)-I, (b) PH(*NL*)-II, and (c) PH(*NL*)-III, subjected to *low level* forced cooling.

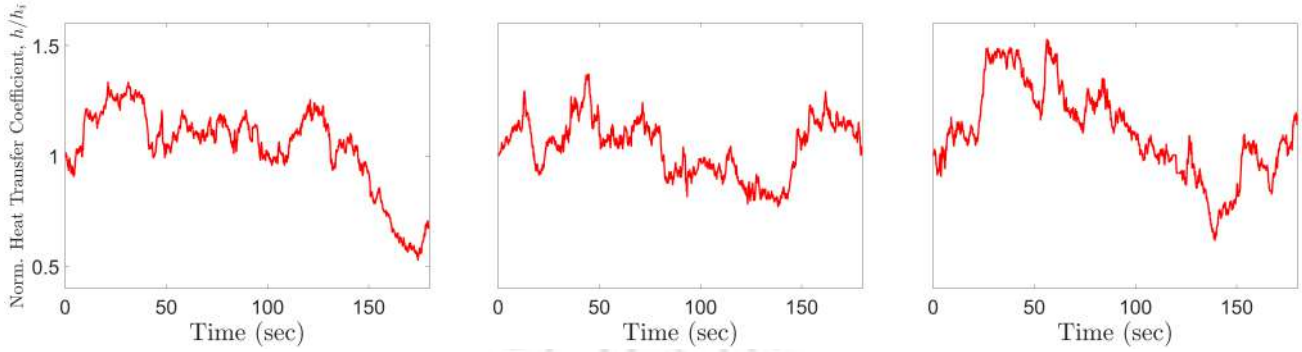

(a) (b) (c)

Figure 5.21: Normalized h estimated by the modified PF, corresponding to (a) PH(*NL*)-I, (b) PH(*NL*)-II, and (c) PH(*NL*)-III, subjected to *medium level* forced cooling.

heat transfer coefficients (h) are depicted in Figs. 5.20 and 5.21, respectively. Here, one can notice the rapid variation in the estimated value of h in regions where forced cooling is introduced. Up to 50% change in the value of h, has been observed.

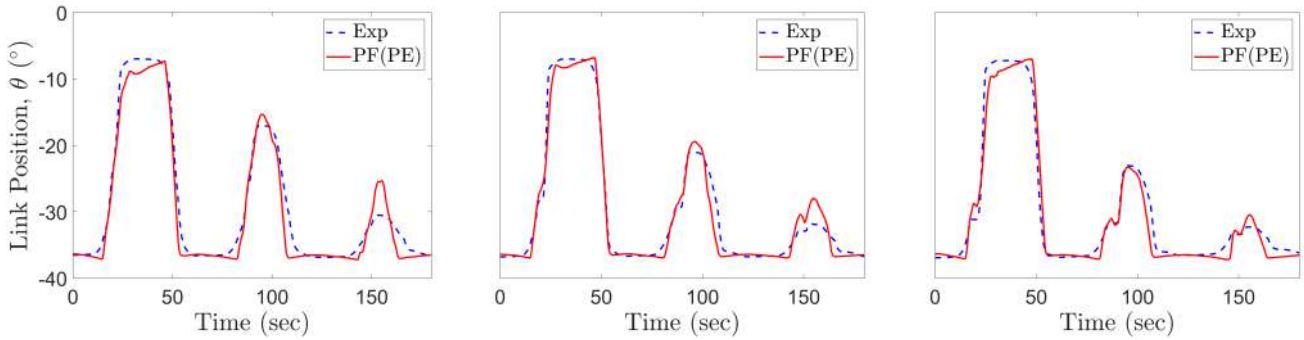

(a) (b) (c)

Figure 5.22: Angular position of the link estimated using the modified PF and the experimental one, corresponding to (a) PH(*NL*)-IV, (b) PH(*NL*)-V, and (c) PH(*NL*)-VI, subjected to *Low level* forced cooling.

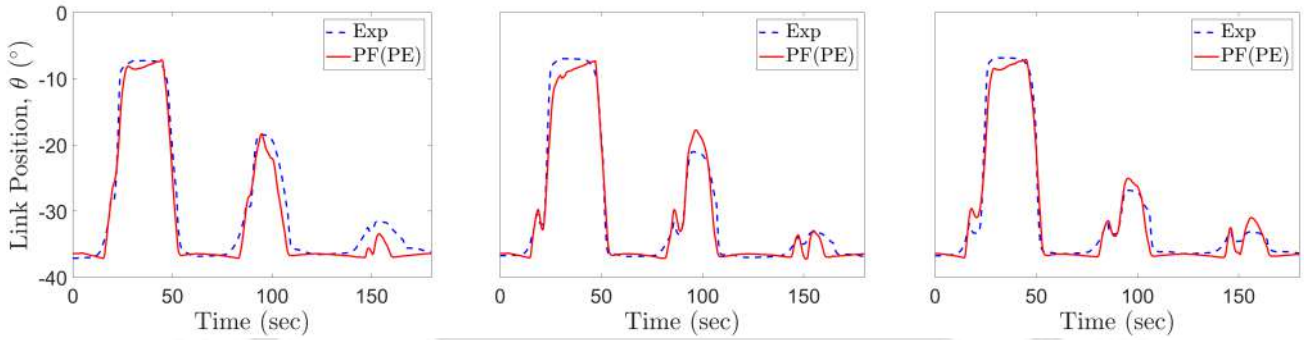

(a) (b) (c)

Figure 5.23: Angular position of the link estimated using the modified PF and the experimental one, corresponding to (a) PH(*NL*)-IV, (b) PH(*NL*)-V, and (c) PH(*NL*)-VI, subjected to *Medium level* forced cooling cases.

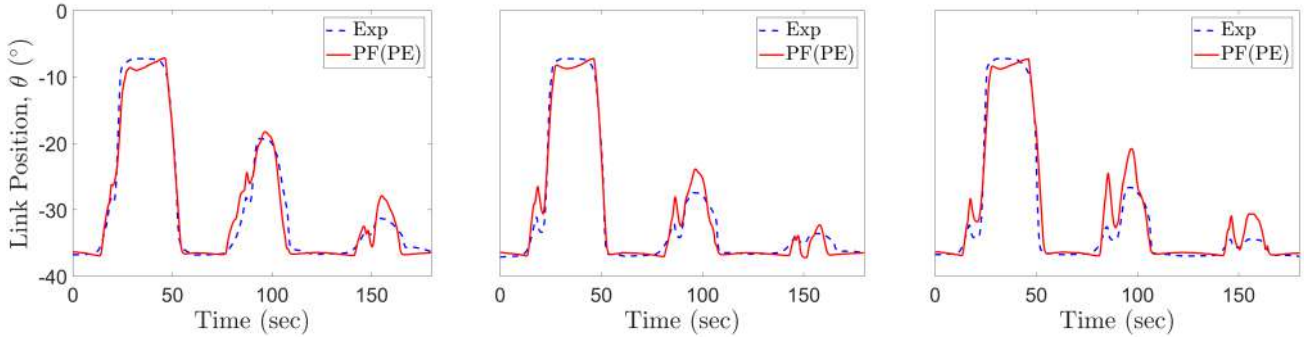

(a) (b) (c)

Figure 5.24: Angular position of the link estimated using the modified PF and the experimental one, corresponding to (a) PH(*NL*)-IV, (b) PH(*NL*)-V, and (c) PH(*NL*)-VI, subjected to *High level* forced cooling.

Figures 5.22, 5.23 and 5.24 illustrate the estimated link position for *low level*, *medium level* and *high level* cooling cases, respectively. Here, the forced cooling is introduced dur-

ing the transient portion of the response, depicted as cooling cases PH(NL)-IV, PH(NL)-V and PH(NL)-VI, in Table 5.1. The estimation of h reveals swift detection of the forced cooling from the variation in R_{sma}, yielding significant accuracy. The maximum estimation error is found to be slightly less than 6°. The variation in the estimated value of h is found to be qualitatively similar, as seen in Figs. 5.20, 5.21 and 5.16, and hence are omitted.

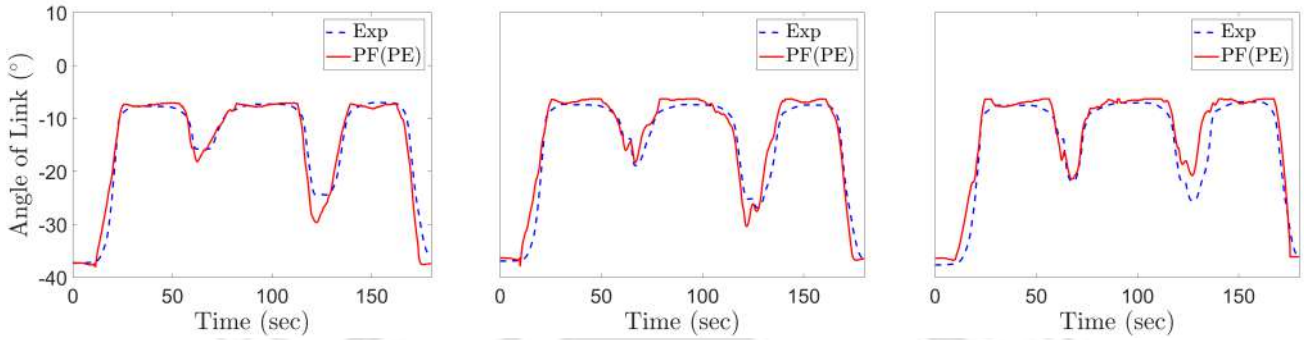

(a) (b) (c)

Figure 5.25: Angular position of the link estimated using the modified PF and the experimental one, corresponding to (a) PC(NL)-I, (b) PC(NL)-II, and (c) PC(NL)-III, subjected to *Low level* forced cooling.

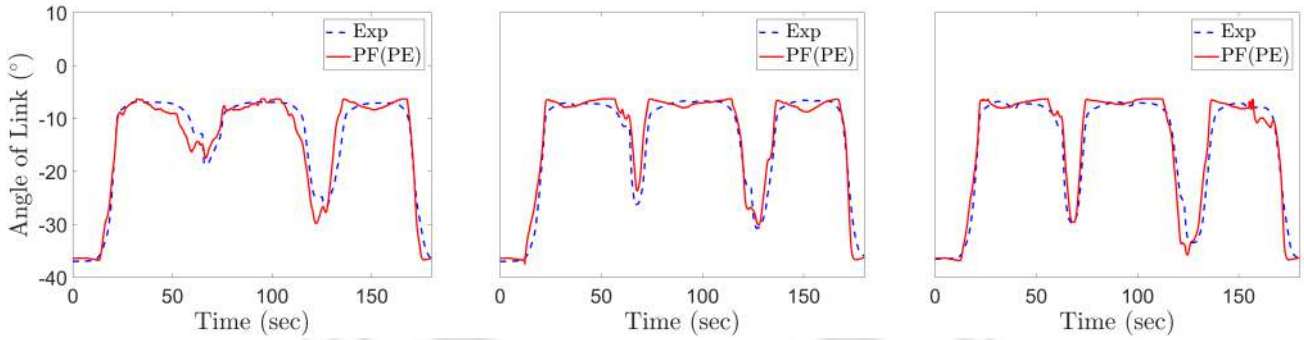

(a) (b) (c)

Figure 5.26: Angular position of the link estimated using the modified PF and the experimental one, corresponding to (a) PC(NL)-I, (b) PC(NL)-II, and (c) PC(NL)-III, subjected to *Medium level* forced cooling.

The estimator's performance is also examined for the partial cooling cases, attained while using the voltage signal shown in Fig.5.11b. Here as well, the forced cooling has been effectuated at different stages of actuation (peak and transient positions), for a diverse set of time intervals (1s, 3s and 5s) and for different intensities (*low*, *medium* and *high levels*). Figures 5.25 and 5.26 show the link position estimated by the modified PF for *low level*

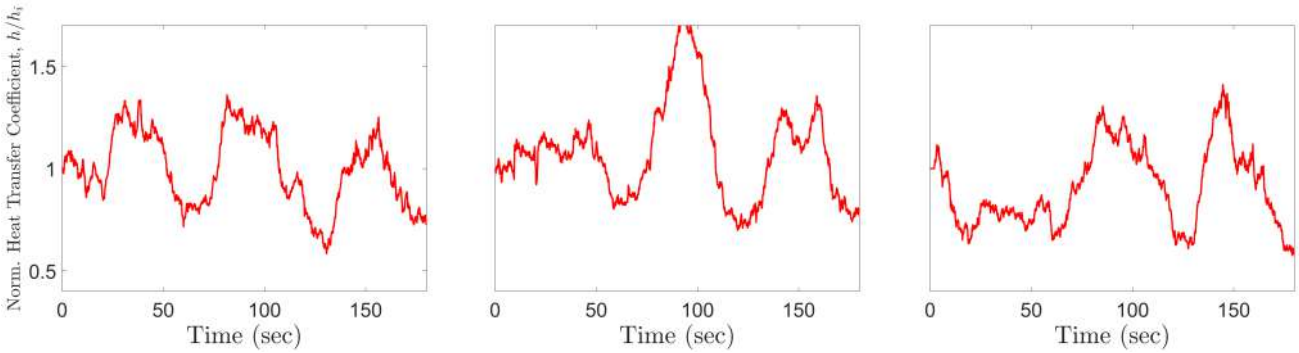

(a) (b) (c)

Figure 5.27: Normalized h estimated by the modified PF, corresponding to (a) PC(NL)-I, (b) PC(NL)-II, and (c) PC(NL)-III, subjected to *low level* forced cooling.

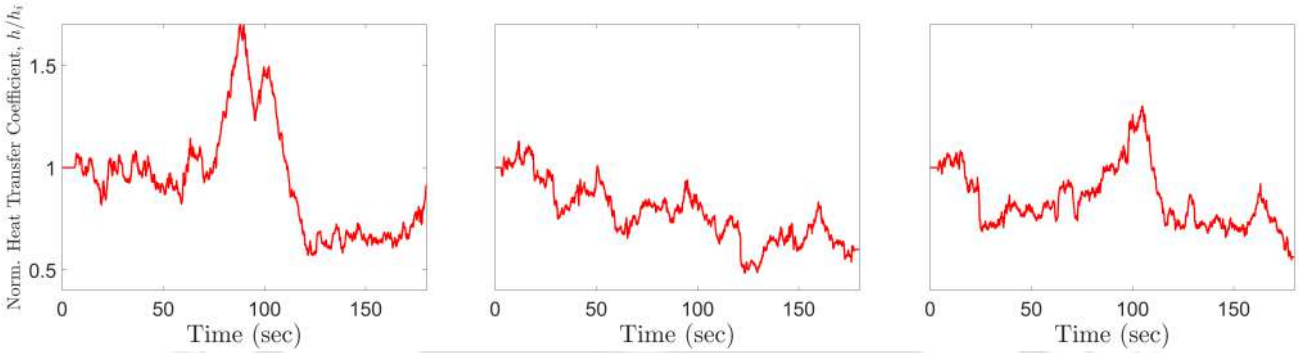

(a) (b) (c)

Figure 5.28: Normalized h estimated by the modified PF, corresponding to (a) PC(NL)-I, (b) PC(NL)-II, and (c) PC(NL)-III, subjected to *medium level* forced cooling.

and *medium level* cooling. The response for cooling periods of 1s, 3s and 5s, *i.e.*, the cases PC(NL)-I, PC(NL)-II and PC(NL)-III in Table 5.2 are indicated as sub-figures (a), (b) and (c), respectively. Here, one can appreciate the accuracy with which the modified PF has estimated the system response. The maximum error in the estimated link position is less than 10% of the span of link rotation, except in at few instances. The corresponding estimated h are presented in Figs.5.27 and 5.28, illustrating the precipitous variation in h as the forced cooling kicks in, resulting in improved accuracy in estimation.

Figures 5.29, 5.30 and 5.31 depict the link position while the SMA wire endures actuation under *low level*, *medium level* and *high level* cooling during the transient response of the system. The sub-figures (a), (b), and (c) correspond to the forced cooling studies PC(NL)-IV, PC(NL)-V and PC(NL)-VI in Table 5.2, respectively. Here again, the modified PF yields significant accuracy in tracing the abrupt drop in the level of actuation

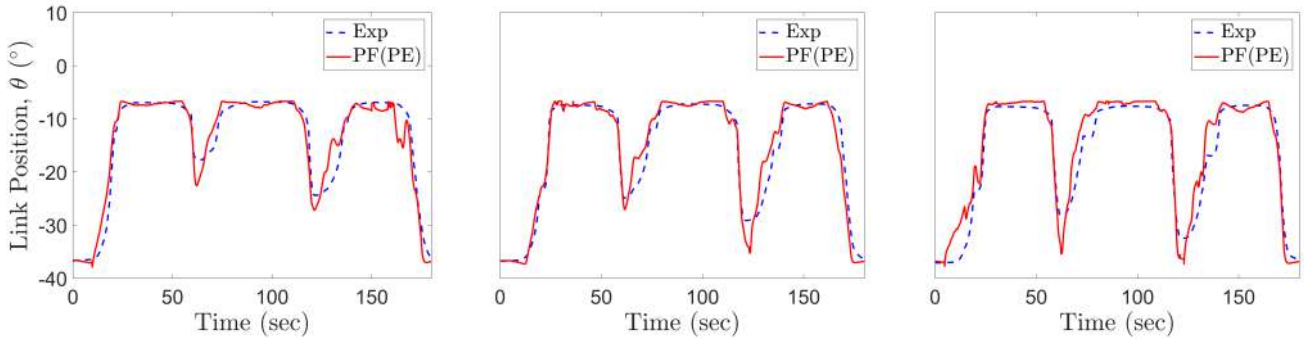

(a) (b) (c)

Figure 5.29: Angular position of the link estimated using the modified PF and the experimental one, corresponding to (a) PC(*NL*)-IV, (b) PC(*NL*)-V, and (c) PC(*NL*)-VI, subjected to *Low level* forced cooling.

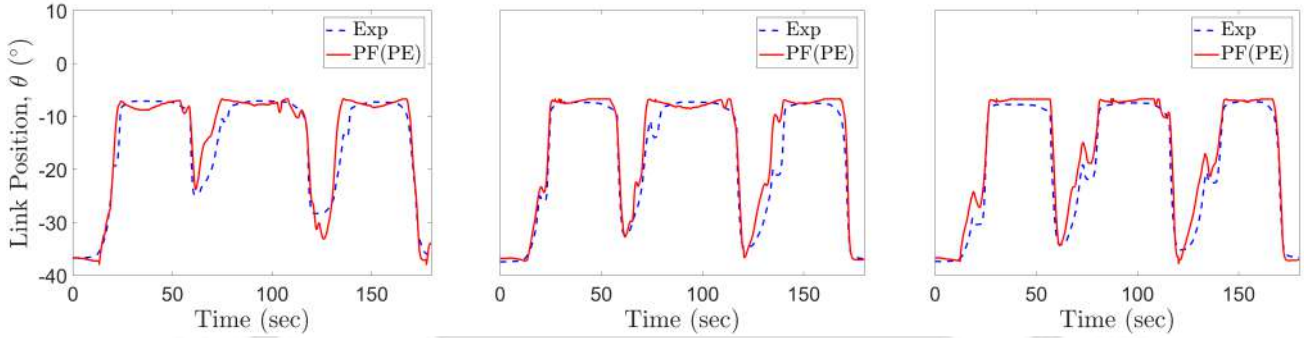

(a) (b) (c)

Figure 5.30: Angular position of the link estimated using the modified PF and the experimental one, corresponding to (a) PC(*NL*)-IV, (b) PC(*NL*)-V, and (c) PC(*NL*)-VI, subjected to *Medium level* forced cooling.

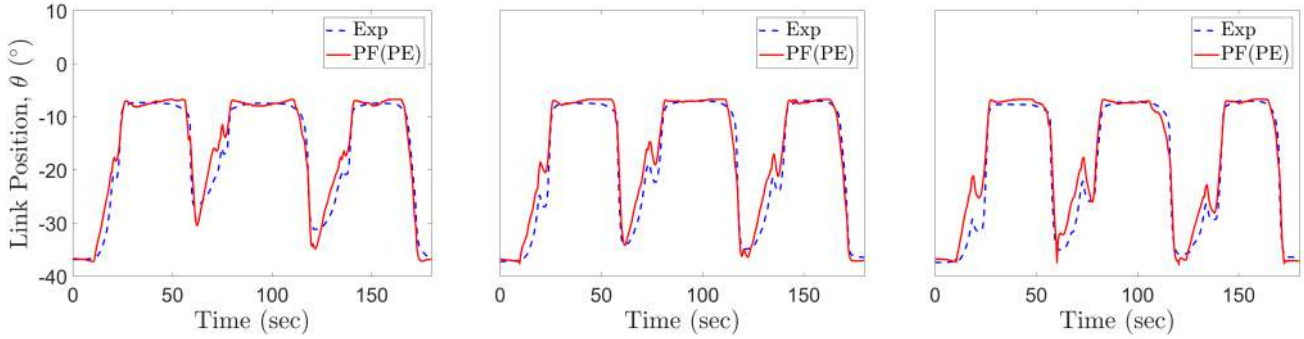

(a) (b) (c)

Figure 5.31: Angular position of the link estimated using the modified PF and the experimental one, corresponding to (a) PC(*NL*)-IV, (b) PC(*NL*)-V, and (c) PC(*NL*)-VI, subjected to *High level* forced cooling.

during forced cooling. The maximum error is less than 10% of the span, except in a few instances. The corresponding estimated h displayed a similar degree of variation during

forced cooling, as shown in Figs. 5.27, 5.28 and 5.17; and hence are skipped.

5.7.3 Non-Proportional Loading

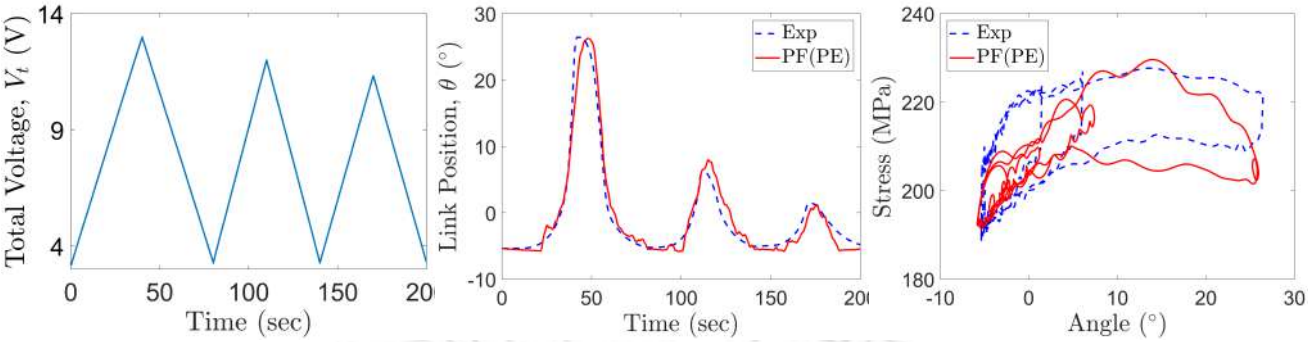

(a) (b) (c)

Figure 5.32: (a) Input voltage applied, and the comparison among the (b) angular position of the link and (c) the stress in the SMA wire, estimated by the modified PF against the experimental one, for non-proportional loading case.

The performance of the modified PF is investigated for the SMA wire actuator under non-proportional variation of stress and temperature. The initial position of the link ($\theta_0 = -5.8°$) and the input voltage (refer Fig. 5.32a) across the SMA wire are designed to ensure that the link goes past the particular configuration, where the SMA wire encounters maximum stress. Using SMA's corresponding measured electrical resistance, the link position is estimated from the modified PF and shown in Fig.5.32b. Here, one can observe that the modified PF has estimated the system response with significant accuracy. Further, the actual stress in the SMA wire is calculated from the measured data of the force sensor and compared with the corresponding stress estimated by the PF, and are depicted in Fig.5.32c. In the beginning, the spring force supports the weight of the link and the payload. Upon heating, the temperature of the SMA wire increases, initiating the reverse transformation, which forces the link to rotate counter-clockwise. At about 35s, the link crosses the maximum stress position, at an angle of about $\theta = 12°$, with the horizontal. After this point, the stress in the SMA wire declines. Consequently, the austenite finish transformation temperature of SMA also drops; thus, subsequent heating results in the swift completion of the reverse transformation. Here, the stress reduces despite an increase in the temperature of the SMA wire. Finally, the applied thermal

loading is gradually reduced, and the link returns to its original configuration, undergoing the same variation of stress, but in the reverse order. The variation of the estimated stress with the link orientation is qualitatively consistent with the measured one. These results demonstrate the true potential of the proposed filter in harnessing the self-sensing feature of the SMA wire actuator while undergoing non-proportional loading conditions as well.

5.8 Conclusions

A PF-based approach has been demonstrated, to exploit the self-sensing behaviour of an SMA wire actuator, under proportional as well as non-proportional loading. The process model of the SMA wire actuated rotary manipulator has been developed considering heat balance, equation of motion, kinematic constraints and the one-dimensional constitutive model of SMA. The set of coupled algebraic differential equations are solved using an incremental iterative approach. Based on this process model, a PF is developed to predict the response of the manipulator from the varying electrical resistance of the SMA wire during actuation. The effectiveness of the PF is demonstrated by comparing the estimated response against the experimentally obtained one. In the absence of any external cooling, the angular position estimated by the PF closely follows the same obtained experimentally with a maximum error of about 2°, exhibiting the efficacy of the proposed filter under the natural convection case.

Next, the SMA wire is intermittently cooled using a fan at different stages of actuation, duration and intensity. Here, a modified PF has been proposed in which the convective heat transfer coefficient is estimated along with its states. In the case of the partial heating condition (PH(NL)-I, PH(NL)-II, PH(NL)-III), the RMS error of the modified PF is found to be around 9% of the maximum displacement (θ_{span}). Additionally, in the case of the partial cooling condition (PC(NL)-I, PC(NL)-II, PC(NL)-III), the RMS error of the modified PF is around 8% of θ_{span}. Next, the manipulator is reconfigured to attain a situation where the SMA wire undergoes non-proportional stress and temperature variation. Here as well, the PF has estimated the system response quite reliably.

Chapter 6

Exploring Self-Sensing of Shape Memory Alloy Wire Actuators Under Practical Loading Conditions Using LSTM

6.1 Introduction

In previous chapters, enhanced state estimation based methodologies have been proposed to accurately predict the response of the SMA wire actuator, addressing its hysteretic and non-linear behaviour, under varied loading situations. However, all of these approaches are generally computationally intensive, requiring a detailed understanding of the non-trivial constitutive model of SMA and experimentally determined material parameters. In such situations, artificial neural networks (ANN) may be utilized as an alternate, owing to ANN's data-based learning approach, resulting in a substantive approximation of the physical system. In this chapter, an LSTM-based deep neural network is developed to evaluate the response of the SMA wire actuated linear system and the non-linear 1-DOF manipulator introduced in Chapters 4 and 5, respectively. The developed network is then trained, and its performance is evaluated against the experimentally obtained responses.

6.2 Neural Network Based Applications of SMA Wire Actuators

Ma *et al.* [120] developed a neural network-based feedback mechanism for position control of the SMA wire actuator, by utilizing the electrical resistance of the SMA wire. Asua *et al.* [121] proposed a neural network-based control algorithm to predict the input current signal to be applied across the SMA wire to achieve a desired actuation. Senthilkumar and Umapathy [122] proposed a neural network based technique for controlling the output of an SMA wire actuator based on the load generated by the SMA wire. Gurung and Banerjee [123] proposed a feed-forward neural network for an SMA wire actuator, to reduce the error in the system displacement, estimated from an Extended Kalman Filter. Sul *et al.* [124] proposed a neural network to predict the actuation generated by an SMA spring by using the frequency and amplitude of the input current. All of these techniques involve feed-forward neural networks, which yield an estimate of reasonable accuracy for cases which are time independent; but may be inadequate for systems having time dependency. The behaviour of SMA wire actuators are not just dependent on the input at the present time instant, but is also dependent on the loading path. Recurrent neural networks (RNNs) are a better fit for such systems. Hannen *et al.* [125] developed a temperature-based hysteretic RNN, to regulate the slope of a flexible structure actuated using SMA tendons. Wang and Song [126] proposed a Jordan-Elman NARX RNN to model a spring-biased SMA wire system, utilizing the applied voltage as the input data and the corresponding displacement as the output data.

Long short term memory (LSTM) networks are a special kind of RNN, which is effective in learning the long-term dependence of the time sequence data. This renders the LSTM as a powerful tool to model the behaviour of SMA wire actuated systems, whose response is load history-dependent. Ruvinov *et al.* [127] proposed a 4-layered and a 2-layered LSTM network to estimate the force and position of the SMA actuator, respectively, taking the electrical resistance and current as inputs. Bhargaw *et al.* [93] presented an LSTM-based neural network to estimate the actuation obtained from an antagonistic SMA wire actuator, by employing the differential electrical resistance data. All existing

works explore the self-sensing feature of SMA wire actuated linear systems under natural cooling conditions and proportional loading-unloading cycles. The present work proposes an LSTM-based deep neural network (DNN) to estimate the response of an SMA wire actuated linear system and a non-linear 1-DOF rotary manipulator, enduring actuation under forced cooling conditions. The developed tool is employed for non-monotonic loading situations, where data-driven techniques like neural networks might be expedient. The proposed DNN utilises the applied voltage, the electrical resistance and their rate of change as inputs, to estimate the system's response.

6.3 RNN and LSTM

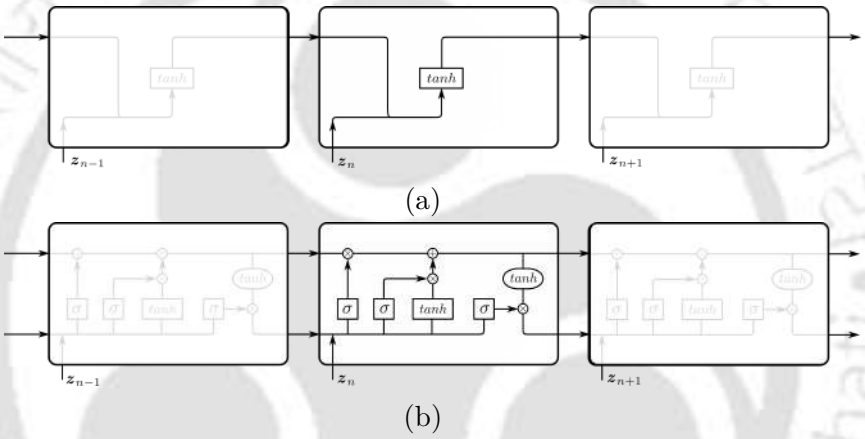

Figure 6.1: Schematic representation of unrolled (a) RNN, and (b) LSTM networks.

Recurrent neural networks (RNN) are used to predict unknown states based on previously remembered states. It has memory in hidden states, which retains some information about a sequence of events that happened in the past. The schematic diagram of an unrolled RNN is shown in Fig.6.1a. Some of the issues with simple RNN include,

- no long term memory,
- can't use information from distant past,
- can't learn patterns with long dependencies, and
- suffers from the vanishing and exploding gradient problem.

6.3.1 Long Short Term Memory

Long Short Term Memory (LSTM) is a special type of RNN, which can learn long-term patterns. The schematic of an LSTM compared against a standard RNN is shown in Fig.6.1. Compared to a standard RNN, an LSTM cell incorporates an additional state parameter termed the cell state, enabling it with long-term memory characteristics. An LSTM cell comprises of,

- an input gate,
- a forget gate, and
- an output gate.

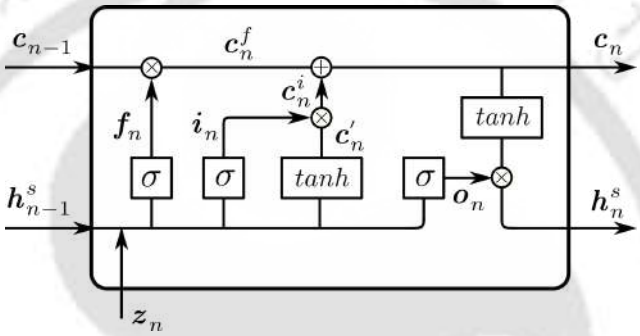

Figure 6.2: LSTM Cell

Here, the gates comprise of dense layers of *sigmoid* or *tanh* activation functions, acting as filters. The hidden state, $\boldsymbol{h}^s$, can be equated to a short-term memory of LSTM, which contains the information of the current state. The cell state, $\boldsymbol{c}$, is responsible for the long term memory. The cell state is updated at 2 points, marked as $\otimes$ and $\oplus$, between $\boldsymbol{c}_{n-1}$ and $\boldsymbol{c}_n$.

- **Forget gate**:

  The forget gate is defined as,

$$\boldsymbol{f}_n = \sigma\left(\boldsymbol{W}_f \boldsymbol{h}_{n-1}^s + \boldsymbol{U}_f \boldsymbol{z}_n + \boldsymbol{b}_f\right), \tag{6.1}$$

$$\boldsymbol{c}_n^f = \boldsymbol{c}_{n-1} * \boldsymbol{f}_n, \tag{6.2}$$

  where, $\boldsymbol{W}_f$ and $\boldsymbol{U}_f$ are the weight matrices for forget layer corresponding to hidden state and input, respectively, and $\boldsymbol{b}_f$ is the associated bias. The symbol '$*$' represents

element-wise multiplication. $\boldsymbol{c}_n^f$ refers to the cell state at the present time step, which is evaluated from its value at the previous time step $\boldsymbol{c}_{n-1}$. $\boldsymbol{f}_n$, which is a *sigmoid* function, having values between 0 and 1, decides the indices to be remembered. Here, the indices closer to zero are forgotten from $\boldsymbol{c}_{n-1}$ and the indices closer to 1 are remembered.

- **Input gate**:

  The input gate is described as,

$$\boldsymbol{i}_n = \sigma\left(\boldsymbol{W}_i \boldsymbol{h}_{n-1}^s + \boldsymbol{U}_i \boldsymbol{z}_n + \boldsymbol{b}_i\right), \tag{6.3}$$

$$\boldsymbol{c}_n' = tanh\left(\boldsymbol{W}_c \boldsymbol{h}_{n-1}^s + \boldsymbol{U}_c \boldsymbol{z}_n + \boldsymbol{b}_c\right), \tag{6.4}$$

$$\boldsymbol{c}_n^i = \boldsymbol{c}_n' * \boldsymbol{i}_n. \tag{6.5}$$

  Here, $\boldsymbol{i}_n$ acts as a filter for the simple RNN (input with *tanh* dense layer). It refines the new cell state, $\boldsymbol{c}_n'$, which is acquired from the present input $\boldsymbol{z}_n$, to obtain $\boldsymbol{c}_n^i$. Finally, the new cell state at time t_n is evaluated as,

$$\boldsymbol{c}_n = \boldsymbol{c}_n^f + \boldsymbol{c}_n^i. \tag{6.6}$$

- **Output gate**:

  The output is evaluated following,

$$\boldsymbol{o}_n = \sigma\left(\boldsymbol{W}_o \boldsymbol{h}_{n-1} + \boldsymbol{U}_o \boldsymbol{z}_n + \boldsymbol{b}_o\right), \tag{6.7}$$

$$\boldsymbol{h}_n^s = \boldsymbol{o}_n * tanh(\boldsymbol{c}_n). \tag{6.8}$$

  Here, $\boldsymbol{h}_n^s$ is the hidden state of the current step, and will be used in the next time step.

6.4 System Description

In this chapter, the SMA wire actuated linear and the non-linear system considered in Chapters 4, and 5 are examined. The brief description of both systems are briefly discussed herewithin, for the sake of readers' convenience. Figure 6.3a illustrates the schematic of the SMA wire actuated linear system. Here, SMA wire position $Y_1 - X - Y_2$ corresponds to its initial pre-stressed configuration, and position $Y_1 - X' - Y_2$ depicts an intermediate state while actuation. The spring AB provides the restoration force, needed to return to its original state upon completion of a loading cycle. Here, with an increment in the applied voltage, the temperature of the SMA wire (T_{SMA}) increases due to resistive heating. As T_{SMA} crosses the austenite start temperature (A_s), reverse transformation sets in and the SMA wire contracts, thereby compressing the spring by 'δ'. With a reduction in the voltage, the SMA wire cools as a result of natural cooling. As T_{SMA} falls below the martensite start temperature (M_s), the forward transformation begins, with the restoration force in the spring bringing the system back to its original state.

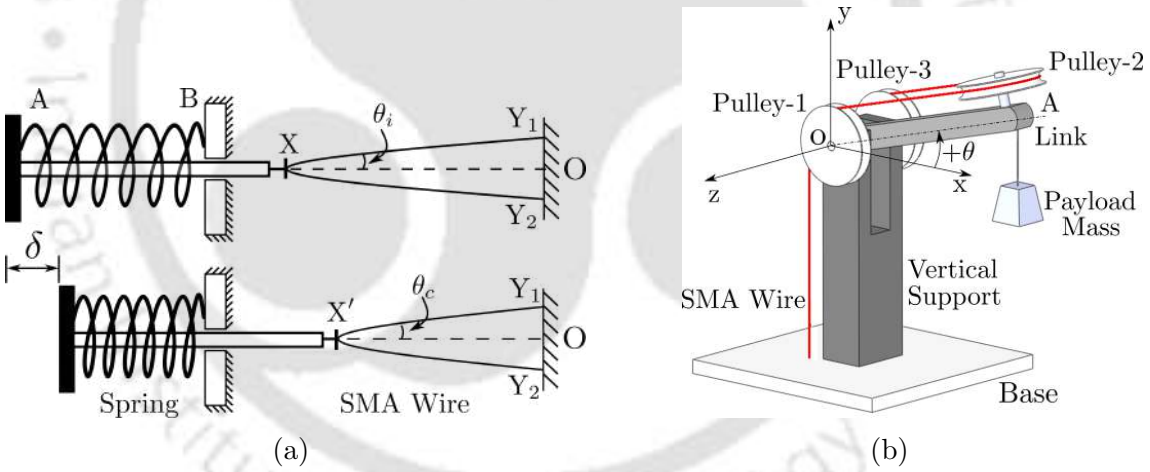

Figure 6.3: Schematic of SMA wire actuated (a) linear system, and (b) non-linear rotary manipulator.

Figure 6.3b depicts the schematic of the SMA wire actuated rotary manipulator. The SMA wire (shown in red), is guided across a set of 3 pulleys, as depicted in the figure. Pulley-1 and Pulley-3 are installed about the o-z axis, and Pulley-2 is held perpendicularly to the rotating link OA. The mass of the link (M_l), payload mass (M_p) and the torsional spring (K_θ) offer the bias force on the SMA wire actuator. With voltage input, the T_{SMA} rises due to Joule's heating, and the wire contracts during reverse transformation. This

rotates the link in the counter-clockwise direction ($+\theta$) about the horizontal axis o-x. As the applied voltage is curtailed, the T_{SMA} drops, and the forward transformation initiates, while the bias forces revert the system to its original configuration.

6.5 Experimental Details

Two experimental setups developed in Chapters 4 and 5 are reused, to examine the effectiveness of an LSTM-based neural network in the self-sensing application of SMA wire actuators under forced cooling situations. Figure 4.3 shows the experimental setup comprising of the SMA wire actuated linear system, labelled as *System*-I. It is actuated by using the voltage input signal shown in Fig.4.6. Figure 5.11 illustrates the voltage signals driving another batch of experiments, developed to study the SMA wire actuated rotary manipulator shown in Fig.5.7, denoted as *System*-II. In both cases, whilst the actuation transpires, the SMA wire is cooled using a fan. The cooling is carried out for distinct time durations (1s, 3s and 5s), and at different stages of SMA actuation (peak or transient), and with increasing magnitudes (*low, medium* and *high levels*), as described in Tables 6.1, 6.2 for *System*-I, and Tables 6.3 and 6.4 for *System*-II. The tables are illustrated again for the readers' convenience. The corresponding change in the electrical resistance (R_{sma}) is evaluated from the voltage-divider circuit, following Eqn.(3.51). The present study's objective is to evaluate the spring displacement 'δ' for *System*-I, and the angular position of the link 'θ' for *System*-II, without the aid of any external sensor; rather by inspecting the change in the electrical properties of the SMA wires. In what follows is a description of the proposed Long Short-Term Memory (LSTM) system, which has been employed to evaluate the system response of the SMA wire actuated systems.

	Max/Min Response	Transient Response
$t_c = 1s$	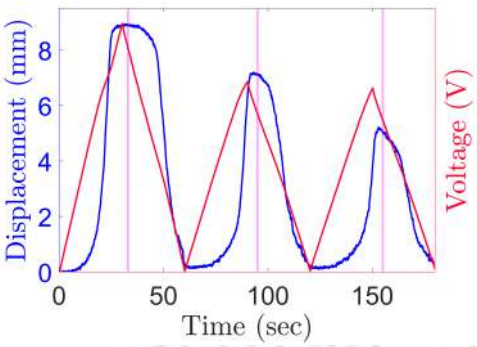 Case PH(L)-I	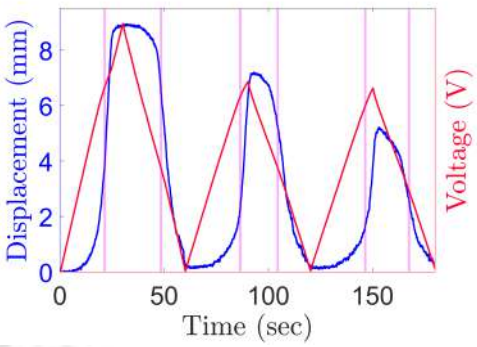 Case PH(L)-IV
$t_c = 3s$	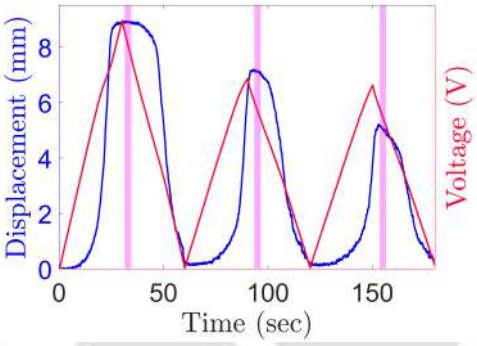 Case PH(L)-II	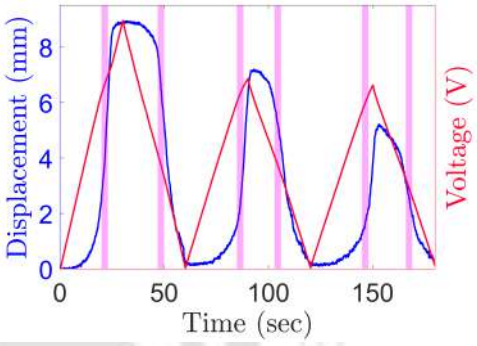 Case PH(L)-V
$t_c = 5s$	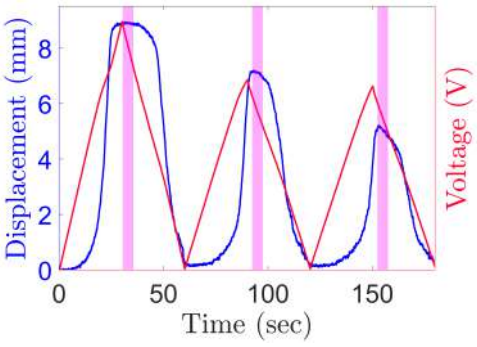 Case PH(L)-III	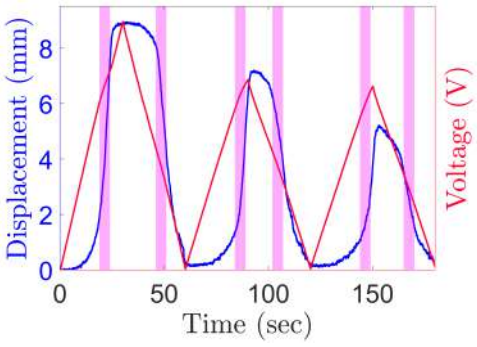 Case PH(L)-VI

Table 6.1: Location and duration of forced cooling during partial heating case, shown with respect to the response of *System*-I under natural cooling

	Max/Min Response	Transient Response
$t_c = 1s$	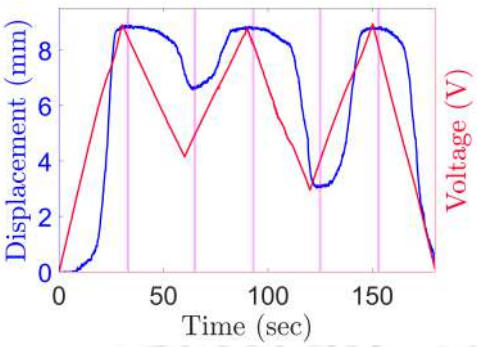 Case PC(L)-I	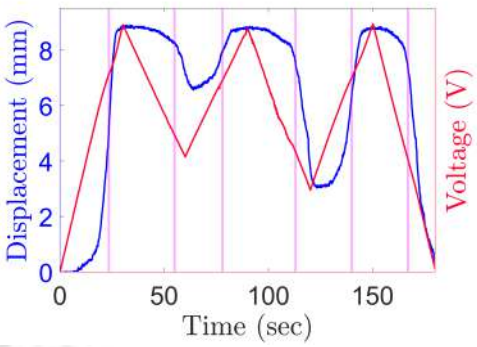 Case PC(L)-IV
$t_c = 3s$	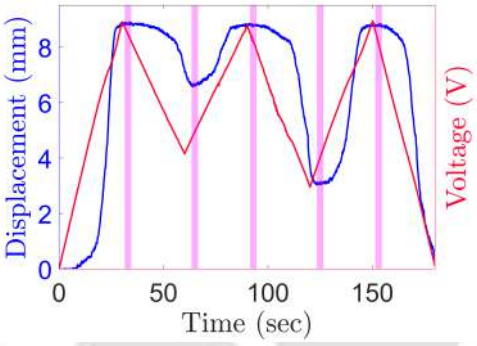 Case PC(L)-II	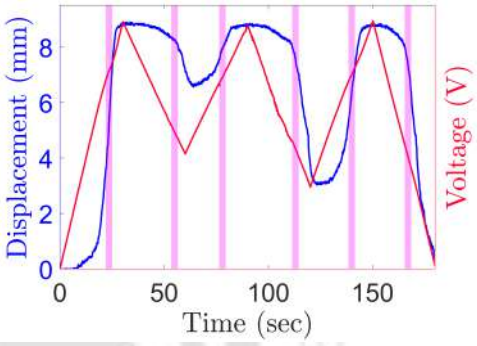 Case PC(L)-V
$t_c = 5s$	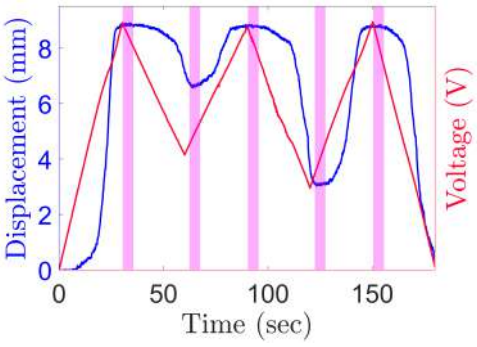 Case PC(L)-III	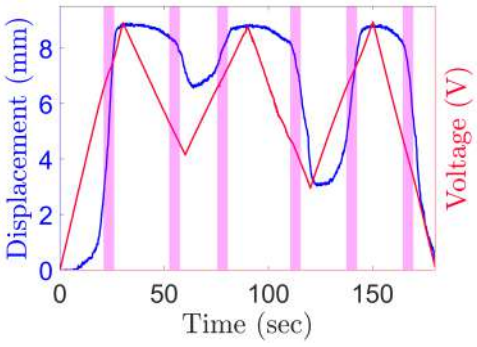 Case PC(L)-VI

Table 6.2: Location and duration of forced cooling during partial cooling case, shown with respect to the response of *System*-I under natural cooling

	Max/Min Response	Transient Response
$t_c = 1s$	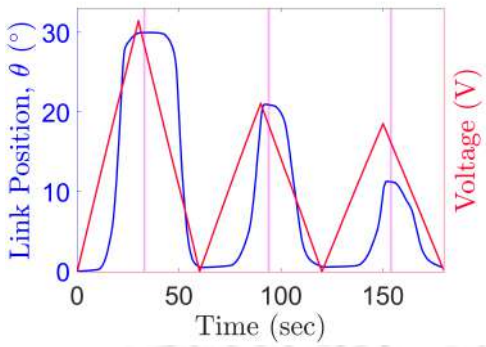 Case PH(NL)-I	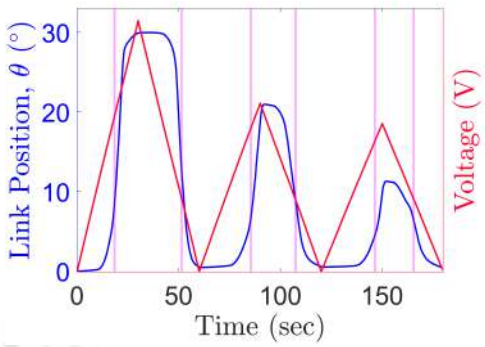 Case PH(NL)-IV
$t_c = 3s$	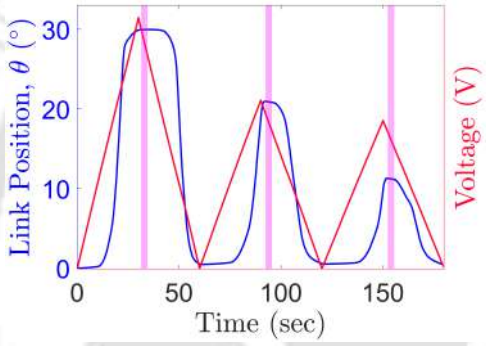 Case PH(NL)-II	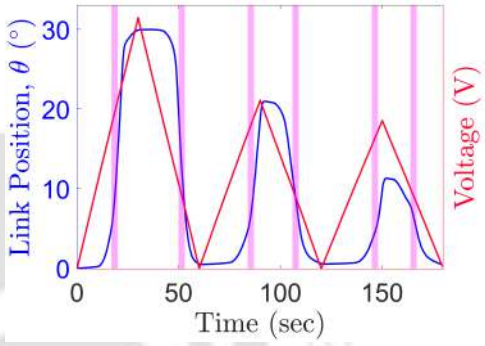 Case PH(NL)-V
$t_c = 5s$	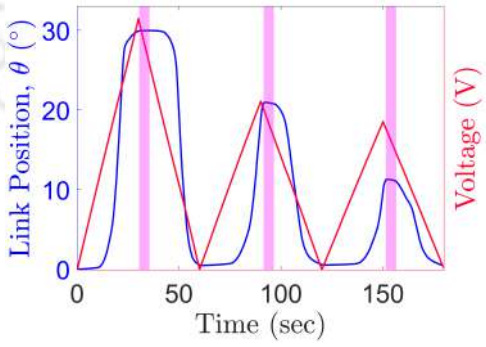 Case PH(NL)-III	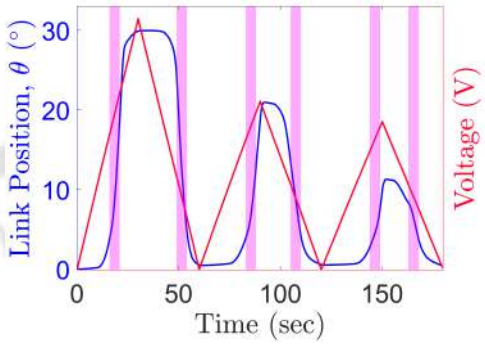 Case PH(NL)-VI

Table 6.3: Location and duration of forced cooling during partial heating case, shown with respect to the response of *System*-II under natural cooling

	Max/Min Response	Transient Response
$t_c = 1s$	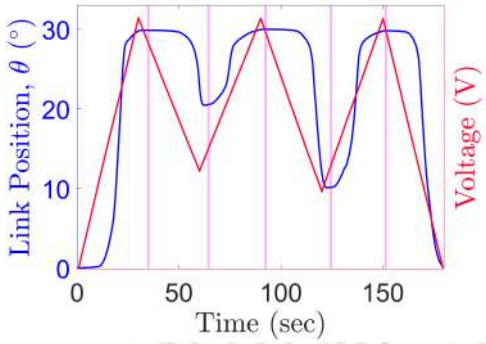 Case PC(NL)-I	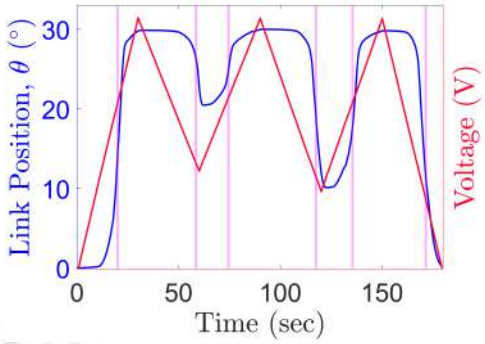 Case PC(NL)-IV
$t_c = 3s$	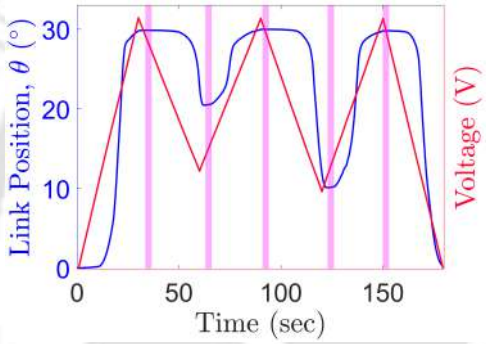 Case PC(NL)-II	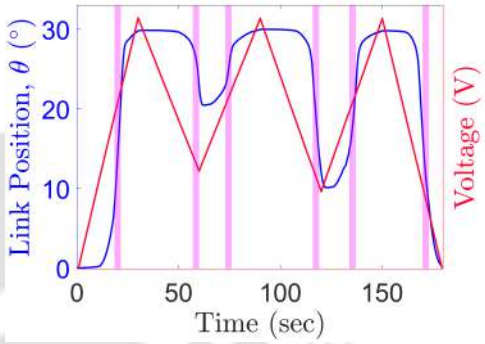 Case PC(NL)-V
$t_c = 5s$	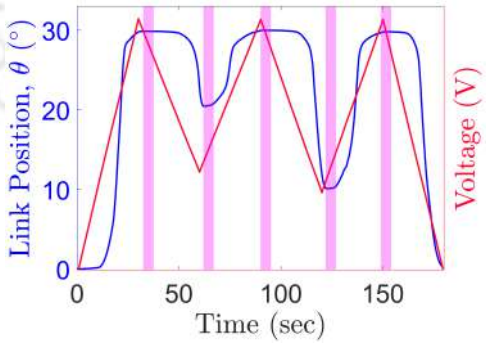 Case PC(NL)-III	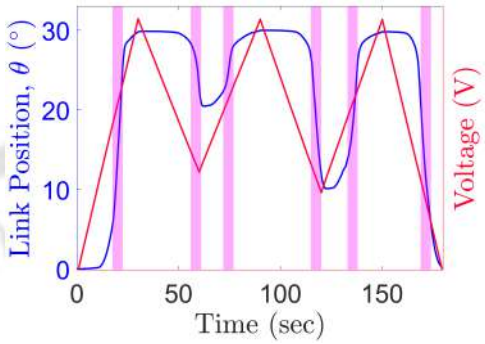 Case PC(NL)-VI

Table 6.4: Location and duration of forced cooling during partial cooling case, shown with respect to the response of *System*-II under natural cooling

6.6 Proposed LSTM system

In this work, a multi-layered LSTM-based Deep Neural Network (DNN) architecture has been developed to model the complex actuation behaviour of SMA wire actuators, by exploiting the variation in the electrical properties of the same. Here, a DNN of three LSTM layers is considered, with each layer consisting of 30 neurons. The LSTM layers have been used to accommodate for the history-dependent nature of SMA behaviour. The number of neurons in each layer and the total number of layers have been obtained heuristically. Any additional increment in each of these parameters showed insignificant improvement in the model's performance, and may have helped in avoiding the issue of over-fitting. The network was trained with input data being the voltage drop across the SMA wire (V_{SMA}), its rate of change ($\dot{V}_{SMA}$), the corresponding electrical resistance (R_{sma}) and its rate change ($\dot{R}_{sma}$), and power (P). Here, $\dot{V}_{SMA}$ defines the loading or unloading state of the SMA wire. Additionally, R_{sma} and $\dot{R}_{sma}$ contain the information regarding the state of the SMA actuator. During experiments, it is observed that there exists a sudden variation in the values of V_{SMA} and R_{sma} as the forced cooling is introduced. This is because the external cooling rapidly reduces the temperature of SMA, resulting in a change in the state of transformation in SMA, which is manifested as the sudden change in V_{SMA} and R_{sma}. Hence their rates of change, *i.e.*, $\dot{V}_{SMA}$ and $\dot{R}_{sma}$, are also used as the input data. Finally, the power P has been employed as an input data since the power dissipated delineates the change in temperature of the SMA wire.

	Linear Spring (*System*-I)	Nonlinear Manipulator (*System*-II)
Training Data Set	PH(L)-I, PH(L)-III, PH(L)-IV, PH(L)-VI PC(L)-I, PC(L)-III, PC(L)-IV, PC(L)-VI (*low/medium/high levels*)	PH(NL)-I, PH(NL)-III, PH(NL)-IV, PH(NL)-VI PC(NL)-I, PC(NL)-III, PC(NL)-IV, PC(NL)-VI (*low/medium/high levels*)
Testing Data Set	PH(L)-II, PH(L)-V PC(L)-II, PC(L)-V (*low/medium/high levels*)	PH(NL)-II, PH(NL)-V PC(NL)-II, PC(NL)-V (*low/medium/high levels*)

Table 6.5: Training and Testing Datasets for the DNN with forced cooling test cases as labeled in Tables 6.1, 6.2, 6.3 and 6.4.

Tables 6.1 and 6.2, in the case of *System*-I and Tables 6.3 and 6.4, in the case of *System*-II, illustrate the various forced cooling cases examined in this study. Here, the

proposed neural network is initially trained for a set of varied forced cooling settings, such that it subsumes the SMA behaviour under different loading situations, and is then later tested for a group of cases involving other experimental conditions. In this study, the training dataset for the deep neural network (DNN) involves *low level*, *medium level* and *high level* forced cooling cases with cooling durations of 1s and 5s. Here, the training data corresponds to the cases where forced cooling is introduced in the max/min displacement position and the transient portion of the response. Furthermore, both the partial heating and partial cooling conditions are considered. The performance of the trained DNN is then tested for cases involving 3s cooling, across different magnitudes and stages of cooling. Table 6.5 summarizes the various training and testing data sets. Also of note is that the neural networks for *System*-I and *System*-II were trained and tested separately. In the case of *System*-I, the DNN is trained for test cases PH(L)-I, PH(L)-III, PH(L)-IV, PH(L)-VI, PC(L)-I, PC(L)-III, PC(L)-IV and PC(L)-VI, undergoing *low*, *medium* and *high levels* of cooling. The trained network for *System*-I is denoted as '*TN*-I'. For *System*-II, the training dataset involve PH(NL)-I, PH(NL)-III, PH(NL)-IV, PH(NL)-VI, PC(NL)-I, PC(NL)-III, PC(NL)-IV and PC(NL)-VI, for 3 *levels* of cooling. The corresponding trained network is referred to as '*TN*-II'. Hence, for each of these systems, the neural network was trained for a data set of 24 forced cooling test cases and tested for the rest of the 12 cooling cases. The neural network toolbox in MATLAB R2021a © MathWorks is used for this study. Initially, both neural networks are trained for the corresponding training dataset illustrated in Table 6.5 and then validated using a few forced cooling cases in the same dataset to check the correctness of the trained network. Figure 6.4 depicts the spring displacement obtained from the trained network *TN*-I for *System*-I. Three forced cooling cases PH(L)-III, PC(L)-III and PC(L)-VI in the training dataset are used for validation. Here, the trained network has delineated the response appreciably, even when forced cooling is introduced. The correctness of the trained network *TN*-II is checked, using the forced cooling cases PH(NL)-VI, PC(NL)-III and PC(NL)-VI. Similar results can be seen in Fig.6.5, wherein the trained network has replicated the response of the training dataset quite accurately. In the following section, the trained networks *TN*-I and *TN*-II have been used to predict the response of the testing dataset of the corresponding system.

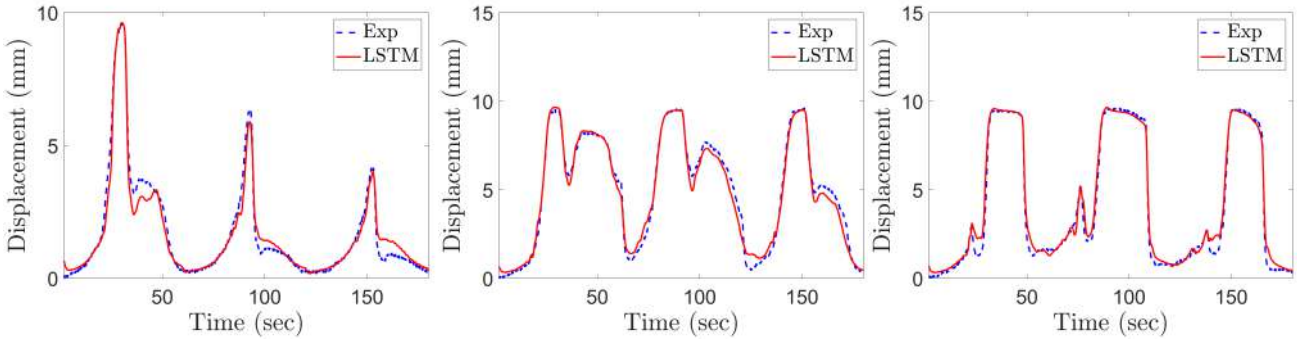

Figure 6.4: Validation of the trained network (for *System*-I) against the experimental data for forced cooling cases PH(L)-III, PC(L)-III and PC(L)-VI.

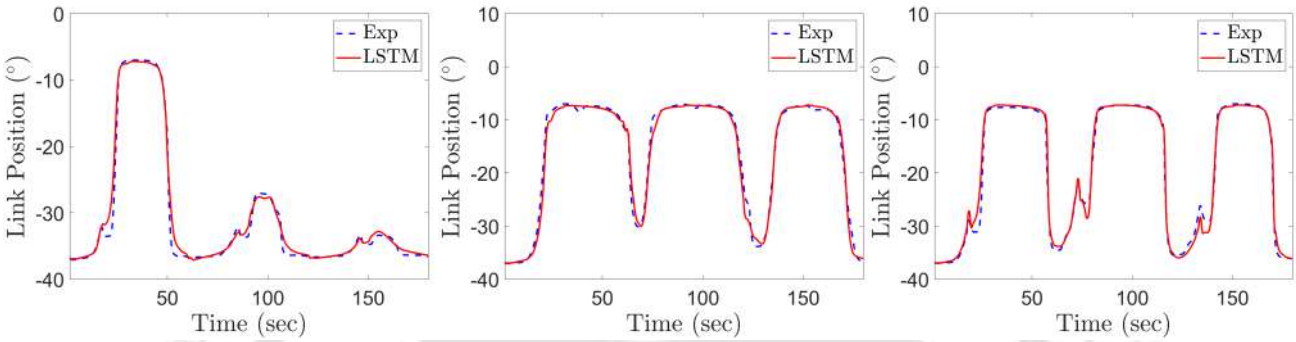

Figure 6.5: Validation of the trained network (for *System*-II) against the experimental data for forced cooling cases PH(NL)-VI, PC(NL)-III and PC(NL)-VI.

6.7 Results and Discussions

In this section, the trained networks *TN*-I and *TN*-II, corresponding to *System*-I and *System*-II, respectively are tested against the testing data set and compared against the measured response, and are presented below.

6.7.1 SMA Wire Actuated Linear System (*System*-I)

Figures 6.6 and 6.7 present the displacement obtained from *TN*-I for the forced cooling cases referred as PH(L)-II and PH(L)-V in Table 6.1, respectively. The measured displacements are shown in the same figure. Here, (a), (b), and (c) correspond to three different cooling magnitudes, referred to as *low level*, *medium level* and *high level* cooling, respectively. Here, one can witness the remarkable accuracy with which the DNN has predicted the spring displacement of the actuator. The maximum error is less than 5%, except

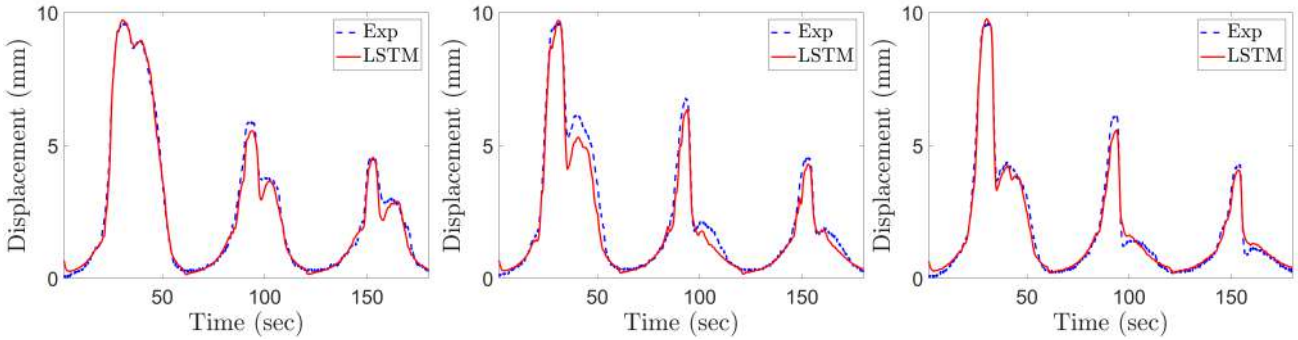

Figure 6.6: Comparison of the actuation predicted by *TN*-I against the experimental one for forced cooling case PH(L)-II, with (a) *Low level* , (b) *Medium level* , and (c) *High level* cooling.

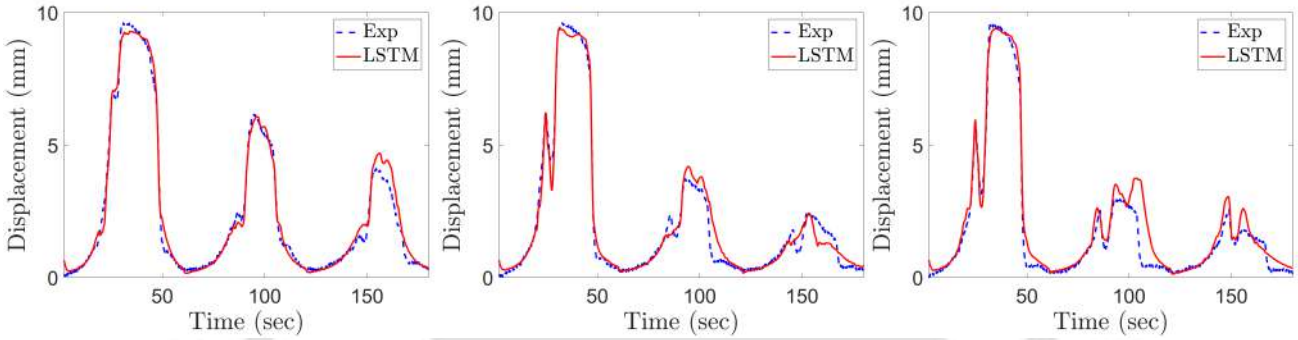

Figure 6.7: Comparison of the actuation predicted by *TN*-I against the experimental one for forced cooling case PH(L)-V, with (a) *Low level* , (b) *Medium level* , and (c) *High level* cooling.

in a few instances, and the RMS error is found to be 2.57% of maximum displacement. As the forced cooling is introduced, the instantaneous drops in the response are neatly delineated by the DNN. One can also observe the notch-like behaviour in the response in Figs.6.6 and 6.7, illustrating that the forced cooling zones are efficiently estimated by the developed tool.

Figures 6.8 and 6.9 illustrate the displacement obtained from the trained network *TN*-I, for the 3s cooling cases dubbed as PC(L)-II and PC(L)-V in Table 6.2, respectively. The spring displacement 'δ' obtained from the displacement sensor are also shown. The sub-figures (a), (b) and (c), represent *low level*, *medium level* and *high level* cooling cases. As the cooling fan is switched ON, the temperature of the SMA wire falls, leading to a rapid drop in displacement. The response of the proposed DNN closely follows the experimental

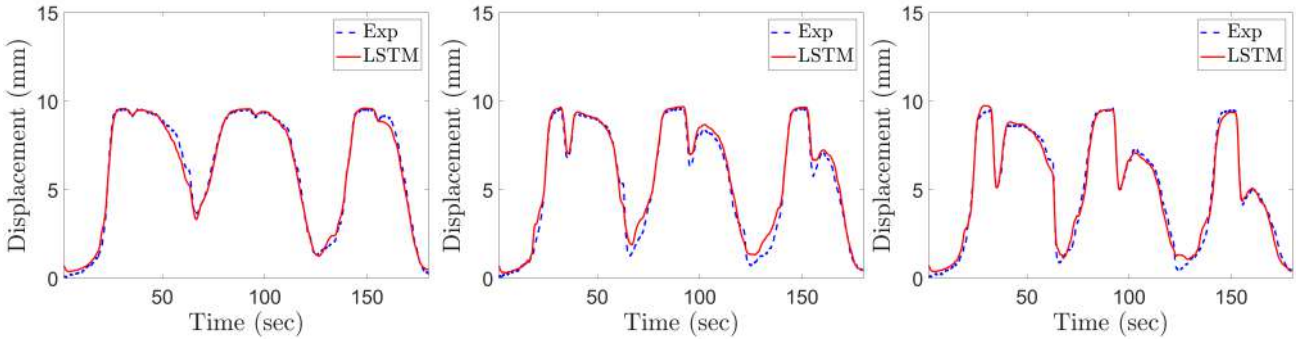

Figure 6.8: Comparison of the actuation predicted by *TN*-I against the experimental one for forced cooling case PC(L)-II, with (a) *Low level* , (b) *Medium level* , and (c) *High level* cooling

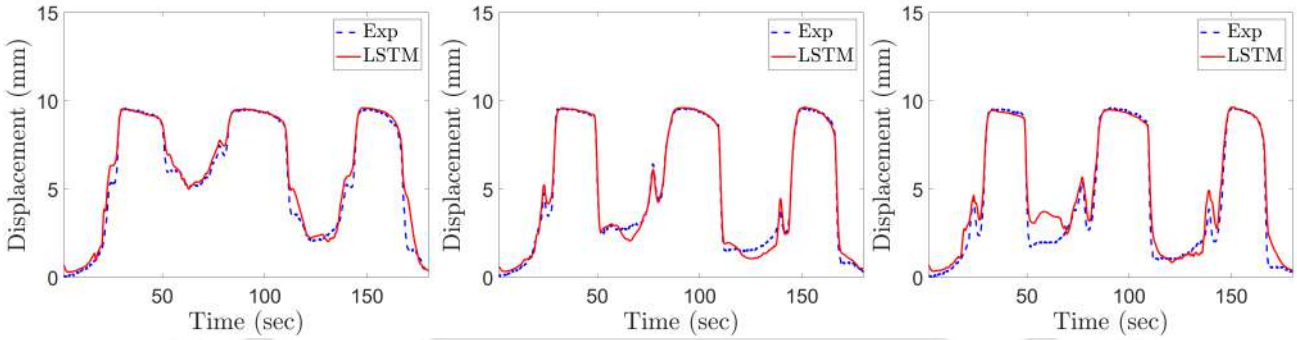

Figure 6.9: Comparison of the actuation predicted by *TN*-I against the experimental one for forced cooling case PC(L)-V, with (a) *Low level* , (b) *Medium level* , and (c) *High level* cooling.

one. This is especially evident at the forced cooling zones, where the trained network has traced the fall in generated actuation with very high accuracy. The maximum and RMS estimation errors of the DNN are found to be below 8% and 2.3%, respectively.

6.7.2 SMA Wire Actuated 1-DOF Manipulator (*System*-II)

The SMA wire actuated rotary manipulator, held at an initial configuration of $\theta_0 = -37°$, is externally cooled, while actuating, at different regions and magnitudes.For the forced cooling cases PH(NL)-II and PH(NL)-V shown in Table 6.3, the link position obtained using *TN*-II are illustrated in Figs. 6.10 and 6.11, respectively. Here, sub-figures (a), (b) and (c) represent the SMA responses for increasing cooling intensities, namely *low level*, *medium level* and *high level* cooling, respectively. The trained network provides a

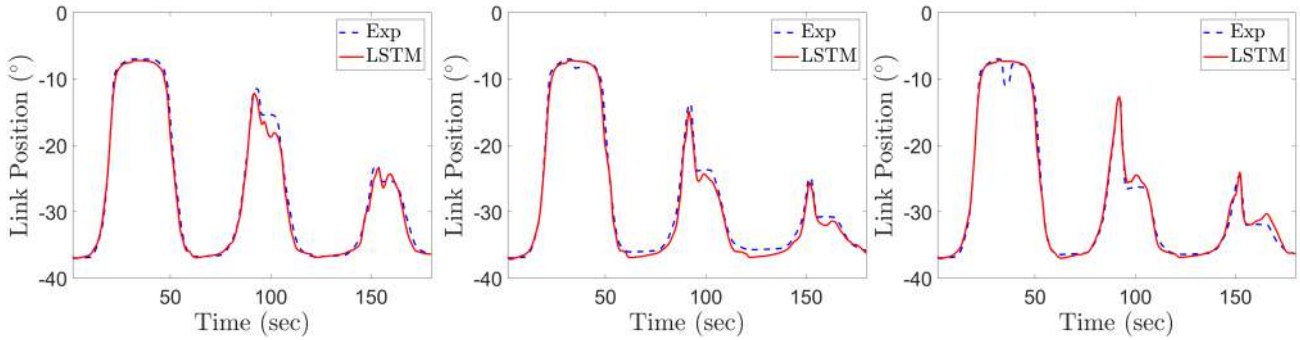

(a) (b) (c)

Figure 6.10: Comparison of the link position predicted by *TN*-II against the experimental one for forced cooling case PH(*NL*)-II, with (a) *Low level* , (b) *Medium level* , and (c) *High level* cooling.

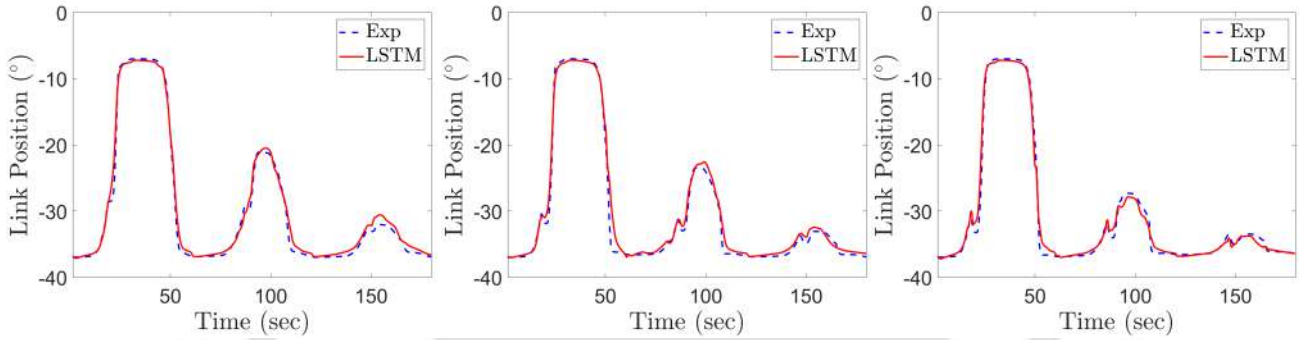

(a) (b) (c)

Figure 6.11: Comparison of the link position predicted by *TN*-II against the experimental one for forced cooling case PH(*NL*)-V, with (a) *Low level* , (b) *Medium level* , and (c) *High level* cooling.

superior estimate of the link position. In Fig.6.10, where the forced cooling occurs at the peak positions of the link, the trained network outlines the massive drops in actuation at the respective cooling zones. Additionally, the sudden drop in the response in Fig.6.11 corresponding to forced cooling, during the transient portions of the response curve, is precisely delineated by the trained network. The maximum and RMS estimation errors of the DNN are found to be less than 7.5% and 2.75%, respectively.

Figures 6.12 and 6.13 depict the link positions, predicted by the trained network *TN*-II, for forced cooling cases PC(*NL*)-II and PC(*NL*)-V in Table 6.4. The sub-figures (a), (b), and (c) correspond to the forced cooling intensities of *low level*, *medium level* and *high level* cooling, respectively. Here, the maximum and RMS estimation errors are found to be less than 8% and 3.4%, respectively. The proposed neural network has estimated the

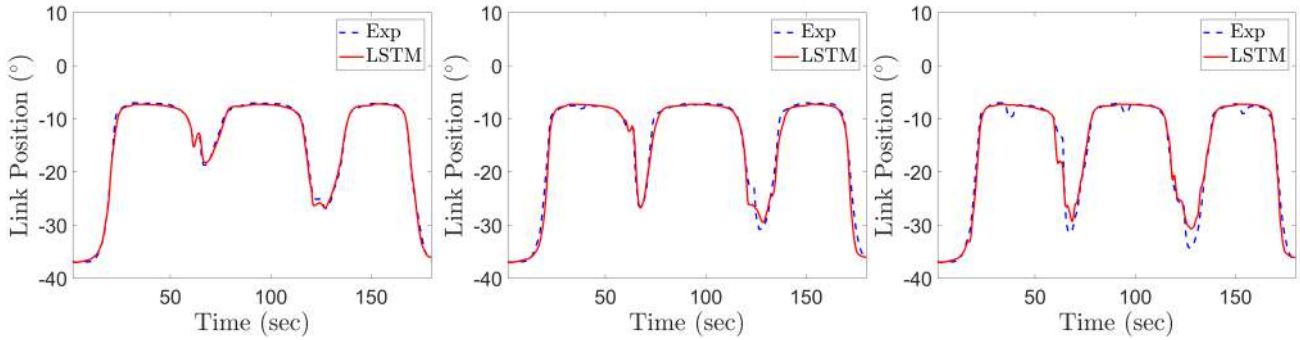

(a) (b) (c)

Figure 6.12: Comparison of the link position predicted by *TN*-II against the experimental one for forced cooling case PC(*NL*)-II, with (a) *Low level* , (b) *Medium level* , and (c) *High level* cooling.

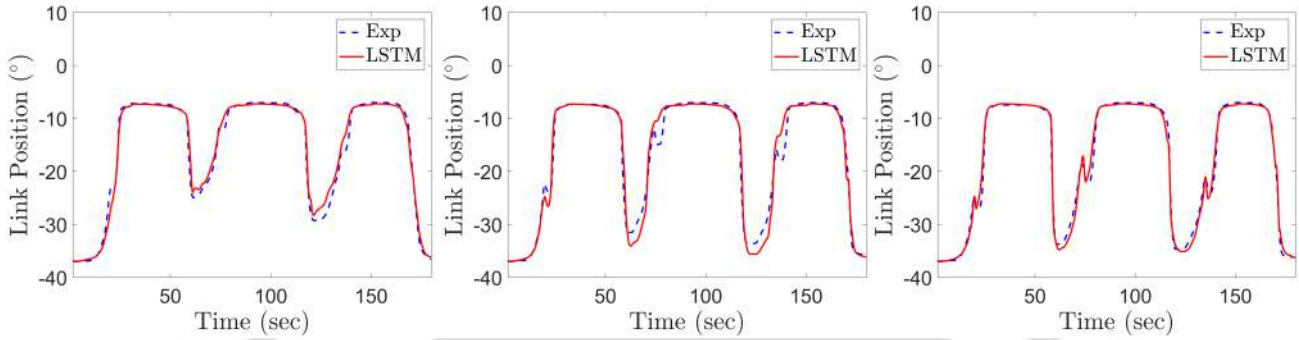

(a) (b) (c)

Figure 6.13: Comparison of the link position predicted by *TN*-II against the experimental one for forced cooling case PC(*NL*)-V, with (a) *Low level* , (b) *Medium level* , and (c) *High level* cooling.

SMA response with high accuracy, by tracing the sharp change in the generated response during forced cooling of the SMA wire actuator.

6.8 Conclusions

In this chapter, the self-sensing capability of the SMA wire actuator is harnessed using an LSTM-based Deep Neural Network (DNN). The need for an LSTM-based neural network has been discussed, followed by a brief description of the proposed LSTM system. For each of the SMA wire actuated systems, the training and testing data sets are defined, and the trained network is tested for a wide variety of loading conditions. It is observed that the derived DNN provides an estimate of superior accuracy across all test cases. For

the SMA wire actuated linear system, the maximum and RMS errors are less than 8% and 2.5% of maximum displacement, respectively. Similar results were found in the case of the 1-DOF manipulator as well, with a maximum and RMS errors being around 8% and 3% of θ_{span}. Thus, the LSTM-based approach provides an estimate with appreciable accuracy, especially in the presence of forced cooling, when there is a sharp change in the thermo-mechanical loading direction; thus demonstrating the true potential of the proposed technique in adeptly modelling the complex SMA behaviour and estimating its response under varied loading conditions.

Chapter 7

Summary and Conclusions

The major contributions of the present work are as follows.

- The constitutive model of SMA proposed by Boyd and Lagoudas [52] has been modified to mimic the minor hysteresis response in SMA during partial phase transformation. It involves a simple but effective methodology, based on the $\sigma - T$ phase diagram. Two new yield parameters (Y_f) as a function of phase transformation parameters, ξ and ξ_r, are introduced in this study. Modified transformation criteria are also defined, using which, the corresponding model parameters are evaluated. The response obtained using the modified model is found to yield an improved response for the partial transformation cases compared to the existing models.

- An Extended Kalman Filter (EKF) has been developed to estimate the response of an SMA wire actuator from its change in electrical resistance. The process model comprises of the modified SMA constitutive relation, heat balance equation, kinematic constraints and force equilibrium equation. Estimated responses are found to mimic the simulated response exactly.

- An experimental setup is designed and fabricated, to measure the electrical resistance variation of the SMA wire, while it is being heated by a set of time-varying voltage input signals and are subjected to natural cooling conditions. Using the measured resistance, the developed EKF has been used to estimate the response of the SMA wire actuated linear system, for complete and partial phase transformation

cases, encountered during heating as well as cooling.

- The estimated system response qualitatively follows the experimental one across all instances. In the case of partial transformation, a maximum estimation error of less than 14% (1.4mm) is observed, as compared to 22% (2.2mm), while using an existing EKF model [84]. Similarly, the RMS error in the present study is found to be 8.36% of δ_{max} as compared to 13.96% of δ_{max}, obtained using existing model [84].

- A Particle filter (PF) based estimator is developed to harness the self-sensing ability of the SMA wire actuator. Using the same process model, the response of the system is estimated using the PF from the measured electrical resistance of the SMA wire. The displacement error was found to be around 4% of the maximum actuation, in the case of natural cooling.

- For the first time in literature, a set of experiments were carried out where the SMA wire actuator is subjected to forced cooling for varied durations, intensities and at different stages of actuation. These experiments provide a holistic understanding of SMA wire performance under a diverse set of loading conditions. Here, the displacement estimated by the proposed PF is slightly better than the existing estimation models, but the improvement is inadequate for practical actuation purposes. The RMS error in the case of the PF ranges from 6-18% compared to 8-20% as found using the developed EKF.

- A modified PF is proposed, estimating the convective heat transfer coefficient in addition to the stress and temperature of the SMA wire. In the presence of forced cooling of the SMA wire actuator, the estimated response obtained using the modified PF has dramatically improved. For partial heating cases (PH(L)-I, PH(L)-II, PH(L)-III), the RMS error is found to be around 6% of the maximum displacement (δ_{max}) as compared to 9-15% of δ_{max} obtained using modified EKF. Additionally, in partial cooling cases (PC(L)-I, PC(L)-II, PC(L)-III), the RMS error of the modified PF is around 6% of δ_{max}, compared to 10-14% of δ_{max} estimated by the modi-

fied EKF. The results reveal the potential of the developed PF as a robust tool in estimating the SMA wire actuator's performance in real-life applications.

- Next, an SMA wire actuated 1-DOF manipulator is considered where the wire is subjected to proportional and non-proportional loading. The process model is derived following the SMA constitutive model, heat balance equation, kinematic constraints and equation of motion. The coupled algebraic differential equation is solved using an incremental iterative approach. Using this model, a PF is developed to estimate the angular position of the SMA wire actuated robotic link by utilizing the measured electrical resistance of the wire.

- An SMA wire actuated manipulator is designed and fabricated. Under natural cooling, the link's angular position, estimated using the PF, closely follows the corresponding measured angle, with a maximum error of 2°. Here, the maximum and RMS errors are found to about 10% and 4.75% of θ_{span}, respectively.

- Another set of experiments are conducted where the SMA wire is cooled intermittently using a fan driven at different speeds, durations, and at distinct stages of actuation. To achieve higher accuracy, the PF is modified to estimate the convective heat transfer coefficient h in addition to the other states of the system. With this modified approach, for partial heating cases, (PH(NL)-I, PH(NL)-II and PH(NL)-III), the RMS error is found to be around 9% of the maximum angular displacement (θ_{span}). Additionally, in the case of the partial cooling condition (PC(NL)-I, PC(NL)-II and PC(NL)-III), the RMS error of the modified PF is around 8% of θ_{span}.

- Next, the initial position of the link (θ_0= -5.8°) is altered to ensure that the link goes past a particular configuration upon activation, wherein the SMA wire encounters the maximum stress condition. This results in a non-proportional variation of stress and temperature of the SMA wire. Here as well, the modified PF provides an estimate with significant accuracy, thus revealing the true potential of the proposed PF.

- An LSTM-based Deep Neural Network has been developed to harness the self-sensing capability of the SMA wire actuators under proportional as well as non-proportional loading. For both the SMA wire actuated linear and non-linear systems, the neural network is trained for forced cooling cases involving cooling duration of 1s and 5s, with the same undergoing at different stages of actuation and of diverse magnitudes. The trained network is tested for cooling cases involving 3s duration. For the SMA wire actuated linear system, a maximum error of about 5% of the maximum displacement and an RMS error of around 2.5% of the maximum displacement are observed. Similar results were found in the case of the 1-DOF manipulator as well, with the maximum and RMS errors being around 8% and 3% of θ_{span}.

List of Publications

Journals

- Sagar Mohan and Atanu Banerjee. "Modelling of minor hysteresis loop of shape memory alloy wire actuator and its application in self-sensing". Smart Materials and Structures, 30(5):055011, 2021.
- Sagar Mohan and Atanu Banerjee. "Particle filter based self sensing shape memory alloy wire actuator under external cooling". Mechanical Systems and Signal Processing, 185:109779, 2023.
- Sagar Mohan, Swarup Kumar Kalita and Atanu Banerjee. "Self Sensing of a Shape Memory Alloy Wire Actuated Manipulator Undergoing Non-Proportional Loading". (under review)
- Sagar Mohan and Atanu Banerjee. "LSTM based Self-Sensing Application of Shape Memory Alloy Wire Actuators under Practical Loading Conditions". (under review)

Book Chapter

- Sagar Mohan and Atanu Banerjee. "Exploring Self-Sensing Behaviour of Shape Memory Alloy Using Kalman Filters Based on Boyd and Lagoudas Model." Recent Advances in Computational and Experimental Mechanics, Vol-I. Springer, Singapore, 2022. 121-130.

Conferences

- Sagar Mohan and Atanu Banerjee. "Exploring Self-Sensing Capability of Shape Memory Alloy Wire Actuator using Kalman Filters". International Conference on Recent Advances in Computational and Experimental Mechanics. September 4-6, 2020, Kharagpur, India.
- Sagar Mohan and Atanu Banerjee. "Modification of Boyd and Lagoudas Model and its Application in Self-Sensing Response of SMA". Congress of the Indian Society of Theoretical and Applied Mechanics. December 9-12, 2020, Hyderabad, India.

Scope of Future Works

- For both natural and forced cooling cases, the developed EKF and the PF models have estimated the systems' response from the change in electrical resistance of the SMA wire actuator quite well. However, in order to replace a feedback sensor, the estimation error needs to be reduced further, which has been taken as a future work.
- Feedback controllers need to be developed based on the estimation of the developed filter models.
- In the present study, only Gaussian noise models are considered; instead, one can explore the effects of the coloured noise as well.

Appendix A

Derivation of Model Parameters - I

Following the discussion in Chapter 2, the model parameters of the modified constitutive model corresponding to cosine hardening (Eqn.(2.17)) and linear Y (Eqn.(2.18)) are derived by using the modified transformation conditions defined in Section 2.4. The cosine hardening function is defined as,

$$h_f(\xi) = \begin{cases} \int_0^{\xi} -\frac{\rho\Delta s_0}{a_1}[\pi - \cos^{-1}(2\xi - 1)]d\xi + (a_3 + a_4)\xi, & \text{for} \quad \dot{\xi} > 0; \\ \int_0^{\xi} -\frac{\rho\Delta s_0}{a_2}[\pi - \cos^{-1}(2\xi - 1)]d\xi + (a_3 - a_4)\xi, & \text{for} \quad \dot{\xi} < 0. \end{cases} \tag{A.1}$$

Following Eqn.(A.1), $\frac{\partial h_f}{\partial \xi}$ is obtained as,

$$\frac{\partial h_f}{\partial \xi} = \begin{cases} -\frac{\rho\Delta s_0}{a_1}[\pi - \cos^{-1}(2\xi - 1)] + (a_3 + a_4), & \text{for} \quad \dot{\xi} > 0; \\ -\frac{\rho\Delta s_0}{a_2}[\pi - \cos^{-1}(2\xi - 1)] + (a_3 - a_4), & \text{for} \quad \dot{\xi} < 0. \end{cases} \tag{A.2}$$

The linear form of yield parameter 'Y' proposed in this study is,

$$Y_f = \begin{cases} Y_1 + Y_2\xi_r(1 - \xi), & \forall \quad \dot{\xi} > 0 \\ Y_1 + Y_3\xi(1 - \xi_r), & \forall \quad \dot{\xi} < 0 \end{cases} \tag{A.3}$$

The thermodynamic force 'Θ' is defined as,

$$\Theta = \sigma H + \frac{1}{2}\sigma^2\Delta S + \sigma\Delta\alpha(T - T_0) - \rho\Delta C_v\left[(T - T_0) - T\ln\left(\frac{T}{T_0}\right)\right]$$

$$+ \rho\Delta s_0 T - \rho\Delta u_0 - \frac{\partial h_f}{\partial \xi}. \tag{A.4}$$

- **Condition 1:** Beginning of forward transformation (point 'a' in Fig.2.1)

  $\sigma = \sigma_{M_s} = C_M(T_0 - M_s),\ \xi = 0,\ \xi_r = 0,\ T = T_0,\ \Theta = Y_f$

$$\Rightarrow \quad \sigma_{M_s} H + \frac{1}{2}\sigma_{M_s}^2 \Delta S + \rho\Delta s_0 T_0 - \rho\Delta u_0 - [(a_3 + a_4)] = Y_1. \tag{A.5}$$

- **Condition 2:** Completion of forward transformation (point 'b' in Fig.2.1)

  $\sigma = \sigma_{M_f} = C_M(T_0 - M_f),\ \xi = 1,\ \xi_r = 0,\ T = T_0,\ \Theta = Y_f$

$$\Rightarrow \quad \sigma_{M_f} H + \frac{1}{2}\sigma_{M_f}^2 \Delta S + \rho\Delta s_0 T_0 - \rho\Delta u_0 - \left[-\frac{\rho\Delta s_0}{a_1}[\pi] + (a_3 + a_4)\right] = Y_1. \tag{A.6}$$

Solving Eqns.(A.5) and (A.6), one obtains

$$\left(\sigma_{M_s} - \sigma_{M_f}\right) H + \frac{1}{2}\left(\sigma_{M_s}^2 - \sigma_{M_f}^2\right) \Delta S - \frac{\rho\Delta s_0 \pi}{a_1} = 0$$

Neglecting $\frac{1}{2}\left(\sigma_{M_s}^2 - \sigma_{M_f}^2\right) \Delta S$, and upon rearranging, the above expression can be written as,

$$a_1 = \frac{\rho\Delta s_0 \pi}{\left(\sigma_{M_s} - \sigma_{M_f}\right) H}$$

$$a_1 = \frac{\rho\Delta s_0 \pi}{C_M\left((T_0 - M_s) - (T_0 - M_f)\right) H} = \frac{\rho\Delta s_0 \pi}{\rho\Delta s_0 \left(M_s - M_f\right)}$$

$$\boxed{a_1 = \frac{\pi}{M_s - M_f}} \tag{A.7}$$

- **Condition 3:** Beginning of reverse transformation (point 'c' in Fig.2.1)

  $\sigma = \sigma_{A_s} = C_A(T_0 - A_s),\ \xi = 1,\ \xi_r = 1,\ T = T_0,\ \Theta = -Y_f$

$$\Rightarrow \quad \sigma_{A_s} H + \frac{1}{2}\sigma_{A_s}^2 \Delta S + \rho\Delta s_0 T_0 - \rho\Delta u_0 - \left[-\frac{\rho\Delta s_0}{a_2}[\pi] + (a_3 - a_4)\right] = -Y_1. \tag{A.8}$$

- **Condition 4:** Completion of reverse transformation (point 'd' in Fig.2.1)

$\sigma = \sigma_{A_f} = C_A(T_0 - A_f),\ \xi = 0,\ \xi_r = 1,\ T = T_0,\ \Theta = -Y_f$

$$\Rightarrow \quad \sigma_{A_f} H + \frac{1}{2}\sigma_{A_f}^2 \Delta S + \rho \Delta s_0 T_0 - \rho \Delta u_0 - [(a_3 - a_4)] = -Y_1. \tag{A.9}$$

Solving Eqns.(A.8) and (A.9), one obtains

$$\left(\sigma_{A_s} - \sigma_{A_f}\right) H + \frac{1}{2}\left(\sigma_{A_s}^2 - \sigma_{A_f}^2\right) \Delta S + \frac{\rho \Delta s_0 \pi}{a_2} = 0 \tag{A.10}$$

Neglecting $\frac{1}{2}\left(\sigma_{A_s}^2 - \sigma_{A_f}^2\right) \Delta S$, and upon rearranging, the above expression can be written as,

$$a_2 = \frac{\rho \Delta s_0 \pi}{\left(\sigma_{A_f} - \sigma_{A_s}\right) H}$$

$$a_2 = \frac{\rho \Delta s_0 \pi}{C_A\left((T_0 - A_f) - (T_0 - A_s)\right) H} = \frac{\rho \Delta s_0 \pi}{\rho \Delta s_0 \left(A_f - A_s\right)}$$

$$\boxed{a_2 = \frac{\pi}{A_f - A_s}} \tag{A.11}$$

Further, solving Eqns.(A.5) and (A.9), one obtains

$$\left(\sigma_{M_s} - \sigma_{A_f}\right) H + \frac{1}{2}\left(\sigma_{M_s}^2 - \sigma_{A_f}^2\right) \Delta S - 2a_4 = 2Y_1 \tag{A.12}$$

Neglecting $\frac{1}{2}\left(\sigma_{M_s}^2 - \sigma_{A_f}^2\right) \Delta S$, and upon rearranging, the above expression can be written as,

$$Y_1 = \frac{1}{2}\left(\sigma_{M_s} - \sigma_{A_f}\right) H - a_4$$

Substituting the values of σ_{M_s} and σ_{A_f}, and upon solving, one obtains

$$\boxed{Y_1 = \frac{\rho \Delta s_0 (M_s - A_f)}{2} - a_4} \tag{A.13}$$

- **Condition 5:** Continuity of G at the point of reversal, *i.e.*, $h_f(\xi = \xi_r)|_{\dot{\xi}>0} = h_f(\xi =$

$\xi_r)|_{\dot{\xi}<0}$.

$$\Rightarrow \int_0^{\xi_{r0}} -\frac{\rho\Delta s_0}{a_1}[\pi - \cos^{-1}(2\xi-1)]d\xi + (a_3+a_4)\xi_{r0}$$

$$= \int_0^{\xi_{r0}} -\frac{\rho\Delta s_0}{a_2}[\pi - \cos^{-1}(2\xi-1)]d\xi + (a_3-a_4)\xi_{r0},$$

$$-\frac{\rho\Delta s_0}{a_1}\left[\pi\xi - \cos^{-1}(2\xi-1)\frac{(2\xi-1)}{2} + \frac{\sqrt{1-(2\xi-1)^2}}{2}\right]_0^{\xi_{r0}} + a_4\xi_{r0}$$

$$= -\frac{\rho\Delta s_0}{a_2}\left[\pi\xi - \cos^{-1}(2\xi-1)\frac{(2\xi-1)}{2} + \frac{\sqrt{1-(2\xi-1)^2}}{2}\right]_0^{\xi_{r0}} - a_4\xi_{r0},$$

$$-\frac{\rho\Delta s_0}{a_1}\left[\left(\pi\xi_{r0} - \cos^{-1}(2\xi_{r0}-1)\frac{(2\xi_{r0}-1)}{2} + \frac{\sqrt{1-(2\xi_{r0}-1)^2}}{2}\right) - \left(\frac{\pi}{2}\right)\right] + a_4\xi_{r0}$$

$$= -\frac{\rho\Delta s_0}{a_2}\left[\left(\pi\xi_{r0} - \cos^{-1}(2\xi_{r0}-1)\frac{(2\xi_{r0}-1)}{2} + \frac{\sqrt{1-(2\xi_{r0}-1)^2}}{2}\right) - \left(\frac{\pi}{2}\right)\right] - a_4\xi_{r0},$$

$$2a_4\xi_{r0} = \left[\left(\pi\xi_{r0} - \cos^{-1}(2\xi_{r0}-1)\frac{(2\xi_{r0}-1)}{2} - \frac{\sqrt{1-(2\xi_{r0}-1)^2}}{2}\right) - \left(\frac{\pi}{2}\right)\right].\left[\frac{\rho\Delta s_0}{a_1} - \frac{\rho\Delta s_0}{a_2}\right].$$

$$\boxed{a_4 = \left[\frac{\pi}{2} - \frac{(2\xi_r-1)\cos^{-1}(2\xi_r-1)}{4\xi_r} - \frac{\sqrt{1-(2\xi_r-1)^2}}{4\xi_r} - \frac{\pi}{4\xi_r}\right]\rho\Delta s_0\left(\frac{1}{a_1}-\frac{1}{a_2}\right)} \tag{A.14}$$

Here, the numerical value of ξ_r, *i.e.*, ξ_{r0} is substituted into above expression to obtain the value of a_4.

Next, following Eqns.(A.5) and (A.12), one obtains

$$\sigma_{M_s}H + \frac{1}{2}\sigma_{M_s}^2\Delta S + \rho\Delta s_0 T_0 - \frac{\rho\Delta s_0(M_s+A_f)}{2} - a_3 - \left[\frac{(\sigma_{M_s}-\sigma_{A_f})H}{2} + \frac{(\sigma_{M_s}^2-\sigma_{A_f}^2)}{4}\right] = 0,$$

$$a_3 = \frac{(\sigma_{M_s}+\sigma_{A_f})H}{2} + \frac{(\sigma_{M_s}^2+\sigma_{A_f}^2)}{4} + \rho\Delta s_0 T_0 - \frac{\rho\Delta s_0(M_s+A_f)}{2}.$$

Substituting the values of σ_{M_s} and σ_{A_f} and solving the above equation, one obtains the expression for a_3 as,

$$\boxed{a_3 = \frac{1}{4}\left[C_M^2(T_0-M_s)^2 + C_A^2(T_0-A_f)^2\right]\Delta S.} \tag{A.15}$$

- **Condition 6:** Beginning of partial reverse transformation (point 'f' in Fig.2.1)

$\sigma = \sigma_{A_s} = C_A(T_0 - A_s),\ \xi = \xi_{r_f},\ \xi_r = \xi_{r_f},\ T = T_0,\ \Theta = -Y_f$

$$\sigma_{A_s}H + \frac{1}{2}\sigma_{A_s}^2\Delta S + \rho\Delta s_0 T_0 - \rho\Delta u_0 - \left[-\frac{\rho\Delta s_0}{a_2}[\pi - \cos^{-1}(2\xi_{r_f} - 1)] + (a_3 - a_4)\right] = -Y_1 - Y_3\xi_{r_f}(1 - \xi_{r_f}),$$

$$\sigma_{A_s}H + \frac{1}{2}\sigma_{A_s}^2\Delta S + \rho\Delta s_0 T_0 - \frac{\rho\Delta s_0(M_s + A_f)}{2} + \frac{\rho\Delta s_0}{a_2}[\pi - \cos^{-1}(2\xi_{r_f} - 1)] - a_3 + (a_4 + Y_1) + Y_3\xi_{r_f}(1 - \xi_{r_f}) = 0.$$

Substituting Eqns.(A.12) and (A.15), one obtains

$$\sigma_{A_s}H + \frac{1}{2}\sigma_{A_s}^2\Delta S + \rho\Delta s_0 T_0 - \frac{\rho\Delta s_0(M_s + A_f)}{2} + \frac{\rho\Delta s_0}{a_2}[\pi - \cos^{-1}(2\xi_{r_f} - 1)] - \frac{\left(\sigma_{M_s}^2 + \sigma_{A_f}^2\right)\Delta S}{4} + \left[\frac{\left(\sigma_{M_s} - \sigma_{A_f}\right)H}{2} + \frac{\left(\sigma_{M_s}^2 - \sigma_{A_f}^2\right)\Delta S}{4}\right] + Y_3\xi_{r_f}(1 - \xi_{r_f}) = 0,$$

$$\left(\sigma_{A_s} - \sigma_{A_f}\right)H + \frac{1}{2}\left(\sigma_{A_s}^2 - \sigma_{A_f}^2\right)\Delta S + \frac{\rho\Delta s_0}{a_2}\pi - \frac{\rho\Delta s_0}{a_2}\cos^{-1}(2\xi_{r_f} - 1) + Y_3\xi_{r_f}(1 - \xi_{r_f}) = 0$$

Following Eqn.(A.10), the above equation can be denoted as,

$$-\frac{\rho\Delta s_0}{a_2}\pi + \frac{\rho\Delta s_0}{a_2}\pi + Y_3\xi_{r_f}(1 - \xi_{r_f}) = \frac{\rho\Delta s_0}{a_2}\cos^{-1}(2\xi_{r_f} - 1)$$

$$\boxed{Y_3 = \frac{\rho\Delta s_0\cos^{-1}(2\xi_r - 1)}{a_2\xi_r(1 - \xi_r)}} \qquad \text{(A.16)}$$

Here, the numerical value of ξ_r, *i.e.*, ξ_{r_f} which is the numerical values of ξ at the point of reversal, f, is substituted into above expression to obtain the value of Y_3. Also, $\xi_{r_f} = \xi_e$, since $e \to f$ is an elastic path.

- **Condition 7:** Beginning of partial forward transformation (point 'h' in Fig.2.1)

$\sigma = \sigma_{M_s} = C_M(T_0 - M_s),\ \xi = \xi_{r_h},\ \xi_r = \xi_{r_h},\ T = T_0,\ \Theta = Y_f$

$$\sigma_{M_s}H + \frac{1}{2}\sigma_{M_s}^2\Delta S + \rho\Delta s_0 T_0 - \rho\Delta u_0 - \left[-\frac{\rho\Delta s_0}{a_1}[\pi - \cos^{-1}(2\xi_{r_h} - 1)] + (a_3 + a_4)\right] = Y_1 + Y_2\xi_{r_h}(1 - \xi_{r_h}),$$

$$\sigma_{M_s}H + \frac{1}{2}\sigma_{M_s}^2\Delta S + \rho\Delta s_0 T_0 - \frac{\rho\Delta s_0(M_s + A_f)}{2} + \frac{\rho\Delta s_0}{a_1}[\pi - \cos^{-1}(2\xi_{r_h} - 1)]$$
$$- a_3 - (a_4 + Y_1) = Y_2\xi_{r_h}(1 - \xi_{r_h}).$$

Substituting Eqns.(A.12) and (A.15), one obtains

$$\sigma_{M_s}H + \frac{1}{2}\sigma_{M_s}^2\Delta S + \rho\Delta s_0 T_0 - \frac{\rho\Delta s_0(M_s + A_f)}{2} + \frac{\rho\Delta s_0}{a_1}[\pi - \cos^{-1}(2\xi_{r_h} - 1)]$$
$$- \frac{\left(\sigma_{M_s}^2 + \sigma_{A_f}^2\right)\Delta S}{4} - \left[\frac{\left(\sigma_{M_s} - \sigma_{A_f}\right)H}{2} + \frac{\left(\sigma_{M_s}^2 - \sigma_{A_f}^2\right)\Delta S}{4}\right] = Y_2\xi_{r_h}(1 - \xi_{r_h}),$$
$$\frac{\left(\sigma_{M_s} + \sigma_{A_f}\right)H}{2} + \rho\Delta s_0 T_0 - \frac{\rho\Delta s_0(M_s + A_f)}{2} + \frac{\rho\Delta s_0}{a_1}[\pi - \cos^{-1}(2\xi_{r_h} - 1)] = Y_2\xi_{r_h}(1 - \xi_{r_h}),$$

$$\boxed{Y_2 = \frac{\rho\Delta s_0[\pi - \cos^{-1}(2\xi_r - 1)]}{a_1\xi_r(1 - \xi_r)}} \tag{A.17}$$

Here, the numerical value of ξ_r, *i.e.*, ξ_{r_h} which is the numerical values of ξ at the point of reversal, h, is substituted into above expression to obtain the value of Y_2. Also, $\xi_{r_h} = \xi_g$, since $g \to h$ is an elastic path.

Appendix B

Derivation of Model Parameters - II

Following the discussion in Chapter 2, the model parameters of the modified constitutive model corresponding to cosine hardening (Eqn.(2.17)) and exponential Y (Eqn.(2.20)) are derived by using the modified transformation conditions defined in Section 2.4. The cosine hardening function is defined as,

$$h_f(\xi) = \begin{cases} \int_0^{\xi} -\frac{\rho\Delta s_0}{a_1}[\pi - \cos^{-1}(2\xi - 1)]d\xi + (a_3 + a_4)\xi, & \text{for} \quad \dot{\xi} > 0; \\ \int_0^{\xi} -\frac{\rho\Delta s_0}{a_2}[\pi - \cos^{-1}(2\xi - 1)]d\xi + (a_3 - a_4)\xi, & \text{for} \quad \dot{\xi} < 0. \end{cases} \tag{B.1}$$

Following Eqn.(B.1), $\frac{\partial h_f}{\partial \xi}$ is defined as,

$$\frac{\partial h_f}{\partial \xi} = \begin{cases} -\frac{\rho\Delta s_0}{a_1}[\pi - \cos^{-1}(2\xi - 1)] + (a_3 + a_4), & \text{for} \quad \dot{\xi} > 0; \\ -\frac{\rho\Delta s_0}{a_2}[\pi - \cos^{-1}(2\xi - 1)] + (a_3 - a_4), & \text{for} \quad \dot{\xi} < 0. \end{cases} \tag{B.2}$$

The exponential form of yield parameter 'Y' proposed in this study is,

$$Y_f = \begin{cases} Y_1 + Y_2\xi_r\left(e^{\gamma(1-\xi)} - 1\right), & \forall \quad \dot{\xi} > 0 \\ Y_1 + Y_3(1 - \xi_r)\left(e^{\gamma\xi} - 1\right), & \forall \quad \dot{\xi} < 0 \end{cases} \tag{B.3}$$

The thermodynamic force 'Θ' is defined as,

$$\Theta = \sigma H + \frac{1}{2}\sigma^2\Delta S + \sigma\Delta\alpha(T - T_0) - \rho\Delta C_v\left[(T - T_0) - T\ln\left(\frac{T}{T_0}\right)\right]$$

$$+ \rho\Delta s_0 T - \rho\Delta u_0 - \frac{\partial h_f}{\partial \xi}. \tag{B.4}$$

- **Condition 1:** Beginning of forward transformation (point 'a' in Fig.2.1)

  $\sigma = \sigma_{M_s} = C_M(T_0 - M_s),\ \xi = 0,\ \xi_r = 0,\ T = T_0,\ \Theta = Y_f$

$$\Rightarrow \quad \sigma_{M_s} H + \frac{1}{2}\sigma_{M_s}^2 \Delta S + \rho\Delta s_0 T_0 - \rho\Delta u_0 - [(a_3 + a_4)] = Y_1. \tag{B.5}$$

- **Condition 2:** Completion of forward transformation (point 'b' in Fig.2.1)

  $\sigma = \sigma_{M_f} = C_M(T_0 - M_f),\ \xi = 1,\ \xi_r = 0,\ T = T_0,\ \Theta = Y_f$

$$\Rightarrow \quad \sigma_{M_f} H + \frac{1}{2}\sigma_{M_f}^2 \Delta S + \rho\Delta s_0 T_0 - \rho\Delta u_0 - \left[-\frac{\rho\Delta s_0}{a_1}[\pi] + (a_3 + a_4)\right] = Y_1. \tag{B.6}$$

Solving Eqns.(B.5) and (B.6), one obtains

$$\left(\sigma_{M_s} - \sigma_{M_f}\right) H + \frac{1}{2}\left(\sigma_{M_s}^2 - \sigma_{M_f}^2\right) \Delta S - \frac{\rho\Delta s_0 \pi}{a_1} = 0$$

Neglecting $\frac{1}{2}\left(\sigma_{M_s}^2 - \sigma_{M_f}^2\right) \Delta S$, and upon rearranging, the above expression can be written as,

$$a_1 = \frac{\rho\Delta s_0 \pi}{\left(\sigma_{M_s} - \sigma_{M_f}\right) H}$$

$$a_1 = \frac{\rho\Delta s_0 \pi}{C_M\left((T_0 - M_s) - (T_0 - M_f)\right) H} = \frac{\rho\Delta s_0 \pi}{\rho\Delta s_0 \left(M_s - M_f\right)}$$

$$\boxed{a_1 = \frac{\pi}{M_s - M_f}} \tag{B.7}$$

- **Condition 3:** Beginning of reverse transformation (point 'c' in Fig.2.1)

  $\sigma = \sigma_{A_s} = C_A(T_0 - A_s),\ \xi = 1,\ \xi_r = 1,\ T = T_0,\ \Theta = -Y_f$

$$\Rightarrow \quad \sigma_{A_s} H + \frac{1}{2}\sigma_{A_s}^2 \Delta S + \rho\Delta s_0 T_0 - \rho\Delta u_0 - \left[-\frac{\rho\Delta s_0}{a_2}[\pi] + (a_3 - a_4)\right] = -Y_1. \tag{B.8}$$

- **Condition 4:** Completion of reverse transformation (point 'd' in Fig.2.1)

$\sigma = \sigma_{A_f} = C_A(T_0 - A_f),\ \xi = 0,\ \xi_r = 1,\ T = T_0,\ \Theta = -Y_f$

$$\Rightarrow \quad \sigma_{A_f} H + \frac{1}{2}\sigma_{A_f}^2 \Delta S + \rho \Delta s_0 T_0 - \rho \Delta u_0 - [(a_3 - a_4)] = -Y_1. \tag{B.9}$$

Solving Eqns.(B.8) and (B.9), one obtains

$$\left(\sigma_{A_s} - \sigma_{A_f}\right) H + \frac{1}{2}\left(\sigma_{A_s}^2 - \sigma_{A_f}^2\right) \Delta S + \frac{\rho \Delta s_0 \pi}{a_2} = 0 \tag{B.10}$$

Neglecting $\frac{1}{2}\left(\sigma_{A_s}^2 - \sigma_{A_f}^2\right) \Delta S$, and upon rearranging, the above expression can be written as,

$$a_2 = \frac{\rho \Delta s_0 \pi}{\left(\sigma_{A_f} - \sigma_{A_s}\right) H}$$

$$a_2 = \frac{\rho \Delta s_0 \pi}{C_A\left((T_0 - A_f) - (T_0 - A_s)\right) H} = \frac{\rho \Delta s_0 \pi}{\rho \Delta s_0 \left(A_f - A_s\right)}$$

$$\boxed{a_2 = \frac{\pi}{A_f - A_s}} \tag{B.11}$$

Further, solving Eqns.(B.5) and (B.9), one obtains

$$\left(\sigma_{M_s} - \sigma_{A_f}\right) H + \frac{1}{2}\left(\sigma_{M_s}^2 - \sigma_{A_f}^2\right) \Delta S - 2a_4 = 2Y_1 \tag{B.12}$$

Neglecting $\frac{1}{2}\left(\sigma_{M_s}^2 - \sigma_{A_f}^2\right) \Delta S$, and upon rearranging, the above expression can be written as,

$$Y_1 = \frac{1}{2}\left(\sigma_{M_s} - \sigma_{A_f}\right) H - a_4$$

Substituting the values of σ_{M_s} and σ_{A_f}, and upon solving, one obtains

$$\boxed{Y_1 = \frac{\rho \Delta s_0 (M_s - A_f)}{2} - a_4} \tag{B.13}$$

- **Condition 5:** Continuity of G at the point of reversal, *i.e.*, $h_f(\xi = \xi_r)|_{\dot{\xi}>0} = h_f(\xi =$

$\xi_r)|_{\dot{\xi}<0}$.

$$\Rightarrow \int_0^{\xi_{r0}} -\frac{\rho\Delta s_0}{a_1}[\pi - \cos^{-1}(2\xi-1)]d\xi + (a_3+a_4)\xi_{r0}$$

$$= \int_0^{\xi_{r0}} -\frac{\rho\Delta s_0}{a_2}[\pi - \cos^{-1}(2\xi-1)]d\xi + (a_3-a_4)\xi_{r0},$$

$$-\frac{\rho\Delta s_0}{a_1}\left[\pi\xi - \cos^{-1}(2\xi-1)\frac{(2\xi-1)}{2} + \frac{\sqrt{1-(2\xi-1)^2}}{2}\right]_0^{\xi_{r0}} + a_4\xi_{r0}$$

$$= -\frac{\rho\Delta s_0}{a_2}\left[\pi\xi - \cos^{-1}(2\xi-1)\frac{(2\xi-1)}{2} + \frac{\sqrt{1-(2\xi-1)^2}}{2}\right]_0^{\xi_{r0}} - a_4\xi_{r0},$$

$$-\frac{\rho\Delta s_0}{a_1}\left[\left(\pi\xi_{r0} - \cos^{-1}(2\xi_{r0}-1)\frac{(2\xi_{r0}-1)}{2} + \frac{\sqrt{1-(2\xi_{r0}-1)^2}}{2}\right) - \left(\frac{\pi}{2}\right)\right] + a_4\xi_{r0}$$

$$= -\frac{\rho\Delta s_0}{a_2}\left[\left(\pi\xi_{r0} - \cos^{-1}(2\xi_{r0}-1)\frac{(2\xi_{r0}-1)}{2} + \frac{\sqrt{1-(2\xi_{r0}-1)^2}}{2}\right) - \left(\frac{\pi}{2}\right)\right] - a_4\xi_{r0},$$

$$2a_4\xi_{r0} = \left[\left(\pi\xi_{r0} - \cos^{-1}(2\xi_{r0}-1)\frac{(2\xi_{r0}-1)}{2} - \frac{\sqrt{1-(2\xi_{r0}-1)^2}}{2}\right) - \left(\frac{\pi}{2}\right)\right].\left[\frac{\rho\Delta s_0}{a_1} - \frac{\rho\Delta s_0}{a_2}\right].$$

$$\boxed{a_4 = \left[\frac{\pi}{2} - \frac{(2\xi_r-1)\cos^{-1}(2\xi_r-1)}{4\xi_r} - \frac{\sqrt{1-(2\xi_r-1)^2}}{4\xi_r} - \frac{\pi}{4\xi_r}\right]\rho\Delta s_0\left(\frac{1}{a_1}-\frac{1}{a_2}\right)} \tag{B.14}$$

Here, the numerical value of ξ_r, *i.e.*, ξ_{r0} is substituted into above expression to obtain the value of a_4.

Next, following Eqns.(B.5) and (B.12), one obtains

$$\sigma_{M_s}H + \frac{1}{2}\sigma_{M_s}^2\Delta S + \rho\Delta s_0 T_0 - \frac{\rho\Delta s_0(M_s+A_f)}{2} - a_3 - \left[\frac{(\sigma_{M_s}-\sigma_{A_f})H}{2} + \frac{(\sigma_{M_s}^2-\sigma_{A_f}^2)}{4}\right] = 0,$$

$$a_3 = \frac{(\sigma_{M_s}+\sigma_{A_f})H}{2} + \frac{(\sigma_{M_s}^2+\sigma_{A_f}^2)}{4} + \rho\Delta s_0 T_0 - \frac{\rho\Delta s_0(M_s+A_f)}{2}.$$

Substituting the values of σ_{M_s} and σ_{A_f} and solving the above equation, one obtains the expression for a_3 as,

$$\boxed{a_3 = \frac{1}{4}\left[C_M^2(T_0-M_s)^2 + C_A^2(T_0-A_f)^2\right]\Delta S.} \tag{B.15}$$

- **Condition 6:** Beginning of partial reverse transformation (point 'f' in Fig.2.1)

$\sigma = \sigma_{A_s} = C_A(T_0 - A_s),\ \xi = \xi_{r_f},\ \xi_r = \xi_{r_f},\ T = T_0,\ \Theta = -Y_f$

$$\Rightarrow \quad \sigma_{A_s} H + \frac{1}{2}\sigma_{A_s}^2 \Delta S + \rho \Delta s_0 T_0 - \rho \Delta u_0 - \left[-\frac{\rho \Delta s_0}{a_2}[\pi - \cos^{-1}(2\xi_{r_f} - 1)] + (a_3 - a_4) \right] = -Y_1 - Y_3(1 - \xi_{r_f}) \left(e^{\gamma \xi_{r_f}} - 1 \right),$$

$$\sigma_{A_s} H + \frac{1}{2}\sigma_{A_s}^2 \Delta S + \rho \Delta s_0 T_0 - \frac{\rho \Delta s_0 (M_s + A_f)}{2} + \frac{\rho \Delta s_0}{a_2}[\pi - \cos^{-1}(2\xi_{r_f} - 1)] - a_3 + (a_4 + Y_1) + Y_3(1 - \xi_{r_f}) \left(e^{\gamma \xi_{r_f}} - 1 \right) = 0.$$

Substituting Eqns.(B.12) and (B.15), one obtains

$$\sigma_{A_s} H + \frac{1}{2}\sigma_{A_s}^2 \Delta S + \rho \Delta s_0 T_0 - \frac{\rho \Delta s_0 (M_s + A_f)}{2} + \frac{\rho \Delta s_0}{a_2}[\pi - \cos^{-1}(2\xi_{r_f} - 1)] - \frac{\left(\sigma_{M_s}^2 + \sigma_{A_f}^2 \right) \Delta S}{4} + \left[\frac{\left(\sigma_{M_s} - \sigma_{A_f} \right) H}{2} + \frac{\left(\sigma_{M_s}^2 - \sigma_{A_f}^2 \right) \Delta S}{4} \right] + Y_3(1 - \xi_{r_f}) \left(e^{\gamma \xi_{r_f}} - 1 \right) = 0,$$

$$\left(\sigma_{A_s} - \sigma_{A_f} \right) H + \frac{1}{2} \left(\sigma_{A_s}^2 - \sigma_{A_f}^2 \right) \Delta S + \frac{\rho \Delta s_0}{a_2}\pi - \frac{\rho \Delta s_0}{a_2} \cos^{-1}(2\xi_{r_f} - 1) + Y_3(1 - \xi_{r_f}) \left(e^{\gamma \xi_{r_f}} - 1 \right) = 0$$

Following Eqn.(B.10), the above equation can be denoted as,

$$-\frac{\rho \Delta s_0}{a_2}\pi + \frac{\rho \Delta s_0}{a_2}\pi + Y_3(1 - \xi_{r_f}) \left(e^{\gamma \xi_{r_f}} - 1 \right) = \frac{\rho \Delta s_0}{a_2} \cos^{-1}(2\xi_{r_f} - 1)$$

$$\boxed{Y_3 = \frac{\rho \Delta s_0 \cos^{-1}(2\xi_r - 1)}{a_2(1 - \xi_r)\left(e^{\gamma \xi_r} - 1 \right)}} \tag{B.16}$$

Here, the numerical value of ξ_r, *i.e.*, ξ_{r_f} which is the numerical values of ξ at the point of reversal, f, is substituted into above expression to obtain the value of Y_3. Also, $\xi_{r_f} = \xi_e$, since $e \rightarrow f$ is an elastic path.

- **Condition 7:** Beginning of partial forward transformation (point 'h' in Fig.2.1)

$\sigma = \sigma_{M_s} = C_M(T_0 - M_s),\ \xi = \xi_{r_h},\ \xi_r = \xi_{r_h},\ T = T_0,\ \Theta = Y_f$

$$\Rightarrow \quad \sigma_{M_s} H + \frac{1}{2}\sigma_{M_s}^2 \Delta S + \rho \Delta s_0 T_0 - \rho \Delta u_0$$
$$- \left[-\frac{\rho \Delta s_0}{a_1}[\pi - \cos^{-1}(2\xi_{r_h} - 1)] + (a_3 + a_4) \right] = Y_1 + Y_2 \xi_{r_h} \left(e^{\gamma(1-\xi_{r_h})} - 1 \right),$$
$$\sigma_{M_s} H + \frac{1}{2}\sigma_{M_s}^2 \Delta S + \rho \Delta s_0 T_0 - \frac{\rho \Delta s_0 (M_s + A_f)}{2} + \frac{\rho \Delta s_0}{a_1}[\pi - \cos^{-1}(2\xi_{r_h} - 1)]$$
$$- a_3 - (a_4 + Y_1) = Y_2 \xi_{r_h} \left(e^{\gamma(1-\xi_{r_h})} - 1 \right).$$

Substituting Eqns.(B.12) and (B.15), one obtains

$$\sigma_{M_s} H + \frac{1}{2}\sigma_{M_s}^2 \Delta S + \rho \Delta s_0 T_0 - \frac{\rho \Delta s_0 (M_s + A_f)}{2} + \frac{\rho \Delta s_0}{a_1}[\pi - \cos^{-1}(2\xi_{r_h} - 1)]$$
$$- \frac{\left(\sigma_{M_s}^2 + \sigma_{A_f}^2\right) \Delta S}{4} - \left[\frac{\left(\sigma_{M_s} - \sigma_{A_f}\right) H}{2} + \frac{\left(\sigma_{M_s}^2 - \sigma_{A_f}^2\right) \Delta S}{4} \right] = Y_2 \xi_{r_h} \left(e^{\gamma(1-\xi_{r_h})} - 1 \right),$$
$$\frac{\left(\sigma_{M_s} + \sigma_{A_f}\right) H}{2} + \rho \Delta s_0 T_0 - \frac{\rho \Delta s_0 (M_s + A_f)}{2}$$
$$+ \frac{\rho \Delta s_0}{a_1}[\pi - \cos^{-1}(2\xi_{r_h} - 1)] = Y_2 \xi_{r_h} \left(e^{\gamma(1-\xi_{r_h})} - 1 \right),$$

$$\boxed{Y_2 = \frac{\rho \Delta s_0 [\pi - \cos^{-1}(2\xi_r - 1)]}{a_1 \xi_r \left(e^{\gamma(1-\xi_r)} - 1 \right)}} \tag{B.17}$$

Here, the numerical value of ξ_r, *i.e.*, ξ_{r_h} which is the numerical values of ξ at the point of reversal, h, is substituted into above expression to obtain the value of Y_2. Also, $\xi_{r_h} = \xi_g$, since $g \rightarrow h$ is an elastic path.

Appendix C

Derivation of Model Parameters - III

Following the discussion in Chapter 4, the model parameters of the modified constitutive model corresponding to smooth hardening (Eqn.(4.6)) and exponential Y (Eqn.(2.20)) are derived by using the modified transformation conditions defined in Section 2.4. The smooth hardening function is defined as,

$$h_f(\xi) = \begin{cases} \frac{1}{2}a_1\left[\frac{\xi^{n_1+1}}{n_1+1} + \frac{(1-\xi)^{n_2+1}}{n_2+1}\right] + (a_3+a_4)\xi & \forall \quad \dot{\xi} > 0 \\ \frac{1}{2}a_2\left[\frac{\xi^{n_3+1}}{n_3+1} + \frac{(1-\xi)^{n_4+1}}{n_4+1}\right] + (a_3-a_4)\xi & \forall \quad \dot{\xi} < 0 \end{cases} \tag{C.1}$$

Following Eqn.(C.1), $\frac{\partial h_f}{\partial \xi}$ is defined as,

$$\frac{\partial h_f}{\partial \xi} = \begin{cases} \frac{1}{2}a_1[\xi^{n_1} - (1-\xi)^{n_2}] + (a_3+a_4), & \text{for} \quad \dot{\xi} > 0; \\ \frac{1}{2}a_2[\xi^{n_3} - (1-\xi)^{n_4}] + (a_3-a_4), & \text{for} \quad \dot{\xi} < 0. \end{cases} \tag{C.2}$$

The exponential form of yield parameter 'Y' proposed in this study is,

$$Y_f = \begin{cases} Y_1 + Y_2\xi_r\left(e^{\gamma(1-\xi)} - 1\right), & \forall \quad \dot{\xi} > 0 \\ Y_1 + Y_3(1-\xi_r)\left(e^{\gamma\xi} - 1\right), & \forall \quad \dot{\xi} < 0 \end{cases} \tag{C.3}$$

The thermodynamic force 'Θ' is defined as,

$$\Theta = \sigma H + \frac{1}{2}\sigma^2\Delta S + \sigma\Delta\alpha(T-T_0) - \rho\Delta C_v\left[(T-T_0) - T\ln\left(\frac{T}{T_0}\right)\right]$$

$$+ \rho\Delta s_0 T - \rho\Delta u_0 - \frac{\partial h_f}{\partial \xi}. \tag{C.4}$$

- **Condition 1:** Beginning of forward transformation (point 'a' in Fig.2.1)

  $\sigma = \sigma_{M_s} = C_M(T_0 - M_s),\ \xi = 0,\ \xi_r = 0,\ T = T_0,\ \Theta = Y_f$

$$\sigma_{M_s} H + \frac{1}{2}\sigma_{M_s}^2 \Delta S + \rho\Delta s_0 T_0 - \rho\Delta u_0 - \left[-\frac{1}{2}a_1 + (a_3 + a_4)\right] = Y_1. \tag{C.5}$$

- **Condition 2:** Completion of forward transformation (point 'b' in Fig.2.1)

  $\sigma = \sigma_{M_f} = C_M(T_0 - M_f),\ \xi = 1,\ \xi_r = 0,\ T = T_0,\ \Theta = Y_f$

$$\sigma_{M_f} H + \frac{1}{2}\sigma_{M_f}^2 \Delta S + \rho\Delta s_0 T_0 - \rho\Delta u_0 - \left[\frac{1}{2}a_1 + (a_3 + a_4)\right] = Y_1. \tag{C.6}$$

Solving Eqns.(C.5) and (C.6), one obtains

$$\left(\sigma_{M_s} - \sigma_{M_f}\right) H + \frac{1}{2}\left(\sigma_{M_s}^2 - \sigma_{M_f}^2\right) \Delta S + a_1 = 0 \tag{C.7}$$

Neglecting $\frac{1}{2}\left(\sigma_{M_s}^2 - \sigma_{M_f}^2\right)\Delta S$, and upon rearranging, the above expression can be written as,

$$a_1 = \left(\sigma_{M_f} - \sigma_{M_s}\right) H$$

$$a_1 = C_M\left((T_0 - M_f) - (T_0 - M_s)\right) H$$

$$\boxed{a_1 = \rho\Delta s_0 \left(M_f - M_s\right)} \tag{C.8}$$

- **Condition 3:** Beginning of reverse transformation (point 'c' in Fig.2.1)

  $\sigma = \sigma_{A_s} = C_A(T_0 - A_s),\ \xi = 1,\ \xi_r = 1,\ T = T_0,\ \Theta = -Y_f$

$$\sigma_{A_s} H + \frac{1}{2}\sigma_{A_s}^2 \Delta S + \rho\Delta s_0 T_0 - \rho\Delta u_0 - \left[\frac{1}{2}a_2 + (a_3 - a_4)\right] = -Y_1. \tag{C.9}$$

- **Condition 4:** Completion of reverse transformation (point 'd' in Fig.2.1)

$\sigma = \sigma_{A_f} = C_A(T_0 - A_f),\ \xi = 0,\ \xi_r = 1,\ T = T_0,\ \Theta = -Y_f$

$$\sigma_{A_f} H + \frac{1}{2}\sigma_{A_f}^2 \Delta S + \rho \Delta s_0 T_0 - \rho \Delta u_0 - \left[-\frac{1}{2}a_2 + (a_3 - a_4)\right] = -Y_1. \tag{C.10}$$

Solving Eqns.(C.9) and (C.10), one obtains

$$\left(\sigma_{A_s} - \sigma_{A_f}\right) H + \frac{1}{2}\left(\sigma_{A_s}^2 - \sigma_{A_f}^2\right) \Delta S = a_2 \tag{C.11}$$

Neglecting $\frac{1}{2}\left(\sigma_{A_s}^2 - \sigma_{A_f}^2\right) \Delta S$, the above expression can be written as,

$$a_2 = \left(\sigma_{A_s} - \sigma_{A_f}\right) H$$

$$a_2 = C_A\left((T_0 - A_s) - (T_0 - A_f)\right) H$$

$$\boxed{a_2 = \rho \Delta s_0 \left(A_s - A_f\right)} \tag{C.12}$$

Further, solving Eqns.(C.5) and (C.10), one obtains

$$\left(\sigma_{M_s} - \sigma_{A_f}\right) H + \frac{1}{2}\left(\sigma_{M_s}^2 - \sigma_{A_f}^2\right) \Delta S + \left(\frac{a_1 - a_2}{2}\right) - 2a_4 = 2Y_1 \tag{C.13}$$

$$a_4 + Y_1 = \frac{\left(\sigma_{M_s} - \sigma_{A_f}\right) H}{2} + \frac{\left(\sigma_{M_s}^2 - \sigma_{A_f}^2\right) \Delta S}{4} + \frac{(a_1 - a_2)}{4} \tag{C.14}$$

Substituting Eqns.(C.7) and (C.11) into the above equation and rearranging, one obtains

$$a_4 + Y_1 = \frac{\left(\sigma_{M_s} - \sigma_{A_f} + \sigma_{M_f} - \sigma_{A_s}\right) H}{4} + \frac{\left(\sigma_{M_s}^2 - \sigma_{A_f}^2 + \sigma_{M_f}^2 - \sigma_{A_s}^2\right) \Delta S}{8} \tag{C.15}$$

Neglecting $\frac{1}{8}\left(\sigma_{M_s}^2 - \sigma_{A_f}^2 + \sigma_{M_f}^2 - \sigma_{A_s}^2\right) \Delta S$, and upon rearranging, the above expression can be written as,

$$Y_1 = \frac{\left(\sigma_{M_s} - \sigma_{A_f} + \sigma_{M_f} - \sigma_{A_s}\right) H}{4} - a_4$$

Substituting the values of σ_{M_s}, σ_{M_f}, σ_{A_s} and σ_{A_f}, and upon solving, one obtains

$$\boxed{Y_1 = \frac{\rho\Delta s_0(M_s + M_f - A_s - A_f)}{4} - a_4} \tag{C.16}$$

- **Condition 5:** Continuity of G at the point of reversal, *i.e.*, $h_f(\xi = \xi_r)|_{\dot{\xi}>0} = h_f(\xi = \xi_r)|_{\dot{\xi}<0}$.

$$\frac{1}{2}a_1\left[\frac{\xi_{r_0}^{n_1+1}}{n_1+1} + \frac{(1-\xi_{r_0})^{n_2+1}}{n_2+1}\right] + (a_3 + a_4)\xi_{r_0}$$
$$= \frac{1}{2}a_2\left[\frac{\xi_{r_0}^{n_3+1}}{n_3+1} + \frac{(1-\xi_{r_0})^{n_4+1}}{n_4+1}\right] + (a_3 - a_4)\xi_{r_0}$$
$$2a_4\xi_{r_0} = \frac{1}{2}a_2\left[\frac{\xi_{r_0}^{n_3+1}}{n_3+1} + \frac{(1-\xi_{r_0})^{n_4+1}}{n_4+1}\right] - \frac{1}{2}a_1\left[\frac{\xi_{r_0}^{n_1+1}}{n_1+1} + \frac{(1-\xi_{r_0})^{n_2+1}}{n_2+1}\right]$$

$$\boxed{a_4 = \frac{a_2}{4}\left[\frac{\xi_r^{n_3}}{n_3+1} + \frac{(1-\xi_r)^{n_4+1}}{\xi_r(n_4+1)}\right] - \frac{a_1}{4}\left[\frac{\xi_r^{n_1}}{n_1+1} + \frac{(1-\xi_r)^{n_2+1}}{\xi_r(n_2+1)}\right]} \tag{C.17}$$

Here, the numerical value of ξ_r, *i.e.*, ξ_{r0} is substituted into above expression to obtain the value of a_4.

Next, following Eqns.(C.5), (C.7) and (C.15), one gets

$$\sigma_{M_s}H + \frac{1}{2}\sigma_{M_s}^2\Delta S + \rho\Delta s_0 T_0 - \rho\Delta u_0 + \left[\frac{\left(\sigma_{M_f} - \sigma_{M_s}\right)H}{2} + \frac{\left(\sigma_{M_f}^2 - \sigma_{M_s}^2\right)\Delta S}{4}\right]$$
$$- a_3 - \left[\frac{\left(\sigma_{M_s} - \sigma_{A_f} + \sigma_{M_f} - \sigma_{A_s}\right)H}{4} + \frac{\left(\sigma_{M_s}^2 - \sigma_{A_f}^2 + \sigma_{M_f}^2 - \sigma_{A_s}^2\right)\Delta S}{8}\right] = 0.$$

Upon solving and rearranging the above equation, one obtains

$$a_3 = \rho\Delta s_0 T_0 - \rho\Delta u_0 + \frac{\left(\sigma_{M_s} + \sigma_{M_f} + \sigma_{A_s} + \sigma_{A_f}\right)}{4} + \frac{\left(\sigma_{M_s}^2 + \sigma_{A_f}^2 + \sigma_{M_f}^2 + \sigma_{A_s}^2\right)\Delta S}{8} \tag{C.18}$$

Substituting the values of σ_{M_s}, σ_{M_f}, σ_{A_s} and σ_{A_f}, and upon solving, one obtains

$$a_3 = \rho\Delta s_0 T_0 - \frac{\rho\Delta s_0\left(M_s + A_f\right)}{2} + \frac{\rho\Delta s_0\left(M_s + A_f + M_f + A_s\right)}{4} - \rho\Delta s_0 T_0$$
$$+ \frac{\left(\sigma_{M_s}^2 + \sigma_{A_f}^2 + \sigma_{M_f}^2 + \sigma_{A_s}^2\right)\Delta S}{8}$$

$$\boxed{a_3 = \frac{\rho\Delta s_0\left(-M_s + M_f + A_s - A_f\right)}{4} + \frac{\left(\sigma_{M_s}^2 + \sigma_{A_f}^2 + \sigma_{M_f}^2 + \sigma_{A_s}^2\right)\Delta S}{8}} \tag{C.19}$$

- **Condition 6:** Beginning of partial reverse transformation (point 'f' in Fig.2.1)

  $\sigma = \sigma_{A_s} = C_A(T_0 - A_s),\ \xi = \xi_{r_f},\ \xi_r = \xi_{r_f},\ T = T_0,\ \Theta = -Y_f$

$$\begin{aligned}
&\sigma_{A_s}H + \frac{1}{2}\sigma_{A_s}^2\Delta S + \rho\Delta s_0 T_0 - \rho\Delta u_0 \\
&\quad - \left[\frac{1}{2}a_2[\xi_{r_f}^{n_3} - (1-\xi_{r_f})^{n_4}] + (a_3 - a_4)\right] = -Y_1 - Y_3(1-\xi_{r_f})\left(e^{\gamma\xi_{r_f}} - 1\right), \\
&\sigma_{A_s}H + \frac{1}{2}\sigma_{A_s}^2\Delta S + \rho\Delta s_0 T_0 - \rho\Delta u_0 - \frac{1}{2}a_2[\xi_{r_f}^{n_3} - (1-\xi_{r_f})^{n_4}] \\
&\quad - a_3 + (a_4 + Y_1) + Y_3(1-\xi_{r_f})\left(e^{\gamma\xi_{r_f}} - 1\right) = 0.
\end{aligned}$$

Substituting Eqns.(C.18) and (C.15) into above equation, one obtains

$$\begin{aligned}
&\sigma_{A_s}H + \frac{1}{2}\sigma_{A_s}^2\Delta S + \rho\Delta s_0 T_0 - \rho\Delta u_0 - \frac{1}{2}a_2[\xi_{r_f}^{n_3} - (1-\xi_{r_f})^{n_4}] \\
&- \left[\rho\Delta s_0 T_0 - \rho\Delta u_0 + \frac{\left(\sigma_{M_s} + \sigma_{M_f} + \sigma_{A_s} + \sigma_{A_f}\right)}{4} + \frac{\left(\sigma_{M_s}^2 + \sigma_{A_f}^2 + \sigma_{M_f}^2 + \sigma_{A_s}^2\right)\Delta S}{8}\right] \\
&+ \left[\frac{\left(\sigma_{M_s} - \sigma_{A_f} + \sigma_{M_f} - \sigma_{A_s}\right)H}{4} + \frac{\left(\sigma_{M_s}^2 - \sigma_{A_f}^2 + \sigma_{M_f}^2 - \sigma_{A_s}^2\right)\Delta S}{8}\right] \\
&\quad + Y_3(1-\xi_{r_f})\left(e^{\gamma\xi_{r_f}} - 1\right) = 0
\end{aligned}$$

Upon solving the above equation, one gets

$$\frac{\left(\sigma_{A_s} - \sigma_{A_f}\right)H}{2} + \frac{\left(\sigma_{A_s}^2 - \sigma_{A_f}^2\right)\Delta S}{4} - \frac{1}{2}a_2[\xi_{r_f}^{n_3} - (1-\xi_{r_f})^{n_4}] + Y_3(1-\xi_{r_f})\left(e^{\gamma\xi_{r_f}} - 1\right) = 0$$

Following Eqn.(C.11), the above equation can be denoted as,

$$Y_3(1-\xi_{r_f})\left(e^{\gamma\xi_{r_f}} - 1\right) = \frac{-a_2}{2} + \frac{a_2[\xi_{r_f}^{n_3} - (1-\xi_{r_f})^{n_4}]}{2}$$

$$\boxed{Y_3 = \frac{-a_2\left[1 - \xi_r^{n_3} + (1-\xi_r)^{n_4}\right]}{2(1-\xi_r)\left(e^{\gamma\xi_r} - 1\right)}} \tag{C.20}$$

Here, the numerical value of ξ_r, *i.e.*, ξ_{r_f} which is the values of ξ at the point of reversal, f, is substituted into above expression to obtain the value of Y_3. Also,

$\xi_{r_f} = \xi_e$, since $e \rightarrow f$ is an elastic path.

- **Condition 7:** Beginning of partial forward transformation (point 'h' in Fig.2.1)

$\sigma = \sigma_{M_s} = C_M(T_0 - M_s),\ \xi = \xi_{r_h},\ \xi_r = \xi_{r_h},\ T = T_0,\ \Theta = Y_f$

$$\begin{aligned}
&\sigma_{M_s}H + \frac{1}{2}\sigma_{M_s}^2\Delta S + \rho\Delta s_0 T_0 - \rho\Delta u_0 \\
&\quad - \left[\frac{1}{2}a_1[\xi_{r_h}^{n_1} - (1-\xi_{r_h})^{n_2}] + (a_3 + a_4)\right] = Y_1 + Y_2\xi_{r_h}\left(e^{\gamma(1-\xi_{r_h})} - 1\right), \\
&\sigma_{M_s}H + \frac{1}{2}\sigma_{M_s}^2\Delta S + \rho\Delta s_0 T_0 - \rho\Delta u_0 - \frac{1}{2}a_1[\xi_{r_h}^{n_1} - (1-\xi_{r_h})^{n_2}] \\
&\quad - a_3 - (a_4 + Y_1) = Y_2\xi_{r_h}\left(e^{\gamma(1-\xi_{r_h})} - 1\right).
\end{aligned}$$

Substituting Eqns.(C.15) and (C.18) into above equation, one obtains

$$\begin{aligned}
&\sigma_{M_s}H + \frac{1}{2}\sigma_{M_s}^2\Delta S + \rho\Delta s_0 T_0 - \rho\Delta u_0 - \frac{1}{2}a_1[\xi_{r_h}^{n_1} - (1-\xi_{r_h})^{n_2}] \\
&- \left[\rho\Delta s_0 T_0 - \rho\Delta u_0 + \frac{\left(\sigma_{M_s} + \sigma_{M_f} + \sigma_{A_s} + \sigma_{A_f}\right)}{4} + \frac{\left(\sigma_{M_s}^2 + \sigma_{A_f}^2 + \sigma_{M_f}^2 + \sigma_{A_s}^2\right)\Delta S}{8}\right] \\
&- \left[\frac{\left(\sigma_{M_s} - \sigma_{A_f} + \sigma_{M_f} - \sigma_{A_s}\right)H}{4} + \frac{\left(\sigma_{M_s}^2 - \sigma_{A_f}^2 + \sigma_{M_f}^2 - \sigma_{A_s}^2\right)\Delta S}{8}\right] \\
&\qquad = Y_2\xi_{r_h}\left(e^{\gamma(1-\xi_{r_h})} - 1\right)
\end{aligned}$$

Upon solving the above equation, one gets

$$\frac{\left(\sigma_{M_s} - \sigma_{M_f}\right)H}{2} + \frac{\left(\sigma_{M_s}^2 - \sigma_{M_f}^2\right)\Delta S}{4} - \frac{1}{2}a_1[\xi_{r_h}^{n_1} - (1-\xi_{r_h})^{n_2}] = Y_2\xi_{r_h}\left(e^{\gamma(1-\xi_{r_h})} - 1\right)$$

Following Eqn.(C.7), the above equation can be denoted as,

$$Y_2\xi_{r_h}\left(e^{\gamma(1-\xi_{r_h})} - 1\right) = \frac{-a_1}{2} - \frac{a_1[\xi_{r_h}^{n_1} - (1-\xi_{r_h})^{n_2}]}{2}$$

$$\boxed{Y_2 = \frac{-a_1\left[1 + \xi_r^{n_1} - (1-\xi_r)^{n_2}\right]}{2\xi_r\left(e^{\gamma(1-\xi_r)} - 1\right)}} \tag{C.21}$$

Here, the numerical value of ξ_r, *i.e.*, ξ_{r_h} which is the values of ξ at the point of reversal, h, is substituted into above expression to obtain the value of Y_2. Also, $\xi_{r_h} = \xi_g$, since $g \rightarrow h$ is an elastic path.

Bibliography

[1] Dimitris C Lagoudas. *Shape memory alloys: modeling and engineering applications*. Springer, 2008.

[2] Alden B Greninger and Victor G Mooradian. Strain transformation in metastable beta copper-zinc and beta copper-Ti alloys. *Aime Trans*, 128:337–369, 1938.

[3] William J Buehler, John V Gilfrich, and RC Wiley. Effect of low-temperature phase changes on the mechanical properties of alloys near composition TiNi. *Journal of applied physics*, 34(5):1475–1477, 1963.

[4] Dieter Stoeckel and Thomas Waram. Use of Ni-Ti shape memory alloys for thermal sensor-actuators. In *Active and adaptive optical components*, volume 1543, pages 382–387. SPIE, 1992.

[5] TW Duerig. Applications of shape memory. In *Materials Science Forum*, volume 56, pages 679–691. Trans Tech Publ, 1990.

[6] Kazuhiro Otsuka and Clarence Marvin Wayman. *Shape memory materials*. Cambridge university press, 1999.

[7] Yves Bellouard, Reymond Clavel, J-E Bidaux, R Gotthardt, and T Sidler. A concept for monolithic shape memory alloy micro-devices. *Le Journal de Physique IV*, 7(C5):C5–603, 1997.

[8] Ming H Wu and LM Schetky. Industrial applications for shape memory alloys. In *Proceedings of the international conference on shape memory and superelastic technologies*, volume 171. The International Organization on Shape Memory and Superelastic Technologies, 2000.

[9] Kazuhiro Otsuka and Tomoyuki Kakeshita. Science and technology of shape-memory alloys: new developments. *mrs bulletin*, 27(2):91–100, 2002.

[10] NB Morgan. Medical shape memory alloy applications-the market and its products. *Materials Science and Engineering: A*, 378(1-2):16–23, 2004.

[11] Yoshihiko Nakamura, Kensuke Onuma, Hiroo Kawakami, and Tsutomu Nakamura. Active forceps for endoscopic surgery. In *Experimental Robotics V: The Fifth International Symposium Barcelona, Catalonia, June 15–18, 1997*, pages 471–480. Springer, 1998.

[12] LG Machado and MA Savi. Medical applications of shape memory alloys. *Brazilian journal of medical and biological research*, 36:683–691, 2003.

[13] Hamed Adldoost, Behnoush Rezaeian Jouibary, and Abolghassem Zabihollah. Design of SMA micro-gripper for minimally invasive surgery. In *2012 19th Iranian conference of biomedical engineering (ICBME)*, pages 97–100. IEEE, 2012.

[14] Minoru Hashimoto, Tsuyoshi Tabata, and Takahiro Yuki. Development of electrically heated SMA active forceps for laparoscopic surgery. In *Proceedings 1999 IEEE International Conference on Robotics and Automation (Cat. No. 99CH36288C)*, volume 3, pages 2372–2377. IEEE, 1999.

[15] Atish Mane, Nilesh Desai, Nilesh Jagtap, Vaibhav Jadhav, and Tushar Nagawade. Review on shape memory alloy on biomedical applications. *Global Journal Of Engineering Science And Researches*, 6(1):229–239, January 2019.

[16] Uddeshya Shukla and Kamal Garg. Journey of smart material from composite to shape memory alloy (SMA), characterization and their applications-a review. *Smart Materials in Medicine*, 2022.

[17] Daniel Amariei, Calin O Miclosina, Ion Vela, Marius Tufoi, and Cornel Mituletu. Contributions to design of systems actuated by shape memory active elements. *International Journal of Mechanical and Mechatronics Engineering*, 4(11):1178–1183, 2010.

[18] Kathryn J De Laurentis and Constantinos Mavroidis. Mechanical design of a shape memory alloy actuated prosthetic hand. *Technology and Health Care*, 10(2):91–106, 2002.

[19] Wei Wang and Sung-Hoon Ahn. Shape memory alloy-based soft gripper with variable stiffness for compliant and effective grasping. *Soft robotics*, 4(4):379–389, 2017.

[20] Filomena Simone, Gianluca Rizzello, and Stefan Seelecke. Metal muscles and nerves-a self-sensing SMA-actuated hand concept. *Smart Materials and Structures*, 26(9):095007, 2017.

[21] Hyung-Il Kim, Min-Woo Han, Sung-Hyuk Song, and Sung-Hoon Ahn. Soft morphing hand driven by SMA tendon wire. *Composites Part B: Engineering*, 105:138–148, 2016.

[22] Fergus Taylor and ChiKit Au. Forced air cooling of shape-memory alloy actuators for a prosthetic hand. *Journal of Computing and Information Science in Engineering*, 16(4), 2016.

[23] Peter L Bishay, Jonathan Fontana, Bret Raquipiso, Julian Rodriguez, M Justin Borreta, Bethany Enos, Thomas Gay, and Kevin Mauricio. Development of a biomimetic transradial prosthetic arm with shape memory alloy muscle wires. *Engineering Research Express*, 2(3):035041, 2020.

[24] Jaronie Mohd Jani, Martin Leary, Aleksandar Subic, and Mark A Gibson. A review of shape memory alloy research, applications and opportunities. *Materials & Design (1980-2015)*, 56:1078–1113, 2014.

[25] Gangbing Song and Ning Ma. Robust control of a shape memory alloy wire actuated flap. *Smart materials and Structures*, 16(6):N51, 2007.

[26] Jan Van Humbeeck. Non-medical applications of shape memory alloys. *Materials Science and Engineering: A*, 273:134–148, 1999.

[27] S Barbarino, S Ameduri, L Lecce, and A Concilio. Wing shape control through an SMA-based device. *Journal of Intelligent Material Systems and Structures*, 20(3):283–296, 2009.

[28] Ugo Icardi and Laura Ferrero. Preliminary study of an adaptive wing with shape memory alloy torsion actuators. *Materials & Design*, 30(10):4200–4210, 2009.

[29] Silvestro Barbarino, EI Saavedra Flores, Rafic M Ajaj, Iman Dayyani, and Michael I Friswell. A review on shape memory alloys with applications to morphing aircraft. *Smart materials and structures*, 23(6):063001, 2014.

[30] Peter L Bishay, Ryan Finden, Shawn Recinos, Christian Alas, Erik Lopez, Dvin Aslanpour, Douglas Flores, and Efrain Gonzalez. Development of an SMA-based camber morphing UAV tail core design. *Smart Materials and Structures*, 28(7):075024, 2019.

[31] Jaronie Mohd Jani, Martin Leary, and Aleksandar Subic. Shape memory alloys in automotive applications. In *Applied Mechanics and Materials*, volume 663, pages 248–253. Trans Tech Publ, 2014.

[32] Eric A Williams, Gordon Shaw, and Mohammad Elahinia. Control of an automotive shape memory alloy mirror actuator. *Mechatronics*, 20(5):527–534, 2010.

[33] T Luchetti, A Zanella, M Biasiotto, and A Saccagno. Electrically actuated antiglare rear-view mirror based on a shape memory alloy actuator. *Journal of materials engineering and performance*, 18(5):717–724, 2009.

[34] Andrea Hein, Daniel Holder, Jonas Maier, and Thomas Maier. Potential analysis of smart materials and methodical approach developing adaptive designs using shape memory alloys. *DS 91: Proceedings of NordDesign 2018, Linköping, Sweden, 14th-17th August 2018*, 2018.

[35] Salvatore Ameduri, Angela Brindisi, Monica Ciminello, Antonio Concilio, Vincenzo Quaranta, and Marco Brandizzi. An SMA seal system for enhanced door sound-

proof performance: Design, prototyping and testing. In *ACTUATOR 2018; 16th International Conference on New Actuators*, pages 1–5. VDE, 2018.

[36] Salvatore Ameduri, Angela Brindisi, Monica Ciminello, Antonio Concilio, Vincenzo Quaranta, and Marco Brandizzi. Car soundproof improvement through an SMA adaptive system. In *Actuators*, volume 7, page 88. MDPI, 2018.

[37] Gangbing Song, N Ma, and H-N Li. Applications of shape memory alloys in civil structures. *Engineering structures*, 28(9):1266–1274, 2006.

[38] Moslem Shahverdi, Christoph Czaderski, and Masoud Motavalli. Iron-based shape memory alloys for prestressed near-surface mounted strengthening of reinforced concrete beams. *Construction and Building Materials*, 112:28–38, 2016.

[39] Hui Qian, Hongnan Li, and Gangbing Song. Experimental investigations of building structure with a superelastic shape memory alloy friction damper subject to seismic loads. *Smart Materials and Structures*, 25(12):125026, 2016.

[40] F Azadpour and AA Maghsoudi. Crack width study for two-span RC beams strengthened with Ni–Ti strands under cyclic loading. *Smart Materials and Structures*, 28(5):055041, 2019.

[41] K Tanaka. A thermomechanical sketch of shape memory effect: One dimensional tensile behavior. *Res Mech.*, 18:251–263, 1986.

[42] C. Liang and C. A. Roger. One-dimensional thermomechanical constitutive relations for shape memory materials. *Journal of Intelligent Material Systems and Structures*, 1(2):207–234, 1990.

[43] L Catherine Brinson. One-dimensional constitutive behavior of shape memory alloys: thermomechanical derivation with non-constant material functions and redefined martensite internal variable. *Journal of intelligent material systems and structures*, 4(2):229–242, 1993.

[44] A Bekker and L Catherine Brinson. Temperature-induced phase transformation in a shape memory alloy: phase diagram based kinetics approach. *Journal of the Mechanics and Physics of Solids*, 45(6):949–988, 1997.

[45] A Bekker and LC Brinson. Phase diagram based description of the hysteresis behavior of shape memory alloys. *Acta materialia*, 46(10):3649–3665, 1998.

[46] Ashish Khandelwal and Vidyashankar R Buravalla. A correction to the brinson's evolution kinetics for shape memory alloys. *Journal of Intelligent Material Systems and Structures*, 19(1):43–46, 2008.

[47] Vidyashankar R Buravalla and Ashish Khandelwal. Differential and integrated form consistency in 1-D phenomenological models for shape memory alloy constitutive behavior. *International journal of solids and structures*, 44(13):4369–4381, 2007.

[48] Vidyashankar Buravalla and Ashish Khandelwal. Evolution kinetics in shape memory alloys under arbitrary loading: experiments and modeling. *Mechanics of materials*, 43(12):807–823, 2011.

[49] Mohammad H Elahinia and Mehdi Ahmadian. An enhanced SMA phenomenological model: I. the shortcomings of the existing models. *Smart materials and structures*, 14(6):1297–1308, 2005.

[50] Mohammad H Elahinia and Mehdi Ahmadian. An enhanced SMA phenomenological model: II. the experimental study. *Smart materials and structures*, 14(6):1309–1319, 2005.

[51] Atanu Banerjee. Simulation of shape memory alloy wire actuator behavior under arbitrary thermo-mechanical loading. *Smart materials and structures*, 21(12):125018, 2012.

[52] James G Boyd and Dimitris C Lagoudas. A thermodynamical constitutive model for shape memory materials. Part I. The monolithic shape memory alloy. *International journal of plasticity*, 12(6):805–842, 1996.

[53] James G Boyd and Dimitris C Lagoudas. A thermodynamical constitutive model for shape memory materials. Part II. The SMA composite material. *International Journal of Plasticity*, 12(7):843–873, 1996.

[54] Zhonghe Bo and Dimitris C Lagoudas. Thermomechanical modeling of polycrystalline SMAs under cyclic loading, Part I: theoretical derivations. *International Journal of Engineering Science*, 37(9):1089–1140, 1999.

[55] Zhonghe Bo and Dimitris C Lagoudas. Thermomechanical modeling of polycrystalline SMAs under cyclic loading, Part III: evolution of plastic strains and two-way shape memory effect. *International Journal of Engineering Science*, 37(9):1175–1203, 1999.

[56] MA Qidwai and DC Lagoudas. Numerical implementation of a shape memory alloy thermomechanical constitutive model using return mapping algorithms. *International Journal for Numerical Methods in Engineering*, 47(6):1123–1168, 2000.

[57] Peter Popov and Dimitris C Lagoudas. A 3-D constitutive model for shape memory alloys incorporating pseudoelasticity and detwinning of self-accommodated martensite. *International Journal of Plasticity*, 23(10-11):1679–1720, 2007.

[58] Miguel M Branco, James M Kelly, and Luís M Guerreiro. An algorithm to simulate the one-dimensional superelastic cyclic behavior of NiTi strings, for civil engineering applications. *Engineering Structures*, 33(12):3737–3747, 2011.

[59] Dimitris Lagoudas, Darren Hartl, Yves Chemisky, Luciano Machado, and Peter Popov. Constitutive model for the numerical analysis of phase transformation in polycrystalline shape memory alloys. *International Journal of Plasticity*, 32:155–183, 2012.

[60] Anargyros A Karakalas, Theodoros T Machairas, Alexandros G Solomou, and Dimitris A Saravanos. Modeling of partial transformation cycles of SMAs with a modified hardening function. *Smart Materials and Structures*, 28(3):035014, 2019.

[61] M Kishore Kumar, K Sakthivel, SM Sivakumar, C Lakshmana Rao, and A Srinivasa. Thermomechanical modeling of hysteresis in SMAs using the dissipationless reference response. *Smart materials and structures*, 16(1):S28, 2007.

[62] KR Rajagopal and AR Srinivasa. On the thermomechanics of shape memory wires. *Zeitschrift für angewandte Mathematik und Physik ZAMP*, 50:459–496, 1999.

[63] Gangbing Song, Brian Kelly, and Brij N Agrawal. Active position control of a shape memory alloy wire actuated composite beam. *Smart Materials and Structures*, 9(5):711, 2000.

[64] G Song, V Chaudhry, and C Batur. Precision tracking control of shape memory alloy actuators using neural networks and a sliding-mode based robust controller. *Smart materials and structures*, 12(2):223, 2003.

[65] Mohammad H Elahinia and Hashem Ashrafiuon. Nonlinear control of a shape memory alloy actuated manipulator. *Journal of Vibration and Acoustics*, 124(4):566–575, 2002.

[66] Yee H Teh and Roy Featherstone. Frequency response analysis of shape memory alloy actuators. In *International conference on smart materials and nanotechnology in engineering*, volume 6423, pages 659–665. SPIE, 2007.

[67] Antonio Visioli. Fuzzy logic based set-point weight tuning of PID controllers. *IEEE Transactions on Systems, Man, and Cybernetics-Part A: systems and humans*, 29(6):587–592, 1999.

[68] Alireza Khodayari, Maryam Talari, and Mohammad Mahdi Kheirikhah. Fuzzy PID controller design for artificial finger based SMA actuators. In *2011 IEEE international conference on fuzzy systems (FUZZ-IEEE 2011)*, pages 727–732. IEEE, 2011.

[69] Koji Ikuta, Masahiro Tsukamoto, and Shigeo Hirose. Shape memory alloy servo actuator system with electric resistance feedback and application for active endoscope. pages 427–430, 1988.

[70] Reg Dunlop and Angelo C Garcia. A nitinol wire actuated stewart platform. In *Australasian conference on robotics and automation*, pages 27–29. Citeseer, 2002.

[71] Z He, KR Gall, and LC Brinson. Use of electrical resistance testing to redefine the transformation kinetics and phase diagram for shape-memory alloys. *Metallurgical and materials transactions A*, 37:579–587, 2006.

[72] Zhi-Qiang Liu, Hui Li, Wen-Li Chen, and Jin-Ping Ou. Study on strain-sense property of TiNi and TiNiCu shape memory alloys. *Advances in Structural Engineering*, 8(6):637–643, 2005.

[73] Sushant M Dutta and Fathi H Ghorbel. Differential hysteresis modeling of a shape memory alloy wire actuator. *IEEE/ASME Transactions on Mechatronics*, 10(2):189–197, 2005.

[74] Di Cui, Gangbing Song, and Hongnan Li. Modeling of the electrical resistance of shape memory alloy wires. *Smart Materials and Structures*, 19(5):055019, 2010.

[75] Yifan Lu, Rongru Zhang, Ye Xu, Lei Wang, and Honghao Yue. Resistance characteristics of SMA actuator based on the variable speed phase transformation constitutive model. *Materials*, 13(6):1479, 2020.

[76] Yifan Lu, Rongru Zhang, Zhijie Xie, Honghao Yue, and Lei Wang. A new variable speed phase transformation constitutive model of shape memory alloys. *Materials Research Express*, 6(10):105705, 2019.

[77] V Novák, P Šittner, GN Dayananda, FM Braz-Fernandes, and KK Mahesh. Electric resistance variation of NiTi shape memory alloy wires in thermomechanical tests: Experiments and simulation. *Materials Science and Engineering: A*, 481:127–133, 2008.

[78] Ravindra Brammajyosula, Vidyashankar Buravalla, and Ashish Khandelwal. Model for resistance evolution in shape memory alloys including R-phase. *Smart materials and structures*, 20(3):035015, 2011.

[79] Kostyantyn Malukhin and KF Ehmann. An experimental investigation of the feasibility of self-sensing shape memory alloy based actuators. *Journal of Manufacturing Science and Engineering*, 130(3):031109, 2008.

[80] Stephen J Furst and Stefan Seelecke. Modeling and experimental characterization of the stress, strain, and resistance of shape memory alloy actuator wires with controlled power input. *Journal of Intelligent Material Systems and Structures*, 23(11):1233–1247, 2012.

[81] N Lewis, A York, and S Seelecke. Experimental characterization of self-sensing SMA actuators under controlled convective cooling. *Smart Materials and Structures*, 22(9):094012, 2013.

[82] Josephine Selvarani Ruth D, Sunjai Nakshatharan S, and K Dhanalakshmi. Differential resistance feedback control of a self-sensing shape memory alloy actuated system. *ISA transactions*, 53(2):289–297, 2014.

[83] K Dhanalakshmi and Josephine Selvarani Ruth D. Shape memory alloy wire for force sensing. *IEEE Sensors Journal*, 17(4):967–975, 2017.

[84] Hema Gurung and Atanu Banerjee. Development of an extended kalman filter for the self-sensing application of a spring-biased shape memory alloy wire actuator. *Smart Materials and Structures*, 25(2):025012, 2016.

[85] Hema Gurung and Atanu Banerjee. Self-sensing shape memory alloy wire actuator based on unscented kalman filter. *Sensors and Actuators A: Physical*, 251:258–265, 2016.

[86] Austin Gurley, Tyler Ross Lambert, David Beale, and Royall Broughton. Dual measurement self-sensing technique of NiTi actuators for use in robust control. *Smart Materials and Structures*, 26(10):105050, 2017.

[87] Tyler Ross Lambert, Austin Gurley, and David Beale. SMA actuator material model with self-sensing and sliding-mode control; experiment and multibody dynamics model. *Smart Materials and Structures*, 26(3):035004, 2017.

[88] Nima Zamani, Mir Behrad Khamesee, and Mohammad Ibraheem Khan. Novel laser processed shape memory alloy actuator design with an embedded strain gauge sensor using dual resistance measurements. Part I: Fabrication and model-based position estimation. *Sensors and Actuators A: Physical*, 263:234–245, 2017.

[89] Sang-Hak Lee and Sang-Woo Kim. Improved position control of shape memory alloy actuator using the self-sensing model. *Sensors and Actuators A: Physical*, 297:111529, 2019.

[90] Chao-Chieh Lan and Chen-Hsien Fan. An accurate self-sensing method for the control of shape memory alloy actuated flexures. *Sensors and Actuators A: physical*, 163(1):323–332, 2010.

[91] Ermira Junita Abdullah, Josu Soriano, Iñaki Fernández de Bastida Garrido, and Dayang Laila Abdul Majid. Accurate position control of shape memory alloy actuation using displacement feedback and self-sensing system. *Microsystem Technologies*, 27:2553–2566, 2021.

[92] Jing-Han Guan, Yong-Chen Pei, Ji-Tuo Wu, Bao-Hua Wang, Wen-Chao Sui, and Sheng-Run Li. A self-sensing and robust resistance phase transition detection method for the displacement estimation of shape memory alloy wires. *Mechanical Systems and Signal Processing*, 170:108862, 2022.

[93] Hari N Bhargaw, Samarth Singh, Bhausaheb Ashok Botre, SA Akbar, SAR Hashmi, and Poonam Sinha. Deep neural network-based physics-inspired model of self-sensing displacement estimation for antagonistic shape memory alloy actuator. *IEEE Sensors Journal*, 22(4):3254–3262, 2022.

[94] Hema Gurung. *Self-sensing shape memory alloy wire actuators using Kalman filters*. PhD thesis, Indian Institute of Technology Guwahati, 2017.

[95] Hossein Talebi, Hossein Golestanian, Mohammad Reza Zakerzadeh, and Hadi Homaei. Thermoelectric heat transfer modeling of shape memory alloy actuators. In *The 22st Annual International Conference on Mechanical Engineering-ISME2014, Ahvaz, Iran*, 2014.

[96] Vijay Choyal, Suhel Khan, Prabu SS Mani, IA Palani, and Pushpendra Singh. Active and passive multicycle actuation characteristics of shape memory alloy-based adaptive composite structures. *Smart Materials and Structures*, 30(9):095022, 2021.

[97] Andrew J Theodore and Peter L Bishay. Experimental analysis of fiber-reinforced laminated composite plates with embedded SMA wire actuators. *Composite Structures*, 292:115678, 2022.

[98] Hyo Jik Lee and Jung Ju Lee. Time delay control of a shape memory alloy actuator. *Smart Materials and Structures*, 13(1):227, 2004.

[99] Nguyen Trong Tai and Kyoung Kwan Ahn. Adaptive proportional–integral–derivative tuning sliding mode control for a shape memory alloy actuator. *Smart Materials and Structures*, 20(5):055010, 2011.

[100] J Jayender, RV Patel, S Nikumb, and M Ostojic. Modelling and gain scheduled control of shape memory alloy actuators. In *Proceedings of 2005 IEEE Conference on Control Applications, 2005. CCA 2005.*, pages 767–772. IEEE, 2005.

[101] Maria Fotopoulou, Stefanos Petridis, Ioannis Karachalios, and Dimitrios Rakopoulos. A review on distribution system state estimation algorithms. *Applied Sciences*, 12(21):11073, 2022.

[102] Monowar Hossain, ME Haque, and Mohammad Taufiqul Arif. Kalman filtering techniques for the online model parameters and state of charge estimation of the Li-ion batteries: A comparative analysis. *Journal of Energy Storage*, 51:104174, 2022.

[103] Masood Ul Hassan, Sajeeb Saha, Md Enamul Haque, Shama Islam, Apel Mahmud, and Nishad Mendis. A comprehensive review of battery state of charge estimation techniques. *Sustainable Energy Technologies and Assessments*, 54:102801, 2022.

[104] Chong Shen, Zesen Bai, Huiliang Cao, Ke Xu, Chenguang Wang, Huaiyu Zhang, Ding Wang, Jun Tang, and Jun Liu. Optical flow sensor/INS/magnetometer inte-

grated navigation system for MAV in GPS-denied environment. *Journal of Sensors*, 2016.

[105] Dan Simon. *Optimal state estimation: Kalman, H infinity, and nonlinear approaches*. John Wiley & Sons, 2006.

[106] A Bhattacharyya, DC Lagoudas, Yand Wang, and VK Kinra. On the role of thermoelectric heat transfer in the design of SMA actuators: theoretical modeling and experiment. *Smart materials and structures*, 4(4):252, 1995.

[107] MG Faulkner, JJ Amalraj, and A Bhattacharyya. Experimental determination of thermal and electrical properties of Ni-Ti shape memory wires. *Smart Materials and Structures*, 9(5):632, 2000.

[108] Muhammad A Qidwai, Abhijit Bhattacharyya, Ivan Vahhi, and Sergei Pulnev. Initial investigation in actuator design using high-temperature shape memory alloy. In *Smart Structures and Materials 2003: Active Materials: Behavior and Mechanics*, volume 5053, pages 81–91. SPIE, 2003.

[109] Takahisa Kobayashi and Donald L Simon. Application of a bank of Kalman filters for aircraft engine fault diagnostics. In *Turbo Expo: Power for Land, Sea, and Air*, volume 36843, pages 461–470, 2003.

[110] Dan Simon and Donald L Simon. Aircraft turbofan engine health estimation using constrained kalman filtering. *J. Eng. Gas Turbines Power*, 127(2):323–328, 2005.

[111] Huazhen Fang, Ning Tian, Yebin Wang, MengChu Zhou, and Mulugeta A Haile. Nonlinear Bayesian estimation: From Kalman filtering to a broader horizon. *IEEE/CAA Journal of Automatica Sinica*, 5(2):401–417, 2018.

[112] PM Djurić, J Zhang, Tadesse Ghirmai, Y Huang, and Jayesh H Kotecha. Applications of particle filtering to communications: A review. In *Signal Processing Conference, 2002 11th European*, pages 1–4. IEEE, 2002.

[113] Sebastian Thrun. Particle filters in robotics. In *Proceedings of the Eighteenth conference on Uncertainty in artificial intelligence*, pages 511–518. Morgan Kaufmann Publishers Inc., 2002.

[114] Ernest J Ohlmeyer and PK Menon. Applications of the particle filter for multi-object tracking and classification. In *American Control Conference (ACC), 2013*, pages 6181–6186. IEEE, 2013.

[115] Georges Oppenheim, Anne Philippe, and Jean de Rigal. The particle filters and their applications. *Chemometrics and Intelligent Laboratory Systems*, 91(1):87–93, 2008.

[116] Anna Elena Tirri, Giancarmine Fasano, Domenico Accardo, and Antonio Moccia. Particle filtering for obstacle tracking in UAS sense and avoid applications. *The Scientific World Journal*, 2014, 2014.

[117] Jonathan Poterjoy, Louis Wicker, and Mark Buehner. Progress toward the application of a localized particle filter for numerical weather prediction. *Monthly Weather Review*, 147(4):1107–1126, 2019.

[118] Salijona Dyrmishi and Amnir Hadachi. Mobile positioning and trajectory reconstruction based on mobile phone network data: A tentative using particle filter. In *2021 7th International Conference on Models and Technologies for Intelligent Transportation Systems (MT-ITS)*, pages 1–7. IEEE, 2021.

[119] Anil K Chopra. *Dynamics of structures*. Pearson Education India, 2007.

[120] N Ma, G Song, and HJ Lee. Position control of shape memory alloy actuators with internal electrical resistance feedback using neural networks. *Smart materials and structures*, 13(4):777, 2004.

[121] Estibaliz Asua, Victor Etxebarria, and Alfredo García-Arribas. Neural network-based micropositioning control of smart shape memory alloy actuators. *Engineering Applications of Artificial Intelligence*, 21(5):796–804, 2008.

[122] P Senthilkumar and M Umapathy. Use of load generated by a shape memory alloy for its position control with a neural network estimator. *Journal of Vibration and Control*, 20(11):1707–1717, 2014.

[123] Hema Gurung and Atanu Banerjee. Self-sensing SMA actuator using extended kalman filter and artificial neural network. *Procedia Engineering*, 144:629–634, 2016.

[124] Bhagoji Bapurao Sul, Chinari Subhechha Subudhi, and K Dhanalakshmi. Neural network based displacement modeling of shape memory alloy spring actuator. In *2018 IEEE SENSORS*, pages 1–4. IEEE, 2018.

[125] Jennifer C Hannen, John H Crews, and Gregory D Buckner. Indirect intelligent sliding mode control of a shape memory alloy actuated flexible beam using hysteretic recurrent neural networks. *Smart Materials and Structures*, 21(8):085015, 2012.

[126] Han Wang and Gangbing Song. Innovative NARX recurrent neural network model for ultra-thin shape memory alloy wire. *Neurocomputing*, 134:289–295, 2014.

[127] Igor Ruvinov, Nima Zamani, Norman Y Zhou, and Mohammad Ibraheem Khan. Novel laser processed shape memory alloy actuator design with an embedded strain gauge sensor using dual resistance measurements. Part II: Recurrent neural network-based position and force estimation. *Sensors and Actuators A: Physical*, 313:112188, 2020.